Transport Processes in Multicomponent Lithium-Ion Electrolytes

Andrew A. Wang

Department of Engineering Science
University of Oxford

A thesis submitted for the degree of Doctor of Philosophy

Trinity 2022

Abstract

This dissertation attends to the processes by which charged and neutral species are transported in lithium-ion electrolytes. Within batteries, electrolytic solutions interact with electrodes to allow charge — and hence energy — to be harmoniously stored and transferred. Thus far, electrolyte engineering remains an underexploited frontier to advance energy storage technologies.

In this dissertation, I take a 'middle-out' approach, studying the responses of electrolytes at the continuum level to understand fundamental concentration and voltage polarisation phenomena. In this way, the work complements 'top-down' (device-level) and 'bottom-up' (molecular-scale) approaches. The insights presented can improve battery control, optimise cell architecture, and evaluate unique formulations.

The work first focuses on experimental design for property characterization. I develop a novel shifting-reference concentration-cell method, which I embed within a broader suite of tests to extract transport and thermodynamic properties of electrolytic solutions. These protocols, based on Newman's concentrated-solution theory, were validated on disparate electrolyte solvation structures. Subsequent chapters build upon this foundation to analyse a range of carbonate solvents, both linear and cyclic, with lithium hexafluorophosphate from high dilution to saturation.

Potentiometric magnetic-resonance imaging is then used to study superconcentrated binary electrolytes. Despite the electrolyte systems of interest exhibiting severe thermodynamic nonideality and complex higher-order speciation, a three-species model — accounting for convective processes — proves to predict the measured microscopic ion distributions and voltages under applied currents. By deducting the solution-phase signal, lithium-metal interfaces can also be isolated to elucidate the confounding consequences of superconcentration on transport and reaction kinetics.

Next, I probed cosolvent segregation in multicomponent ternary (two solvent, one salt) electrolytes with the help of machine-learning techniques. Counter to what state-of-the-art continuum models of battery electrolytes assume, neutral species are shown to migrate under electric fields, such that electrodes encounter intra-cycle solvent-composition swings. This effect illuminates new guiding principles for electrolyte discovery.

More broadly, I posit that macroscopically observable transport phenomena should play an active role in informing battery development. The contributions presented here are expected to be generalisable to conceptually equivalent electrolyte chemistries comprising salts, solvents, and additives.

Transport Processes in Multicomponent Lithium-Ion Electrolytes



Andrew A. Wang

Department of Engineering Science

University of Oxford

A thesis submitted for the degree of

Doctor of Philosophy

Trinity 2022

Acknowledgements

I express my sincerest gratitude for the guidance provided by my thesis advisor: Professor Charles Monroe. His analytical rigour, lucid insight, and creative flair have been inspiring to both the scientist and engineer in me. Throughout this DPhil degree, Charles has been generous with resources, support, autonomy, and patience when needed. I am proud to have flourished as an independent researcher under his mentorship here at the University of Oxford.

It has been an honour to work alongside my amazing colleagues in the Monroe Research Group. Thank you to senior members Priyamvada Goyal, Saber Hou, and Guanchen Li for embracing and encouraging my eagerness in the early days. I am particularly grateful to Saber for paving the experimental runway that set my research trajectory. Kirk "Dirk" Smith and Howie "Howard" Chu were my closest co-conspirators in the laboratory. Together we indulged in lab equipment maintenance and 45-minute vintage Vine compilations, though not at the same time. I will forever treasure the antics that kept us sane through this degree and global pandemic. Current and former members Alexander Van-Brunt, Taeho Jung, Rohit Rungta, Amangeldi Torayev, Zeyang Geng, Jie Lin, and Maxim Zyskin have been a continued source of learning and rounded out my fond experiences with the group. I am excited to celebrate their future accomplishments. I must also extend my thanks to project managers Gemma, Ralph, and Helen, who have been our pillars in the department.

Professor David Howey has also been a much appreciated advocate of mine. I have thoroughly enjoyed interacting with my friends Trishna, Jorn, Sam, Antti, Gosia, and Adam in the Battery Intelligence Lab. Special mention goes to Trishna Raj for her great choreography at Priyam's wedding, Jorn Reniers for serving both great Pimms and as a batteries-rowing bridge, and Samuel Greenbank for teaching me fancy regression.

I am indebted to the research partnerships forged with Anna Gunnarsdóttir from the Grey Group, Jack Fawdon from the Pasta Group, and the wider Faraday Institution Multi-scale Modelling community. Thank you for expanding my research perspectives during our fruitful collaborations.

My DPhil experience was also enriched by the opportunity to supervise and learn from several undergraduates and master's students. Minnie Karanjavala, Joshua Ilelaboye, Andrew Huang, Aaron Chen, Tina Mu, Delia Persa, and Sara Helin have all impressed me with their adept and inquisitive natures. Their exuberant personalities have been a joy to have in our group over the summers.

Previous mentors have played an indispensable role in my career path. For that, I give thanks to my own graduate students Jacob Thelen, Whitney Loo, and Michael Galluzzo from the Balsara Lab back at UC Berkeley. Professors Nitash Balsara and Bryan McCloskey both provided me with introductory opportunities in the field of electrochemistry. I also appreciate the direction from my industry mentors Sarah Stewart, Jake Christensen, and Sanketh Gowda.

Building out Intercalation Station has helped me develop my own voice in the battery industry. I have learned so much in the process with my cofounder Nicholas Yiu, and we should be proud to have created a valued knowledge platform for the wider energy storage community. Ethan, Pooja, Gaël and the rest of our eclectic team have been an absolute joy to work with.

Many bonds were formed during these years in Oxford. My flatmates, the Botley Boys John, Andy, Peter, Marius, and Botley Girl Rand, threw the best lockdown formal dinners and fiercely contested board-game sessions. The entire Wolfson College Boat Club taught me the joy of rowing. I will especially miss my time with the M1 crew, and going full-send down the river during bumps racing. Thank you to Mary, Jorn, James, Adam, Kit, Ben, and Andy of the Pub-Wolves gang for our jaunts across Oxford's best pubs. The Subtle Asians of Keble: David, Sabrina, Andre, Jack, and Sydney provided me with my cultural fix during our very scientific dumpling-making nights. Hours of basketball were also played with the St Cross and Kellogg squad on the Iffley courts. I also thank the Begbroke Science Park minibus shuttle for encouraging my passion for cycle commuting.

Old friends across the world have also been a constant fountain of entertainment. I'm still not sure how any work got done with all the activity in the Muted and TTOPC chats spanning more than five timezones and four messaging platforms. The A-Class mates back in New Zealand have also kept me in touch with home. To the late Daniel Abaya Duazo, the memory of your love is your greatest gift to us friends. I know you must have enjoyed Cal's recent Big-Game wins as much as we did.

Most importantly, my family has been a source of unconditional love and support. My grandparents Wang Tianwen (王天文), Yun Zhimei (云志梅), Yang Xiangbi (杨襄璧), and Liu Fengming (刘凤鸣) instilled respect for scholarly endeavours. My parents have provided me with every opportunity imaginable, and for that privilege, I am forever grateful. With this DPhil, I scale the academic trail blazed by my grandfather Yang Xiangbi, Professor of Mechanical Engineering, and my father Weidong Wang, PhD in Electrochemical Engineering. Their shoulders provide the confident stage on which I stand. My mother, Qing Yang, receives my deepest acknowledgement for teaching me the value of hard work and raising me to be all that I am capable of being. Finally, my thanks go to my partner Margie Zhou, whose strength of character and unwavering support has been a constant source of inspiration. I owe to her more than she would ever claim.

It takes a village to finish a DPhil and I dedicate this work to you all.

List of Papers

This thesis is established on the following articles:

1. *"Shifting-reference concentration cells to refine composition-dependent transport characterization of binary lithium-ion electrolytes"*
   A.A. Wang, T. Hou, M. Karanjavala, C.W. Monroe
   Electrochimica Acta, vol. 358. p. 136688, **(2020)**

2. *"Potentiometric MRI of a Superconcentrated Lithium Electrolyte: Testing the Irreversible Thermodynamics Approach"*
   A.A. Wang, A.B. Gunnarsdóttir, J. Fawdon,
   M. Pasta, C.P. Grey, C.W. Monroe
   ACS Energy Letters, vol. 6, no. 9., pp. 3086–3095, **(2021)**

3. *"Review of parameterisation and a novel database (LiionDB) for continuum Li-ion battery models"*
   A.A. Wang, S.E.J. O'Kane, F.B. Planella, J. Le Houx, K. O'Regan, M. Zyskin, J. Edge, C.W. Monroe, S.J. Cooper, D.A. Howey, E. Kendrick, J.M. Foster
   Progress in Energy, vol. 4, no. 3., p. 032004, **(2022)**

4. *"Current-driven solvent segregation in lithium-ion battery electrolytes"*
   A.A. Wang, S. Greenbank, G. Li, D.A. Howey, C.W. Monroe
   Cell Reports Physical Science, p. 101047, **(2022)**

5. *"Rethinking electrolyte transport: Which comes first, the property or the effect?"*
   A.A. Wang, D.A. Howey, C.W. Monroe
   Manuscript in preparation, **(2022)**

Abstract

This dissertation attends to the processes by which charged and neutral species are transported in lithium-ion electrolytes. Within batteries, electrolytic solutions interact with electrodes to allow charge — and hence energy — to be harmoniously stored and transferred. Thus far, electrolyte engineering remains an underexploited frontier to advance energy storage technologies.

In this dissertation, I take a 'middle-out' approach, studying the responses of electrolytes at the continuum level to understand fundamental concentration and voltage polarisation phenomena. In this way, the work complements 'top-down' (device-level) and 'bottom-up' (molecular-scale) approaches. The insights presented can improve battery control, optimise cell architecture, and evaluate unique formulations.

The work first focuses on experimental design for property characterization. I develop a novel shifting-reference concentration-cell method, which I embed within a broader suite of tests to extract transport and thermodynamic properties of electrolytic solutions. These protocols, based on Newman's concentrated-solution theory, were validated on disparate electrolyte solvation structures. Subsequent chapters build upon this foundation to analyse a range of carbonate solvents, both linear and cyclic, with lithium hexafluorophosphate from high dilution to saturation.

Potentiometric magnetic-resonance imaging is then used to study superconcentrated binary electrolytes. Despite the electrolyte systems of interest exhibiting severe thermodynamic nonideality and complex higher-order speciation, a three-species model — accounting for convective processes — proves to predict the measured microscopic ion distributions and voltages under applied currents. By deducting the solution-phase signal, lithium-metal interfaces can also be isolated to elucidate the confounding consequences of superconcentration on transport and reaction kinetics.

Next, I probed cosolvent segregation in multicomponent ternary (two solvent, one salt) electrolytes with the help of machine-learning techniques. Counter to what state-of-the-art continuum models of battery electrolytes assume, neutral species are shown to migrate under electric fields, such that electrodes encounter intra-cycle solvent-composition swings. This effect illuminates new guiding principles for electrolyte discovery.

More broadly, I posit that macroscopically observable transport phenomena should play an active role in informing battery development. The contributions presented here are expected to be generalisable to conceptually equivalent electrolyte chemistries comprising salts, solvents, and additives.

Contents

List of Figures **ix**

1 Introduction **1**
1.1 Characteristics of performant liquid battery electrolytes 2
1.1.1 Fundamental aspects of electrolytes 2
1.1.2 Device and cell-level considerations 5
1.1.3 Micro-scale properties 6
1.1.4 Bulk electrolyte transport 7
1.2 Impact of electrolyte transport in emerging cell designs and applications 8
1.3 The role of properties and models in describing transport phenomena 10
1.3.1 Dilute-solution theory 11
1.3.2 Concentrated-solution theory 13
1.3.3 Inclusion of solute-volume effects 15
1.3.4 Further extensions for multicomponent-solutions 17
1.4 Ensuring the longevity of transport studies 18
1.4.1 Raw experimental results are model independent 19
1.5 Outline of this dissertation 20
1.A Appendices 23
1.A.1 Full-cell model sensitivity analyses 23

2 Shifting-reference concentration cells to refine composition-dependent transport characterization of binary lithium-ion electrolytes **28**
2.1 Introduction 29
2.2 Experimental 31
2.2.1 Electrolyte preparation 31
2.2.2 Densitometry and composition 32
2.2.3 Viscometry 32
2.2.4 Hittorf experiment 33
2.2.5 Shifting-reference concentration cells 34
2.2.6 Ionic conductivity 37
2.2.7 Restricted diffusion 38
2.3 Results 39

2.3.1 Density and composition . . . 39
2.3.2 Transference number . . . 40
2.3.3 Thermodynamic factor . . . 42
2.3.4 Conductivity, viscosity, and Stokes law model . . . 46
2.3.5 Diffusion coefficient . . . 50
2.3.6 Onsager–Stefan–Maxwell coefficients . . . 51
2.3.7 On ion association . . . 54
2.3.8 Parameter summary and validation . . . 56
2.4 Conclusion . . . 59
2.A Appendices . . . 60
2.A.1 Partial molar volumes . . . 60
2.A.2 Validation of property correlations for $LiPF_6$:EMC . . . 61
2.B Supplementary data . . . 61
2.B.1 Raw data measurements . . . 61
2.B.2 Fitting process for equivalent conductance . . . 69
2.B.3 MacMullin geometry correction . . . 70
2.B.4 Parameter confidence intervals . . . 72

3 Potentiometric MRI of a superconcentrated lithium electrolyte: Testing the irreversible thermodynamics approach 75
3.1 Introduction . . . 76
3.2 Results and discussion . . . 80
3.2.1 Species interactions increase with salt molarity . . . 80
3.2.2 Ex-situ property measurements . . . 82
3.2.3 Potentiometric MRI . . . 85
3.2.4 Voltametric validation . . . 89
3.3 Conclusion . . . 92
3.A Experimental procedures . . . 93
3.A.1 Preparation of $LiPF_6$:EMC solutions . . . 93
3.A.2 Ex-situ transport and thermodynamic property characterization 93
3.A.3 Raman spectroscopy . . . 96
3.A.4 Potentiometric MRI . . . 96
3.B Supporting discussion . . . 97
3.B.1 Transport model formulation with solute volume effects . . . 97
3.B.2 Partial molar volume, composition bases, thermodynamic factor 98
3.B.3 Transport and thermodynamic property correlations . . . 99
3.B.4 Onsager–Stefan–Maxwell diffusion coefficients . . . 100
3.B.5 Raman spectra . . . 101
3.B.6 In-situ MRI experiment . . . 104
3.B.7 Electrochemical response and surface kinetics analysis . . . 107

3.B.8 Dynamic viscosities 111
3.B.9 Other raw data 111

4 Current-driven solvent segregation in lithium-ion electrolytes 115
4.1 Introduction 116
4.2 Results and discussion 118
4.2.1 Data-driven composition analysis 118
4.2.2 Hittorf results indicate cosolvent segregation 121
4.2.3 Amplification of polarization at boundaries 123
4.3 Conclusion 127
4.A Experimental procedures 129
4.A.1 Electrolyte formulation & physicochemical property measurements 129
4.A.2 Hittorf cell experimental procedure 129
4.A.3 Gaussian process regression 131
4.B Supporting Discussion 132
4.B.1 Physicochemical training dataset 132
4.B.2 Cross-validation of the GP regression model 133
4.B.3 Visualizing the GP regression-model fit 134
4.B.4 Multicomponent transport model 136
4.B.5 Hittorf transference number calculation 138

5 Conclusions 141

References 145

List of Figures

1.1 Schematic of a lithium-ion cell . . . 3
1.2 Impact of electrolyte transport on cell performance . . . 9
1.3 Survey of electrolyte transport and thermodynamic properties . . . 11
1.4 Relation ship between raw data, model, and parameter . . . 20
1.A.1 Conductivity performance sensitivity . . . 24
1.A.2 Diffusivity performance sensitivity . . . 25
1.A.3 Transference number performance sensitivity . . . 25
1.A.4 Thermodynamic factor performance sensitivity . . . 26
1.A.5 Overpotential sensitivity to property scalings . . . 26

2.1 Overview of shifting-reference concentration-cell experiment . . . 35
2.2 Restricted diffusion coin cell schematic . . . 38
2.3 Density/composition measurements for $LiPF_6$:EMC . . . 40
2.4 Hittorf measurements for the cation transference number t_+^0 of Li^+ relative to EMC . . . 41
2.5 Liquid-junction potentials and thermodynamic factors for $LiPF_6$:EMC and $LiPF_6$:PC . . . 44
2.6 Equivalent conductance for $LiPF_6$:EMC and $LiPF_6$:PC . . . 47
2.7 Dynamic viscosity for $LiPF_6$:EMC and $LiPF_6$:PC . . . 48
2.8 Walden analysis for $LiPF_6$:EMC and $LiPF_6$:PC . . . 50
2.9 Diffusion coefficients for $LiPF_6$:EMC . . . 52
2.10 Stefan–Maxwell coefficients for $LiPF_6$:EMC . . . 55
2.A.1 Partial molar volumes for $LiPF_6$:EMC . . . 60
2.A.2 Validation of property correlations for $LiPF_6$:EMC . . . 61
2.B.1 Measured ionic condutivities for $LiPF_6$:EMC . . . 66
2.B.2 Voltage relaxation data from restricted diffusion measurements . . . 68
2.B.3 Bruggeman exponent spread from restricted diffusion . . . 71

3.1 Variation of physicochemical properties and molecular interactions with salt concentration from 0 M to saturation . . . 81
3.2 Transport and thermodynamics properties for $LiPF_6$:EMC . . . 84
3.3 Comparison between simulated and measured potentiometric MRI profiles for superconcentrated $LiPF_6$:EMC . . . 87

3.4 Voltage response during galvaonstatic polarization and open-circuit relaxation . . . 90
3.A.1 Open circuit voltametric response during restricted diffusion experiment . . . 94
3.A.2 Schematic of Hittorf cell experiment . . . 95
3.B.1 Onsager drag coefficients . . . 102
3.B.2 Full Raman spectra for $LiPF_6$:EMC . . . 102
3.B.3 Stacked Raman spectra in the range of 720 – 780 cm^{-1} for PF_6^- and 920 – 980 cm^{-1} . . . 103
3.B.4 Position of max peak height for PF_6^- with concentration. . . . 104
3.B.5 Schematic of cylindrical MRI cell . . . 104
3.B.6 RF signal and calibration cell for MRI experiment . . . 105
3.B.7 Initial and final intensity profiles for MRI experiment . . . 105
3.B.8 Low-pass-filtering timeseries composition data . . . 106
3.B.9 Comparison between simulated and measured potentiometric MRI profiles for 2 M $LiPF_6$:EMC . . . 107
3.B.10 Surface overpotential and surface concentration during polarization step . . . 110
3.B.11 Effective exchange current density . . . 110
3.B.12 Dynamic viscosities measured for $LiPF_6$:EMC . . . 111

4.1 Hittorf experiment and Gaussian process regression analysis of cosolvent segregation . . . 119
4.2 Comparison of Hittorf polarizations with predictions of the single-solvent approximation . . . 122
4.3 Dynamic Hittorf salt and solvent compositions predicted by four-component transport model . . . 126
4.4 Generalized degree of solvent-segregation under steady limiting-current conditions . . . 127
4.A.1 Representative Hittorf electrochemical polarization curve . . . 130
4.B.1 Physicochemical property variation with respect to the mass fractions of $LiPF_6$, EC, and EMC . . . 132
4.B.2 GPR model uncertainty . . . 133
4.B.3 Cross validation of the GP regression model . . . 134
4.B.4 Ternary composition slice for GPR visualisation . . . 135
4.B.5 Predicted physicochemical properties using GPR model . . . 136

Nomenclature

Roman

A	Cross-sectional area. [m^2]
b	Bruggeman exponent. [unitless]
c_T	Total particle molarity. [mol/m^3]
c_i	Molar concentration of species i. [mol/m^3]
$\mathscr{D}$	Thermodynamic diffusion coefficient. [m^2/s]
$\mathscr{D}_{ij}$	Stefan–Maxwell binary diffusion coefficient between species i and j. [m^2/s]
D	Fickian diffusion coefficient. [m^2/s]
$D_\times$	Cross diffusion coefficient. [m^2/s]
D_i	Ideal-dilute self-diffusion coefficient of species i. [m^2/s]
F	Faraday's constant, 96485.3 C/mol.
f_{+-}	Mean molar activity coefficient on a molar basis.
ΔG_{el}	Electrostatic Gibbs free energy of solvation. [J]
$\vec{i}$	Current density. [A/m^2]
i_0	Exchange current density. [A/m^2]
I_{pulse}	Applied current pulse. [A]
K_{ij}	Frictional drag coefficients between species i and j. [$N{\cdot}s/m^4$]
L	Domain thickness. [m]
L_{ij}	Onsager correlation decay rates between species i and j. [$mol^2/J{\cdot}m{\cdot}s$]
k_i	Kinetic reaction rate constant of reaction i. [unitless]
M_i	Molar mass of species i. [kg/mol]
m_i	Molality of species i. [mol/kg]
$\vec{N}_i$	Molar flux of species i. [$mol/m^2{\cdot}s$]
n	Number of moles. [mol]
N_A	Avogadro's number, $6.0221{\times}10^{23}$ mol^{-1}

p	Pressure. [Pa]
Q	Total charge passed. [C]
q	Bjerrum critical distance. [m]
R	Universal gas constant, 8.314 J/mol·K.
R_+	Stokes solvated cation radius. [m]
T	Absolute temperature. [K]
t	Time duration. [s]
t_+	Cation transport number. [unitless]
t_+^0	Cation transference number with reference to the solvent. [unitless]
ΔU	Measured potential difference. [V]
u_+	Cation mobility. [m^2/s·V]
$\overline{V}_i$	Partial molar volume of species i. [m^3/mol]
$\vec{v}_i$	Velocity of species i. [m/s]
V_{chamber}	Chamber volume in Hittorf cell. [L]
y_i	Particle fraction of species i. [unitless]
z_i	Equivalent charge of species i. [unitless]

Greek

α	Inverse MacMullin number. [unitless]
β	Charge transfer symmetry factor. [unitless]
γ_{+-}	Mean molar activity coefficient on a molal basis. [unitless]
ε	Porosity. [unitless]
ε_0	Dielectric permittivity of vacuum. [C^2/J·m]
ε_{r}	Relative permittivity of solvent. [unitless]
η	Dynamic viscosity. [Pa·s]
η_{c}	Concentration overpotential. [V]
η_{ohm}	Solution-phase ohmic drop. [V]
η_{s}	Surface overpotential. [V]
κ	Ionic conductivity. [S/m]
Λ	Equivalent conductance. [Sm^2/mol]

λ_+	Cation equivalent conductance. [Sm^2/mol]
λ_{+-}	Mean molar activity coefficient over particle-fraction basis. [unitless]
μ_i	Electrochemical potential of species i. [J/mol]
ν	Total ions in a salt formula unit. [unitless]
ν_i	Stoichiometric formula unit of species i. [unitless]
Ξ	Electro-osmotic coefficient. [unitless]
ξ	Extent of dissociation. [unitless]
ρ	Mass density. [kg/m^3]
Φ	Electric potential. [V]
χ	Darken thermodynamic factor. [unitless]
ω	Mass fraction. [unitless]
Ω_{bulk}	Bulk impedance measured with EIS. [Ω]

Abbreviations

ARD	Automatic relevance determination.
CST	Concentrated-solution theory.
DST	Dilute-solution theory.
EC	Ethylene carbonate.
EIS	Electrochemical impedance spectroscopy.
EMC	Ethyl methyl carbonate.
FEC	Fluoroethylene carbonate.
GP	Gaussian process.
HCE	Highly concentrated electrolyte.
LHCE	Localised highly concentrated electrolyte.
MRI	Magnetic resonance imaging.
NMR	Nuclear magnetic resonance.
OCP	Open-circuit potential.
OSM	Onsager–Stefan–Maxwell.
PC	Propylene carbonate.
PEEK	Polyether ether ketone.

PFG Pulse-field gradient.

PTFE Polytetrafluoroethylene.

PyBaMM Python Battery Mathematical Modelling package.

RBF Radial basis function.

RF Radio frequency.

SEI Solid electrolyte interphase.

SOC State of charge.

VC Vinylene carbonate.

WISE Water in salt electrolyte.

Subscript

$_+$ Cationic species in the electrolytes, Li^+ in the case of $LiPF_6$.

$_-$ Anionic species in the electrolytes, PF_6^- in the case of $LiPF_6$.

$_0$ Neutral solvent species.

$_\infty$ Equilibrium bulk property.

$_a$ Anodic property.

$_c$ Cathodic property.

$_{eff}$ Micro-porous-adjusted effective property.

$_e$ Electrolyte solute.

$_f$ Final measurement after Hittorf experiment.

$_o$ Secondary neutral cosolvent species.

$_{ref}$ Reference composition property.

$_{test}$ Test composition property.

Superscript

^{0} Referring to the solvent frame.

$^\square$ Referring to a volume-average quantity.

^{surf} Surface property.

1 Introduction*

Electrochemical processes reside at the nexus of several technological advances, many of which have been driven by the proliferation of renewable electricity sources [2]. Rather than relying on temperature and pressure driving forces alone, electrochemical devices exploit electrical potential, useful in processes such as energy conversion and storage, as well as materials synthesis [3]. Rechargeable batteries, in particular, are being rapidly deployed to decarbonise the transportation and distributed-grid energy-storage sectors [4]. To accelerate this process, several improvements in battery material, design, and management are necessary to meet performance, cost, and safety targets for these applications [5]. This thesis elucidates phenomena relevant to concentrated Li-ion battery electrolytes, with the intention of aiding the future simulation, design, and discovery of higher-performing materials for next-generation electrochemical devices.

*Portions of this chapter were adapted from *Progress in Energy* **2022**, DOI: 10.1088/2516-1083/ac692c [1]

1.1 Characteristics of performant liquid battery electrolytes

1.1.1 Fundamental aspects of electrolytes

Almost all practical electrochemical systems contain an electrolyte as a key component. The primary role of an electrolytic phase within an electrochemical device is to facilitate the transport of redox-active materials to and from electrode surfaces, at which heterogeneous reactions occur. Electrolytes are ionic conductors but electronic insulators, providing chemical contact between the anode and cathode while an external circuit completes the electrical contact [6]. When an electrochemical device operates, anions and cations are constantly redistributed to maintain charge neutrality as reactions occur. Figure 1.1 shows a schematic diagram of instantaneous property distributions within a Li-ion battery by way of example. As a consequence of this close coupling between ion redistribution and current flow, transport processes in electrolytes directly influence the performance characteristics of every electrochemical device.

Electrolyte selection criteria are application specific. Systems are diverse and can range from aqueous solutions in alkaline or redox-flow batteries, to molten salts in industrial electrometallurgy, to ion-conducting polymers and ceramics in fuel cells and solid-state batteries [7].

Nonaqueous electrolytes have been critical to the development of rechargeable lithium-ion batteries, where aprotic solvents were chosen to avoid reacting with lithium [8]. Initial electrolyte formulations relied on cosolvent blends of cyclic carbonates such as ethylene carbonate (EC) and linear carbonates, along with a lithium salt such as lithium hexafluorophosphate ($LiPF_6$). These solutions were optimised for ionic conductivity and compatibility with intercalation electrodes. Today's commercial Li-ion batteries still use similar formulations, with slight additive modifications to inhibit degradation reactions [9]. It has been demonstrated that cells with the right combination of carbonaceous anode, metal-oxide cathode, electrolyte

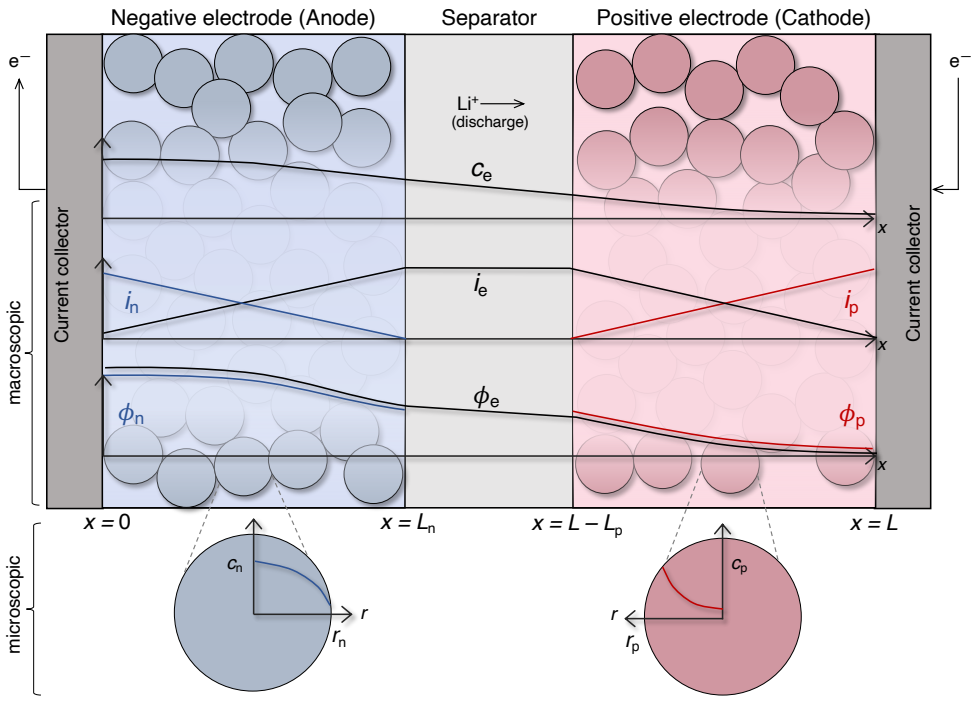


Figure 1.1: Schematic of a lithium-ion cell with liquid electrolyte permeating both porous electrodes and a separator membrane. During a discharge, lithium ions are consumed and replaced at the positive and negative electrode, respectively. The resulting distribution of cation molarity through the electrolyte is plotted (c_e), along with the associated solution-phase potential gradient (ϕ_e). The current density profile i is also plotted. Subscripts e, n and p denote the electrolyte, negative-electrode active material, and positive-electrode active material. The geometry indicates both the macroscopic and microscopic coordinate systems commonly used in continuum-scale physics-based models [1]. The positions $x = 0$, $x = L_n$, $x = L - L_p$, and $x = L$ represent domain interfaces between current collector and porous negative electrode, porous negative electrode and separator, separator and porous positive electrode, and porous positive electrode and current collector, respectively. The variable r represents the microscopic scale within each individual electrode particle.

additives, and operating conditions can have the ability to last for over 1.6 million kilometers in electric vehicle or over 20 years in grid storage applications [10].

There is also a considerable effort dedicated to research on novel battery chemistries — so-called 'beyond lithium-ion' technologies [11]. The broad impetus for these is to achieve cost-effective cells made of more earth-abundant materials with higher power and higher energy density than today's lithium-ion batteries. Such advanced batteries might pair better with emerging long-duration storage

applications [12], or lead to longer-range or faster-charging electric vehicles [13] and electric aircraft [14]. To these ends, several novel chemistries are being developed, with alternatives to traditional anode, cathode, and electrolyte materials, such as lithium–sulfur [15] and lithium–air [16] cells. Other changes of paradigm aim for lithium-metal anodes with novel liquid [17] and solid [18] electrolyte formats. The lithium cation has also been substituted to create alkali-metal and multivalent-ion batteries of various types [19].

Next-generation battery systems invariably require new electrolyte specifications. For liquid electrolytes, however, overarching formulation approaches still typically revolve around the optimisation of some combination of salts, solvents, and additives [9]. Currently popular design strategies include:

1. Highly-concentrated electrolytes (HCEs), with an increased salt-to-solvent ratio [20, 21]

2. Specifically using water as a solvent in a water-in-salt (WISE) style of HCE [22]

3. Diluting an HCE back down while preserving desirable solvation structures with a localized-highly-concentrated electrolyte (LHCE) [23]

4. Incorporating ionic liquids as solvents [24]

5. Going to ultra-low salt concentrations [25]

6. Using volatile solvents in a liquified-gas-style electrolyte [26]

7. Multi-salt blends [27, 28]

Beyond a fundamental ability for charge transport, several other requirements must be considered across relevant length scales when selecting and designing optimal electrolyte formulations. We will briefly consider them here before discussing mass-transfer effects, which are the emphasis of the following chapters.

1.1.2 Device and cell-level considerations

Electrolyte properties influence battery characteristics such as safety, component cost, and manufacturability, both on the device level and the cell level. In commercial lithium-ion batteries, carbonate solvents, $LiPF_6$, and the solid-electrolyte interphase (SEI) they form with electrodes have low thermal stability [29] and high flammability [30]. Consequently, thermal runaway events in cells, modules, and packs can have catastrophic consequences [31]. Components and compositions of the electrolyte can be chosen to reduce overall vapor pressure and flammability, as is the case with HCEs [32] and ionic liquids [33]. Water-in-salt electrolytes also enable safer aqueous lithium-ion batteries [34]. Fire-retardant compounds such as various phosphates are commonly included as a solvent additive for safety [35]. Wider operating ranges for temperature can also be achieved by making appropriate choices of solvents and salts [26].

Fluorinated compounds tend to be expensive constituents (on a per-mass basis) of current electrolytes [36]. This includes anions such as hexafluorophosphate (PF_6^-) and bis(fluorosulfonyl)imide (FSI^-), as well as protective solvent additives such as fluoroethylene carbonate (FEC) [37]. Several research groups have explored using more cost-competitive electrolyte formulations, for example, by moving to a completely fluorine-free chemistry, while still reaching desired battery performance targets [38, 39].

Manufacturability is also very important, since lithium-ion battery production must scale to meet the demands of large industries including automotive and personal electronics. The filling of liquid electrolytes into the porous electrodes and separators in energy-dense cells is a common bottleneck [40]. This process is directly linked to electrolyte viscosity, which, along with surface tension, determines wetting dynamics [41]. Battery engineers must consider multifaceted trade-offs when selecting electrolytes: although a given HCE might achieve more optimal electrochemical properties, its exponentially higher viscosity, due to salt crowding, could render cells unmanufacturable with traditional methods [42].

1.1.3 Micro-scale properties

Recent research has placed considerable effort on understanding the microscopic interactions between electrodes and electrolytes. Electrochemically stable interfaces only form via a passivation process, whereby electrolyte constituents decompose to form a SEI film [9]. An ideal SEI is one that forms in a durable manner and does not expand or reorganize during battery cycling. Various additives such as vinylene carbonate (VC) and FEC are common sacrificial compounds that have been found to form better performing SEIs [43, 44]. Anion-derived SEIs have also been reported to improve battery longevity [45]. LHCEs are an avenue to increase the availability of anions, relative to free solvent, for anion-rich SEI forming reactions that improve the cycling stability of lithium-metal anodes [46].

Many benefits of new electrolyte designs (HCE, LHCE, WISE) have been attributed to altered solvation environments. In a strong electrolyte [47], the solvent acts as a dielectric that facilitates the dissociation of a salt into its constituent anions and cations within the solution phase. Battery electrolytes with practical salt concentrations, however, tend to be weaker, forming more complex solution structures such as ion pairs and larger-order aggregates [48]. This speciation and ion association driven by salt crowding can also inhibit the reductive decomposition of electrolyte, because solvation structures shield the solvent [49]. By leveraging these micro-scale molecular interactions, the voltage stability window of electrolytes can hypothetically be extended to enable compatibility with next-generation high voltage (>5V) cathodes [50, 51].

Microscopic association phenomena between ions and solvents will also alter the (de)solvation energetics of Li^+, in turn changing interfacial reaction kinetics [52]. The morphology of electrodeposited lithium metal has shown sensitivity to the molecular tuning of solvents [53]. Being able to reversibly plate lithium without any electrolyte consumption will allow higher coulombic efficiencies to be achieved [54]. The solvent-loss degradation mode has to be managed if lithium metal batteries with superior energy density and cycle life are to be commercialised [17].

Continued interest in the exact details of speciation within electrolytic solutions has also led to detailed quantum-chemical simulations of solution structures in non-aqueous electrolytes [55, 56]. Equilibrium properties attained from such computational approaches, as well as spectroscopic data, have been correlated with the properties of SEIs formed on various electrodes [57–60]. The exact formation mechanisms that link electrolyte composition to SEI characteristics remain circumstantial at present [46].

1.1.4 Bulk electrolyte transport

Bulk electrolyte transport and thermodynamic phenomena act as the continuum connection between molecular- or meso-scale and device-level performance. Ion mobility is a crucial function for any electrolyte. Ideally, facile mass transport is desirable, because this limits voltage drops associated with applied currents. Ideally, the potential drop across the electrolyte (ϕ_e in Figure 1.1) should also be minimized [61]. With these characteristics, batteries are able to charge and discharge at higher rates before reaching limiting conditions.

If the cation and anion mobilities are comparable, species concentration gradients — arising from the balance of diffusion and migration (drift) — also build up as lithium ions are consumed and replaced at opposing electrodes. The limiting steady-state current density — the maximum current that can be sustained by a battery before all charge carriers (Li^+) are depleted at the cathode — is a strong function of electrolyte transport parameters [62]. Concentration overpotential (the portion of the voltage drop in the electrolyte phase attributable to concentration polarisation) can also introduce inefficiencies during fast charging, since voltage cut-off limits can be reached before any appreciable change in state of charge (SOC) [13].

The distributions of solution-phase Li^+ concentration and electrolyte-phase voltage also dictate the distributions of intercalation reactions [63]. If unaccounted for, this subtler form of polarisation can mask the operating limits of graphite electrodes, leading to damaging lithium metal plating [64]. It is important to bear in mind that microscopic speciation always occurs within the context of mesoscale

material balances. Local ion content affects the nature of the solvation shell, and consequently its redox energetics, and can also alter the dendritic microstructure of plated lithium in alkali-metal cells [65, 66]. Similarly, the availability of other solvent additives, independent of the ion-solvation environment, will also regulate the kinetics of SEI formation and degradation reactions [67].

1.2 Impact of electrolyte transport in emerging cell designs and applications

Given experimental resource constraints, electrolyte development has often emphasized device-level and molecular-level characteristics (as discussed in sections 1.1.2 and 1.1.3) over ion transport [54]. Exhaustive characterisations across the space of available compositions and operating temperatures are often considered impractical given the large number of independent equilibrium and transport properties needed to fully characterise a given combination of salts, solvents, and additives.

Nevertheless, as batteries progress towards faster-charging, more densely packed, and thicker porous electrodes, solution-phase transport inefficiencies will almost certainly increase in significance [46, 68]. Minimising porosity in electrode microstructures raises cell energy density, which is critical for mobile applications [69, 70]. Thicker electrodes have also been explored as a strategy to manufacture cost-effective cells with reduced inactive-material weight [71, 72]. Both of these attributes come at the detriment of rate capability, however, as has been demonstrated by both experiments and simulations [73–75]. While a lower power-to-energy ratio may be tolerable in stationary-storage applications, cells that charge faster are necessary for electric vehicles [13].

To illustrate how electrolyte transport phenomena affect battery design parameters, we simulate the charging behaviour of a $LiCoO_2$/graphite cell [76] using the PyBaMM electrochemical model framework [77]. In these simulations we have incorporated known composition-dependent electrolyte transport properties for $LiPF_6$:EC:EMC [78]. Figure 1.2 presents a sensitivity analysis for the simulations. In each scenario, we model a constant-current charge up to the upper cutoff voltage

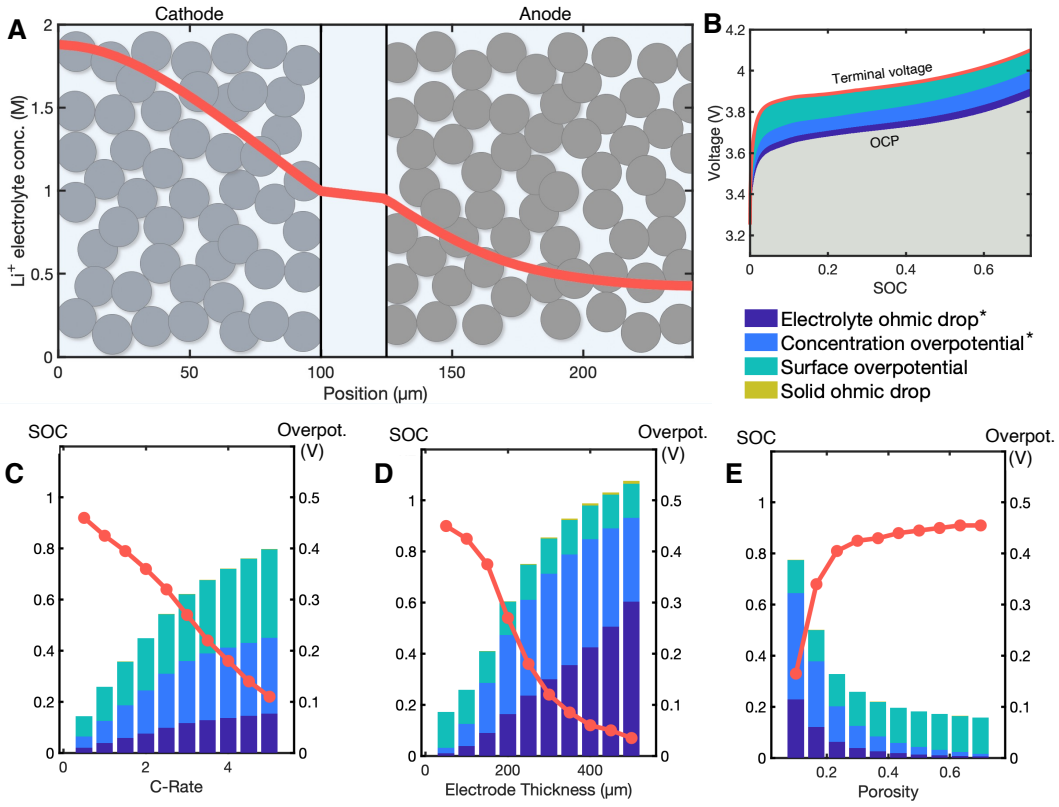


Figure 1.2: Relation between cell design parameters and electrolyte-phase inefficiencies. (A) A simulated lithium-ion cell at the end of a 2C constant current charge showing a large degree of concentration polarisation across the electrolyte domain. (B) Voltage signal from a 2C charging simulation, with shading corresponding to individual sources of overpotential. Sensitivity of accessible SOC and overpotential contributions to variations in C-rate (C), electrode thickness (D), and porosity (E). Bulk electrolyte transport inefficiencies, which dominate towards more advanced cell design regimes, are labelled in the legend with an *.

of 4.1 V. At the end of this charge, the fraction of total SOC and overpotential contributions are plotted as a function of C-rate, electrode thickness, and porosity in Figure 1.2 C, D, and E respectively. Baseline conditions include a C-rate of 1C, cathode thickness of 100 μm, and electrode porosity of 0.3. The polarized Li^+ cation concentration profile as a function of position through the cell at the end of a 2C charge is also plotted in Figure 1.2 A, with the voltage signal and overpotentials depicted in Figure 1.2 B. Full details of the model are provided in Appendix 1.A.1.

The attainable SOC is severely affected as charging rates and electrode coating thickness increases, and as the electrode microstructure becomes more constrained. The voltage inefficiencies attributed to electrolyte transport phenomena are also

shown in blue shading, with ionic conductivity contributing to the electrolyte ohmic drop, and the Li^+ concentration gradient contributing to concentration overpotential. Notably, electrolyte transport related voltage losses also dominate as the cell design parameters are varied. These results, as well as further sensitivity tests that probe variations in the magnitude of electrolyte properties (Appendix 1.A.1), show that tuning electrolyte-phase ion transport can benefit the performance of emerging battery-cell designs. An accurate understanding of electrolyte transport limitations will also enable engineers to optimise the efficiency of battery operation.

1.3 The role of properties and models in describing transport phenomena

The mobilities of charged and neutral species in electrolytes are typically assessed by measuring a set of macroscopic transport properties, such as ionic conductivity κ, diffusivity D, and cation transference number t_+^0. These properties have commonly understood definitions [61, 79]: ionic conductivity quantifies the total mobility of ions under an electric field in the absence of concentration gradients, the salt diffusivity determines the contribution to the ionic flux by salt concentration gradients, and the transference number is the fraction of conductivity that owes to cation motion. Thermodynamic properties, such as the Darken thermodynamic factor χ [80], determine how concentration differences translate into concentration overpotentials. All of these properties together govern the spatiotemporal distribution of concentration and voltage through the solution phase. Figure 1.3 presents the general magnitudes of the macroscopic properties, as well as trends in their composition dependence. These data were extracted from the 'LiionDB' parameter database, a compilation of many property measurements from the literature [1].

The interpreted physical significance of each property is inextricably linked to a chosen transport model. When one measures a parameter experimentally, the value one finds depends on assumptions made in the underpinning model formulation. This relationship is also reciprocated: in any battery simulation, the chosen model

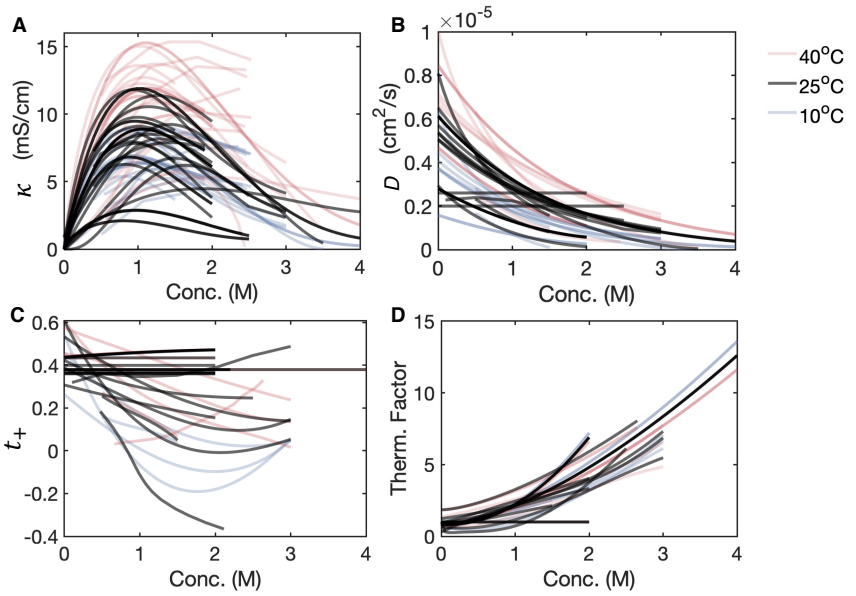


Figure 1.3: Transport and thermodynamic property survey of $LiPF_6$-containing electrolytes at temperatures of 10 °C (blue), 25 °C (black) and 40 °C (red), reported in the LiionDB literature parameter database [1].

formulation also affects one's interpretation of how predicted concentration and voltage distributions evolve and influence performance.

Just as electrolyte designs can span diverse regimes across solvent-in-salt, localised-highly-concentrated, polymeric, and other strategies, so too can the models, which can be extended to include phenomena such as thermodynamic nonideality, ion association on the microscale, and neutral-solvent convection. Below, we briefly survey a range of theories before discussing the implications of variations in transport-model construction. In each case we shall consider a solution consisting of a monovalent salt within a single electron transfer reaction stoichiometry, as is the case of $LiPF_6$ and most Li-ion electrolytes.

1.3.1 Dilute-solution theory

The earliest transport models stemmed from analytical electrochemistry, and focused on producing the most accurate mathematical descriptions of electrolytes under thermodynamically ideal and infinitely dilute conditions [47].

Within the Nernst–Planck dilute-solution framework, the vector quantities indicating species movement are given by constitutive laws for flux [61]. Driving

forces for the transport of ion i include migration under an electric field $-\vec{\nabla}\Phi$, diffusion due to ion concentration gradients $\vec{\nabla}c_i$, and convection through a bulk-flow velocity $\vec{v}$, as

$$\vec{N}_i = -D_i\left(\frac{Fz_ic_i}{RT}\vec{\nabla}\Phi + \vec{\nabla}c_i\right) + c_iv, \tag{1.1}$$

Here $\vec{N}_i$ is the species flux of species i, D_i its diffusivity in the solvent (which obeys the ideal Nernst–Einstein relation for ion mobility [61]), z_i its equivalent charge ($+1$ for the cation, -1 for the anion), and c_i, its concentration; F is Faraday's constant, R the gas constant, and T, the absolute temperature.

Dilute-solution theory (DST) assumes cations ($+$) and anions ($-$) are thermodynamically ideal, as well as being completely dissociated within the solvent medium and non-interacting. Transport effects in this case are therefore fully specified by the diffusivities D_+ and D_-. It is conventional to map these parameters into three macroscopically observable quantities of ionic conductivity κ, Fickian diffusivity D, and cation transference number t_+:

$$\kappa = \frac{F^2c}{RT}\left(D_+ + D_-\right), \tag{1.2}$$

$$D = \frac{2D_+D_-}{D_+ + D_-}, \tag{1.3}$$

$$t_+ = \frac{D_+}{D_+ + D_-}. \tag{1.4}$$

The cation flux determining the concentration gradient (Eq. 1.5) and voltage response from applied current density $\vec{i}$ (Eq. 1.6) can then be written in terms of these three parameters [61, 81]:

$$\vec{N}_+ = -D\vec{\nabla}c_+ + t_+\frac{\vec{i}}{F} + c\vec{v}, \tag{1.5}$$

$$\vec{\nabla}\Phi = -\frac{\vec{i}}{\kappa} + \frac{RT(1-2t_+)}{F}\vec{\nabla}c. \tag{1.6}$$

According to this theory, there are only two independent transport parameters, whereas the irreversible thermodynamics of Onsager suggests there should be three [82]. Should DST hold, one should be able to retrieve experimental values of κ entirely from those of D and t_+ (or indeed, any of the three from the other two). Bizeray et al. performed such an analysis and found that this relationship is not upheld, even at relatively high dilution, across the literature [81]. The ideal–dilute approximation has also been shown to break down for lithium-ion electrolytes at salt concentrations of 0.1 M [83]. To achieve closer agreement with internal states of the electrolyte, some parameterisation efforts have allowed all three parameters to vary independently within the DST model formulation, despite the fact that this violates the model's fundamental assumptions [84].

1.3.2 Concentrated-solution theory

Practical nonaqueous electrolytes in electrochemical devices generally employ concentrations well outside the dilute regime. For example, conventional Li-ion batteries often use electrolytes with molarities near their conductivity maxima, typically circa 1 M [8]. Newman's concentrated-solution theory (CST) can be used to describe transport phenomena in these formulations [61]. It is rooted in the Onsager–Stefan–Maxwell (OSM) multicomponent transport formalism [82, 85]. OSM theory is based on principles of irreversible thermodynamics, and takes electrochemical-potential gradients as the fundamental driving forces for mass transport. Within this theory, isothermal and isobaric electrolytes consisting of n chemically distinct species require $n(n-1)/2$ transport properties to describe all possible pairwise interactions. Therefore, in a binary electrolyte composed of a cation (+), anion (−), and neutral-solvent (0) species, three transport properties are necessary. Further, a thermodynamic factor χ is needed to connect concentration gradients with gradients of salt chemical potential.

The OSM framework is formulated in a force-explicit manner, expressing the gradient in electrochemical potential μ_i of each species i in terms of its velocity v_i relative to that of every other species j:

$$-c_i\vec{\nabla}\mu_i = \sum_{j\neq i} K_{ij}\left(\vec{v}_i - \vec{v}_j\right) = \sum_{j\neq i} \frac{RTc_ic_j}{c_{\mathrm{T}}\mathscr{D}_{ij}}\left(\vec{v}_i - \vec{v}_j\right), \tag{1.7}$$

where the left hand term is the thermodynamic force per unit volume driving motion of species i and c_{T} represents the total molarity of the solution; K_{ij} may be interpreted as a friction coefficient, and $\mathscr{D}_{ij}$ is the Stefan–Maxwell diffusivity of species i through j. CST may also be formulated with a flux-explicit expression using Onsager conductivities L_{ij} [86], but this requires the specification of a consistent reference velocity for convection. Both the force-explicit and flux-explicit approaches produce thermodynamically consistent electrolyte transport models.

For the binary electrolyte case specified in Section 1.3.1, three Stefan–Maxwell diffusivities, $\mathscr{D}_{0+}$, $\mathscr{D}_{0-}$, and $\mathscr{D}_{+-}$ describe species/species interactions: solvent–cation, solvent–anion, and cation–anion, respectively. Unlike DST, OSM CST explicitly accounts for the diffusional drag between ions. Three independent and macroscopically-observable transport properties can also be derived from the Stefan–Maxwell diffusivities [61]:

$$\frac{1}{\kappa} = \frac{RT}{c_{\mathrm{T}}F^2}\left(\frac{1}{\mathscr{D}_{+-}} + \frac{c_0}{c_+}\frac{1}{\mathscr{D}_{0+}+\mathscr{D}_{0-}}\right), \tag{1.8}$$

$$\mathscr{D} = \frac{2\mathscr{D}_{0+}\mathscr{D}_{0-}}{\mathscr{D}_{0+}+\mathscr{D}_{0-}}, \tag{1.9}$$

$$t_+^0 = \frac{\mathscr{D}_{0+}}{\mathscr{D}_{0+}+\mathscr{D}_{0-}}. \tag{1.10}$$

In this case, $\mathscr{D}$ is the thermodynamic diffusivity based on chemical potential gradients (which can be converted to a Fickian D based on concentration gradients using the expression $D = \chi\mathscr{D}$), and t_+^0 is the cation transference number relative to

the solvent velocity. As cation transference defines the relative fraction of charge carried by Li^+, CST requires one to specify a reference frame for consistency [87].

Composition gradients and concentration overpotentials are connected through a Darken thermodynamic factor χ [88]. This equilibrium property can also be defined in terms of other composition bases, such as the mean-molar bases used by Newman, as shown in Equation 2.2 and discussed in Section 2.1 [61].

Inverting the transport matrix $\mathbf{K}$ yields the cation flux law (Eq. 1.11), and the MacInnes equation (modified Ohm's law) provides the current–voltage relation (1.12) [61, 89]:

$$\vec{N}_+ = -D\vec{\nabla}c_+ + t_+^0\frac{\vec{i}}{F} + c\vec{v}_0, \tag{1.11}$$

$$\vec{\nabla}\Phi = -\frac{\vec{i}}{\kappa} + \frac{2RT(1-t_+^0)\chi}{Fc_{\mathrm{T}}\overline{V}_0}\vec{\nabla}c, \tag{1.12}$$

with $c_{\mathrm{T}}\overline{V}_0$ being an excluded-volume factor based on the chosen composition basis of χ. The excluded-volume factor relates to solute-volume effects, discussed in more detail in Section 1.3.3.

Ion transport within the electrolyte for Doyle–Fuller-Newman (DFN) full-cell models was originally described using multi-component CST [90]. The concentrated-transport model accounts for additional underlying physics that DST does not, so that it captures the effects of thermodynamically non-ideal and interacting ions of concentrations higher than infinite dilution. Richardson et al. review the discrepancies between dilute, moderately-concentrated, and concentrated models [91].

1.3.3 Inclusion of solute-volume effects

Solute-volume effects encompass transport mechanisms associated with the volume occupied by different species in electrolytic solutions [89]. While initially accounted for in the description by Newman and Chapman [92], canonical electrolyte transport modelling studies have subsequently neglected such phenomena [78, 83, 93–95].

As evidenced in Chapter 3, however, solute-volume effects can become significant for some emerging electrolyte designs.

An 'excluded-volume effect' occurs when solution-density changes due to local composition differences cause global redistribution of volume — driving bulk diffusion [89]. The first DFN models make the assumption that this factor is negligible, through an explicit assumption that solvent concentration does not vary with the overall electrolyte concentration $\left(1 - \frac{d \ln c_0}{d \ln c}\right)_{\mathrm{T,P}} = 1$. This also equivalent to setting the partial molar volume of salt $\overline{V}_{\mathrm{e}}$ to zero, which is an especially poor simplification at higher concentrations [96].

'Faradaic convection' can also be driven by interfacial reactions [89, 97, 98]. During lithium deposition or intercalation or stripping, there is a net Li^+ flux at the electrode boundary. Since there is a volume associated with dissolved salt, cation flux induces bulk flow. As the partial molar volume of salt $\overline{V}_{\mathrm{e}}$ is a measure of the salt's effective solvated volume [99], the fraction of solution volume attributed to the mobile salt ($c\overline{V}_{\mathrm{e}}$) increases dramatically as strongly-coordinated electrolytes near saturation.

Liu and Monroe analysed the relative influence of solute-volume phenomena [89, 97] on electrolyte transport. Their CST transport model incorporates excluded-volume and Faradaic convection effects via a volume-balance governing equation, and by casting the convection reference in terms of the volume-average velocity $\vec{v}^{\square}$, which is defined by the averaged volume flux across all species i:

$$\vec{v}^{\square} = \sum_i \overline{V}_i \vec{N}_i. \tag{1.13}$$

Several other choices of reference velocity may be made, such as the mass-average velocity $\vec{v}$, molar-average velocity $\vec{v}^{*}$, and solvent velocity $\vec{v}_0$. These may be appropriate when accounting for momentum in fluid dynamics, reaction stoichiometry, and when free solvent is available in excess, respectively.

From equation 1.13, the quantification of species partial molar volumes is hence crucial to understand solute-volume effects. Partial molar volumes can be calculated

by examining how solution density ρ changes as a function of salt concentration [61]. For a binary electrolyte, the partial molar volumes of solvent ($\overline{V}_0$) and solvated salt ($\overline{V}_\mathrm{e}$) are given by:

$$\overline{V}_0 = \frac{M_0}{\rho - c\frac{d\rho}{dc}}, \tag{1.14}$$

$$\overline{V}_\mathrm{e} = \frac{M_\mathrm{e} - \frac{d\rho}{dc}}{\rho - c\frac{d\rho}{dc}}, \tag{1.15}$$

with M_0 and M_e being the respective molar masses.

Convective transport phenomena are commonly disregarded in Li-ion electrolyte studies [78, 83, 93–95]. However, their inclusion is warranted in systems with a high bound-solvent fraction [96, 100–103]. The mobility of neutral solvents is now increasingly recognised as a mode of transport in electrolytes [104]. Separate to externally driven flow, this is induced by the migration of charged species under an electric field, and occurs in the absence of temperature and pressure gradients. Several groups have now directly measured solvent motion using spectroscopic techniques [105–108]. These observations have also been used to rationalise negative transference number measurements [87, 104, 109–111].

1.3.4 Further extensions for multicomponent-solutions

Recent research has also elucidated microscopic mechanisms beyond the classical 'vehicular' transport mode, where ions carry their local solvation shell through solution. This is especially the case in superconcentrated electrolytes, where species association between multiple components dominates the solvation structure [20]. Molecular dynamics simulations show that in the presence of strong ion/ion interactions, a transition to a 'structural' mode occurs, in which ions participate in a ligand-exchange or ion-hopping process similar to what is observed in polymeric solutions [112–114]. Highly coordinated aggregates can form percolating networks for ion clusters [115]. McEldrew and colleagues have treated these higher-order

charged and neutral clusters as distinct multicomponent species in OSM transport model formulations [116].

Experimental measurements of self-diffusivity have suggested that dilute theories cannot capture Li^+ hopping conduction transport processes [117]. It is still unclear, however, how these microscopic mechanisms connect with macroscale species balances across the electrolyte domain. Work in Chapter 3 of this thesis does show that the importance of distinguishing between various coordinated species may be overstated within transport characterisation efforts based on OSM CST. Although the solution structure may vary dramatically, a consistent OSM model based on single ions and solvent molecules can still account for all the dominant microscopic interactions. This simplification requires that speciation processes reach equilibrium on timescales much faster than the characteristic timescale for diffusion, which appears to be the case for most processes relevant to lithium ion batteries [96, 118].

Most battery formulations consist of more than a single salt and solvent. Full experimental measurement of all independent transport properties $\mathscr{D}_{ij}$ in these multicomponent solutions becomes prohibitively difficult [119]. A combination of atomistic modelling and self-diffusion measurements using pulse-field gradient nuclear magnetic resonance (PFG-NMR) is a promising route to probing ion transport in more complex formulations [86, 120–122]. Nevertheless, further development is required to both strengthen the tenuous link with OSM diffusivities and validate predictions for macroscopic species concentration and voltage profiles [123, 124].

1.4 Ensuring the longevity of transport studies

Studies on identical electrolytes often measure differing transport and thermodynamic parameter values. The spread can be visualised through the plots in Figure 1.3 and the accompanying composition information in the literature database [1]. As battery-electrolyte performance is typically assessed via transport properties, ongoing debate in the literature over the validity of reported properties impedes the ability for to benchmark electrolyte formulations against one another.

The topic of transference numbers presents an archetypal discourse. Appreciable effort has been spent by the community in recent years on distinguishing approximate and rigorous measures of transference [87, 104, 110, 112, 125–132]. Distinctions raised span the validity of the Bruce–Vincent method, presence and validity of negative values, physical interpretation of NMR-based measurements, choice of reference velocity, how solvent motion is accounted for, whether bulk signals are isolable from interfacial effects, and more.

What deserves more consideration — and what is emphasized here — is the dynamic nature of transport models themselves. We discussed in Section 1.3 that individual material parameters are defined and quantified based on chosen model assumptions. Instead of advocating for a single 'correct' method [127], we hope to highlight the need to understand that the extraction of every property value represents the interpretation of a raw experimental result through the lens of a chosen model (Figure 1.4). Given that model formulations are fluid in terms of chosen complexities and represented phenomena, this impacts the ability to compare electrolytes based on transport properties reported in different studies.

1.4.1 Raw experimental results are model independent

Raw experimental results, on the other hand, provide a 'ground truth' that encompasses all physicochemical interactions, regardless whether post-processing accounts for them or not. One way to ensure the longevity of characterisation studies and circumvent the issues raised above is to report raw experimental data clearly alongside experimental and model descriptions [134].

This route also allows prior data to be reviewed through alternative theoretical lenses, enabling studies based on different prior assumptions to be compared in a consistent manner. For example, inclusion of the polarisation curves in steady-state current experiments — used to determine transference numbers [133] — allows for results based on infinitely-dilute assumptions to be reprocessed with concentrated-solution theory (Figure 1.4) [131].

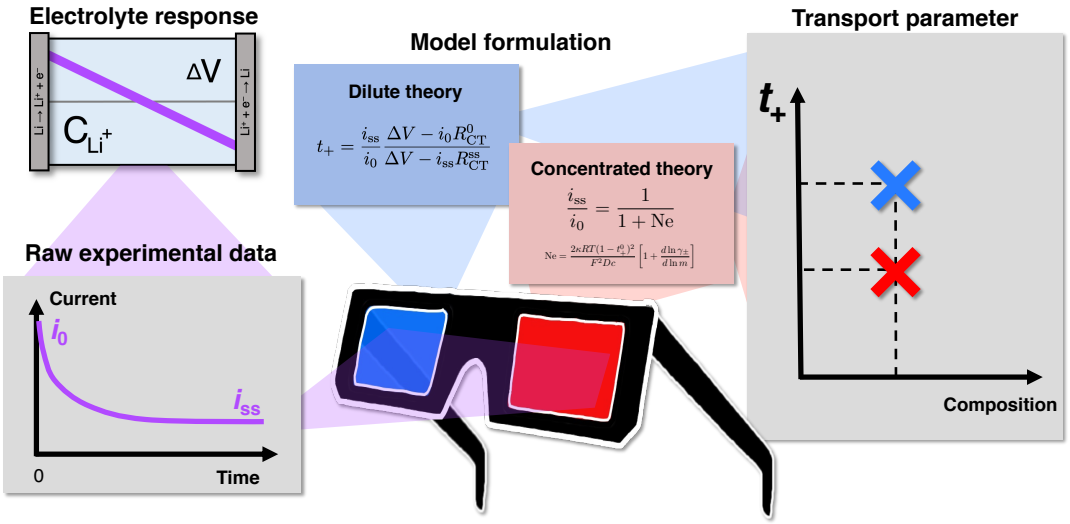


Figure 1.4: Same data, different filters. Schematic of the relationship between electrolyte response, raw experimental data, chosen model formulation, and extracted transport parameters, using transference measurement as an example. The selected phenomena and model assumptions (for example dilute [133] or concentrated solution theory [131]) affects the interpretation of results and therefore the comparability of electrolytes across differing studies of the same transport parameters.

By embracing the variability in transport models and including raw experimental results, the community can move to ensure the longevity and applicability of transport characterisation studies by presenting data in a way that allows new modelling hypotheses to be tested.

1.5 Outline of this dissertation

This thesis investigates the processes by which species are transported in multi-component Li-ion electrolytic solutions. I first develop a refined characterisation methodology, before applying it to comprehend transport phenomena in emerging highly concentrated electrolyte designs. Next, I turn to contemporary electrolyte blends and elucidate migration effects in neutral cosolvents. Insights presented here should be of interest to those developing advanced electrolytes for next-generation batteries.

Chapter 2 begins by augmenting the traditional liquid-junction potential measurements that have been used to determine electrolyte thermodynamic factors. This bespoke 'shifting-reference concentration-cell' method employs an array of reference compositions to improve accuracy and validity across a wider salt composition regime, and also reduces error arising from transference number variation. Both thermodynamic factors and transference numbers have equal influence on the overall electrolyte voltage inefficiencies. The method is validated against conventional measurements for $LiPF_6$ in PC. It is then incorporated into a broader experimental suite and used to systematically characterise $LiPF_6$:EMC transport parameters from high dilution up to 2 M. PC and EMC solvents have contrasting polarities, allowing for a comparison of physicochemical characteristics. Notably, non-ideal thermodynamic activity, conductance, viscosity, and OSM diffusivities all indicate that $LiPF_6$:EMC is poorly dissociated at lower Li^+ concentrations. Nevertheless, agreement between polarisation simulations and experiments suggests that speciation can be successfully accounted for in the OSM-CST framework. This conclusion motivated continued exploration of transport phenomena in highly-associated electrolytes.

Chapter 3 extends the macroscopic transport and thermodynamic property characterisation of $LiPF_6$:EMC to saturation. Salt-volume-fraction and Raman-spectroscopic analyses indicate that superconcentrated electrolytes are extremely thermodyamically nonideal, with ion aggregation and solvent coordination dominating. A polarisation-relaxation experiment is then performed on 3 M $LiPF_6$:EMC while using MRI to track the evolution of voltage and Li^+ concentration profiles. The recorded signals are then compared to simulations from a CST model parameterised ex-situ with the methods developed in Chapter 2. The potentiometric MRI data agree closely with the predicted ion distributions and overpotentials, providing a completely independent validation of the theory. Importantly, the model with Faradaic convection accounts for kinematic transport phenomena in superconcentrated solutions. It is shown that even in a near-saturated electrolyte with complex solution structures, the OSM theory consistently captures internal states, given local association/dissociation equilibria occur faster than diffusion

time scales. Finally, it is shown that, with a fully-parameterised electrolyte, one can isolate true surface overpotentials and gain insight into the kinetics of lithium plating/stripping. This approach also allows bulk and interfacial superconcentrated electrolyte performance gains to be deconvoluted.

Transport effects in formulations with an additional neutral species are examined in Chapter 4. Cosolvent ratios in state-of-the-art electrolytes are commonly assumed to remain constant throughout the solution domain during battery operation. On the microscale, however, preferential solvation is well accepted. To test this approximation, a machine-learning model is trained on a library of simple, precisely measured solution properties, and subsequently used to extract the compositions of ternary $LiPF_6$:EC:EMC electrolytes after polarization in a Hittorf cell. It is found that the pseudo-single-solvent assumption is violated on the macroscale. Neutral EC and EMC solvents are found to migrate at noticeably different rates under applied current. By parameterising a streamlined four-species OSM-CST model, it is shown that the cosolvent segregation effect is most severe near electrode surfaces, suggesting this phenomena can be exploited to design electrolytes to target degradative interfacial reactions.

Finally, conclusions are drawn regarding macroscopically observable electrolyte transport phenomena. An outlook towards experimental and modelling approaches that could accelerate the discovery of high-performance electrochemical materials is given.

1.A Appendices

1.A.1 Full-cell model sensitivity analyses

We perform a sensitivity analysis on full-cell performance as a function of transport property variation using the Doyle–Fuller–Newman (DFN) physics-based model via the Python Battery Mathematical Modelling (PyBaMM) package, version 0.4.0 [77]. The '*Marquis2019*' parameter set was chosen for the electrode chemistry ($LiCoO_2$/graphite) [76], and the composition-dependent parameter set '*lipf6_EC_EMC_3_7_Landesfeind2019*' was selected for the electrolyte chemistry ($LiPF_6$ in 3:7 ratio of EC:EMC) [78]. Cell design parameters were then varied, with positive electrode thickness, C-rate, electrode porosity, and other ranges and baseline values detailed in Table 1.A.1.

Table 1.A.1: Modified baseline values and ranges for cell model parameters.

Property	Baseline	Range	Units
C-rate	1, (2 for Fig. 1.2, 1.A.5)	0.1 — 5	-
Positive electrode thickness	100	50 — 500	µm
Negative electrode thickness	scaled via original capacity ratio	-	-
Electrode porosity	0.3	0.1 — 0.7	-
Separator porosity	1	-	-
Initial positive electrode lithiation	0.96	-	-
Initial negative electrode lithiation	0.03	-	-
Voltage cut off limit	4.1	-	V
Electrolyte conductivity	*lipf6_EC_EMC_3_7_Landesfeind2019*	0.5 — 2× scaling	mS/cm
Electrolyte diffusivity	*lipf6_EC_EMC_3_7_Landesfeind2019*	0.5 — 2× scaling	cm^2/s
Transference number	*lipf6_EC_EMC_3_7_Landesfeind2019*	0.5 — 2× scaling	-
Thermodynamic factor χ	*lipf6_EC_EMC_3_7_Landesfeind2019*	1+ (0.5 — 2× scaling)$(\chi - 1)$	-

When varying cell thickness and porosity, the anode thickness was scaled to maintain

the original active-material capacity ratio (NP ratio). The initial state of lithiation was also adjusted to simulate constant-current charging behaviour, up to a voltage cut off of 4.1 V.

Figure 1.2 demonstrates that voltage inefficiencies related to bulk transport effects (electrolyte ohmic drop and concentration overpotential) dominate as rate, thickness, and active material packing increases.

Transport parameters are then varied in addition to the cell-design specifications. This was accomplished by adjusting the parameter functions reported by Landesfeind et al [78]. Ionic conductivity, diffusivity, and transference were directly scaled by a constant value as in Table 1.A.1, while thermodynamic factor was shifted to maintain ideality at infinite dilution. In Figures 1.A.1, 1.A.2, 1.A.3, 1.A.4, we first visualise the composition-dependence of the scaled transport properties. Then we show their impact on the SOC range accessed during a constant-current charge to 4.1 V. In Figure 1.A.5 we plot overpotential contribution trends as transport properties are varied by their scaling factors.

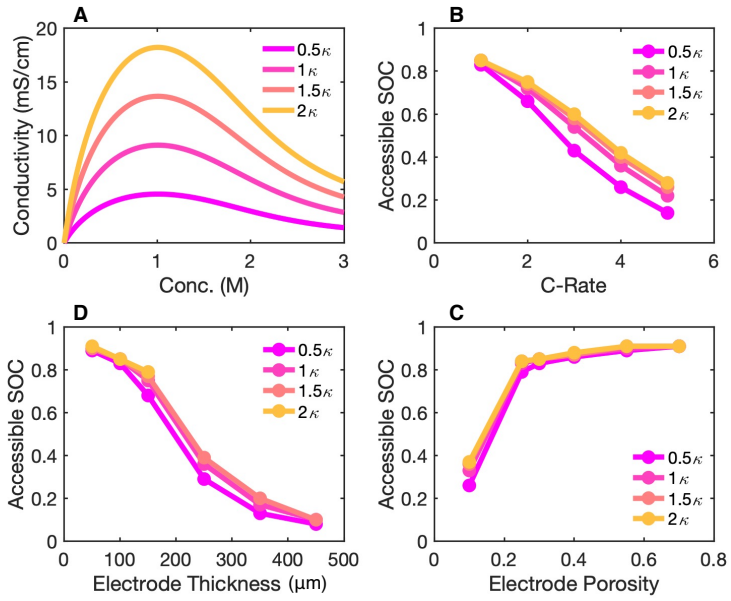


Figure 1.A.1: Relation between ionic conductivity, cell design parameters, and achievable SOC.

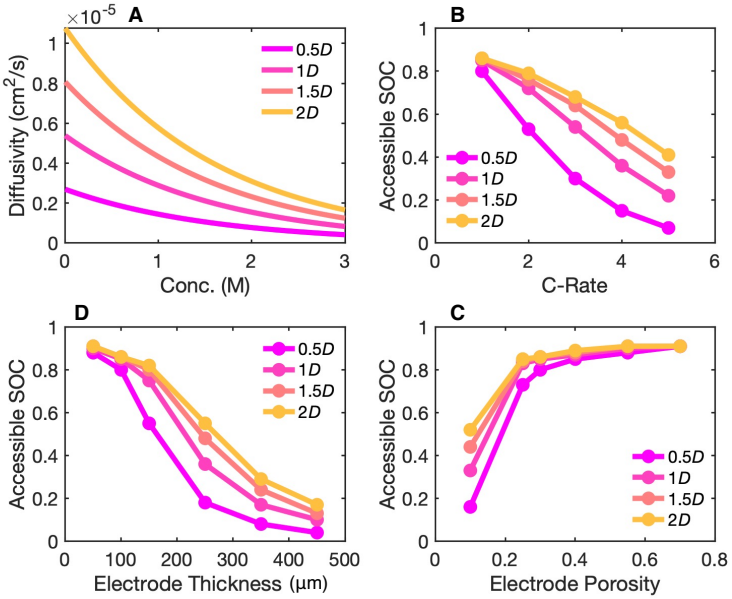


Figure 1.A.2: Relation between salt diffusivity, cell design parameters, and achievable SOC.

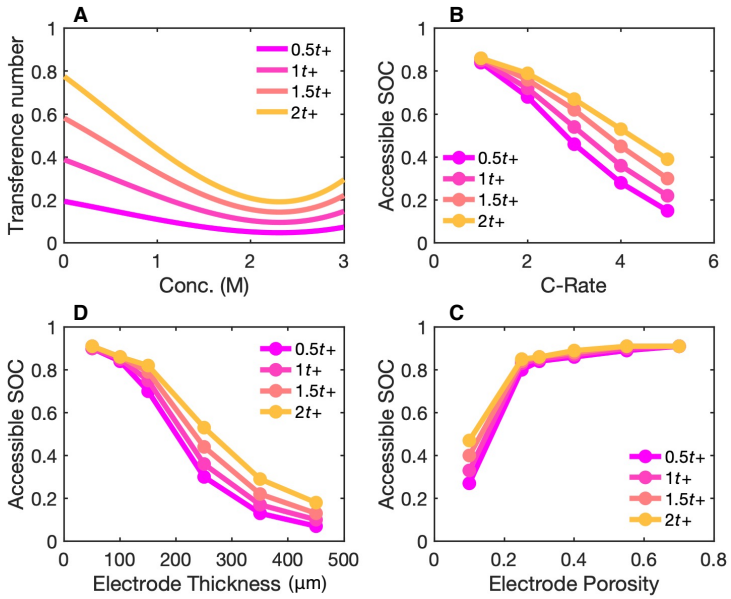


Figure 1.A.3: Relation between cation transference number, cell design parameters, and achievable SOC.

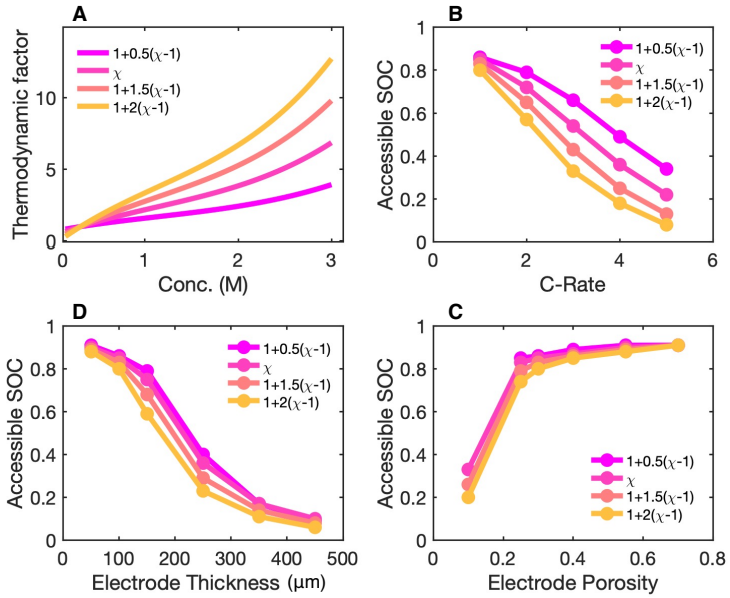


Figure 1.A.4: Relation between thermodynamic factor, cell design parameters, and achievable SOC.

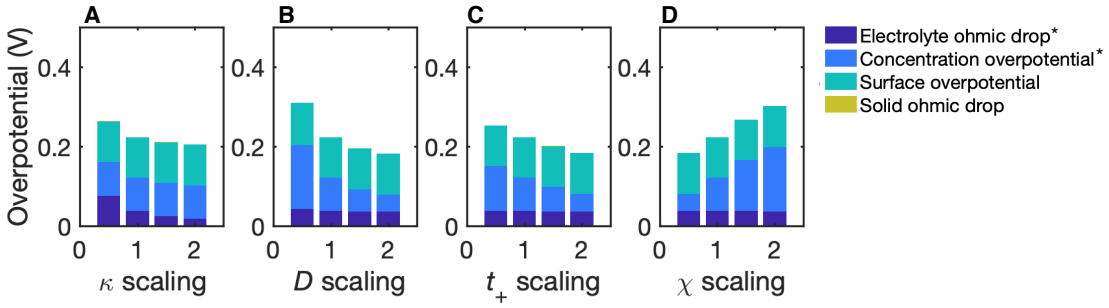


Figure 1.A.5: Overpotential sensitivity to property scalings. The voltage contributions here represent those when the voltage limit of 4.1 V is reached during a constant-current 2C charge. Bulk electrolyte transport inefficiencies are labelled in the legend with an *

The scaling method was used to preserve concentration dependence of the electrolyte transport properties. This is important in aggressive cycling regimes, such as those tested in these simulations. A crucial property here is the thermodynamic factor. As ultimately all concentration polarisation is reflected in the electrolyte voltage, the thermodynamic factor is necessary to accurately account for non-idealities, and also to predict when overall cell voltage limits are reached.

Note here our choice of scaling method means that subplots B, C, and D for Figures 1.A.1, 1.A.2, 1.A.3, 1.A.4 should not be compared across parameters. The

sensitivity of accessible SOC to transport property magnitude does not necessarily relate to the relative importance of each property. However, results from this percentage-scaling approach does allow practitioners of transport characterisations to propagate experimental property uncertainties into cell-level performance uncertainty estimates.

2

Shifting-reference concentration cells to refine composition-dependent transport characterization of binary lithium-ion electrolytes*

Abstract

We present a novel 'shifting-reference concentration-cell' method, altering the traditional protocol for measuring liquid-junction potentials by using a sequence of reference concentrations in regularly spaced intervals, rather than a fixed reference. The method, applied to solutions of lithium hexafluorophosphate ($LiPF_6$) in propylene carbonate (PC) and ethyl methyl carbonate (EMC) at 25 °C, helps to determine thermodynamic factors more accurately, and is useful across a wider concentration range. For $LiPF_6$:PC, good agreement with prior fixed-reference measurements is shown, and new data at low concentrations is consistent with Debye–Hückel theory. Original composition-dependent property correlations are produced for $LiPF_6$:EMC up to 2 M, including the density and thermodynamic factor, as well as isothermal-transport properties such as transference number, conductivity, diffusivity, and viscosity. Polarization-relaxation simulations validate these correlations. For $LiPF_6$:EMC, the low thermodynamic factor and cation/anion Stefan–Maxwell diffusivity, as well as Walden analysis, suggest that ion association dominates, even at high dilution.

*This chapter was reported in *Electrochimica Acta* **2020**, DOI: 10.1016/j.electacta.2020.136688 [118]

2.1 Introduction

Although it may be possible to improve the performance of lithium-ion batteries by altering their electrolytes, the possibilities afforded by liquid-electrolyte design remain unclear. More complete and accurate parameterization of thermodynamic and transport properties can be used in conjunction with phenomenological models to shed light on how electrolyte composition affects cell efficiency, degradation, and power capability.

The widely adopted concentrated-solution theory [61] describes solution-phase mass-transport phenomena in electrochemical cells. For a simple binary electrolyte, the theory involves three macroscopic transport properties — ionic conductivity, cation transference number, and thermodynamic diffusivity — which derive from parameters that describe microscopic species/species interactions. As well as these dynamical properties, the description of a binary electrolyte requires a thermodynamic factor and partial molar volumes for salt and solvent, which together describe the electrolyte's equilibrium state.

Thermodynamic factors express how concentration variation within an electrolyte translates into the open-circuit voltage drop across it. They relate closely to activity coefficients, which measure deviation of the chemical (or electrochemical) potential of a species from ideal-mixing behavior [47]. Activity-coefficient data for nonaqueous electrolytes is not abundant, although direct measurement of thermodynamic factors via colligative properties (melting-point depression) [135] been performed by Stewart and Newman [136] for lithium-battery electrolytes. It has been more common to use concentration-cell experiments – which measure liquid-junction potentials between a test and reference electrolyte in electrochemical contact – to determine a property that convolutes the thermodynamic factor with a transference number. Most concentration-cell analyses assume the transference number to be constant, or use model-dependent numerical optimization to deconvolute the transference number and thermodynamic factor, introducing unwanted uncertainties [83, 94, 101, 103, 136]. All prior concentration-cell studies have employed fixed, arbitrary reference

concentrations, which can introduce inaccuracies when measuring highly dilute or concentrated test concentrations [83, 94, 101–103, 110, 136–140].

The thermodynamic factor χ of a binary electrolyte is defined in terms of the solvent chemical potential μ_0, through the relation [89]

$$y_0 \vec{\nabla} \mu_0 = -\nu R T \chi \vec{\nabla} y, \tag{2.1}$$

where R is the universal gas constant, T is the absolute temperature, and $\nu = 2$ is the number of ions in a formula unit of $LiPF_6$. Here y is the salt particle fraction, which is convenient to describe composition when considering solute-volume effects [89]; particle fractions are similar to mole fractions, but are based on a measure of total molar content in which each ion is considered as a separate species. In a binary solution, the solvent particle fraction y_0 relates to y through the phase rule $y_0 + \nu y = 1$.

Through the isothermal, isobaric, locally electroneutral Gibbs–Duhem equation, χ can be understood as a Darken factor [80], which expresses how the salt's activity in the liquid varies with its concentration. In terms of salt activity coefficients [61, 89, 141], can be written as

$$\chi = 1 + \left(\frac{\partial \ln \lambda_{+-}}{\partial \ln y}\right)_{T,p} = \frac{1}{y_0}\left[1 + \left(\frac{\partial \ln \gamma_{+-}}{\partial \ln m}\right)_{T,p}\right] = c_{\mathrm{T}} \overline{V}_0 \left[1 + \left(\frac{\partial \ln f_{+-}}{\partial \ln c}\right)_{T,p}\right], \tag{2.2}$$

in which $\overline{V}_0$ is the partial molar volume of solvent, m is salt molality, c is salt molarity, and c_{T} is total particle molarity; λ_{+-}, γ_{+-}, and f_{+-} respectively represent mean molar salt activity coefficients over particle-fraction, molal, and molar bases.

Below we introduce the shifting-reference concentration-cell method, an approach to diffusion-potential measurement that minimizes the difference between reference and test concentrations across the studied composition range, thereby mitigating intrinsic error from the convoluted composition dependences of the thermodynamic factor and transference number, as well as maintaining a good signal-to-noise

ratio in highly dilute or concentrated regimes. The method is validated against fixed-reference concentration-cell data for lithium hexafluorophosphate ($LiPF_6$) in propylene carbonate (PC), and also carried out for $LiPF_6$ in ethyl methyl carbonate (EMC). The thermodynamic factor is isolated using transference-number correlations obtained by applying the Hittorf method presented by Hou and Monroe [102].

Additional transport and thermodynamic property characterization from 0 to 2.5 M for $LiPF_6$ in EMC complements the thermodynamic-factor measurement. It also enables quantification of the three Onsager–Stefan–Maxwell diffusivities, which parameterize interspecies diffusional drag forces in solution. Viscosity data for both $LiPF_6$:PC and $LiPF_6$:EMC are also reported, to underpin Walden analyses that give further insight about ion pairing. Taken together, the data suggest that $LiPF_6$:PC behaves as a typical strong electrolyte, whereas $LiPF_6$:EMC is weak.

A suite of techniques that includes the shifting-reference concentration-cell method can be applied to both strongly and weakly dissociated electrolytes. The results reported below highlight how ion association can impact the composition-dependent transport and thermodynamic properties of binary electrolytes.

2.2 Experimental

2.2.1 Electrolyte preparation

All solutions were prepared in a temperature-controlled (25.0 ± 0.5 °C), argon-filled glovebox (Inert Technologies) with sub-ppm H_2O and O_2 levels. Fresh containers of $LiPF_6$ salt (99.99%, battery grade, Sigma Aldrich) were first opened inside the glovebox; the salt was vacuum dried in a heated antechamber for 24 h at 60 °C. EMC and PC solvents (99.9%, anhydrous, Sigma Aldrich) were dried using 3 Å molecular sieves in the glovebox for a week before use. Karl Fischer titration was performed on prepared electrolytic solutions, in which the water content was determined to be less than 10 ppm.

2.2.2 Densitometry and composition

Electrolyte standards for density/composition correlations were prepared gravimetrically with given salt mass fractions ω, according to procedures described by Hou and Monroe [102]. Measurements of density ρ were performed using a high-precision oscillation density meter (DMA4100, Anton Paar) inside the glovebox. The apparatus quantifies density with five-digit precision and controls temperature within ±0.02°C. Densities that were used to produce composition correlations were measured in triplicate at 20.0, 25.0, and 30.0 °C.

Salt molarity c relates to mass fraction and density through

$$c = \frac{\omega\rho}{M_\mathrm{e}}, \tag{2.3}$$

where M_e is the molar mass of $LiPF_6$ (151.905 gmol^{-1}). For a binary electrolyte, partial molar volumes of solvent and salt can also be calculated using a density/molarity correlation [61], a process which is also described in Appendix 2.A.1.

In terms of species molarities $y = c/(c_+ + c_- + c_0)$, where subscripts +, −, and 0 respectively denote cations, anions, and solvent. In locally electroneutral binary electrolytes, salt particle fraction can be written in terms of salt molarity or mass fraction as

$$y = \frac{M_0 c}{\rho + (\nu M_0 - M_\mathrm{e})c} = \frac{M_0\omega}{M_\mathrm{e} + (\nu M_0 - M_\mathrm{e})\omega}, \tag{2.4}$$

where M_0 is the molar mass of solvent (104.105 gmol^{-1} for EMC and 102.089 gmol^{-1} for PC).

2.2.3 Viscometry

Dynamic viscosity η was measured with an in-line rolling-ball viscometer attachment to the densitometer (Lovis 2000, Anton Paar). A capillary with a 1.59 mm diameter was used for viscosity measurements across the same concentration range probed by densitometry, at temperatures of 20.0 ± 0.02, 25.0 ± 0.02, and 30.0 ± 0.02 °C.

2.2.4 Hittorf experiment

Cation transference number relative to the solvent velocity, t_+^0, was measured with a custom-made gravimetric Hittorf cell. A detailed theoretical analysis of the Hittorf experiment, a derivation of equation 2.5, and schematic diagrams of the experimental cell were provided previously by Hou and Monroe [102].

The Hittorf cell (as depicted in figure 3.A.2) has two configurations, designated 'open' and 'closed'. In the open configuration, the cell contains a single cylindrical cavity, whose ends are terminated by lithium metal electrodes. Two stopcocks can be turned to put the cell into the closed configuration, wherein the central cavity is segmented into anodic, neutral and cathodic chambers of known volume, which can be separately drained through access plugs. To perform the Hittorf experiment, lithium was prepared by polishing lithium foil (99.9% Alfa Aesar) with a PTFE brush to remove any trace oxidized surface layer, punched into discs, and placed on either end of the Hittorf cell. Current-collector endcaps were screwed on to hold the lithium discs with a 1 cm active diameter in place and seal the central cavity. Then, the stopcocks were set in the open configuration and electrolyte of known density was loaded in through the access plugs, which were subsequently sealed. Finally, the cell was oriented vertically, and a constant current $I_{\text{pulse}} = 0.2$ mA was passed for duration $t_{\text{pulse}} = 20$ h with a potentiostat/galvanostat (PGSTAT302N, Metrohm). During the current flow, lithium is plated onto the cathode (top of cell) and stripped from the anode (bottom of cell), inducing a concentration difference across the central chamber. The magnitudes of I_{pulse} and t_{pulse} were selected such that the concentration boundary layers remained within the anodic and cathodic chambers during the experimental period [97]; the total charge passed was restricted below 20 C (translating to an areal charge of *ca.* 7 mAh·cm^{-2}) to minimize the possibility of side reactions [47]. Immediately after the current was cut off, the stopcocks were set to the closed configuration, and solutions extracted from the sealed chambers were stirred for 2 h to homogenize their concentrations. Densities of these solutions were measured at 25 °C, and their molarities were found by inverting the density/molarity correlation $\rho_{25^\circ\text{C}}(c)$ established by densitometry. Then, t_+^0 was calculated from

$$t_+^0 = 1 - \frac{FV_{\text{chamber}}|c_\text{f} - c|}{I_{\text{pulse}}t_{\text{pulse}}(1 - \overline{V}_\text{e}c)}, \tag{2.5}$$

a Hittorf formula derived under the assumption that lithium ions are the only liquid-phase species which reacts at the electrodes. Here $V_{\text{chamber}} = 4.0 \pm 0.1$ mL is the volume the cathodic or anodic chamber, c_f is the concentration of the homogenized solution extracted from said chamber, c is the initial concentration of the sample, and $\overline{V}_\text{e}$ is the salt partial molar volume at c, calculated from the density correlation via equation 2.A.1 in appendix 2.A.1.

2.2.5 Shifting-reference concentration cells

Concentration cells place electrolytes containing similar molecular species with two different compositions in chemical contact: these are called the 'reference' solution, with composition y_{ref}, and the 'test' solution, y_{test}. A porous grade D frit (10–16 μm) between the electrolytes impedes diffusion across the cell, as depicted in Fig. 2.1(a). The difference in salt chemical potential across the frit results in a measurable liquid-junction potential ΔU. For a concentration cell in which the electrodes are reversible only to cations, ΔU is a functional of salt composition y through the thermodynamic factor χ and transference number t_+^0 [61, 102, 136],

$$\Delta U = \frac{\nu RT}{F}\int_{y_{\text{test}}}^{y_{\text{ref}}} \chi(1 - t_+^0)d\ln y. \tag{2.6}$$

Writing equation 2.6 in terms of properties correlated to the salt-fraction composition basis obviates the need for excluded-volume corrections, simplifying the integrand considerably [89].

Traditional concentration-cell studies employ a single reference composition across all test compositions. The use of a single reference composition can lead to issues, however. Although the thermodynamic factor χ is a state function, dependent only on the (presumably constant) surface concentrations at the electrodes, the integral in equation 2.6 also involves the composition dependence of t_+^0. Furthermore,

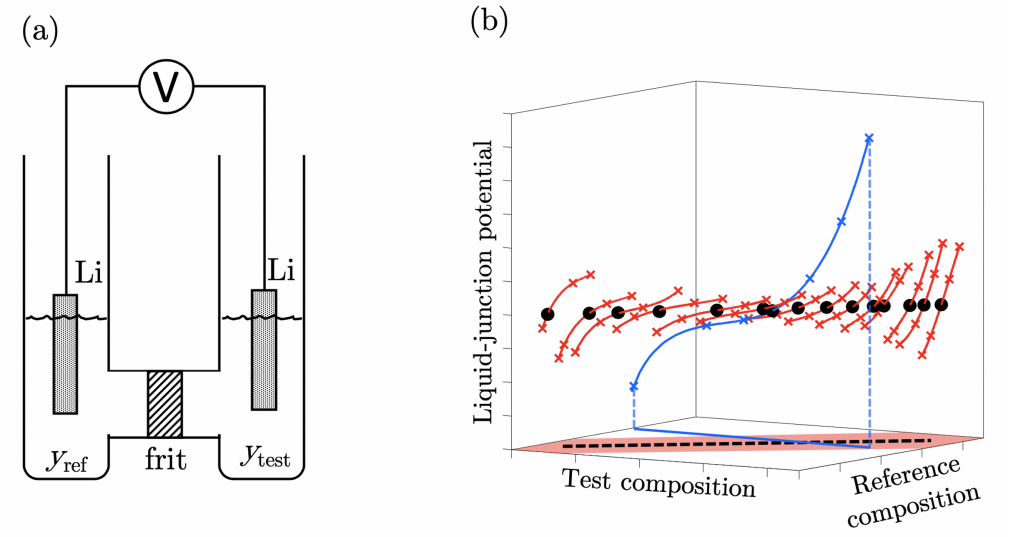


Figure 2.1: (a) Schematic of the glass 'H' shaped concentration cells. (b) Surface produced by shifting-reference concentration-cell measurements (red) and curve yielded by the single-reference concentration cell method (blue). Reference concentrations are demarcated with dots (•) and test concentrations, with crosses (x).

when differences between y_{test} and y_{ref} are large, a steady voltage plateau may never arise because the diffusion driving forces are larger, causing large transient variation of concentration profiles that incurs a concomitant change in t_+^0 with time. This has been confirmed experimentally in some studies of concentrated electrolytes, which have shown that the dependence of liquid-junction potentials on integral averages of transference numbers can be problematic [103, 142]. Issues arise in the dilute regime as well: if y_{test} is close to 0, the natural dependence of ΔU on $\ln y$ means that small variations in test concentrations can result in very large voltage changes if the reference composition is fixed.

The shifting-reference concentration-cell approach employs a matrix of liquid-junction potentials banded about a variable reference composition, minimizing the concentration difference across the liquid junction to mitigate potential errors due to local t_+^0 variation. By measuring two test compositions y_{test} above and below each reference composition y_{ref}, a band of several concentration-cell measurements (five in the present case) can be fit by a function describing ($\Delta U(y)$), which can subsequently be used to interpolate the derivative of the liquid-junction potential

with respect to composition at y_{ref}, removing the need to involve the integral that appears in equation 2.6.

By direct differentiation of equation 2.6 with respect to the test concentration, Newman [61] showed that

$$\chi(1-t_+^0) = \frac{F}{\nu RT}\left(\frac{d\Delta U}{d\ln y}\right) = \frac{Fy}{\nu RT}\left(\frac{d\Delta U}{dy}\right). \tag{2.7}$$

Thus a differential measurement of $\chi(1-t_+^0)$ can be found by interpolating a local value of $d\Delta U/dy|_{y_{\text{ref}}}$ — the change in liquid-junction potential with respect to composition at the reference composition. To analyze the data, we fit $d\Delta U/d\ln y$ to a second-order polynomial, so that

$$\frac{d\Delta U}{dy} = \frac{U_1 + U_2 y + 2U_3 y^2}{y}. \tag{2.8}$$

Integration of this expression with respect to composition produces a function that can be fit directly to experimental liquid-junction-potential data.

When repeated for multiple y_{ref} values across the concentration range, the method produces a distinct value of $\chi(1-t_+^0)$ at each composition y_{ref}. Thus the method produces a differential measurement with respect to composition, rather than a measurement involving an integral that convolutes the composition dependences of χ and t_+^0.

Fig. 2.1(b) illustrates the qualitative differences between shifting-reference and fixed-reference concentration-cell data sets, with the surface of banded liquid-junction potentials (red) more closely applying the differential form of equation 2.6 embodied by equation 2.7. In principle it is possible to fit a 2-dimensional surface to the data obtained with the shifting-reference method. Resolution in a narrow band of ΔU due to smaller composition differences was found to result in highly variable surface fits, however, so a band of concentrations around $y_{\text{test}} = y_{\text{ref}}$ was fit to produce a $\chi(1-t_+^0)$ for each y_{ref}. The number of individual experiments was also halved by noting that y_{ref} and y_{test} can be interchanged in the matrix of ΔU measurements.

2. Shifting-reference concentration cells to refine composition-dependent transport characterization of binary lithium-ion electrolytes

Inside the glovebox, 5.0 mL samples of test and reference electrolytes were simultaneously pipetted into each chamber of the glass H-cell. Temperature control was achieved using the in-built glovebox thermal management and thermostat units. Lithium foil was prepared as described in section 2.2.4 before being cut into strips and submerged in each chamber to act as symmetric, reversible reference electrodes. After allowing the liquid-junction potential to stabilize over 1 h in the glovebox at 25 °C, the steady-state open-circuit potential was recorded with a potentiostat (PGSTAT302N, Metrohm). Reference concentrations of $LiPF_6$:PC were varied in increments of approximately 0.1 M from 0.1 to 2.5 M, and test concentrations were targeted at ±0.1, ±0.2 M intervals around the reference concentration. Increments for $LiPF_6$:EMC were larger to improve voltage resolution of the potentiostat measurement, with 0.2 M reference spacing from 0.2 to 2 M and ±0.2, ±0.4 M test-concentration bands. Additional shifting-reference concentration-cell measurements were performed at lower concentrations — spaced evenly in $\sqrt{y}$ to match expectations based on Debye and Hückel's infinite-dilution limiting law — for both $LiPF_6$:PC and $LiPF_6$:EMC binary electrolyte systems. All liquid-junction potentials were measured in triplicate.

2.2.6 Ionic conductivity

Ionic conductivity κ was measured with an AC conductivity probe (Orion A212, Thermo Scientific) in a sealed cell placed in a temperature-controlled water bath, following the procedure described in Ref. [102]. Bulk resistances for cells with separators were obtained by electrochemical impedance spectroscopy (EIS) using an impedance module embedded in the potentiostat/galvanostat (Octostat5000, Ivium Technologies). This data was used to compute MacMullin numbers (geometric factors), which were subsequently used to correct restricted-diffusion measurements for the effects of porous separators, as described by Hou and Monroe [102]. Macmullin numbers and Bruggeman factors are presented in figure 2.B.3 of the supplementary information that accompanies this article.



Figure 2.2: Restricted diffusion coin cell schematic. (A) top coin cell can, (B) Li foil electrodes, (C) glass fibre separators soaked with electrolyte, (D) PEEK spacer, (E) bottom coin cell can, (F) top-down view of PEEK spacer showing annular geometry. Figure components not to scale.

2.2.7 Restricted diffusion

The Fickian diffusivity D can be measured in a restricted-diffusion experiment, wherein the relaxation of a nonuniform concentration distribution in a confined volume of electrolyte is tracked by monitoring the decay in concentration polarization between two fixed points. Thompson and Newman demonstrated that irrespective of the initial nonuniform concentration profile, the exponential decay in polarization follows Fick's second law ($\frac{\partial c}{\partial t} = D\frac{\partial^2 c}{\partial x^2}$), and will occur for relaxation timescales $t > \frac{0.005L^2}{D}$, where L is the length of the cell [143]. Transient concentration gradients can be tracked voltammetrically using open-circuit-potential (OCP) measurements between two identical reference electrodes. For small enough concentration gradients, the OCP will be directly proportional to concentration differences [97, 140, 144].

A planar, parallel-electrode symmetric cell (depicted in figure 2.2) was assembled by sandwiching an annular polyether ether ketone (PEEK) spacer (thickness: L = 2.00 mm, inner diameter: 8.00 mm, outer diameter: 16.00 mm) between two lithium discs. These discs were punched from lithium foil that was roller pressed such that the foil thickness was approximately 0.6 mm as measured via micrometer gauge. The spacer gap was filled with electrolyte in an inert glass-fiber separator (FisherBrand, porosity $\varepsilon = 0.85$) to minimize the effects of externally induced vibrations and lithium malleability. This cell sandwich was sealed in a coin cell (CR2032, MTI) using a pneumatic crimper at 380 kPa. The consistency in sealing pressure, cell

dimension, and lithium disc dimensions further mitigates error introduced by possible lithium deformation.

Linear fits of $-\ln(\mathrm{OCP})$ *vs.* time were performed, and the slope was used to determine an effective Fickian diffusivity D_{eff}:

$$\lim_{t\to\infty} \frac{d\ln(\mathrm{OCP})}{dt} = -\frac{\pi^2 D_{\mathrm{eff}}}{L^2 \varepsilon}, \tag{2.9}$$

where D_{eff} and porosity ε account for the effective diffusivity of solution in the porous separator medium. Concentration gradients were introduced by potentiostatically holding the cell at 100 mV for 12 h (Octostat5000, Ivium Technologies). Once a steady-state current was reached, the current was shut off and OCP relaxation was recorded. The potentiostatic hold and its duration were chosen such that the OCP achieved immediately after the initial capacitive relaxation of cell voltage remained below 50 mV, a range within which the relationship between OCP and concentration polarization is more linear [97]. Experiments were all performed by placing the apparatus in a thermal chamber (Binder) at 25.0 °C.

2.3 Results

2.3.1 Density and composition

Density data is plotted as a function of salt molarity in Fig. 2.3. A correlation was produced following Hou and Monroe [102], using a functional form in line with Debye–Hückel theory that also minimizes confidence intervals on the parameters:

$$\rho = \rho_0 + \rho_1 c + \rho_2 c^{3/2}. \tag{2.10}$$

Thermodynamics allows that parameters ρ_0, ρ_1, and ρ_2 may vary with temperature and pressure. Correlations in this form for $LiPF_6$:PC were reported previously [102]; parameters for $LiPF_6$:EMC at are provided in Table 2.2, which appears near section 2.3.8 below.

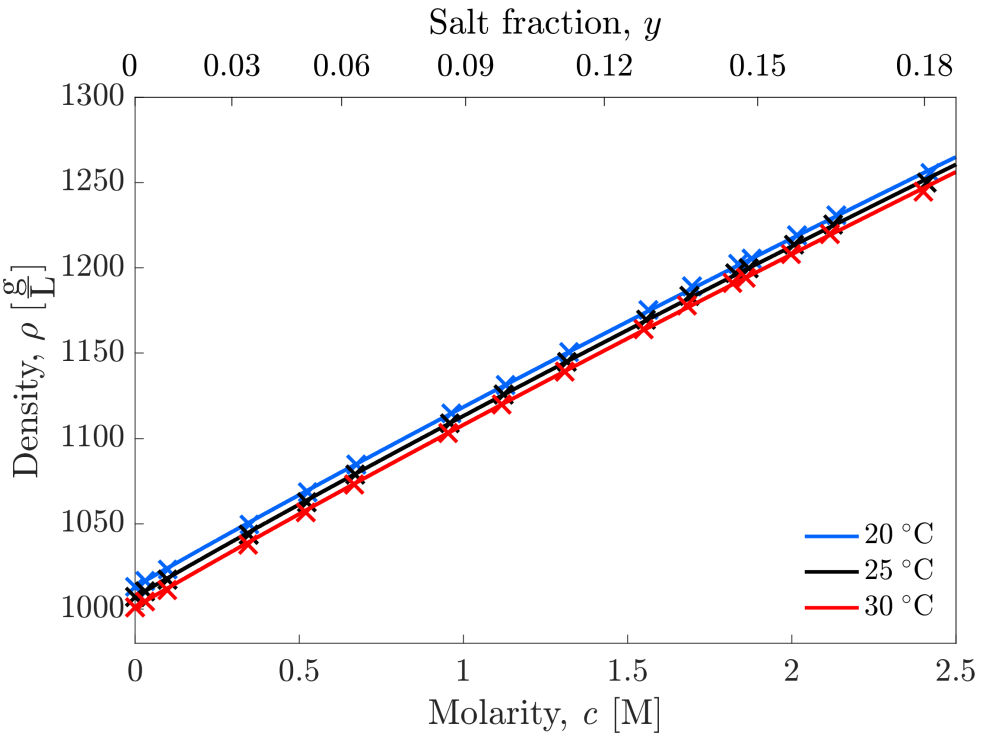


Figure 2.3: Density/composition measurements for $LiPF_6$:EMC (x) and correlations from equation 2.10 (—) at 20 °C (blue), 25 °C (black), and 30 °C (red).

Partial molar volumes of salt $\overline{V}_e$ and solvent $\overline{V}_0$ for $LiPF_6$:EMC were determined using equation 2.A.1 of the appendix. The variation of these properties was similar to previous observations for $LiPF_6$:PC [102] in the 0–2.2 M range, with $\overline{V}_e$ increasing comparatively more (∼33.5%) than the decrease in $\overline{V}_0$ (∼1%). Raw density data are tabulated in table 2.B.1 in the supplementary information that accompanies this article.

2.3.2 Transference number

The cation transference number with respect to the solvent velocity, t_+^0, is plotted in Fig. 2.4 for various Hittorf experiments at 25 °C. Results from both the anodic and cathodic chambers of the Hittorf cell were gathered, and the combined data set was fit with a second-order polynomial, yielding the correlation

$$t_+^0 = 0.4130 - 1.551y + 3.942y^2 \tag{2.11}$$

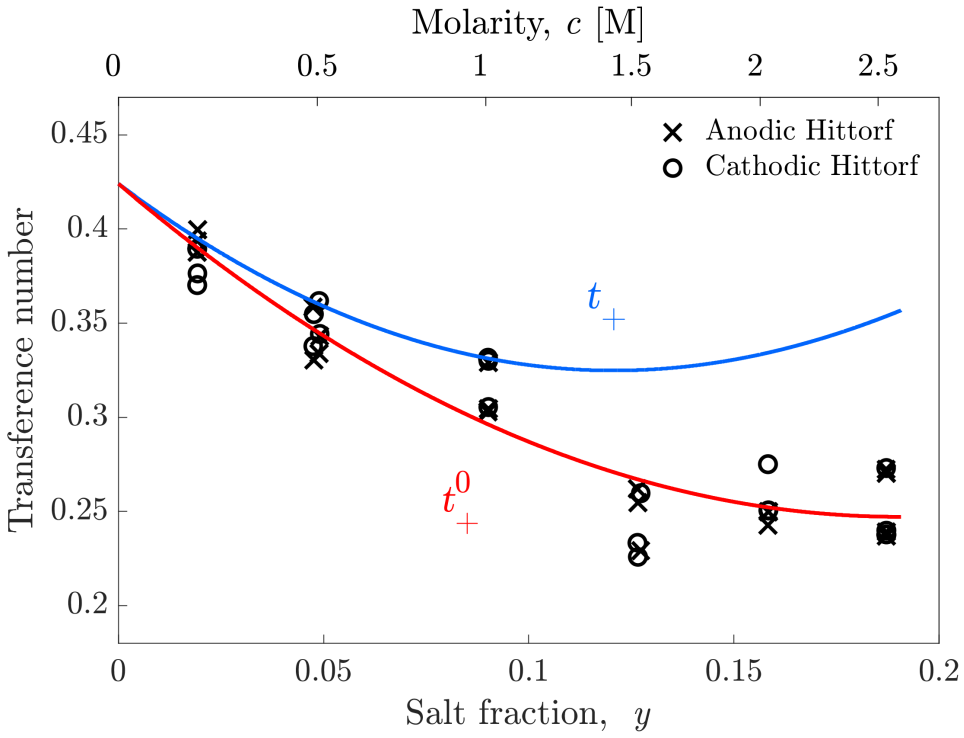


Figure 2.4: Hittorf measurements at 25 °C for the cation transference number t_+^0 of Li^+ relative to EMC, based on analysis of the anodic Hittorf chamber (x) and cathodic Hittorf chamber (o). The cation transference number (t_+^0) correlation from equation 2.11 (red —) is plotted alongside the cation transport number (t_+) from equation 2.12 (blue —).

for $LiPF_6$:EMC solutions. The Hittorf transference number t_+^0 decreases monotonically with increasing concentration, from Li^+ carrying approximately 40% of the total charge ($t_+^0 \approx 0.4$) near infinite dilution to approximately 25% at 2.5 M. Raw data from the Hittorf experiments are presented in table 2.B.2.

Note that the Hittorf formula, equation 2.5, was derived under the assumption that the electrolyte is a three-species system comprising a single positive species, a single negative species, and a neutral solvent [89, 102]. There is widespread discussion in the literature about possible speciation of the lithium salt, into (say) solvent-coordinated ions, neutral ion pairs, charged ion aggregates such as Li_2X^+ or LiX_2^-, or even solvent-coordinated polyionic superstructures [112, 145]. Since each of these secondary structures is formed by local association/dissociation reactions involving lithium cations, hexafluorophosphate anions, and solvent molecules, the

electrochemical potentials of said structures are linearly dependent on those of the primary species in an equilibrium state. Therefore, if the timescale for reaching speciation equilibrium is fast compared to the timescale for salt diffusion, a three-species model can still be applied to systems with significant speciation, but the interpretation of the parameters needs to be relaxed. In cases where speciation is appreciable, the number t_+^0 should be interpreted as a measure of the net drift of all the Li-containing species, relative to a reference frame set by the velocity of free solvent molecules. This issue has been discussed in more detail by Onsager [82], Newman [61], and Lacey [146]; the presence of speciation equilibria can justify surprising experimental observations such as negative transference numbers [110].

Fig. 2.4 also shows the ideal cation transport number t_+ (the Bruce–Vincent transference number [147]), which is obtained if the Hittorf experiment is analyzed with a model that ignores solute-volume effects, such as Nernst–Planck dilute-solution theory [102] or a concentrated-solution theory that neglects the salt's partial molar volume [148]. Since the apparent t_+ value is influenced by Faradaic convection, it varies with applied current; by contrast, t_+^0 is a truly isolable bulk property of an electrolytic solution. The validity of equation 2.5 also requires that only cations react at the electrode in the half-cell being modelled, in which case t_+^0 relates to t_+ through the volume fraction of salt, $c\overline{V}_\mathrm{e}$,

$$t_+ = 1 - (1 - t_+^0)(1 - c\overline{V}_\mathrm{e}) \tag{2.12}$$

The terms in equations 2.5, 2.12 proportional to the solvent volume fraction, $(1 - c\overline{V}_\mathrm{e})$, correct Hittorf's standard formula to account for the displacement of solvent volume by salt as interfacial reactions progress. This phenomenon has been analyzed previously by Lindbergh et al. [94, 101] and Monroe et al. [89, 102].

2.3.3 Thermodynamic factor

Liquid-junction potentials measured at 25 °C with the shifting-reference concentration-cell method are shown in Fig. 2.5(a) for $LiPF_6$:EMC with reference concentrations

ranging from $y_{\text{ref}} = 0.0012$—0.1678 (0.012 M–2.18 M) and Fig. 2.5(b) for $LiPF_6$:PC with references from $y_{\text{ref}} = 0.0007$–0.1436 (0.007 M—2.083 M). Primary data are tabulated in the supplementary information, tables 2.B.3 and 2.B.4. Each curve in plots (a) and (b) represents a banded fit about each y_{ref} with the correlation

$$\Delta U(y) = U_0'(y - y_{\text{ref}}) + U_1'(y - y_{\text{ref}})^2 + U_2' \left[\ln \frac{y}{y_{\text{ref}}} + 1 - \frac{y}{y_{\text{ref}}} \right], \tag{2.13}$$

arrived at by integrating equation 2.8 from y_{ref} to y. Fitting with the function from equation 2.13 is convenient for data analysis, because the fit parameter U_0' directly produces the value of $d\Delta U/dy|_{y_{\text{ref}}}$ that appears in equation 2.7. Using the composition correlation for t_+^0 obtained from Hittorf experiments, one can also insert $t_+^0(y_{\text{ref}})$ into this equation, allowing the thermodynamic factor $\chi(y_{\text{ref}})$ to be isolated:

$$\chi(y_{\text{ref}}) = \frac{1}{1 - t_+^0(y_{\text{ref}})} \frac{F y_{\text{ref}}}{\nu RT} U_0'|_{y_{\text{ref}}}. \tag{2.14}$$

Results for χ obtained in this way are plotted for $LiPF_6$:EMC and $LiPF_6$:PC in Fig. 2.5(c) and (d), respectively.

The Debye–Hückel theory of ionicity suggests that the thermodynamic factors of strong electrolytes vary with the square root of composition [149]. Thus, correlations for $\chi(y)$ were determined by testing power series up to various orders in $\sqrt{y}$, optimizing to obtain tight parameter confidence intervals while maintaining goodness-of-fit. Correlations for χ_{EMC} and χ_{PC} based on this fitting approach are

$$\chi_{\text{EMC}} = 1 - 18.38y^{1/2} + 155.3y - 465.6y^{3/2} + 1647y^{5/2}, \tag{2.15}$$

$$\chi_{\text{PC}} = 1 - 2.655y^{1/2} + 26.23y + 1490y^{7/2}, \tag{2.16}$$

functions plotted on Fig. 2.5(c) and (d). Hou and Monroe [102] presented fixed-reference concentration-cell data for $LiPF_6$:PC ($y_{\text{ref}} = 0.07648$). Fig. 2.5(d) shows

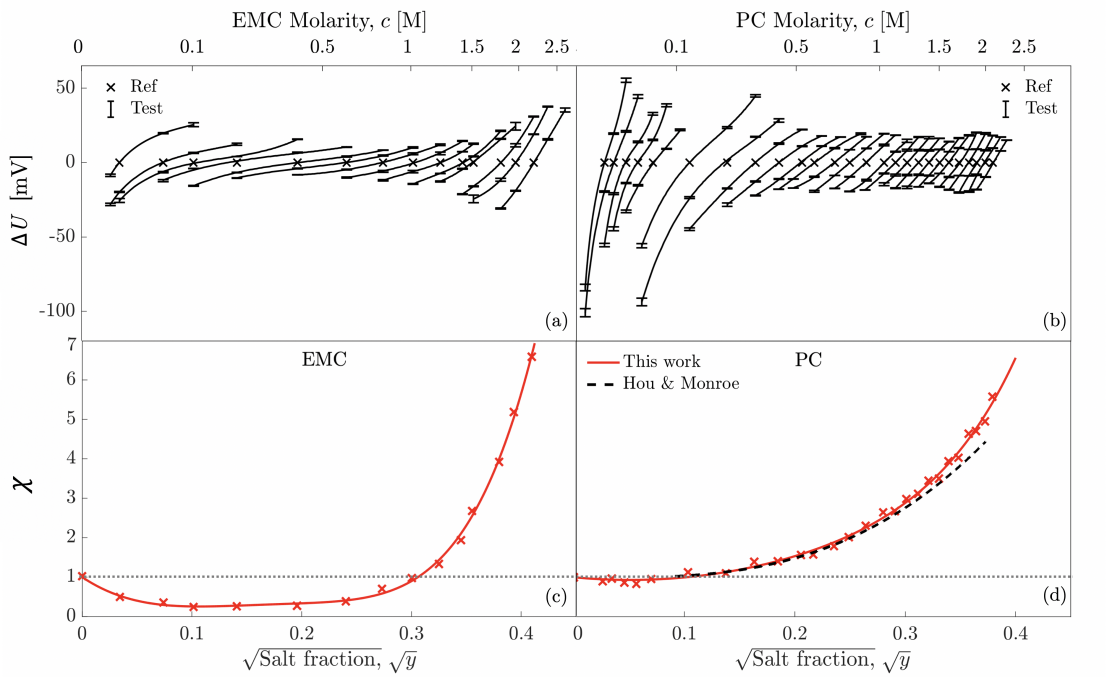


Figure 2.5: Banded liquid-junction potentials measured using the shifting-reference concentration-cell method for $LiPF_6$:EMC (a) and $LiPF_6$:PC (b). Error bars represent the standard deviation in the average of three replicate measurements and (x) indicate each reference composition y_{ref}. Each band is fit by equation 2.13 (black —). Thermodynamic factor χ is plotted for $LiPF_6$:EMC (c) and $LiPF_6$:PC (d) at each y_{ref} (x) with correlations from equations 2.15, 2.16 (red —), with $\chi = 1$ indicated by (gray $\cdots$). Panel (d) also shows the fitting from Hou and Monroe [102] using the fixed-reference method (black – – –).

good agreement between the fixed–reference and shifting-reference approaches for $LiPF_6$:PC in the 0.2 M — 2 M range where Hou and Monroe's correlation is valid for interpolation.

At infinite dilution the thermodynamic factor χ for any dilute solute must go to unity, and the analysis of electrostatic interactions provided by Debye–Hückel theory [149] suggests that thermodynamic factors of electrolytes should fall with the square root of salt concentration when dilution is high. Although parameter ranges were not restricted during data fitting, the coefficients of the $\sqrt{y}$ terms in correlations 2.15 and 2.16, which we notate as $\chi_{\sqrt{y}}$ for brevity, were both naturally negative. An implementation of Debye–Hückel theory following Newman and Thomas–Alyea [61] shows that $\chi_{\sqrt{y}}$ is expected to follow the limiting law

$$\chi_{\sqrt{y}} = -\frac{1}{8\pi N_{\mathrm{A}}}\sqrt{\frac{\rho_0}{2M_0}\left(\frac{F^2}{\varepsilon_{\mathrm{r}}\varepsilon_0 RT}\right)^3}, \tag{2.17}$$

in which N_{A} is Avogadro's number, ε_{r} is the relative permittivity of the solvent, and ε_0 is the permittivity of vacuum. Shifting-reference concentration-cell results remain consistent and achieve good signal-to-noise in the highly dilute regime, making them suitable to probe the validity of this relationship.

For $LiPF_6$:PC, Debye–Hückel theory predicts that $\chi_{\sqrt{y}}$ is –2.67, in good agreement with the value of –2.655 that appears in correlation 2.16. (NB: The fixed-reference concentration-cell data of Hou and Monroe for $LiPF_6$:PC suggested a $\chi_{\sqrt{y}}$ value of –0.3243. They observed that this value was error-prone, however, because it required extrapolation of the correlation far outside their range of experimental test concentrations [102].)

For $LiPF_6$:EMC solutions, equation 2.17 predicts a much steeper theoretical Debye–Hückel slope: –250, far different from the value of –18.76 obtained from correlation 2.15. This discrepancy can be understood by recognizing that the Debye–Hückel analysis assumes that the concentrations of dissolved ions in solution arise from complete dissociation of the host salt — *i.e.*, it assumes that as well as measuring the salt content, y also measures the ionic strength [149]. If salt dissociation is incomplete, so that the extent of salt dissociation is some fraction $0 \leq \xi < 1$, then the slope will be lower in magnitude than the prediction of equation 2.17 by a factor of $\sqrt{\xi}$. The ratio of $18.38/250 = 0.074$ suggests that the extent of dissociation for $LiPF_6$ in EMC is no more than 27% in the approach to infinite dilution — and could be much less.

Significant deviation of χ from the Debye–Hückel limiting law, as is observed for both $LiPF_6$:PC and $LiPF_6$:EMC at moderate concentrations, generally indicates that specific species/species interactions are causing non-ideal behavior that is not amenable to analysis with a classical electrostatic theory. Such chemical interactions can be interpreted qualitatively following the general principles laid out by Robinson and Stokes [47]. First, ion/ion interactions such as ion pairing and association

serve to decrease the free energy of the solute in comparison to the solvent, hence decreasing the salt activity coefficient and, along with it, χ, which relates to the derivative of activity with respect to composition through equation 2.2. Second, ion/solvent interactions hold more solvent molecules in the solution phase, effectively decreasing the solvent's vapor pressure [135] and causing a corresponding increase in the solute's activity coefficient, leading to a consequent increase in χ. These competing trends are also substantiated by more recent electrolyte theories such as the binding mean spherical approximation [150]. Note that the crossing points where $\chi_{\mathrm{PC}} = 1$ at $\sqrt{y} \approx 0.1$ (0.12 M) and $\chi_{\mathrm{EMC}} = 1$ at $\sqrt{y} \approx 0.3$ (1.01 M) merely reflect compositions at which competing nonideal factors are in balance, rather than indicating thermodynamic ideality.

2.3.4 Conductivity, viscosity, and Stokes law model

Ionic conductivity κ trends through a maximum near 1.8 M for $LiPF_6$:EMC, as can be seen from the plot in figure 2.B.1 of the supplementary information. Experimental conductivity data are tabulated in table 2.B.5 of the supplementary information. Equivalent conductance Λ is plotted in Fig. 2.6; it is determined by dividing the ionic conductivity by the salt molarity, as well as the cation's charge and its stoichiometric coefficient in the neutral salt,

$$\Lambda = \frac{\kappa}{z_+ \nu_+ c}. \tag{2.18}$$

The hypothesis that dilute $LiPF_6$:EMC is a weak electrolyte is consistent with the nonlinear dependence of its equivalent conductance on $\sqrt{y}$ near infinite dilution, which contrasts the more typical response of a strong electrolyte exhibited by $LiPF_6$:PC. For data fitting of $LiPF_6$:EMC equivalent conductance, the functional form

$$\Lambda = \left(\Lambda_1 y^{1/4} + \Lambda_2 y^{1/2} + \Lambda_3 y^{5/4}\right)^2 \tag{2.19}$$

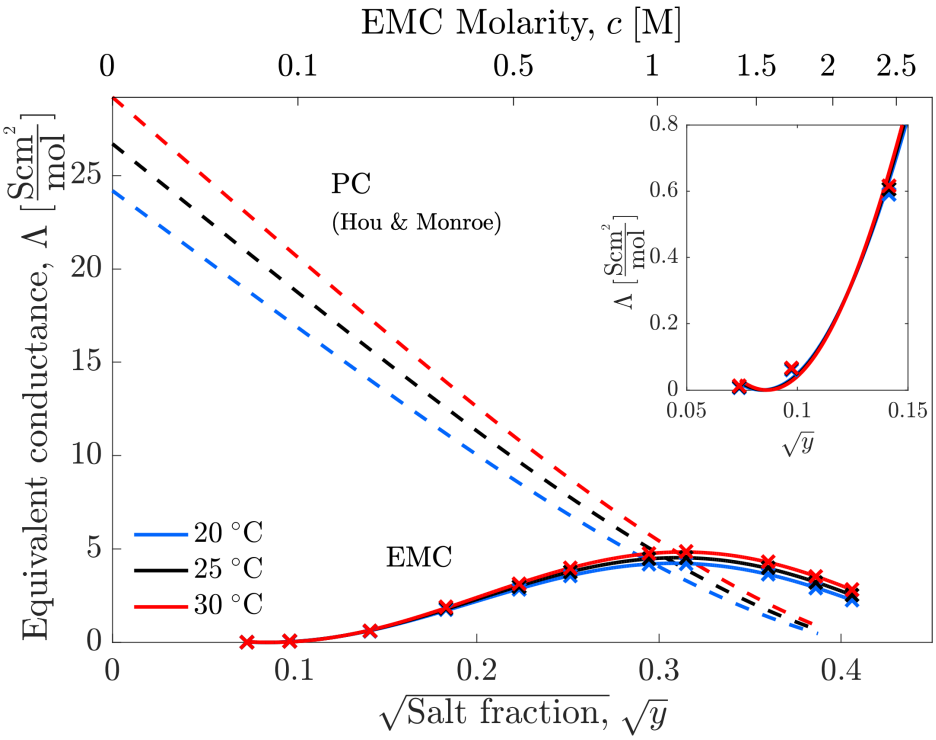


Figure 2.6: Equivalent conductances Λ at 20, 25, and 30 °C for $LiPF_6$:EMC (x) with (—) representing correlations based on fitting in equation 2.19 in the region valid for interpolation. Equivalent–conductance correlations for $LiPF_6$:PC from Hou and Monroe [102] are plotted for comparison (– – –)

was chosen by systematically iterating through various functions of the form $\Lambda = \left[P_7(y^{1/4})\right]$, where $P_7(x)$ represents a 7th-order polynomial in x. An optimization algorithm was written to vary the number of nonzero coefficients in the polynomial, as well as the combination of powers associated with said coefficients, seeking the fit with the fewest parameters, highest R-squared value, and tightest confidence intervals. (More details are provided in the supplementary information.) All functions with fewer than 2 or more than 4 nonzero coefficients had higher error; the function in equation 2.19 had both the highest R-squared and tightest root-mean-squared average confidence intervals of all the 3-parameter fits. It is worth noting that when a constant term (nonzero coefficient of x^0) was included in P_7, the error was generally higher, and a null value of the constant was always within its confidence interval. Thus the fitting process does not confirm that the electrolyte reaches a finite equivalent conductance at infinite dilution, as Onsager–Fuoss theory

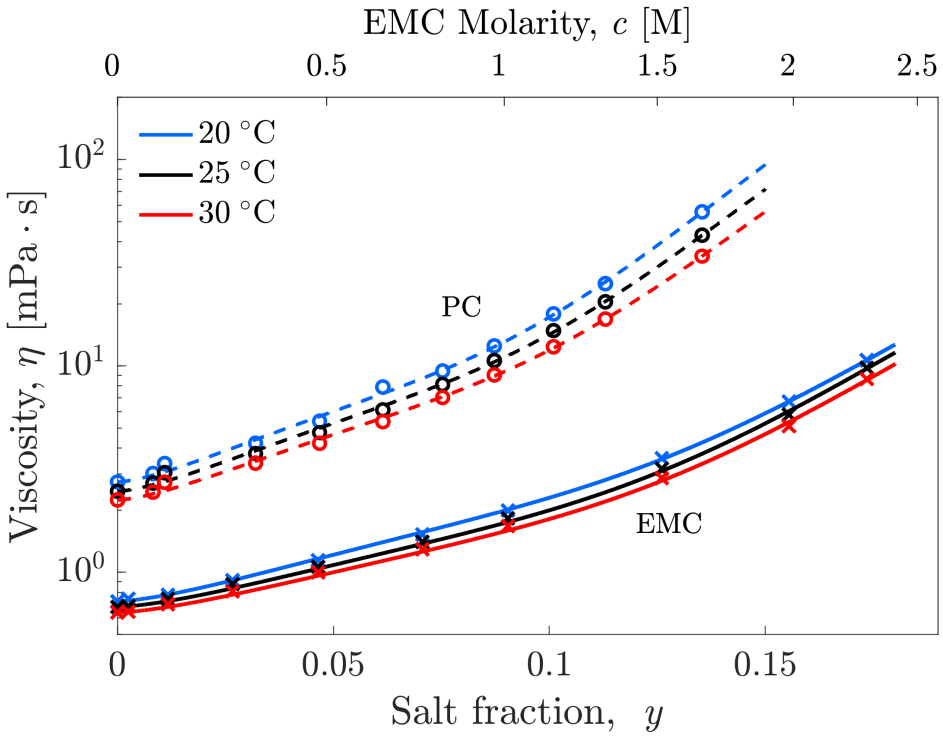


Figure 2.7: Dynamic viscosity η at 20, 25, and 30 °C for $LiPF_6$:EMC (x) and $LiPF_6$:PC (o), along with correlations at each temperature for $LiPF_6$:EMC (—) and $LiPF_6$:PC (– – –).

would suggest [47]. Due to the qualitative nature of its development, it should be emphasized that correlation 2.19 is only strictly valid for interpolation, and should not be used outside the range of 0.05–2.15 M. Each parameter Λ_k is provided for temperatures 20, 25, and 30 °C in the correlation summary, Table 2.2.

Dynamic viscosity η was measured with respect to salt fraction y for both $LiPF_6$:EMC and $LiPF_6$:PC solutions. It generally increases with salt concentration, as shown in Fig. 2.7. Data were fit by a power series in $\sqrt{y}$, found using the error-minimization principles discussed earlier,

$$\eta = \eta_0 + \eta_1 y^{3/2} + \eta_2 y^{13/2}. \tag{2.20}$$

Each coefficient is listed in Table 2.2 for EMC and PC, at temperatures of 20, 25, and 30 °C, and the raw data is tabulated in Tables 2.B.6 and 2.B.7. $LiPF_6$:PC solutions were more viscous than $LiPF_6$:EMC at similar salt fractions across the range studied.

2. Shifting-reference concentration cells to refine composition-dependent transport characterization of binary lithium-ion electrolytes

A Walden analysis using Stokes mobilities can be applied to further elucidate differences in salt dissociation between the electrolytes studied. In very dilute solutions, the Stokes–Einstein relation suggests that the mobility u_i of solvated ion i in a homogenous background solvent relates to its hydrodynamic radius R_i through the solvent viscosity [151]. For mobile Li^+ cations,

$$u_+ = \frac{N_A}{6\pi\eta R_+}. \tag{2.21}$$

Nernst–Planck dilute-solution theory further suggests that equivalent conductance provides a measure of total ionic mobility, and that the transference number of a species measures its fractional contribution to this total. A cation equivalent conductance λ_+ can thus be defined by [61]

$$\lambda_+ = \Lambda t_+^0 = |z_+|F^2 u_+. \tag{2.22}$$

Walden's rule puts equations 2.21,2.22 together to draw the conclusion that the equivalent conductance should vary in direct proportion to the inverse viscosity ($\Lambda t_+^0 \propto 1/\eta$). The validity of this relationship is probed by the Walden plot in Fig. 2.8, which presents lithium equivalent conductance as a function of inverse viscosity — both of which are parametric functions of composition — for $LiPF_6$:EMC and $LiPF_6$:PC. The plot was created using the η correlations presented above for both solutions. Experimental correlations for Λ and t_+^0 of $LiPF_6$:EMC are also presented in Table 2.2; for $LiPF_6$:PC, these correlations were taken from Hou and Monroe [102].

The Stokes–Einstein relation assumes that ion/ion interactions do not affect their mobilities and that changes in the solvent's volume fraction do not impact the ions' hydrodynamic radii. A comparison of the curves in Fig. 2.8 for $LiPF_6$:PC and $LiPF_6$:EMC with a reference line parallel to the curve for KCl:H_2O — often taken as the standard in literature for a well-dissociated electrolyte [152] — suggests that $LiPF_6$ appears well dissociated in PC across the concentration range studied, while $LiPF_6$ in EMC does not at concentrations below 1.01 M. The inflection point

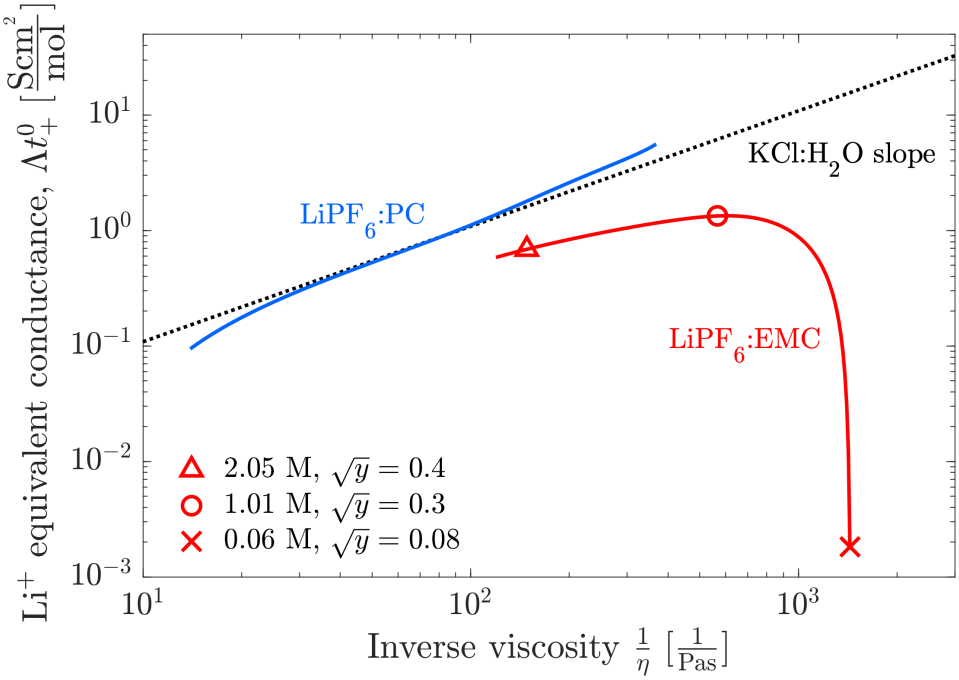


Figure 2.8: Walden analysis for cation equivalent conductance Λt_+^0 plotted against the inverse of viscosity η^{-1} at 25 °C for $LiPF_6$:EMC (red), and $LiPF_6$:PC (blue). Plot markers (△, o, x) serve to indicate composition trends while $(\cdots)$ represents the slope parallel to that of KCl in water to represent a well dissociated electrolyte [152].

at $\sqrt{y} = 0.3$ ($c = 1.01$ M) — indicated by the (o) marker for $LiPF_6$:EMC, above which the slope conforms better to Walden's rule — correlates well with the point in thermodynamic factor χ in Fig. 2.5(c) at $\sqrt{y} = 0.3$ where the thermodynamic effects of ion pairing balance solvation interactions ($\chi_{\text{EMC}} \approx 1$). This observation highlights the important link between phenomenological transport properties and a solution's thermodynamic state.

2.3.5 Diffusion coefficient

Values of the effective Fickian diffusivity D_{eff} obtained from potentiometric restricted-diffusion experiments for $LiPF_6$:EMC are plotted in figure 2.B.2 and summarized in table 2.B.8 of the supplementary information. These were corrected to obtain Fickian diffusivities of the pure solution D via EIS measurements of inverse MacMullin numbers α, following the method of Hou and Monroe [102], who used the formula

$D_{\text{eff}}/D = \kappa_{\text{eff}}/\kappa = \alpha$. This cell-specific MacMullin scaling of restricted-diffusion data helps resolve separator-to-separator variation, which arises in the present case from the highly variable tortuosity of randomly woven glass fiber. Although not used in the data processing for restricted diffusion, Bruggeman exponents b were calculated from experimental MacMullin-number measurements with the formula $\alpha = \varepsilon^b$ [101, 153] and the manufacturer's reported separator porosity $\varepsilon = 0.85$, yielding that $b = 1.23 \pm 0.74$. All the experimental MacMullin-number data are summarized in the supplementary information (figure 2.B.3).

Fickian diffusivity D for $LiPF_6$:EMC at 25 °C decreases across the concentration range and was fit with a second-order polynomial:

$$D = 504.8\frac{\mu\text{m}^2}{\text{s}} \times (1 - 6.064y + 11.35y^2). \tag{2.23}$$

Fig. 2.9 presents the composition dependence of Fickian diffusivity D as well as a thermodynamic diffusivity $\mathscr{D}$, based on a salt chemical-potential gradient driving force for diffusion, rather than a molarity gradient. The thermodynamic factor χ relates these through

$$D = \mathscr{D}\chi; \tag{2.24}$$

data on the plot were computed using equation 2.15. Ion association would be expected to increase the apparent thermodynamic diffusivity of the salt, because the merging of two or more species into a single particle implies a lower apparent resistance to the single particle's motion [47].

2.3.6 Onsager–Stefan–Maxwell coefficients

The Onsager–Stefan–Maxwell formalism expresses transport laws in terms of thermodynamic forces that drive diffusion. Under isothermal, isobaric conditions, the balance between the thermodynamic force driving species k and the friction forces exerted on k by the relative motion of all other species is

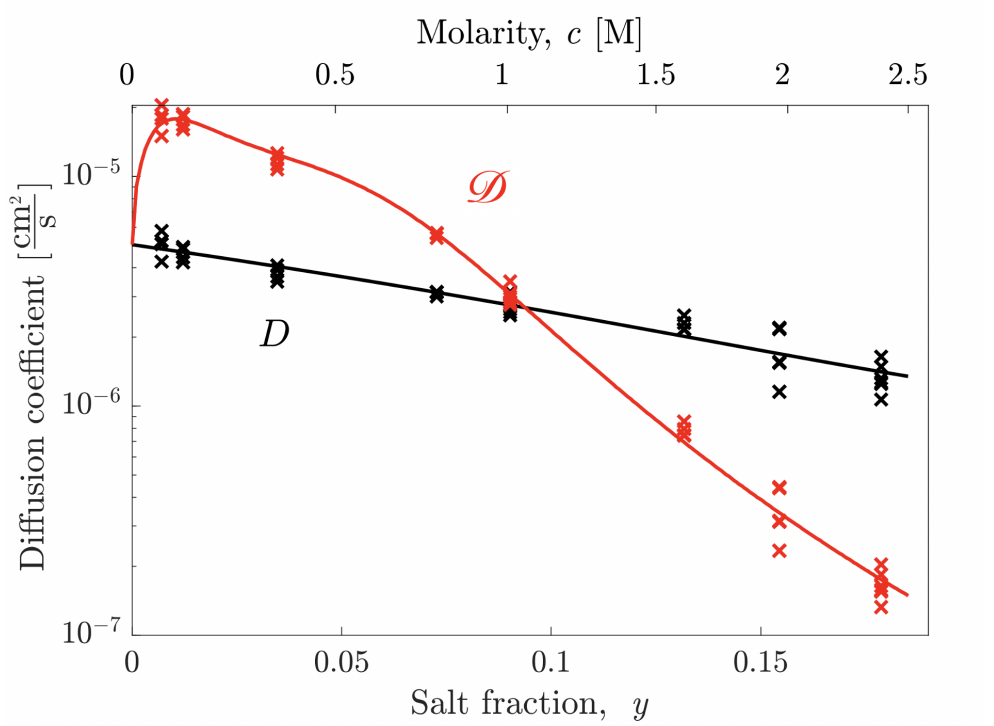


Figure 2.9: Fickian diffusion coefficient D (black) and thermodynamic diffusion coefficient $\mathscr{D}$ (red) of $LiPF_6$ in EMC at 25 °C. Curves show correlations that derive from equations 2.23, 2.24.

$$-c_{\mathrm{T}} y_k \overrightarrow{\nabla} \mu_k = RT \sum_{k \neq j} \frac{y_j \overrightarrow{N}_k - y_k \overrightarrow{N}_j}{\mathscr{D}_{kj}}, \tag{2.25}$$

where $\overrightarrow{N}_k$ is the molar flux of species k, μ_k is its electrochemical potential, and y_k, its particle fraction; $\mathscr{D}_{kj}$ is the Stefan–Maxwell diffusivity of species k through species j, which may be interpreted as an inverse friction factor [61, 89, 102]. Transport models based on Onsager–Stefan–Maxwell theory incorporate microscopic species/species interactions, which can be significant in both concentrated electrolytes and weakly-dissociated dilute electrolytes. In a binary electrolytic solution, Stefan–Maxwell diffusivities can be directly computed from bulk transport properties through the mappings [61]

$$\mathscr{D}_{0-} = \frac{\nu_- \mathscr{D}}{\nu t_+^0}, \quad \mathscr{D}_{0+} = \frac{\nu_+ \mathscr{D}}{\nu(1 - t_+^0)}, \quad \frac{1}{\mathscr{D}_{\pm}} = \frac{F^2 z_+}{RT \nu_- \Lambda y} - \frac{\nu(1 - \nu y) t_+^0 (1 - t_+^0)}{\nu_+ \nu_- \mathscr{D} y}. \tag{2.26}$$

When analyzing the binary $LiPF_6$:EMC electrolytes studied here, the individual species were taken to be the cation Li^+ (+), anion PF_6^- (–), and solvent EMC (0), and y was consequently computed assuming complete dissociation of the salt. As first pointed out by Onsager [82], this possible misidentification of species' states in a weak electrolytic solution will not affect the number of independent parameters in a thermodynamic model so long as the number of independently variable species concentrations assigned to the system is correct. Thus the assumption that an electrolyte is strong when defining and computing its properties does not have an effect if it exists in a dissociation equilibrium. Within a multicomponent transport model, the same observation holds true so long as local association/dissociation equilibrium is achieved with very rapid kinetics compared to the characteristic timescales associated with transport phenomena.

It is worth noting that the explicit consideration of associated $[(\mathrm{Li})_x(\mathrm{PF_6})_y(\mathrm{solvent})_z]^{x-y}$ complexes as additional species, both within the system's equilibrium constitutive formulation and the transport constitutive laws, could permit a more detailed understanding of how the phenomenological material properties depend on composition. Under the assumption that the kinetics of every speciation reaction is fast, both $LiPF_6$:PC and $LiPF_6$:EMC are treated here as 'pseudo-binary' electrolytic solutions, which can be described completely by a three-species transport model. Explicit accounting for ion pairs has been attempted recently using simulations based on Nernst–Planck–Poisson transport equations [154], but that constitutive framework neglects solute/solute interactions and does not explicitly couple the species electrochemical potentials through reaction equilibria. A similar extension of the present theory is possible, but would introduce many unknown parameters into both the thermodynamic model and the Onsager–Stefan–Maxwell formulation, as well as complicating the theoretical relationships among macroscopic and microscopic parameters (cf. equation 2.26. For example, the consideration of a single additional dissolved species — say, undissociated salt, as well as dissociated cations and anions – would introduce two additional thermodynamic factors and a new partial molar

volume, as well as three additional Stefan–Maxwell diffusivities, into the parameter space of the model. An explicit accounting for ion-association effects will therefore be left to a future, more theoretical analysis, which may also shed light on the macroscopic impacts of slow speciation reaction kinetics.

Fig. 2.10 shows the Stefan–Maxwell coefficients for $LiPF_6$:EMC solutions, calculated using the transport-property correlations at 25 °C summarized in Table 2.2. The relatively low value of the ion/ion diffusivity $\mathscr{D}_{+-}$, being up to five orders of magnitude lower than the solvent/ion Stefan–Maxwell coefficients at high dilution, suggests substantial ion pairing. This observation is consistent with both the Robinson–Stokes perspective on thermodynamic factor and the Walden analysis of cation equivalent conductance. As $LiPF_6$ content increases, $\mathscr{D}_{0-}$ and $\mathscr{D}_{0+}$ decrease by two orders of magnitude, as the solvent exerts stronger drag on solvated cations and anions; the fall is steeper at compositions where $\chi_{\mathrm{EMC}} > 1$ in Fig. 2.5(c). Unlike the $\mathscr{D}_{+-}$ values measured for $LiPF_6$ in PC by Hou and Monroe [102], $\mathscr{D}_{+-}$ for $LiPF_6$ in EMC increases across the concentration range, and does not pass through a maximum at the same composition as ionic conductivity does. This suggests that the effects of cation/anion coordination due to a lack of free solvent are not important for this electrolyte below 2 M.

2.3.7 On ion association

Results from sections 2.3.3 Thermodynamic factor, 2.3.4 Conductivity, viscosity, and Stokes law model, 2.3.6 Onsager–Stefan–Maxwell coefficients for $LiPF_6$ salt in EMC and PC are better understood by comparing the physicochemical properties of EMC and PC associated with solvation, which are presented in Table 2.1. Pure PC has a much higher relative permittivity and polarity (dipole moment) compared to pure EMC. Ion pairing has been demonstrated to depend on solvent donicity and Lewis-base characteristics [155, 156], but a purely electrostatic perspective on solvation suffices to rationalize how higher-polarity PC molecules should stabilize isolated ions more than EMC. The electrostatic (Born) free energy of solvation $-\Delta G_{\mathrm{el}}$ is less exergonic for EMC, as it scales with $1 - \varepsilon_{\mathrm{r}}^{-1}$ [47]. Finally, in the

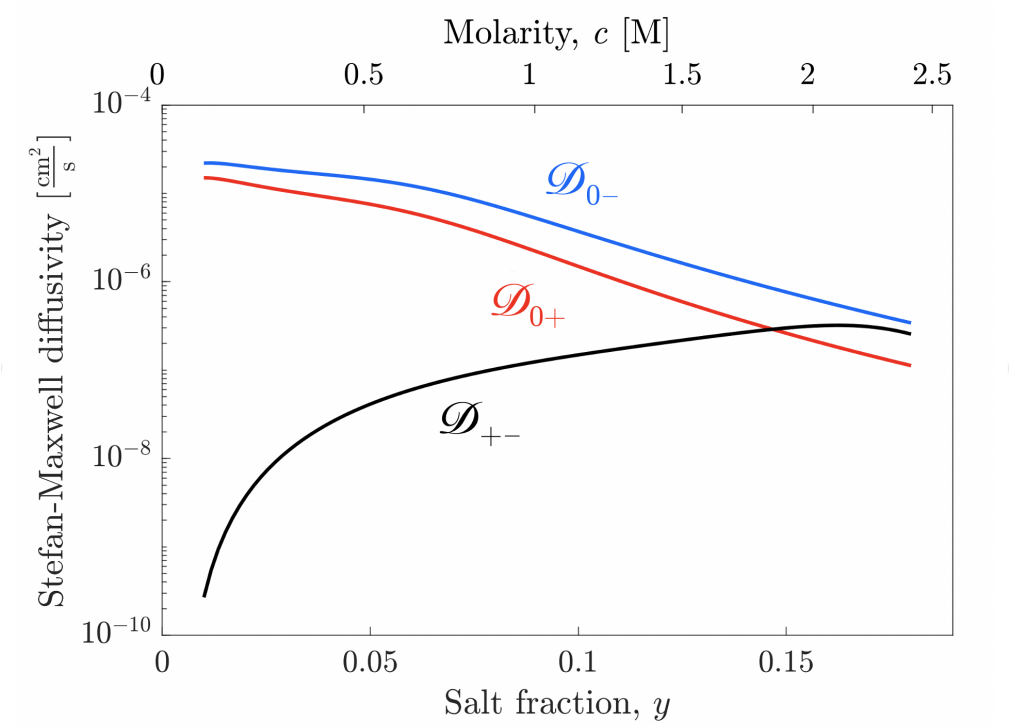


Figure 2.10: Stefan–Maxwell coefficients for $LiPF_6$:EMC at 25 °C calculated from property correlations in the composition ranges valid for interpolation.

Table 2.1: Relative permittivity ε_r, dipole moment, and calculated Bjerrum critical distance q for EMC and PC solvents at 25 °C [8].

Solvent	ε_r	dipole moment (D)	q (nm)
EMC	2.958	0.89	9.474
PC	64.92	4.81	0.431

Bjerrum theory [157], two opposing ions may be considered associated if they are separated by less than the Bjerrum critical distance where the coulombic attractive energy overcomes dissociative driving forces [145], indicating that Li^+ and must be much closer together in PC for electrostatic interactions to favor ion pairing [47].

The suppressed thermodynamic factor χ, non-linear Walden plot, and low ion/ion Stefan–Maxwell diffusivity all corroborate the hypothesis that the extent of dissociation is low for dilute $LiPF_6$ in EMC. This contrasts $LiPF_6$:PC, for which no significant ion-pairing effects are seen below 0.5 M.

Ion pairing has consequences for measured thermodynamic properties as well as ion-transport mechanisms. The interpretation of spectroscopic data for ion

association often relies on observations of relative changes in absorption spectra and bond symmetry; hence the thermodynamic and transport markers of ion pairing provide additional context when absorption spectra for solvent and solute molecules overlap [158]. In addition, the comparison between $LiPF_6$:EMC and $LiPF_6$:PC properties here supports the preferential-solvation narrative for cyclic carbonate solvents over acyclic carbonates in conventional commercial Li-ion electrolytes [9, 57]. Even minor addition of a strongly-solvating cyclic carbonate such as PC or ethylene carbonate to $LiPF_6$ in a linear carbonate such as EMC causes the electrolyte's properties to adhere disproportionately to those associated with cyclic-carbonate solvation [94, 158–160]. Future multicomponent transport models based on Onsager–Stefan–Maxwell concentrated-solution theory for co-solvent systems may yield further insights when combined with spectroscopy and compared against the data presented for binary electrolytes in this work. Yet for electrolytic solutions wherein ion speciation or association is locally quasi-equilibrated on the timescales relevant to bulk transport, the distinction between free ions and associated pairs may not be important for continuum-level electrolyte models.

A consistent composition basis and a complete thermodynamic and transport parametrization allows for the accurate simulation of dynamical electrolyte behavior regardless of degree of dissociation, as shown by Hou and Monroe for $LiPF_6$:PC [102] and in section 2.3.8 and appendix 2.A.2.

2.3.8 Parameter summary and validation

Table 2.2 summarizes the property correlations discussed throughout this work. Note that composition bases may be easily interchanged between salt fraction y, molarity c, and mass fraction ω by applying equations 2.3, 2.4.

The full transport and thermodynamic property characterization of $LiPF_6$:EMC presented here allows the implementation of the electrolyte transport models put forward by Hou, Liu, and Monroe [89, 97, 102], which are based on an extended concentrated-solution theory that includes solute-volume effects. The measured voltage drop across the electrolyte relates to changes in cation electrochemical potential,

which are dictated in part by the composition dependence of the thermodynamic factor χ. Figure 2.A.2 of the Appendix shows good agreement between experimental and simulated results of restricted-diffusion voltage relaxations at 25 °C, validating the parameter correlations presented here for $LiPF_6$:EMC solutions.

Table 2.2: Summary of parameter correlations for properties measured in this work. Note the composition basis is salt fraction y for all correlations except density ρ where molarity is used to calculate partial molar volumes more easily, as discussed in appendix 2.A.1. Remaining $LiPF_6$:PC correlations are available in Ref. [102]. Constants in these functions are reported to 3 or 4 significant figures to ensure smooth fits; measurements of parameter uncertainties (95% confidence intervals) are reported in supplementary table 2.B.9 and 2.B.10.

Electrolyte	Property	T / °C	Correlation	Units
$LiPF_6$:EMC	$\rho(c\ [M])$	20	$1013.1 + 113.19c - 7.8842c^{3/2}$	gL^{-1}
		25	$1007.1 + 114.20c - 8.1212c^{3/2}$	gL^{-1}
		30	$1001.1 + 115.13c - 8.3005c^{3/2}$	gL^{-1}
	$\eta(y)$	20	$0.724 + 43.80y^{3/2} + 5.964 \times 10^5 y^{13/2}$	mPa•s
		25	$0.680 + 36.01y^{3/2} + 5.655 \times 10^5 y^{13/2}$	mPa•s
		30	$0.639 + 32.17y^{3/2} + 4.917 \times 10^5 y^{13/2}$	mPa•s
	$\Lambda(y)$	20	$\left(-9.273y^{1/4} + 33.39y^{1/2} - 58.50y^{5/4}\right)^2$	Scm^2mol^{-1}
		25	$\left(-9.631y^{1/4} + 34.46y^{1/2} - 59.64y^{5/4}\right)^2$	Scm^2mol^{-1}
		30	$\left(-9.970y^{1/4} + 35.47y^{1/2} - 60.66y^{5/4}\right)^2$	Scm^2mol^{-1}
	$\chi_{EMC}(y)$	25	$1 - 18.38y^{1/2} + 155.3y - 465.6y^{3/2} + 1647y^{5/2}$	—
	$t_+^0(y)$	25	$0.4240 - 1.858y + 4.880y^2$	—
	$D(y)$	25	$504.8(1 - 6.064y + 11.35y^2)$	$\mu m^2 s^{-1}$
$LiPF_6$:PC	$\eta(y)$	20	$2.74 + 287.9y^{3/2} + 1.702 \times 10^7 y^{13/2}$	mPa•s
		25	$2.47 + 246.7y^{3/2} + 1.245 \times 10^7 y^{13/2}$	mPa•s
		30	$2.24 + 212.3y^{3/2} + 9.382 \times 10^6 y^{13/2}$	mPa•s
	$\chi_{PC}(y)$	25	$1 - 2.655y^{1/2} + 26.23y + 1490y^{7/2}$	—

2.4 Conclusion

A refined experimental methodology for concentration-cell measurements was implemented by using a shifting reference concentration, which creates a banded surface of liquid-junction potentials that can be fit to interpolate how the potential changes with composition. The method was demonstrated and combined with Hittorf transference-number measurements and densitometry data to quantify composition-dependent thermodynamic factors χ for $LiPF_6$ in EMC and $LiPF_6$ in PC up to approximately 2 M concentrations. The shifting-reference concentration-cell method reduces error in the liquid-junction potential resulting from proportionally large concentration differences and the composition dependence of the cation transference number. This combination of techniques can be applied to new electrolyte formulations to assess their departures from thermodynamic ideality, which in turn governs the concentration overpotentials expected in full-cell configurations operated at high power. Conductivity and viscosity measurements were used to implement a Walden analysis that showed the mobility of lithium of $LiPF_6$:EMC to differ substantially from expectations based on the Stokes–Einstein relation. Finally, a full set of macroscopic transport properties: transference number, equivalent conductance, and thermodynamic diffusivity, was mapped into Stefan–Maxwell coefficients that describe the microscopic species/species interactions in $LiPF_6$:EMC.

All three of these approaches help to demonstrate the impact of ion pairing. Suppression of the thermodynamic factor χ, an askew Walden plot, and extremely high cation/anion friction factors in the dilute regime are exhibited by weakly-dissociated $LiPF_6$:EMC, but not by strongly-dissociated $LiPF_6$:PC.

Agreement between simulation and experiment for both weak and strong binary electrolytes suggests that the weakness of the $LiPF_6$:EMC electrolyte does not affect the accuracy of transport models rooted in concentrated-solution theory based on an Onsager–Stefan–Maxwell formalism that accounts for three independent species. Further spectroscopic measurements, as well as measurements across wider temperature ranges, could provide additional information about association/dissociation equilibrium and kinetics in the future.

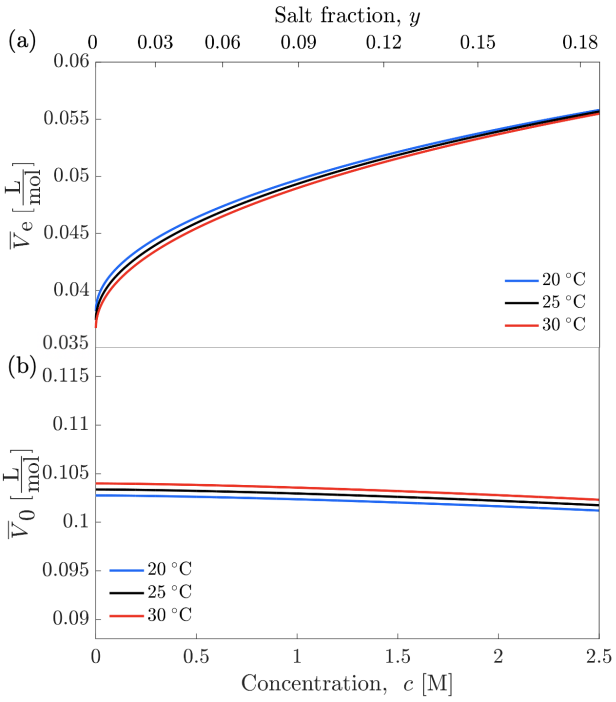


Figure 2.A.1: (a) Partial molar volume of solute $\overline{V}_e$ and (b) partial molar volume of solvent $\overline{V}_0$ as a function of $LiPF_6$ molarity in EMC at 20, 25, and 30 °C.

2.A Appendices

2.A.1 Partial molar volumes

Partial molar volumes of salt $\overline{V}_e$ and solvent $\overline{V}_0$ describe how volume is distributed across the species in a binary electrolytic solution. They are critical for quantifying solute-volume effects such as Faradaic convection and the excluded-volume effect, which are transport mechanisms distinct from diffusion, migration, and convection, and are explicitly incorporated in the polarization-cell models used for simulations in this work [89]. For a binary electrolyte, partial molar volumes can be derived from density/molarity correlations through [61]

$$\overline{V}_e = \frac{M_e - \frac{d\rho}{dc}}{\rho - c\frac{d\rho}{dc}} \quad \text{and} \quad \overline{V}_0 = \frac{M_0}{\rho - c\frac{d\rho}{dc}}. \tag{2.A.1}$$

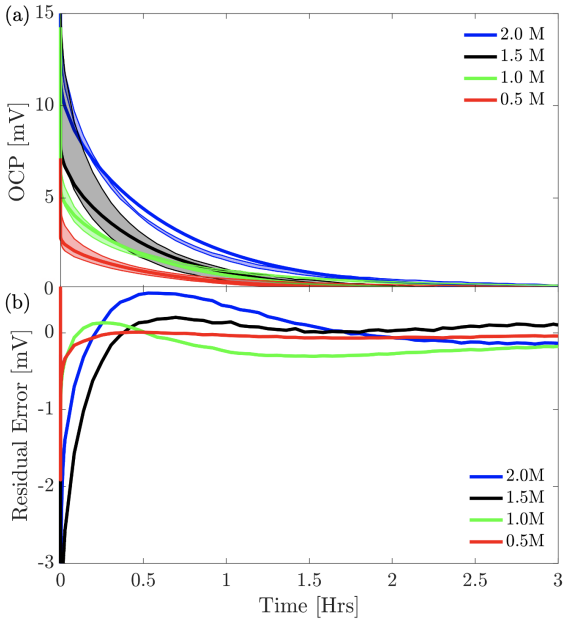


Figure 2.A.2: (a) Comparison between simulated results (solid —) and an average of three restricted-diffusion experiments with standard deviation in relaxation profiles plotted as the shaded region for four concentrations of $LiPF_6$:EMC. (b) Mean of residual errors between experiment and simulated results.

2.A.2 Validation of property correlations for $LiPF_6$:EMC

The parameter correlations from Table 2.2 were incorporated into a polarization-cell model to simulate restricted diffusion, as implemented by Hou and Monroe for $LiPF_6$:PC with COMSOL multiphysics software [102]. Restricted-diffusion measurements on cells constructed following the method outlined in section 2.2.7 at 25 °C were performed in triplicate at each $LiPF_6$ concentration, with an applied constant-current pulse at 0.199 mA/cm2 for a duration of 12 h. Data from the cells that were simulated, along with the transient measure of the residual error in mV, are presented in Figure 2.A.2. These cells were excluded from the parameterization process.

2.B Supplementary data

2.B.1 Raw data measurements

Table 2.B.1: Summary of density-composition calibration measurements for $LiPF_6$:EMC solutions. Recorded under an argon atmosphere in a glovebox. Temperatures are accurate within 0.02 °C.

m_{LiPF_6} [g]	m_{EMC} [g]	ω	$\rho_{20°C}$ [g/L]	$\rho_{25°C}$ [g/L]	$\rho_{30°C}$ [g/L]
0.0000	10.0523	0.00000E+00	1013.1	1007.1	1001.1
0.0466	10.0145	4.63170E-03	1016.5	1010.5	1004.5
0.1502	10.0020	1.47948E-02	1023.2	1017.3	1011.2
0.4981	9.3821	5.04145E-02	1049.6	1043.7	1037.8
0.8075	9.9860	7.48135E-02	1068.5	1062.6	1056.7
1.0395	9.9670	9.44442E-02	1084.6	1078.8	1073.0
1.5037	9.9434	1.31361E-01	1114.7	1108.9	1103.1
1.9668	11.0127	1.51531E-01	1131.4	1125.7	1119.9
2.1150	10.0013	1.74558E-01	1150.6	1144.9	1139.2
2.5535	10.0793	2.02133E-01	1175.3	1169.6	1164.0
2.7691	10.0052	2.16771E-01	1189.1	1183.5	1177.9
3.0231	10.0040	2.32062E-01	1202.3	1196.8	1191.2
3.1650	10.2081	2.36669E-01	1205.3	1199.8	1194.2
3.3133	9.8747	2.51236E-01	1219.1	1213.6	1208.0
3.4413	9.6132	2.63610E-01	1230.8	1225.3	1219.8
4.2843	10.3339	2.93080E-01	1255.5	1250.0	1244.6

Table 2.B.2: Summary of Hittorf-cell measurements for $LiPF_6$:EMC solutions. Transference numbers were calculated following section 2.2.4.

$\rho_{20°C}^{initial}$ [g/L]	$I_{pulse}T_{pulse}$ [C]	$\rho_{20°C}^{anodic}$ [g/L]	$\rho_{20°C}^{cathodic}$ [g/L]	t_+^0 *anodic*	t_+^0 *cathodic*
1033.7	14.1316	1036.1	1031.3	0.388	0.389
1033.7	14.2718	1036.1	1031.2	0.394	0.370
1033.8	14.4155	1036.2	1031.3	0.400	0.376
1065.7	17.03	1068.6	1062.7	0.358	0.338
1065.9	16.32	1068.8	1063.1	0.330	0.355
1067.4	14.1701	1069.9	1065.0	0.334	0.362
1067.6	14.3684	1070.1	1065.1	0.343	0.344
1119.2	14.4239	1121.7	1116.7	0.304	0.305
1119.1	14.389	1121.6	1116.7	0.303	0.332
1119.2	14.355	1121.6	1116.8	0.329	0.330
1170.6	14.4125	1173.1	1168.0	0.262	0.233
1170.8	14.2758	1173.3	1168.2	0.255	0.226
1171.8	14.3714	1174.4	1169.3	0.229	0.260
1220.4	14.4157	1222.8	1218.0	0.250	0.251
1220.3	14.412	1222.7	1217.9	0.250	0.251
1220.2	14.277	1222.6	1217.9	0.243	0.275
1268.3	14.3747	1270.5	1266.0	0.270	0.238
1268.3	14.3747	1270.6	1266.0	0.237	0.238
1268.2	14.4146	1270.4	1266.0	0.272	0.273
1268.3	14.4146	1270.6	1266.0	0.239	0.240

Table 2.B.3: Summary of liquid-junction potentials for $LiPF_6$:EMC at 25 °C. Data presented figure 2.5(a) is arrived at by interchanging $\rho^A_{25^\circ C}$ and $\rho^B_{25^\circ C}$ between reference and test concentrations to achieve a full matrix of results.

$\rho^A_{25\,^\circ C}$ [g/L]	$\rho^B_{25\,^\circ C}$ [g/L]	U [mV]	SD [mV]
1008.3	1012.6	19.73	0.40
1008.3	1017.6	25.47	1.37
1012.6	1017.6	6.46	0.40
1012.6	1027.8	12.24	0.70
1017.6	1027.8	4.03	0.08
1017.6	1048.7	15.65	0.22
1027.8	1048.7	6.73	0.24
1027.8	1072.2	10.37	0.15
1048.7	1072.2	4.01	0.32
1048.7	1093.9	8.30	0.08
1072.2	1093.9	4.70	0.35
1072.2	1114.8	10.06	0.40
1093.9	1114.8	5.89	0.58
1093.9	1136.3	11.98	0.47
1114.8	1136.3	6.11	0.85
1114.8	1155.6	14.43	0.26
1136.3	1155.6	7.32	0.11
1136.3	1165.9	12.65	0.33
1155.6	1165.9	4.14	0.28
1155.6	1193.0	21.27	0.30
1165.9	1193.0	15.99	0.27
1165.9	1209.0	24.41	2.53
1193.0	1209.0	11.61	1.01
1193.0	1229.5	30.87	0.31
1209.0	1229.5	18.99	0.23
1209.0	1246.3	37.62	0.21
1229.5	1246.3	15.48	0.44
1229.5	1268.1	35.33	1.31
1246.3	1268.1	20.50	0.26
1246.3	1285.4	41.12	0.92

Table 2.B.4: Summary of liquid-junction potentials for $LiPF_6$:PC at 25 °C. Data presented figure 2.5(b) is arrived at by interchanging $\rho^A_{25°C}$ and $\rho^B_{25°C}$ between reference and test concentrations to achieve a full matrix of results.

$\rho^A_{25\,°C}$ [g/L]	$\rho^B_{25\,°C}$ [g/L]	U [mV]	SD [mV]
1203.4	1203.8	19.44	0.51
1203.4	1204.6	55.30	1.46
1203.8	1204.6	20.89	0.55
1203.8	1205.6	44.40	1.17
1204.6	1205.6	13.93	0.55
1204.6	1207.1	32.76	0.87
1205.6	1207.1	15.22	0.40
1205.6	1208.7	38.49	1.02
1207.1	1208.7	9.19	0.24
1207.1	1210.7	21.99	0.58
1212.2	1219.9	23.50	0.62
1212.2	1227.4	44.78	0.80
1219.9	1227.4	17.35	0.26
1219.9	1234.7	28.26	1.17
1227.4	1234.7	12.74	0.40
1227.4	1243.2	22.17	0.25
1234.7	1243.2	10.99	0.26
1234.7	1251.3	17.92	0.08
1243.2	1251.3	11.04	0.14
1243.2	1260.0	17.12	0.04
1248.2	1257.3	9.61	0.35
1248.2	1270.5	19.36	0.61
1257.3	1264.6	8.67	0.01
1257.3	1273.6	17.38	0.09
1264.6	1273.6	9.48	0.20
1264.6	1283.8	19.38	0.14
1273.6	1283.8	11.79	0.52
1273.6	1291.0	18.40	0.09
1283.8	1291.0	7.31	0.24
1283.8	1298.6	14.57	1.00
1291.0	1298.6	8.35	0.64
1291.0	1306.6	17.20	0.24
1298.6	1306.6	8.39	0.42
1298.6	1314.3	16.67	0.72
1306.6	1314.3	8.17	0.41
1306.6	1322.2	16.30	0.14
1314.3	1322.2	8.75	0.21
1314.3	1329.9	14.01	0.18

Continued:

$\rho^{A}_{25\,°C}$ [g/L]	$\rho^{B}_{25\,°C}$ [g/L]	U [mV]	SD [mV]
1322.2	1329.9	7.30	0.11
1322.2	1338.2	16.36	0.27
1329.9	1338.2	9.71	0.30
1329.9	1346.9	18.28	0.32
1338.2	1346.9	8.76	0.06
1338.2	1353.5	20.13	0.30
1346.9	1353.5	8.91	0.15
1346.9	1361.9	19.55	0.47
1353.5	1361.9	8.23	0.38
1353.5	1368.9	18.14	0.13
1361.9	1368.9	9.69	0.23
1361.9	1376.7	17.14	0.08
1368.9	1376.7	7.74	0.08
1368.9	1382.7	15.01	0.11

Table 2.B.5: Summary of ionic conductivity measurements for $LiPF_6$:EMC solutions.

$\rho_{20\,°C}$ [g/L]	$\kappa_{20\,°C}$ [µS/cm]	$\kappa_{25\,°C}$ [µS/cm]	$\kappa_{30\,°C}$ [µS/cm]
1018.9	0.349	0.503	0.668
1023.2	5.995	6.321	6.568
1034.6	117.3	119.8	121.0
1049.6	611.1	634.6	655.1
1068.5	1492	1563	1632
1084.6	2406	2533	2654
1114.7	4045	4294	4536
1131.4	4760	5100	5433
1175.3	5705	6212	6688
1205.3	5452	5996	6560
1230.8	4836	5401	5983

Table 2.B.6: Summary of dynamic viscosity measurements for $LiPF_6$:EMC solutions.

$\rho_{20\,°C}$ [g/L]	$\eta_{20\,°C}$ [mPa·s]	$\eta_{25\,°C}$ [mPa·s]	$\eta_{30\,°C}$ [mPa·s]
1013.1	0.724	0.680	0.639
1015.8	0.745	0.686	0.644
1025.6	0.778	0.743	0.701
1041.9	0.916	0.877	0.808
1064.5	1.143	1.063	1.000
1093.9	1.524	1.405	1.294
1119.6	1.994	1.825	1.673
1169.9	3.570	3.176	2.860
1215.6	6.726	5.807	5.104
1245.2	10.650	9.797	8.648

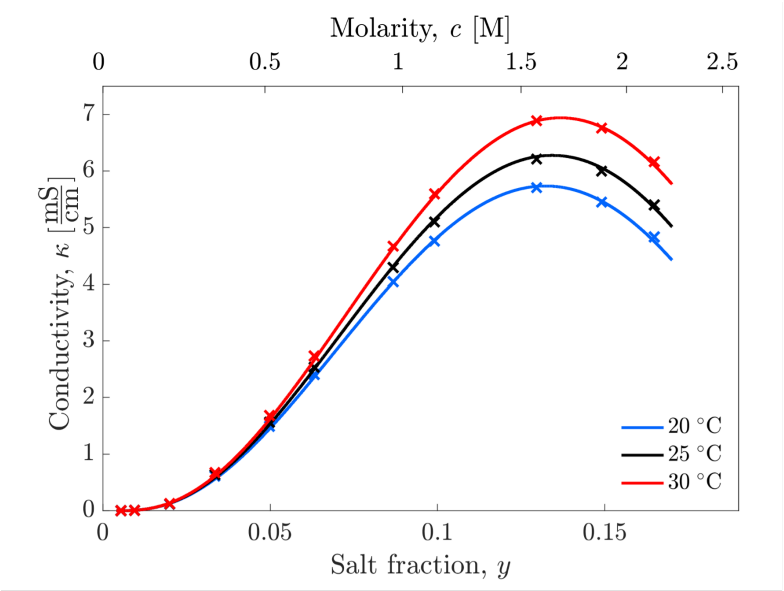


Figure 2.B.1: Measured ionic condutivities for $LiPF_6$:EMC at 20, 25, and 30 °C.

Table 2.B.7: Summary of dynamic viscosity measurements for $LiPF_6$:PC solutions.

$\rho_{20\,°C}$ [g/L]	$\eta_{20\,°C}$ [mPa·s]	$\eta_{25\,°C}$ [mPa·s]	$\eta_{30\,°C}$ [mPa·s]
1204.9	2.74	2.47	2.24
1213.3	3.008	2.707	2.449
1216.0	3.362	3.038	2.734
1237.7	4.229	3.766	3.374
1253.6	5.394	4.75	4.218
1269.9	7.899	6.132	5.373
1285.8	9.461	8.129	7.04
1300.0	12.48	10.59	9.033
1316.8	17.89	14.83	12.36
1332.0	25.08	20.43	16.85
1361.0	55.72	42.93	34.02

Table 2.B.8: Summary of restricted-diffusion measurements for $LiPF_6$:EMC solutions. κ_{eff} was obtained using electrochemical impedance spectroscopy (EIS).

$\rho_{20\,°C}$ [g/L]	slope fit [s^{-1}]	D_{eff} [cm^2/s]	κ_{eff} [mS/cm]	b
1020.1	1.18E-03	4.77E-06	9.34E-04	0.58
1020.1	1.29E-03	5.22E-06	9.24E-04	0.65
1020.1	1.04E-03	4.21E-06	8.52E-04	1.15
1020.1	7.88E-04	3.19E-06	7.70E-04	1.77
1025.3	1.16E-03	4.69E-06	1.23E-02	0.32
1025.3	9.41E-04	3.81E-06	1.02E-02	1.45
1025.3	1.02E-03	4.13E-06	1.20E-02	0.45
1025.3	9.51E-04	3.85E-06	1.17E-02	0.58
1049.3	6.13E-04	2.49E-06	0.398	2.79
1049.3	7.09E-04	2.87E-06	0.490	1.51
1049.3	5.42E-04	2.20E-06	0.395	2.84
1049.3	8.41E-04	3.41E-06	0.521	1.14
1094.7	6.47E-04	2.62E-06	2.51	1.07
1094.7	5.29E-04	2.14E-06	2.03	2.36
1094.7	7.42E-04	3.01E-06	2.87	0.25
1094.7	5.42E-04	2.20E-06	2.09	2.20
1094.7	5.42E-04	2.19E-06	2.18	1.92
1117.9	6.55E-04	2.65E-06	3.58	1.03
1117.9	5.11E-04	2.07E-06	3.32	1.49
1117.9	5.49E-04	2.23E-06	3.80	0.66
1117.9	5.97E-04	2.42E-06	4.01	0.34
1117.9	5.31E-04	2.15E-06	3.38	1.39
1117.9	5.72E-04	2.32E-06	3.53	1.11
1178.8	4.47E-04	1.81E-06	4.52	1.46
1178.8	3.97E-04	1.61E-06	4.26	1.83
1178.8	5.43E-04	2.20E-06	5.09	0.73
1178.8	4.40E-04	1.78E-06	4.76	1.14
1215.3	4.32E-04	1.75E-06	4.12	1.38
1215.3	3.45E-04	1.40E-06	4.63	0.66
1215.3	5.18E-04	2.10E-06	5.01	0.18
1215.3	3.39E-04	1.37E-06	4.59	0.72
1215.3	2.62E-04	1.06E-06	4.74	0.52
1255.5	3.85E-04	1.56E-06	4.38	0.29
1255.5	2.46E-04	9.99E-07	3.66	1.38
1255.5	2.06E-04	8.35E-07	3.07	2.47
1255.5	2.07E-04	8.41E-07	3.04	2.54
1255.5	2.36E-04	9.56E-07	3.32	1.98
1255.5	2.21E-04	8.97E-07	3.85	1.07
1255.5	3.23E-04	1.31E-06	4.05	0.76

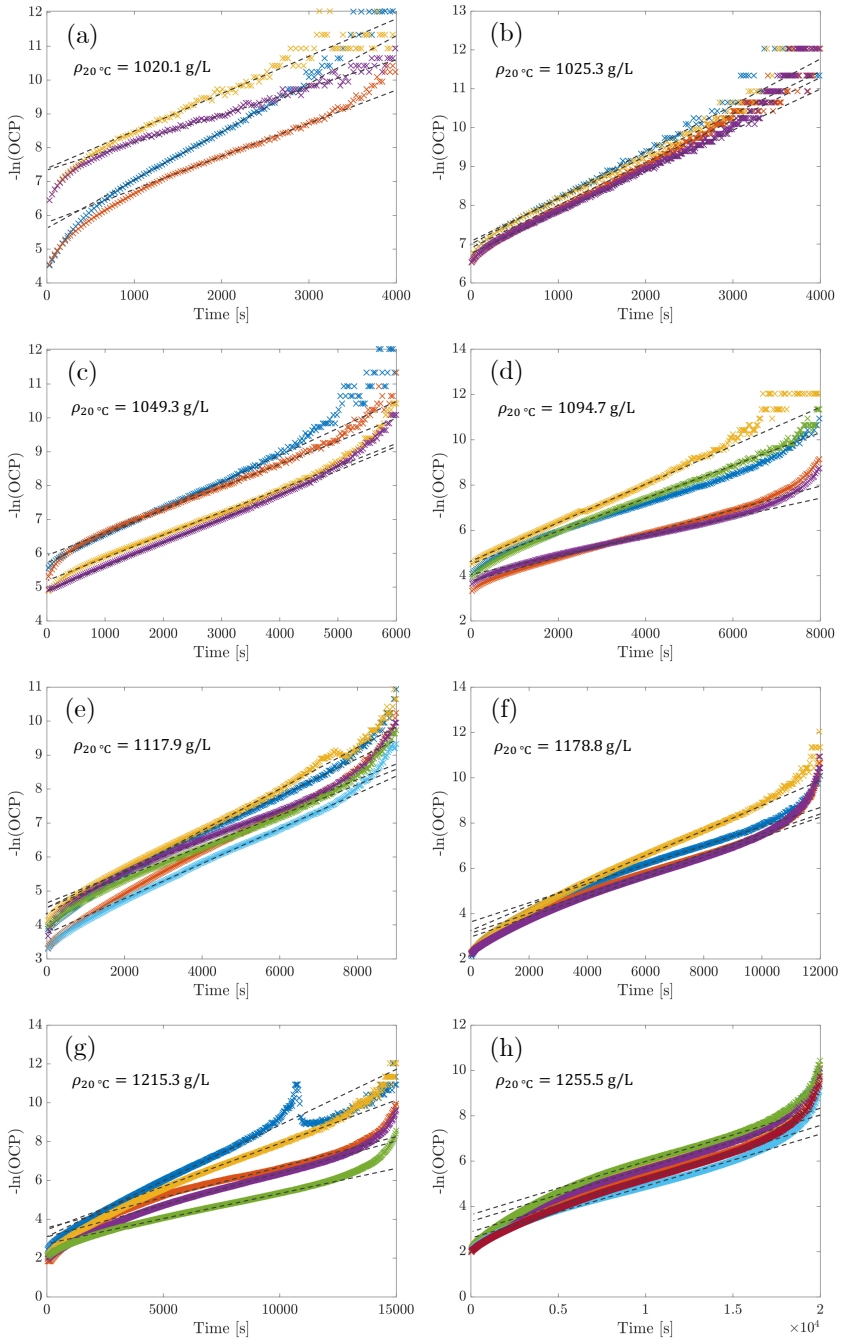


Figure 2.B.2: Voltage relaxation data from restricted diffusion measurements for $LiPF_6$:EMC. Dashed lines (– – –) indicate region of slope used to compute D_{eff}.

2.B.2 Fitting process for equivalent conductance

A power series in $y^{1/4}$ was used to fit equivalent-conductance data. The general form studied with the optimization algorithm was

$$\Lambda = \Lambda_0 + \left[\sum_{k=1}^{7} \Lambda_k \left(\sqrt{y}\right)^{\frac{k}{2}}\right]^2 . \tag{2.B.1}$$

By minimizing number of parameters, maximizing R^2, and minimizing the root-mean-squared error (RMSE) in the 95% confidence interval, it was found that a 3-parameter fit with average $R^2 = 0.9997$ and average confidence interval RMSE = 0.077 was optimal, using the programmatic Curve Fitting Toolbox by MathWorks, which returned best-fit parameter values as a vector (Λ_k,CI$_($left$, k)$,CI$_($right$, k)$), where CI$_($left$, k)$ and CI$_($right$, k)$ respectively represent the lower and upper bounds of the 95% confidence interval (CI) on Λ_k.

For each possible collection of nonzero parameters in equation 2.B.1, CI RMSE was calculated with the formula

$$\mathrm{RMSE_{CI}} = \sqrt{\frac{1}{n_{\mathrm{terms}\neq 0}} \sum_{k:\Lambda_k \neq 0} \left(\frac{\mathrm{CI_{right},}k - \mathrm{CI_{left},}k}{\Lambda_k}\right)^2}. \tag{2.B.2}$$

We note that 0 always fell between the confidence intervals for the constant term Λ_0, and so it was not included in the final correlation. The presence of Λ_0 has physical meaning for strong electrolytes, which would be expected to obey Onsager–Fuoss conductance law at limiting dilution, but does not appear to be justified for $LiPF_6$:EMC based on our experimental data.

This process identified the error-minimizing final functional form to be equation 2.19 in the main-body text.

2.B.3 MacMullin geometry correction

EIS measurements made following the *bulk impedance* section in Hou and Monroe [102] with this equation:

$$\kappa_{\text{eff}} = \frac{L}{\Omega_{\text{bulk}} A}, \tag{2.B.3}$$

where Ω_{bulk} is the bulk impedance measured with EIS, L is the PEEK spacer thickness (0.2 cm), and A is the PEEK spacer cross sectional area (0.503 cm^2).

The MacMullin number α depends on pore geometry and is found by scaling the effective conductivity κ_{eff} with the pure liquid electrolyte conductivity κ [153]:

$$\alpha = \frac{\kappa_{\text{eff}}}{\kappa}. \tag{2.B.4}$$

By taking the manufacturer specification for porosity ε=0.85, one may then calculate the Bruggeman exponent b based on effective medium theory *via.*:

$$\alpha = \varepsilon^b. \tag{2.B.5}$$

Figure 2.3 reports the spread in b, and an average of $b = 1.23$ with a standard deviation of 0.74 is found. This wide variability in the Bruggeman exponent suggests a correspondingly wide variability in the pore structure of the glass fiber.

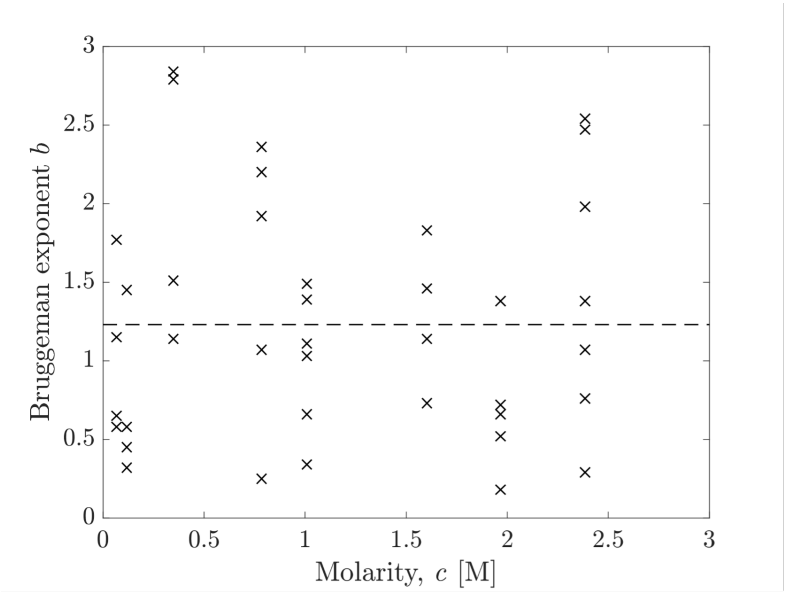


Figure 2.B.3: Bruggeman exponent $b(x)$ calculated for each individual restricted-diffusion measurement for $LiPF_6$:EMC. An average value of 1.23 with standard deviation 0.74 is indicated (– – –).

2.B.4 Parameter confidence intervals

Table 2.B.9: $LiPF_6$:EMC parameters and 95% confidence intervals to accompany correlations presented in Table 2.2 from main text.

Electrolyte	Property	T / °C	Fit parameters & confidence intervals		
$LiPF_6$:EMC	$\rho(c\ [M])$	20	1013.1	113.19	−7.8842
			—	±2.70	±1.998
		25	1007.1	114.20	−8.1212
			—	±2.80	±2.029
		30	1001.1	115.13	−8.3005
			—	±2.70	±2.04
	$\eta(y)$	20	0.724	43.80	5.964×10^5
			—	±1.02	±8800
		25	0.680	36.01	5.655×10^5
			—	±4.2000	±36500
		30	0.639	32.17	4.917×10^5
			—	±4.49	±39000
	$\Lambda(y)$	20	−9.273	33.39	−58.50
			±0.558	±1.336	±1.981
		25	−9.631	34.46	−59.64
			±0.600	±1.437	±2.125
		30	−9.970	35.47	−60.66
			±0.602	±1.442	±2.127
	$\chi_{EMC}(y)$	25	1	−18.38	155.3
			—	±4.330	±48.35
	$t_+^0(y)$	25	0.4240	−1.858	4.880
			±0.020	±0.467	±2.179
	$D(y)$	25	504.8	−6.064	11.35
			±27.05	±1.417	±7.345

Table 2.B.10: $LiPF_6$:PC parameters and 95% confidence intervals to accompany correlations presented in Table 2.2 from main text.

Electrolyte	Property	T / °C	Fit parameters & confidence intervals			
$LiPF_6$:PC	$\eta(y)$	20	2.74 ±0.353	287.9 ±22.15	1.702×10^7 ±545000	
		25	2.47 ±0.234	246.7 ±14.75	1.245×10^7 ±365000	
		30	2.24 ±0.184	212.3 ±11.50	9.382×10^6 ±283000	
	$\chi_{PC}(y)$	25	1 —	−2.655 ±1.209	26.23 ±5.075	1490 ±336.5

2. Shifting-reference concentration cells to refine composition-dependent transport characterization of binary lithium-ion electrolytes

Statement of Authorship for joint/multi-authored papers for PGR thesis

To appear at the end of each thesis chapter submitted as an article/paper

The statement shall describe the candidate's and co-authors' independent research contributions in the thesis publications. For each publication there should exist a complete statement that is to be filled out and signed by the candidate and supervisor **(only required where there isn't already a statement of contribution within the paper itself).**

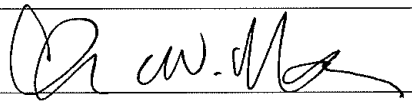
Title of Paper	Shifting-reference concentration cells to refine composition-dependent transport characterization of binary lithium-ion electrolytes
Publication Status	Published
Publication Details	Wang, A.; Hou, T.; Karanjavala, M.; Monroe, C. Shifting-Reference Concentration Cells to Refine Composition-Dependent Transport Characterization of Binary Lithium-Ion Electrolytes. *Electrochim. Acta* **2020**, *358*, 136688. https://doi.org/10.1016/j.electacta.2020.136688.

Student Confirmation

Student Name:	Andrew A. Wang		
Contribution to the Paper	Conceptualization, Methodology, Investigation, Formal Analysis, Writing		
Signature		Date	04/07/2022

Supervisor Confirmation

By signing the Statement of Authorship, you are certifying that the candidate made a substantial contribution to the publication, and that the description described above is accurate.

Supervisor name and title: Charles W. Monroe (Associate Professor)			
Supervisor comments Andrew is first author.			
Signature		Date	5 July 2022

This completed form should be included in the thesis, at the end of the relevant chapter.

3

Potentiometric MRI of a superconcentrated lithium electrolyte: Testing the irreversible thermodynamics approach*

Abstract

Superconcentrated electrolytes, being highly thermodynamically nonideal, provide a stringent proving ground for continuum transport theories. Herein, we test an ostensibly complete model of $LiPF_6$ in ethyl-methyl carbonate (EMC) based on the Onsager–Stefan–Maxwell theory from irreversible thermodynamics. We perform synchronous magnetic resonance imaging (MRI) and chronopotentiometry to examine how superconcentrated $LiPF_6$:EMC responds to galvanostatic polarization and open-circuit relaxation. We simulate this experiment using an independently parametrized model with six composition-dependent electrolyte properties, quantified up to saturation. Spectroscopy reveals increasing ion association and solvent coordination with salt concentration. The potentiometric MRI data agree closely with the predicted ion distributions and overpotentials, providing a completely independent validation of the theory. Superconcentrated electrolytes exhibit strong cation–anion interactions and extreme solute-volume effects that mimic elevated lithium transference. Our simulations allow surface overpotentials to be extracted from cell-voltage data to track lithium interfaces. Potentiometric MRI is a powerful tool to illuminate electrolytic transport phenomena.

*This chapter was reported in *ACS Energy Letters* **2021**, DOI: 10.1021/acsenergylett.1c01213 [96]

3.1 Introduction

A spatiotemporal understanding of how chemical species and potential are distributed—on both microscopic and mesoscopic scales—is vital to lithium-battery development. As lithium batteries proliferate across more demanding applications, a strong grasp of electrolytic thermodynamics and mass-transport phenomena will be critical to the optimization of existing technologies and the design of new formulations with advanced capabilities [8, 13, 20, 161].

Local concentration and potential within electrolytic solutions must be managed during battery operation, because their distributions affect several distinct phenomena across a wide range of systems. Polarization of the composition and voltage within a cell as it cycles leads to capacity underutilization and also restricts fast-charging efficiency [162, 163]. Concentration overpotentials are particularly important during operation at high current densities, where they can obfuscate operational limits based on the equilibrium potentials for lithiating graphitic anodes, ultimately leading to lithium-metal plating [64, 164]. The dendritic morphology of plated lithium, a key barrier to lithium-metal batteries, is strongly affected by the instantaneous liquid-phase composition and voltage near the electrode surfaces, as well as by additives that alter solution thermodynamics [37, 65, 165–167]. Both solid-electrolyte interphase (SEI) formation and degradation side reactions are governed by reaction processes whose rates depend on interfacial electrolyte concentrations [67, 168, 169]. On a more fundamental level, studies of electrode kinetics based on cell voltage require true surface overpotentials to be distinguished from potential drops away from the interfaces, such as ohmic and diffusive losses [170].

The properties of liquid electrolytes depend strongly on their salt content. Renewed attention has been given to superconcentrated electrolytes, which in some cases exhibit widened voltage stability windows and higher apparent rate capabilities [142, 171, 172]. In the superconcentrated regime, cation, anion, and solvent speciation is incredibly complex, dominated by coordinated aggregation phenomena such as solvent binding and ion pairing [20, 55, 100, 113, 173]. Because many studies of superconcentrated electrolytes do not include complete assessments

of transport and thermodynamic properties, the literature remains unclear about whether the advantages stem from interfacial or bulk characteristics [174–176]. It is therefore of interest to examine how concentration and potential polarization evolve within superconcentrated electrolytes subjected to applied currents.

Newman's concentrated-solution theory derives from the Onsager–Stefan–Maxwell (OSM) model of multicomponent diffusion—an implementation of irreversible thermodynamics that takes electrochemical-potential gradients, rather than concentration gradients, to be the fundamental forces that drive diffusion [61]. Unlike Nernst–Planck dilute-solution theory, OSM theory also accounts explicitly for ion/ion diffusional drag interactions, which generally cannot be neglected in battery electrolytes [81] The thermodynamic principles that underpin OSM theory also support the consistent inclusion of standard equilibrium properties, such as component partial molar volumes and Darken thermodynamic factors [80, 88].

For binary electrolytic solutions wherein speciation kinetics is very fast, a single (Darken) thermodynamic factor χ accounts for deviation from the ideal Nernstian relationship between concentration polarization and concentration overpotential. Also, effective electrolyte and solvent partial molar volumes, denoted $\overline{V}_{\mathrm{e}}$ and $\overline{V}_{0}$, respectively, parametrize the concentration dependence of the solution's density. Together these three thermodynamic properties should provide a complete description of an equilibrated electrolyte at constant temperature T and pressure p. With the thermodynamic parameters in hand, the three Stefan–Maxwell diffusivities describing pairwise species/species diffusional-drag interactions map into an ionic conductivity κ, salt diffusion coefficient D, and cation transference number relative to the solvent velocity t_{+}^{0}. Thermodynamic constraints demand that these six essential material properties vary only with local salt molarity c at fixed T and p.

When applied to a three-species electrolytic solution,[†] OSM theory produces two independent force-explicit transport equations that describe the dynamical

[†]As discussed earlier by the authors, the superconcentrated $LiPF_6$:EMC electrolyte studied here should be amenable to description by eqs 3.1 and 3.2, so long as all local association/dissociation reactions reach equilibrium on a time scale much faster than the characteristic time scale for diffusion [118, 154].

state [61]. Inversion of these equations leads to two flux-explicit transport laws, parametrized by the six key composition-dependent properties [89, 92, 177]. First, the total molar cation flux $\vec{N}_+$ is described in terms of contributions from diffusion, migration driven by the ionic current density $\vec{i}$ and convection at the volume-average velocity $\vec{v}^{\square}$ (defined in the Supporting Information, eq 3.B.2) as:

$$\vec{N}_+ = -D\vec{\nabla}c + \frac{t_+^0}{F}\vec{i} + c\vec{v}^{\square} \tag{3.1}$$

where F represents Faraday's constant. Second, a modified form of Ohm's law breaks the current density down into an ohmic contribution, driven by the local potential gradient, and a Nernstian contribution, driven by gradients in composition:

$$\vec{i} = -\kappa\vec{\nabla}\Phi + \frac{2\kappa RT\chi(1-t_+^0)}{F[1+(2\overline{V}_0 - \overline{V}_e)c]} \tag{3.2}$$

in which R is the gas constant and T is the absolute temperature. To produce the simulations below, eqs 3.1 and 3.2 were augmented by local state equations, material balances, and boundary conditions, which are detailed in section 3.B.1 of the Supporting Information.

Several attempts to parametrize the composition dependences of all six key properties in eqs 3.1 and 3.2 have been made, involving a range of experimental and numerical approaches [78, 93, 101–103, 118, 128, 178]. The convection term in eq 3.1 is typically disregarded, but volume-related transport phenomena such as faradaic convection may become dominant in electrolytes where the salt fraction is high [89, 98, 179]. Only a few groups have attempted to validate measured parameters, by comparison of theoretical predictions to voltage measurements or otherwise [102, 103, 118, 178].

In situ methods such as nuclear magnetic resonance imaging (MRI), X-ray scattering, and confocal Raman spectroscopy have been employed to visualize the time evolution of electrolyte-concentration profiles [65, 180–182]. In particular, inverse modeling techniques have been applied to MRI data to extract transport

parameters [180, 183–185]. Material properties determined in this way are highly sensitive to prior assumptions about the composition dependences of properties, as well as to the model variant that is chosen when fitting the data. Most inverse modeling of MRI has used models reliant on several restrictive assumptions, e.g., dilute-solution theory [186], modeling without independent consideration of the thermodynamic factor [180], or neglect of solute-volume effects [84], or has employed ad hoc adaptations to account for additional phenomena such as dendrite growth [154, 186, 187]. Most recently, Bazak et al. extracted composition-dependent transference numbers and diffusivities from steady-state concentration profiles measured with MRI by inverse modeling based on a concentrated-solution theory that excluded the thermodynamic factor χ and the faradaic-convection phenomenon [183]. No MRI studies have validated the properties extracted from concentration measurements against the cell voltage, which should be wholly determined by the transport model during open-circuit relaxations [140].

In situ approaches to date have focused on parameter estimation, but a more foundational question remains: is the concentrated-solution transport theory itself valid? That is, does an ostensibly "complete" transport model based on irreversible thermodynamics, fully parametrized ex situ in the traditional, circumstantial way, in fact predict the concentration profiles and transient cell voltages seen in situ?

To address this question, we report a complete set of thermodynamic and transport properties for solutions of lithium hexafluorophosphate ($LiPF_6$) in ethyl methyl carbonate (EMC) across the entire solubility range, including the superconcentrated regime near the salt's saturation limit. The $LiPF_6$:EMC system is representative of superconcentrated electrolytes based on linear-carbonate solvents [171]. Highly nonideal speciation in the superconcentrated regime is confirmed by observations with Raman spectroscopy. Structural observations derived from the Raman spectra correlate well with trends in the partial molar volumes, confirming that the inclusion of solute-volume phenomena within the OSM model of the bulk electrolyte is critical to predict ion fluxes accurately at high salt concentrations [89, 102, 118]. The transport model is parametrized using a bespoke suite of electrochemical

measurements designed to isolate the concentration dependences of individual properties [118]. Finally, potentiometric MRI data gathered during galvanostatic polarization/relaxation demonstrate strong agreement with transient concentration and voltage profiles predicted by model simulations. These results confirm the high fidelity and microscopic predictive capability of the solution-phase transport model, justifying its use to isolate the voltage signatures of interfacial phenomena.

3.2 Results and discussion

3.2.1 Species interactions increase with salt molarity

Figure 3.1 presents physicochemical data and Raman spectra for $LiPF_6$:EMC solutions as functions of their salt molarity c. As the saturation limit of $LiPF_6$:EMC at $c = 3.8$ M is approached, the solution's mass density ρ, shown in Figure 3.1A, levels off. These data were gathered from filtered supernatant liquid, so the horizontal slope above 3.8 M reflects that all the added salt has not dissolved. The change in the density's slope with respect to molarity, from 85 g/mol at 3 M to 0 g/mol beyond the saturation limit of 3.8 M, indicates a large increase in the salt partial molar volume $\overline{V}_e$, as described in the Supporting Information (eq 3.B.12). Figure 3.1B shows that the salt's volume fraction within solution rises sharply near saturation, reaching nearly 40% at 3.8 M. This suggests that significant faradaic convection (bulk flow driven by the volume flux of Li^+ across electrode boundaries) should accompany interfacial redox reactions in concentrated electrolytes [89].

Changes in the Raman bands associated with PF_6^- and EMC, shown in panels C and D of Figure 3.1, respectively, indicate dramatic changes in solution structure as salt content rises. Figure 3.1C shows increased shift of the PF_6^- stretching vibration from its expected 741 cm^{-1} band and an increase in intensity as molarity rises, trends which have been correlated with a rising extent of ion association [188–190]. Data from Figure 3.1D was used to assess the coordination of solvent with lithium cations by comparing the integrated peak fit area around ∼930 cm^{-1}, associated with asymmetric C–O stretching of the free molecule, with that around ∼946 cm^{-1} associated with Li^+–EMC coordination [57, 191]. There is also a peak

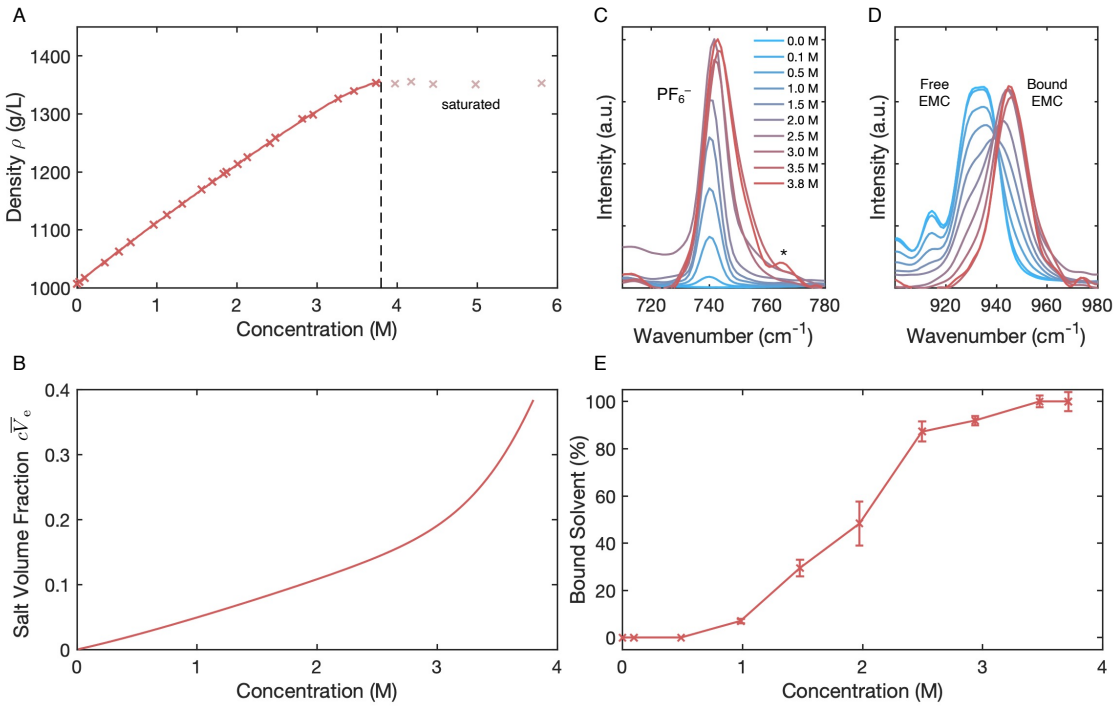


Figure 3.1: Variation of physicochemical properties and molecular interactions with salt concentration from 0 M to saturation (3.8 M). (A) Density measurements for $LiPF_6$:EMC solutions at 25 °C. The dashed line (- - -) at 3.8 M demarcates saturation. (B) Salt volume fraction, derived from salt molarity c and solute partial molar volume $\overline{V}_e$ computed with Supporting Information eq 3.B.12). (C) Raman spectra for $LiPF_6$:EMC in the range of 720–780 cm^{-1}; the asterisk indicates crystalline $LiPF_6$. (D) Raman spectra for $LiPF_6$:EMC in the range of 920–980 cm^{-1} showing solvent interaction. (E) Bound solvent fraction, as calculated by comparing the change in peak fit areas between the neat EMC solvent and saturated $LiPF_6$:EMC solution. Error bars represent uncertainty due to peak fitting of the EMC C–O stretching band (see the Supporting Information for further details).

at ∼918 cm^{-1}, which has been attributed to the stretching of C=O double bonds [192]; in unbound EMC its height correlates with the peak height at ∼930 cm^{-1}. Figure 3.1E presents how the percentage of bound solvent, computed using these peak areas, varies with molarity. Below 1 M — the concentration regime for standard lithium-ion-battery electrolytes — our Raman analysis indicates that the majority of EMC moves freely, but the opposite holds above 3 M, where more than 90% of the EMC is coordinated with lithium. The monotonic increase in solvent coordination with concentration qualitatively agrees with prior studies of $LiPF_6$ in linear-carbonate solvents [193], although infrared spectroscopy tends to show higher coordination at lower concentrations [194].

A relatively steady transition to a state wherein ions and solvent are highly coordinated occurs across the 1–3 M range, commensurate with behavior observed for other nonaqueous solutions [20]. As such, theories that assume infinite dilution or neglect ion–ion interactions cannot account entirely for transport at high concentrations, which is driven by both the typical "vehicular" transport mode, in which solvated ions move freely through the solution, as well as a "structural" mode, in which cations move by rearranging the bonds in their local coordination networks [81, 113]. Dilute-solution theory and many popular concentrated-solution models also neglect a "kinematic" transport mode, in which the bulk electrolyte is driven to move because salt flux carries a portion of the solution volume along with it. Faradaic convection is an example of a kinematic transport mode. Consistent models must include both species–species interactions and solute-volume effects [89, 102, 118].

3.2.2 Ex-situ property measurements

Prior measurements of transport and thermodynamic properties for $LiPF_6$:EMC up to 2 M were extended into the superconcentrated regime [20] using the experimental characterization suite developed by Wang et al [118]. The composition dependence of every material parameter involved in eqs 3.1 and 3.2 is presented in Figure 3.2. Ionic conductivity κ (Figure 3.2A) trends through a maximum at $\sim$1.5 M, as the driving force for salt dissociation at high dilution is counterbalanced by the increased diffusional drag that ions experience at higher concentrations. Salt diffusivity D (Figure 3.2B) falls monotonically with concentration, consistent with a decrease in both ions' mobilities relative to the solvent. The Hittorf transference number t_+^0 (Figure 3.2C) trends downward, showing that Li^+ carries a decreasing fraction of the ionic current as salt content rises. Note that this observation has been reported before [175] and opposes the conclusion drawn by other groups that lithium transference appears higher in the superconcentrated regime [142, 195]. The discrepancy can be explained by a difference in definitions between the Hittorf transference number t_+^0 and the transport number t_+, which is equivalent to the transference parameter extracted by the Bruce–Vincent method [102, 132, 142, 195].

Whereas t_+^0 is defined within concentrated-solution theory to ensure that it is a truly isolable property of the bulk electrolyte [118], the formulas used to quantify t_+ derive from Nernst–Planck dilute-solution theory, thereby neglecting both ion–ion diffusional interactions [131] and convective effects [89] in the data processing. When the volume fraction of salt in a solution is appreciable, the solution-volume change that accompanies interfacial reactions drives a bulk flow, which elevates the apparent transport number t_+ [89, 118] through convection — an effect that has nothing to do with bulk transference [101]. Thus, the "enhanced transference" of superconcentrated electrolytes seen by prior researchers may more accurately be interpreted as enhanced faradaic convection owing to the high volume fraction of salt.

The thermodynamic properties shed light on solution behavior in the superconcentrated regime as well. At moderate concentrations, up to 1 M, poor salt dissociation suppresses χ below its ideal value of unity, as a consequence of EMC's low relative permittivity (approximately 3) [8, 47, 118]. Solution nonidealities grow at concentrations above 1 M, driving a dramatic increase in χ (Figure 3.2D). In line with the Raman spectra presented in Figure 1, the rise in salt activity (Supporting Information eq 3.B.15) likely is due to an ever-increasing extent of solute–solvent coordination [47]. Note also that changes in the thermodynamic factor ultimately reflect changes in the salt's chemical potential. This interpretation of the thermodynamic factor is also consistent with the trends seen in the partial molar volumes (Figure 3.2E): the electrolyte's partial molar volume rises steadily, with a steeper change above 3 M. Salt formula units in solution would be expected to attain elevated effective volumes if more solvent molecules become coordinated with them. Thus, these extreme nonideal variations in thermodynamic behavior would be expected to impact the thermodynamics of solvation/desolvation reactions at electrode surfaces.

Finally, OSM diffusivities, shown in Figure 3.2F, express the mobility of one species relative to another. Casting these data in terms of Onsager drag coefficients (Figure 3.B.1A), rather than diffusivities, also corroborates the observations that solute–solvent drag interactions increase steadily as the concentration tends toward

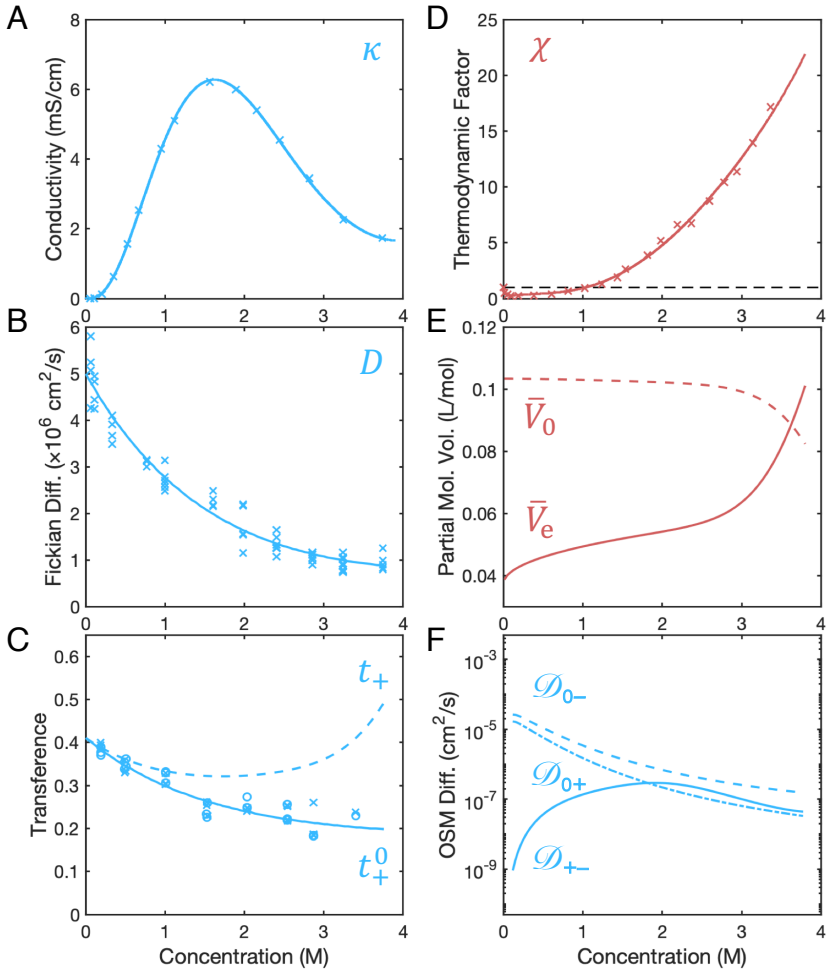


Figure 3.2: Transport (blue) and thermodynamic (red) properties for $LiPF_6$:EMC measured at 25 °C. Composition-dependent correlation curves with confidence intervals and tables of the raw experimental data are provided in Tables 3.B.1 and 3.B.2. (A) Ionic conductivity κ as measured by AC conductometry. (B) Salt diffusivity D as measured by potentiometric restricted diffusion. (C) Transference number t_+^0 (—) as measured by Hittorf experiments, determined from the cathodic (○) and anodic (×) chambers of the Hittorf cell as depicted in Figure 3.A.2, alongside the transport number t_+ (- - -) that would arise from data processing without faradaic convection. (D) Darken thermodynamic factor χ as measured by shifting-reference concentration cells. The dashed line shows the ideal value of unity. (E) Partial molar volumes for solvent $\overline{V}_0$ (- - -) and salt $\overline{V}_e$ (—) from densitometry (Supporting Information eqs 3.B.11 and 3.B.11). (F) Onsager–Stefan–Maxwell diffusion coefficients between EMC and PF_6^- $\mathscr{D}_{0-}$ (- - -), EMC and Li^+ $\mathscr{D}_{0+}$ (· - ·), and Li^+ and PF_6^- $\mathscr{D}_{+-}$ (—), determined from properties presented in panels A–E (see the Supporting Information, section 3.B.4).

saturation, that significant cation–anion coordination impacts the ionic conductivity nonmonotonically with concentration, and that all three pairwise diffusional drag interactions (cation–solvent, anion–solvent, and cation–anion) have similar magnitudes in the superconcentrated regime (3.B.1B). The Supporting Information (3.B.1C) also presents Onsager diffusivities, which can be interpreted as measures of correlation decay. These reveal that cation/anion fluctuations transition from correlated to anticorrelated at the conductivity maximum.

3.2.3 Potentiometric MRI

The response of a 3 M $LiPF_6$:EMC solution sandwiched between planar lithium-metal electrodes with an 8 mm interelectrode spacing was investigated to probe concordance between potentiometric MRI data and the predictions of irreversible thermodynamics based in the OSM concentrated-solution theory. Experiments were performed using sealed custom Swagelok-style polyether ether ketone (PEEK) cells with cylindrical internal geometry (Figure 3.B.5). The cells were subjected to galvanostatic pulse–relaxation experiments, in which a 60 μA (0.48 mA/cm^2) current pulse was applied for 2 h, followed by an open-circuit (0 mA/cm^2) hold; the cell voltage and MRI signal were tracked during both the pulse and the relaxation. Cells were oriented vertically, with positive current in an upward direction to minimize buoyancy effects (free convection) arising from density gradients that accompany concentration polarization within the cell [61, 180]. ^{19}F MRI concentration profile imaging was performed on the PF_6^- anion, with ^{19}F representing the strongest signal from all the ions present in this system which enables a rapid profile acquisition time; Li^+ concentration was inferred via the local electroneutrality approximation. Image acquisition occurred approximately every 4 min, using a 1D spin–echo pulse sequence with the external magnetic field aligned along the direction of ion transport [196]. Synchronous cell-voltage data was gathered throughout the duration of the experiment and is discussed below.

Model calculations were performed using COMSOL Multiphysics software; the code used to perform simulations is available on GitHub [197]. Transient balances

of charge, volume, and cation concentration in the axial direction, a coupled partial differential equation system determined by eqs 3.1 and 3.2, were solved with appropriate boundary conditions, as detailed in the Supporting Information (section 3.B.1).

Simulation output is compared with the experimental data in Figure 3.3. It should be emphasized that the only parameters input to the model are the electrode spacing, the pulse duration, and the applied current density; no material parameters from the property set in Table 3.B.1 were tuned to achieve the agreement between panels A and B or panels D and E of Figure 3.3. The macroscopic model indeed predicts those microscopic states with good accuracy: panels C and F of Figure 3.3 demonstrate that the theoretical and experimental concentrations align within ±5% at all times. This validation exercise supports the use of continuum-scale theories based in irreversible thermodynamics to complement the modeling of degradation or formation processes in lithium batteries, which usually involve mechanistic reaction models that incorporate solution-phase species concentrations local to interfaces [198].

The concentration response during the constant-current pulse, shown in Figure 3.3A,B, is governed by diffusion, migration, and faradaic convection (eq 3.1) [89, 97]. The balance of these effects determines the slope of the concentration profile at the electrolyte's boundaries, which is generally proportional to the applied current. As time passes, diffusion boundary layers penetrate toward the center of the cell, a process dominated by the balance between diffusion, which controls the penetration depth of the layer, and migration, which determines the rate that the excess concentration grows or decreases at the boundaries.

Figure 3.3E presents the open-circuit concentration relaxation recorded by MRI. Whereas previous in situ MRI characterizations have studied the galvanostatic polarization step exclusively [180, 183, 185, 187], the relaxation data reported here is particularly useful because it is governed by diffusion alone. During the relaxation, the concentration profile becomes flat at the boundaries, confirming the absence of the current-proportional effects of migration and faradaic convection. Previous

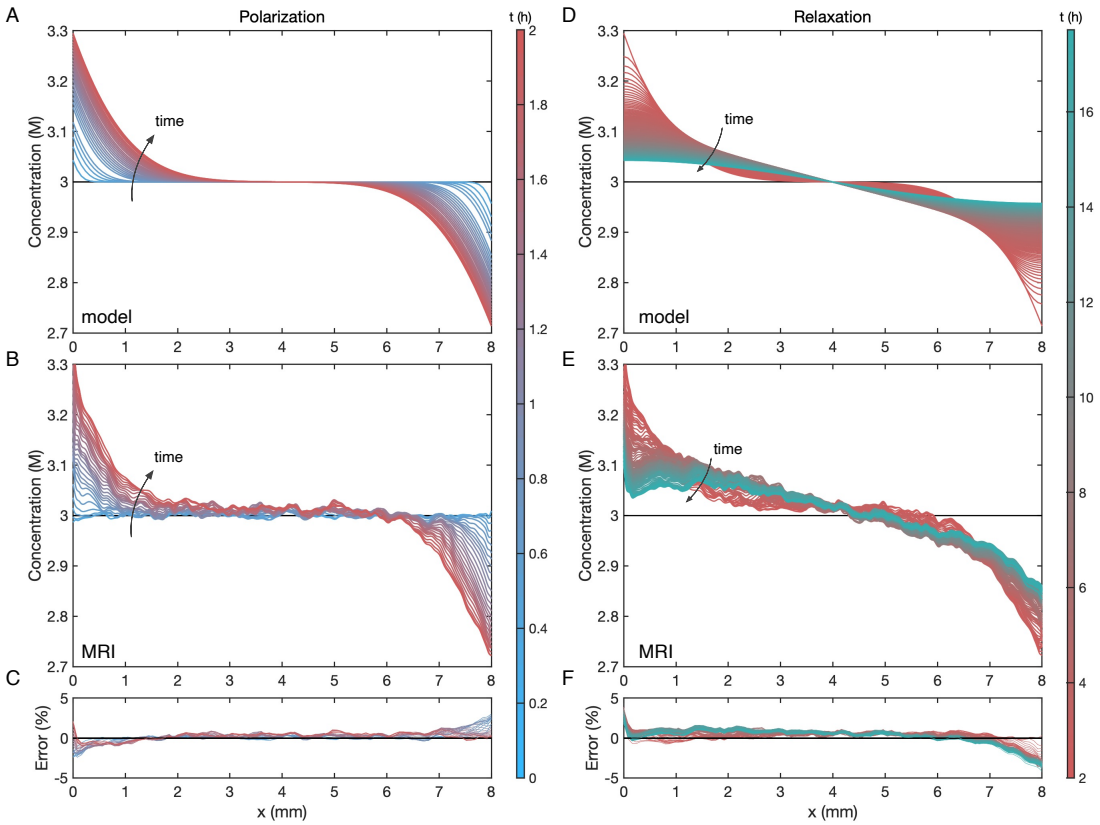


Figure 3.3: Comparison between dynamic concentration gradients simulated via the ex situ parametrized model and profiles captured by potentiometric ^{19}F MRI during galvanostatic polarization/relaxation of 3 M $LiPF_6$:EMC between planar Li-metal electrodes at 25 °C. Color varies from steel blue, through maroon, to sea green as time increases. (A) Model-simulated concentration profiles for a 2 h pulse polarization at 0.48 mA/cm^2. (B) ^{19}F MRI concentration profiles measured for a 2 h pulse polarization at 0.48 mA/cm^2. (C) Percentage error in microscopic concentration between MRI measurements and model predictions during the polarization step. (D) Model-simulated concentration profiles during open-circuit relaxation after the 2 h pulse. (E) ^{19}F MRI concentration profiles measured during open-circuit relaxation after the 2 h pulse. (F) Percentage error between MRI measurements and model predictions during the relaxation step.

analyses of restricted diffusion experiments have relied on alternative single-point or integral-average composition indicators, such as concentration overpotential, ultraviolet–visible spectroscopy, or local conductivity measurements [92, 118, 129, 143, 199], which cannot validate details of the microscopic concentration distributions revealed by MRI.

Note that the disagreement between the predicted and simulated concentration responses, quantified in Figure 3.3C,F, is always largest at the electrolyte's

edges—the spatial domain that is also subject to higher experimental error [84]. This is due in part to susceptibility effects from the Li metal electrodes. The presence of an electronic conductor commonly causes radio frequency (RF) attenuation or dispersion, which affects the MRI calibration significantly. Still, there is notable additional error on the side of the cell where Li plating occurs ($x = 8$ mm in Figure 3.3). Over a distance of about 0.5 mm from the edge on the right of Figure 3.3E, the transient MRI profiles do not appear to relax as fast as the predictions in Figure 3.3D, but the left sides of the distributions in both panels relax on apparently similar time scales.

It should be emphasized that lithium plating occurred at the right side of the domain shown in panels B and E of Figure 3.3, whereas lithium was stripped at the left. Changes in lithium surface morphology during plating are well-documented and might be a source of the apparently slower relaxation at the right. Formation of a mossy lithium layer would lower the effective diffusivity observed in regions where lithium was deposited, but this is unlikely given the relatively small amount of lithium plated during the current pulse. A charge density of 0.95 mAh/cm^2 was passed during the pulse, which would correspond to a dense Li layer 4.7 μm thick. If the mossy lithium were to spread over the distance suggested by the figure, the porosity of plated lithium would have to be more than 99%, which is unlikely in light of the microscopic observations of lithium electrodeposition by, for example, Wood and colleagues [200]. The volume of lithium plated is far too low to produce structures that isolate pockets of electrolyte. If needle-like lithium filaments were present, it would be possible for them to protrude hundreds of micrometers into the electrolyte. This deposit morphology cannot account for the slow observed concentration relaxation, however; porosities above 99% would have negligible impact on effective diffusivity and therefore cannot explain the apparently slower relaxation [201, 202]. It is much more likely that the anomalous region near the electrode is due to intrinsic error in the MRI measurement. RF shielding and distortion effects are commonly observed in the nuclear magnetic resonance (NMR) of metallic materials. Layers of metal powders, which one would expect are

structurally similar to mossy lithium from the electromagnetic standpoint, have been observed to induce inhomogeneities in MRI signals much larger than the layer thickness [203–205]. It is noteworthy that an enhanced dispersive phenomenon due to the porosity of deposited lithium may be further exacerbated in experiments that rely on longer-duration polarizations (and thus a greater thickness of mossy Li) to achieve steady-state concentration profiles. Past sources from the inverse-modeling literature have typically navigated this issue by excluding data within some distance of the electrode from the data processing [180, 183].

For electrolytes in the superconcentrated regime, consistent multicomponent transport models are necessary to account for the complex interactions present. In particular, because ∼25% of the electrolyte volume is contributed by salt (*cf.* Figure 3.1B), there is a substantial faradaic convection effect, in which the cation exchange owing to plating and stripping of lithium at the solution boundaries induces a volume flux in the bulk whose current dependence differs from that of migration [89, 118]. The neglect of solute-volume phenomena explains why inverse modeling of MRI data has yielded current-density-dependent transference numbers, such as those reported by Bazak et al [183]. Profiles in Figures 3.3 and 3.B.9 show that the parameter sets in this work, which are taken to depend only on local electrolyte composition, suffice to predict the system response.

3.2.4 Voltametric validation

During a galvanostatic pulse, the measured voltage consists of contributions from ohmic drop associated with ionic conductivity; concentration overpotential due to the developing concentration difference across the cell; and two surface overpotentials, which drive stripping and plating half-reactions at the Li metal electrodes. The concentrated-solution theory accounts only for the potential drop within the bulk solution phase and therefore models only the first two of these contributions (Figure 3.4A, solid line) [89]. During the open-circuit hold the surface overpotentials vanish and the model used here should account for all of the cell voltage.

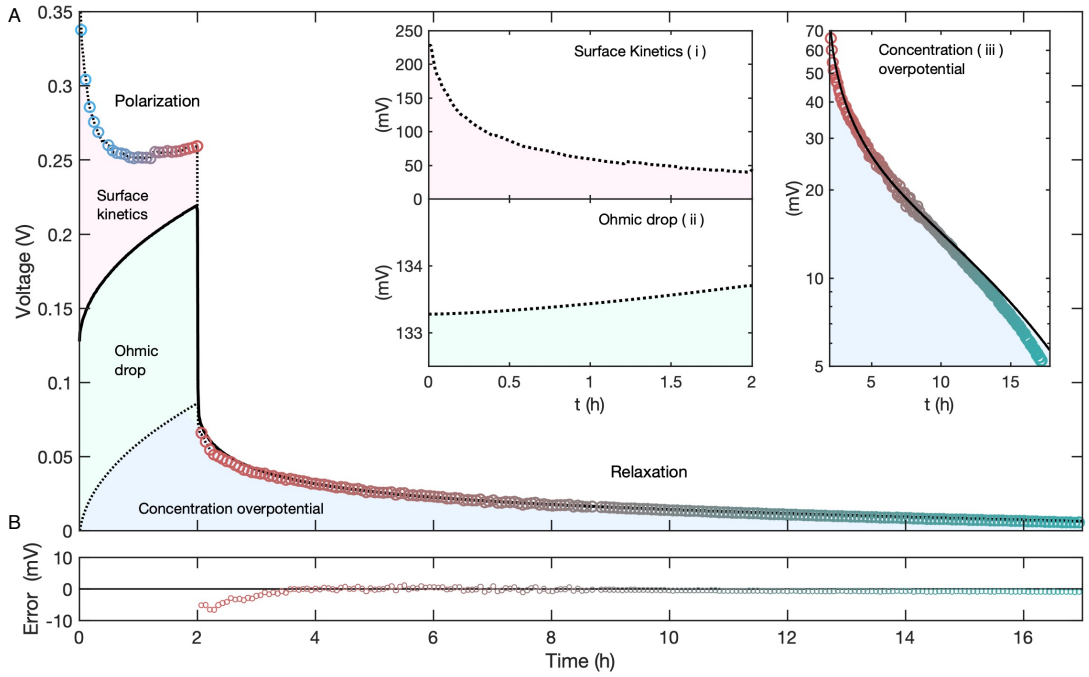


Figure 3.4: Voltage response of highly concentrated electrolyte during 2 h, 0.48 mA/cm^2 galvanostatic polarization, and subsequent open-circuit relaxation. (A) Experimental cell voltage recorded during in situ MRI (∘); colors vary over time consistently with the legends in Figure 3.3. COMSOL-simulation predictions of solution-phase overpotentials (solid —) due to ohmic and nernstian contributions. Inset A.i: Surface-overpotential contribution to cell voltage (red-shaded area) as inferred from the difference between model-predicted overpotentials and measured voltage response. Inset A.ii: Ohmic drop (green-shaded area) as calculated from simulation output by integration of the corresponding term in eq 3.2. Inset A.iii: Semilog plot of concentration overpotential (blue-shaded area) showing its transient decay during the relaxation step. (B) Voltage residual between experiment and simulation during the relaxation step.

Model prediction matches the observed voltage decay well (within 7 mV at all times in Figure 3.4B) during the open-circuit relaxation step, confirming the validity of the OSM parameters quantified ex situ. Notably, independent consideration of the composition dependence of the thermodynamic factor, χ, is crucial for translating concentration polarization into accurate concentration overpotentials across the electrolyte. Dilute-solution models based on Nernst–Planck theory require that $\chi = 1$ in eq 3.2 and therefore have no means of accounting for the extreme nonideality of superconcentrated electrolytes, for which matching the observed diffusion potentials requires χ values of order 10 (*cf.* Figure 3.2D) [118, 136].

In battery configurations containing superconcentrated electrolytes, overpotential

management is critical to performance optimization. Electrolytes typically permeate porous separators and electrodes in practical cells. Additional mass-transport limitations due to pore geometry generally exacerbate the development of both concentration gradients and overpotentials [153]. Although shorter interelectrode distances reduce the barriers to high-rate operation by raising the mass-transfer-limited current, physics-based simulations similar to the one deployed here have shown that practical cell geometries are susceptible to severe concentration gradients that can swing from the equilibrium composition by ±100% under reasonable power loads [206].

The close agreement between the experimental and predicted voltages during open-circuit relaxation justifies further processing of the voltages observed during the current pulse. By ascribing the difference between observation and prediction to surface overpotentials, quantitative insight can be gained about the redox kinetics of Li-metal electrodes immersed in superconcentrated electrolytes. The nonmonotonic voltage response to applied current has been attributed to surface-morphology changes of lithium electrodes by Wood and colleagues [200, 201]. Figure 3.4A(i) shows that when concentration overpotentials and bulk ohmic losses are corrected out of the data, the net surface overpotential in fact decreases monotonically. Note that this surface overpotential encapsulates all interfacial phenomena, for example, lithium plating/stripping kinetics and ohmic resistance of the SEI. The accuracy of the MRI concentration profiles further allows this surface overpotential to be analyzed in terms of two composition-dependent Butler–Volmer kinetic mechanisms in series [207]. A fitting procedure based on a simple Butler–Volmer kinetic model (Supporting Information, section 3.B.7) produces an effective exchange-current density that increases linearly with respect to the square root of time, traditionally consistent with a diffusion-limited surface roughening process during Li deposition [200, 208, 209]. This overall trend suggests that for the galvanostatic polarization experiments presented, the increase in Li surface area (and its accompanying SEI) outcompetes any increase in interfacial resistance from SEI thickening elsewhere.

3. Potentiometric MRI of a superconcentrated lithium electrolyte: Testing the irreversible thermodynamics approach

It is difficult to construct reference-electrode configurations that offer position-dependent information within an electrochemical cell [93]; complete transport and thermodynamic descriptions of bulk electrolytes could enable further quantitative analysis of interfacial processes.

3.3 Conclusion

In conclusion, superconcentrated electrolytes have distinctive structures, evidenced by the partial molar volumes of their components, their extreme thermodynamic nonideality, and their high degree of solvent coordination. Within $LiPF_6$:EMC, more than 25% of the solution volume is carried by salt in the superconcentrated regime above 3 M, and concentration overpotentials are amplified by a factor of 10 or more. The OSM concentrated-solution theory accounts for all the quasi-equilibrated pairwise species interactions that occur locally within this system. This study reveals that the theory remains suitable in the superconcentrated regime, so long as the thermodynamic factor and faradaic convective effects are included.

A systematic parametrization of transport and thermodynamic properties for $LiPF_6$:EMC was performed using a suite of independent experiments across the solution's solubility range. Significantly, instead of applying an inverse-modeling approach, we instead validated the theoretical framework by comparing model predictions to independently gathered potentiometric MRI data. We found that local states within an electrolyte pulsed with a constant current are predicted well by a model whose parameters are circumstantially inferred by a set of independent experiments that record global system characteristics. For superconcentrated $LiPF_6$:EMC, artificially higher lithium transference is more accurately attributed to a solute-volume effect. By exploiting open-circuit relaxations, we also eliminated the voltage signatures of phenomena that are not described by the solution-phase transport model, such as interfacial reactions.

This work confirms that models based in irreversible thermodynamics provide accurate predictions of local states within electrolytes. Theories of this type allow ready extension to include thermal and viscous properties, which enables rigorous

modeling beyond the isothermal and isobaric scenarios assumed by most continuum electrolyte models in use today. Appropriately parametrized simulations like those described here could be combined with potentiometric MRI in the future to study polarization limitations in demanding applications, manage composition-dependent degradation reactions, and infer morphological evolution of Li-metal interfaces to unlock the performance of next-generation batteries.

3.A Experimental procedures

3.A.1 Preparation of $LiPF_6$:EMC solutions

Electrolyte solutions were formulated on a mass fraction basis under an argon glovebox (Inert Technologies) environment ($H_2O < 1$ ppm, $O_2 < 1$ ppm). $LiPF_6$ salt (99.99%, battery grade, Sigma Aldrich) was dried in a heated vacuum antechamber for 24 hours at 60 °C, and EMC (99.9%, anhydrous) was dried under 3 Å molecular sieves for a week. Solutions were mixed with magnetic stir bars in polypropylene bottles for over 48 hours to ensure full dissolution. Moisture content by Karl Fischer titration was determined to be sub 10 ppm.

3.A.2 Ex-situ transport and thermodynamic property characterization

Parameterization of transport and thermodynamic properties followed experimental procedures described in detail in previous publications [102, 118]. Below we summarize the key methods: Solution densities were measured with a temperature controlled oscillating densitometer (DMA4100, Anton Paar) within the argon glovebox environment. Ionic conductivity was measured with an AC probe (Orion A212, Thermo Scientific) in a sealed cell placed in a temperature-controlled water bath at 25 °C.

Li-Li coin cells with PEEK 2 mm spacers were assembled and restricted diffusion was performed [92]. Effective Fickian diffusivities were fit from the exponential voltage decay at open circuit after applying a 100 mV potentiostatic hold for 12-hours within a 25 °C thermal chamber following equation 3.A.1:

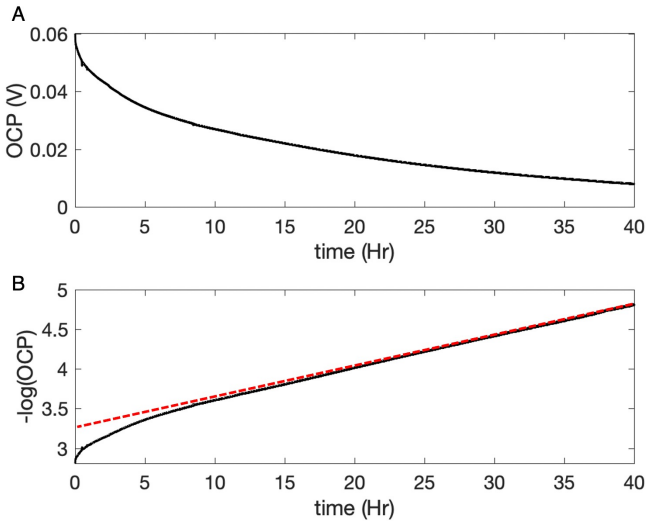


Figure 3.A.1: (A) Representative open circuit voltametric response during restricted diffusion experiment, and (B) shows the semi-log response with the fitted linear decay region (red - - -).

$$\lim_{t\to\infty} \frac{d\ln(\mathrm{OCP})}{dt} = -\frac{\pi^2 D_{\mathrm{eff}}}{L^2\varepsilon}, \tag{3.A.1}$$

where ε is the separator porosity used in the coin cell. Figure 3.A.1 shows a representative voltage trace and fitting. The chosen annular spacer thickness and potentiostatic hold ensure a less noisy, longer relaxation period, as discussed earlier by Wang et al [118].

Custom Hittorf cells with three chambers separated by two valves were used to determine transference numbers, by recording the relative changes in solution density of the anodic and cathodic chambers relative to the central chamber. After passing 14.4 C of charge (Q), both valves were closed and the solution density within each chamber was measured after combing to equilibrium. Hittorf measurements were completed within the glovebox, thermostatted at 25 °C. The transference number was calculated from the change in moles (Δn) of lithium moved relative to the initial bulk concentration (c_∞) during the experiment:

$$t_+^0 = 1 - \frac{\Delta n F}{Q(1 - c_\infty \bar{V}_{\mathrm{e}})}. \tag{3.A.2}$$

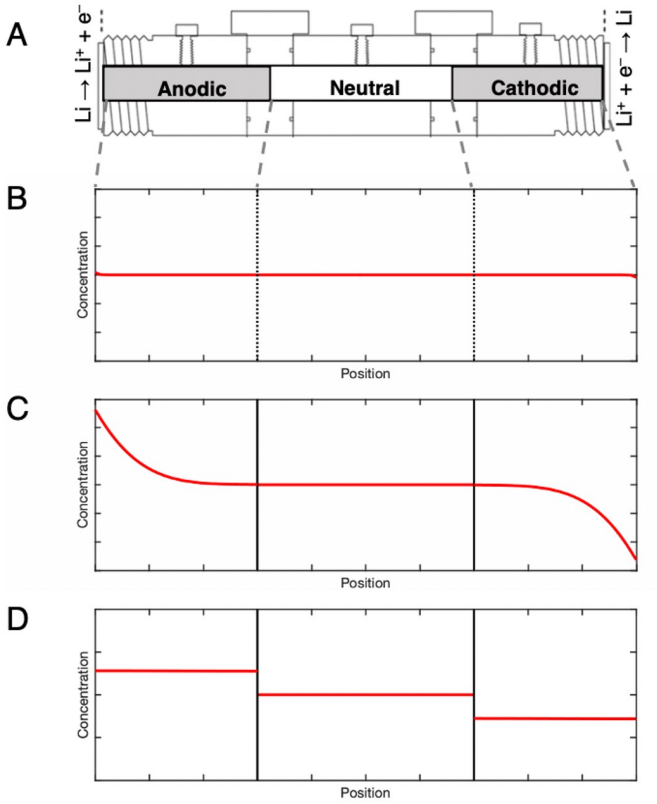


Figure 3.A.2: (A) Schematic of the valved Hittorf cell with anodic, neutral, and cathodic electrolyte chambers. (B) represents the initial concentration profile, followed by the gradient during polarization depicted in (C) and finally the resting concentrations after current and valves are shut and each chamber is allowed to settle after mixing (D).

A derivation and error analysis for equation 3.A.2 was provided by Hou and Monroe [102]. Below we illustrate an exemplary schematic of the concentration profiles during the Hittorf experiment.

Finally, fritted concentration cells with an "H" geometry were used to determine liquid-junction potentials. A matrix of test concentrations was probed using a shifting reference concentration, as described in detail by Wang et al [118].

3.A.3 Raman spectroscopy

A Renishaw inVia Reflex laser confocal Raman microscope equipped with a near-IR 785 nm laser and a 5× magnification objective (Leica, 0.12 NA, 14 WD) was used to gather Raman spectra for intermolecular structural characterization. Specifically, full scans were performed from 1600 cm^{-1} to 700 cm^{-1}, with a 5% laser power and 10 second exposure time to identify bands of note. Following acquisition, the data was processed using Renishaw WiRE 5.5 software and the background signal was removed. Spectra were then imported into Origin Pro software for further analysis and peak fitting (see supporting discussion 3.B.5).

3.A.4 Potentiometric MRI

The custom Swagelok-type PEEK cell used in the MRI experiments consisted of a cylindrical cell with 4 mm inner diameter and column length of 8 mm, PEEK screw caps, machined Cu plungers as current collectors and Viton o-rings for sealing (see schematic, figure 3.B.5). The cell was assembled with two pieces of Li metal (LTS research, 99.95%) cut into cylindrical discs with a puncher, 4 mm in diameter, adhered to the Cu current collector. The electrolyte loading was 130 μL, more than the cell volume of 100 μL, to avoid formation of gas bubbles. The excess electrolyte is displaced by the lithium electrode as the cell is sealed (see Fig. 3.B.6)). The PEEK cell was connected to shielded coaxial cables going through the open MicWB40 probe. Outside the probe, the cables were connected to a low-pass filter with 5 MHz cut-off to minimize noise pickup by the rf-coil. Additional shielded coaxial cables then connected to the potentiostat.

Electrochemical measurements were performed using a Biologic SP-150 potentiostat with EC-Laboratory software. The MRI cell was preconditioned with a cycling protocol consisting of +4 μA for one minute, and –4 μA for one minute, with 5 repeats. This was done to encourage electrochemical SEI formation before the potentiometric MRI. After a rest period, the final open-circuit potential recorded for 30 min (13 mV) was used to offset the recorded voltage behavior during polarization and relaxation to ensure compatibility with COMSOL assumptions [129].

60 μA (0.48 mA/cm^2) was then applied to the MRI cell for 2 hours, followed by a measurement of the open-circuit relaxation for 8 hours. The constant current was orientated so that Li plating occurred on the top electrode, to suppress free convection due to induced density gradients [180].

The ^{19}F MRI experiments were performed on a Bruker Avance III 300 spectrometer operating at 7.05 T (^{19}F frequency = 282.4 MHz). The spectra were acquired with a MicWB40 probe and a Micro2.5 triple axis gradient system at 298 K, using a water-cooler unit, and 10 mm exchangeable ^{1}H–^{19}F/^{7}Li coil. The cell was aligned such the Li metal electrodes were perpendicular to the external magnetic B_0-field (and to the z-axis of the gradient).

One-dimensional image profiles were acquired axially (in the z-direction) to get concentration profiles. The image profiles were acquired using the 1D spin-echo sequence (diffprof) reported by Klamor et al [196]. 64 scans were acquired with a recycle delay of 4 s, which resulted in acquisition time of 4.25 min for one image profile. The 90° pulse length was set to 18 μs and a gradient strength of 22.5 G cm^{-1}. The field of view (FOV) was 20 mm, resulting in a nominal resolution of 19.5 μm per point. The duration between the 90° pulse and the composite 180° pulse was 1.1 ms, yielding an echo time of 2.2 ms (T_2 = 300 ms). The gradient stabilization time was set to 100 μs and the dephasing time to 800 μs. The cells were aligned in the centre of the coil to ensure uniform excitation. An RF sensitivity profile was measured on an NMR tube filled with the electrolyte, shown in Fig. 3.B.6.

3.B Supporting discussion

3.B.1 Transport model formulation with solute volume effects

The polarization-cell model implemented in COMSOL Multiphysics software follows that outlined by Hou and Monroe [102].

Constituitive laws and balances:

$$\vec{N}_+ = -D\vec{\nabla}c + \frac{t_+^0}{F}\vec{i} + c\vec{v}^{\square} \tag{3.B.1}$$

$$\vec{v}^{\square} = \overline{V}_{\mathrm{e}}\left[t_-^0\vec{N}_+ + t_+^0\vec{N}_-\right] + \overline{V}_0\vec{N}_0 \tag{3.B.2}$$

$$-\vec{\nabla}\cdot\vec{v}^{\square} = \frac{\overline{V}_{\mathrm{e}}}{F}\vec{i}\cdot\vec{\nabla}t_+^0 + \frac{D}{1-\overline{V}_{\mathrm{e}}c}\vec{\nabla}c\cdot\vec{\nabla}\overline{V}_{\mathrm{e}} \tag{3.B.3}$$

$$\vec{\nabla}\cdot\vec{i} = 0 \tag{3.B.4}$$

$$\frac{\partial c}{\partial t} = -\vec{\nabla}\cdot\vec{N}_+ \tag{3.B.5}$$

$$\vec{\nabla}\Phi = -\frac{\vec{i}}{\kappa} + \frac{2RT\chi(1-t_+^0)}{F\left[1+(2\overline{V}_0-\overline{V}_{\mathrm{e}})c\right]}\vec{\nabla}\ln c \tag{3.B.6}$$

Boundary conditions:

$$\vec{i} = \frac{I(t)}{A} \tag{3.B.7}$$

$$\vec{N}_+\Big|_{x=0} = \frac{I(t)}{FA} \tag{3.B.8}$$

$$\frac{\vec{v}^{\square}}{\overline{V}_{\mathrm{e}}(1-t_+^0)}\Bigg|_{x=0} = \frac{I(t)}{FA} \tag{3.B.9}$$

Initial condition:

$$c(0,x) = c^{\mathrm{eq}} \tag{3.B.10}$$

3.B.2 Partial molar volume, composition bases, thermodynamic factor

Partial molar volumes for solvent $\overline{V}_0$ and solute $\overline{V}_0$ plotted on figure 3.1E are calculated by examining how solution density changes as a function of salt concentration. The following expressions extract partial molar volumes from the density/molarity correlation [61]:

$$\overline{V}_0 = \frac{M_0}{\rho - c\frac{d\rho}{dc}} \tag{3.B.11}$$

$$\overline{V}_{\mathrm{e}} = \frac{M_{\mathrm{e}} - \frac{d\rho}{dc}}{\rho - c\frac{d\rho}{dc}} \tag{3.B.12}$$

Here M_0 is the molar mass of EMC (104.105 g/mol) and M_{e} is the molar mass of $LiPF_6$ (151.905 g/mol). Electrolytes in parameterization experiments use a variety of composition bases including molarity c, mass fraction ω, and cation particle fraction y. They may be converted based on the following expressions for binary electrolytic solutions:

$$c = \frac{\omega\rho}{M_{\mathrm{e}}} \tag{3.B.13}$$

$$y = \frac{M_0 c}{\rho + (2M_0 - M_{\mathrm{e}})\, c} = \frac{M_0\omega}{M_{\mathrm{e}} + (2M_0 - M_{\mathrm{e}})\,\omega} \tag{3.B.14}$$

The thermodynamic factor χ expresses how the salt's activity in the liquid varies with its concentration. In terms of salt activity coefficients, χ can be written as

$$\chi = 1 + \left(\frac{\partial \ln \lambda_{+-}}{\partial \ln y}\right)_{T,p} = \frac{1}{y_0}\left[1 + \left(\frac{\partial \ln \gamma_{+-}}{\partial \ln m}\right)_{T,p}\right] = \frac{\bar{V}_0}{y_0}\left[1 + \left(\frac{\partial \ln f_{+-}}{\partial \ln c}\right)_{T,p}\right] \tag{3.B.15}$$

in which m is salt molality and c is salt molarity; λ_{+-}, γ_{+-}, and f_{+-} respectively represent mean molar salt activity coefficients over particle-fraction, molal, and molar bases.

3.B.3 Transport and thermodynamic property correlations

Below is a summary of property correlations used in the transport model, arrived at by following the same fitting procedure described by Wang et al. [118] and the experimental data presented in Fig. 3.2. The following expressions are valid for $LiPF_6$:EMC up to 3.8 M at 25 °C.

Table 3.B.1: Correlations for for $LiPF_6$:EMC

Property	Correlation	Units
$\rho(c\ [M])$	$1007.1 + 114.2c - 8.121c^{\frac{3}{2}} - 4.013 \times 10^{-5}c^{10}$	gL^{-1}
$\kappa(y)$	$\left(48.93y^{\frac{3}{2}} - 284.8y^{\frac{5}{2}} + 817.7y^{4}\right)^{2}$	Sm^{-1}
$D(y)$	$(4.998 - 29.96y + 53.78y^{2}) \times 10^{-10}$	m^2s^{-1}
$t_+^0(y)$	$0.4107 - 1.487y + 2.547y^{2}$	—
$\chi(y)$	$1 - 18.38y^{\frac{1}{2}} + 155.3y - 450.6y^{\frac{3}{2}} + 1506y^{\frac{5}{2}}$	—

Table 3.B.2: Coefficient values from Table 3.B.1 correlations with 95% confidence intervals

Property	Coefficients			
$\rho(c\ [M])$	114.2 ± 2.3	-8.121 ± 1.527	-4.013×10^{-5} $\pm 0.779 \times 10^{-5}$	
$\kappa(y)$	48.93 ± 0.61	-284.8 ± 5.6	817.7 ± 28.7	
$D(y)$	4.998 ± 0.201	-29.96 ± 3.84	-53.78 ± 14.84	
$t_+^0(y)$	0.4107 ± 0.0201	-1.487 ± 0.414	2.547 ± 1.717	
$\chi(y)$	-18.38 ± 12	155.3 ± 111.5	-450.6 ± 276.7	1506 ± 422

3.B.4 Onsager–Stefan–Maxwell diffusion coefficients

OSM diffusivities for the binary monovalent electrolyte $LiPF_6$:EMC can be mapped from bulk transport properties through

$$\mathscr{D}_{0-} = \frac{\mathscr{D}}{2t_+^0} \tag{3.B.16}$$

$$\mathscr{D}_{0+} = \frac{\mathscr{D}}{2(1-t_+^0)} \tag{3.B.17}$$

$$\frac{1}{\mathscr{D}_{+-}} = \frac{F^2}{RT\Lambda y} - \frac{2(1-2y)t_+^0(1-t_+^0)}{\mathscr{D}y} \tag{3.B.18}$$

where $\mathscr{D}$ is the thermodynamic diffusivity, equal to the Fickian diffusivity scaled by the thermodynamic factor, D/χ, and Λ is the equivalent conductance, equal to κ/c.

The extended Stefan–Maxwell equation with electrochemical potential μ_i and species velocity $\vec{v}_i$ for species i and j is given by:

$$-c_i\vec{\nabla}\mu_i = \sum_{j\neq i}\frac{RTc_ic_j}{c_{\mathrm{T}}\mathscr{D}_{ij}}(\vec{v}_i-\vec{v}_j) = \sum_{j\neq i}K_{ij}(\vec{v}_i-\vec{v}_j) \tag{3.B.19}$$

where K_{ij} simplifies notation as a diffusional drag coefficient with units of force per volume per velocity, as is plotted below in figure 3.B.1A. Ion correlations via the Onsager L matrix may also be computed in terms of drag following the mapping by Fong et al [210].

The ionic conductivity κ for a lithium electrolyte in the absence of concentration gradients can be identified as

$$\frac{1}{\kappa} = \frac{RT}{F^2c_{\mathrm{T}}}\left[\frac{1}{\mathscr{D}_{+-}} + \frac{2c_0t_+^0(1-t_+^0)}{\mathscr{D}c}\right] \tag{3.B.20}$$

Thus the ionic resistivity can be calculated in terms of fractional contributions from cation-anion interactions and solute-solvent interactions, as plotted in figure 3.B.1B and given respectively by

$$\frac{\frac{1}{\mathscr{D}_{+-}}}{\frac{1}{\mathscr{D}_{+-}}+\frac{2c_0t_+^0(1-t_+^0)}{\mathscr{D}c}} \quad \text{and} \quad \frac{\frac{2c_0t_+^0(1-t_+^0)}{\mathscr{D}c}}{\frac{1}{\mathscr{D}_{+-}}+\frac{2c_0t_+^0(1-t_+^0)}{\mathscr{D}c}} \tag{3.B.21}$$

3.B.5 Raman spectra

Full spectra collected for $LiPF_6$:EMC from 0 M to saturation are plotted in figure 3.B.2. It is observed that the scattering efficiency of $LiPF_6$ electrolytes in the super-concentrated regime is poor [211].

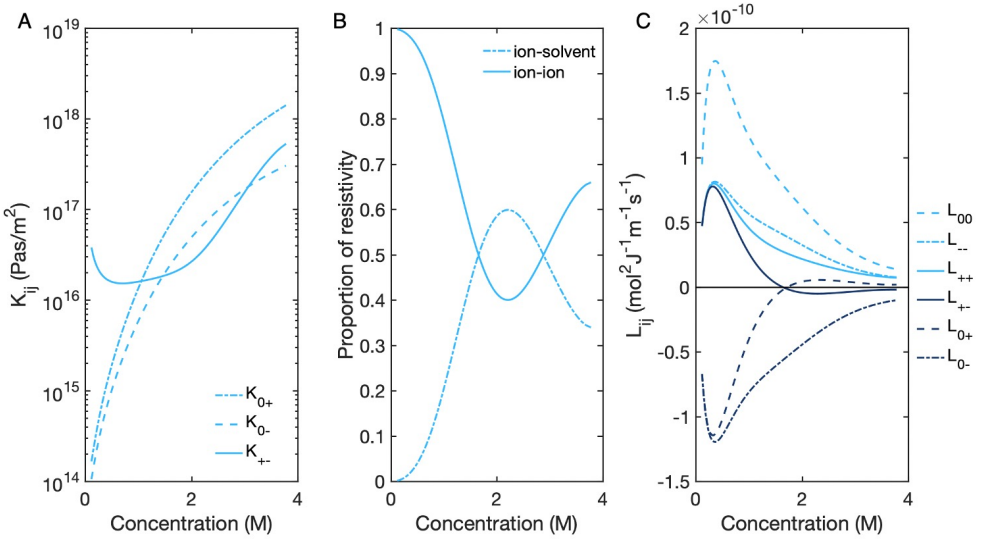


Figure 3.B.1: Onsager drag coefficients K_{ij} determined from equation 3.B.18, (B) the proportion of ionic resistivity contributed by ion-ion and ion-solvent interactions as calculated from equation 3.B.19–3.B.20, and (C) Onsager correlation decay rates L_{ij} computed with the inverse of the mapping given by Fong et al [210].

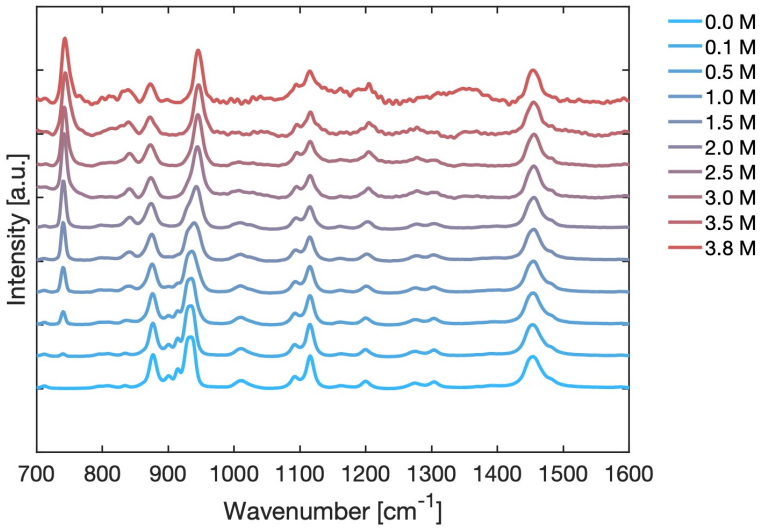


Figure 3.B.2: Full Raman spectra for $LiPF_6$:EMC at room temperature. Vertically offset for legibility.

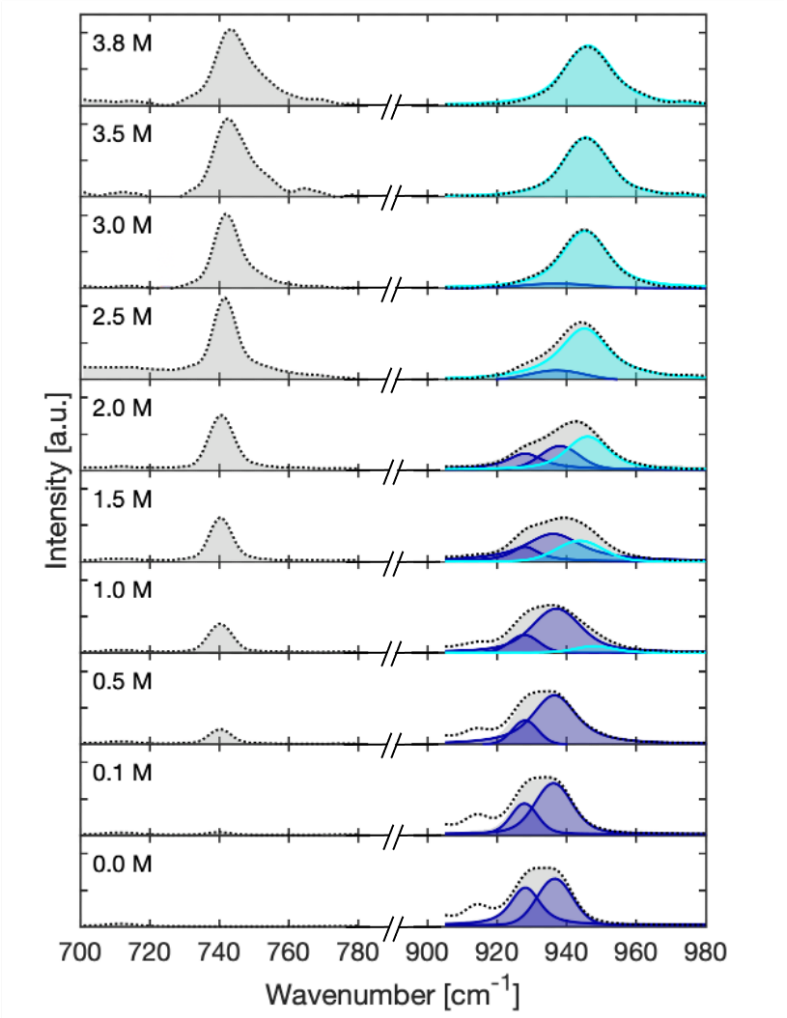


Figure 3.B.3: Stacked Raman spectra in the range of 720 – 780 cm^{-1} for PF_6^- and 920 – 980 cm^{-1} for EMC with peak deconvolution fitting for free (navy) and coordinated (cyan) EMC

Figure 3.B.3 demonstrates the peak area fitting with Voigt functions in Origin Pro. The neat EMC solvent has a characteristically broad peak at 928 and 937 cm^{-1}, which is attributed to the free C–O stretching modes influenced by the asymmetric ethyl and methyl groups in EMC [191]. The coordinated solvent peak is seen to emerge at approx. 946 cm^{-1}, as plotted in figure 3.B.3.

Without prescribing specific speciation for PF_6^-, the shifting position of maximum peak height in figure 3.B.4 suggests that ion association occurs. It is expected that a quasi-equilibrium exists between solvent-separated ion pairs, contact ion pairs, and higher order aggregates.

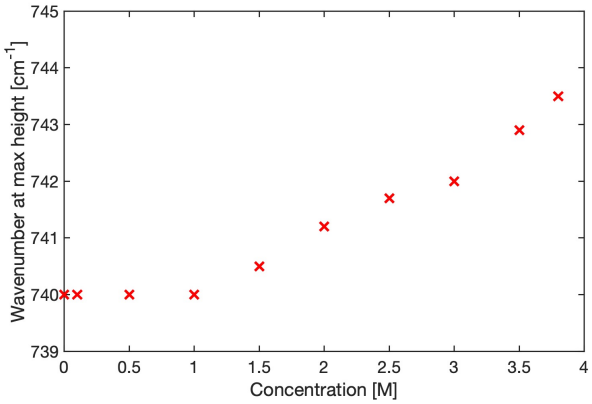


Figure 3.B.4: Position of max peak height for PF_6^- with concentration.

3.B.6 In-situ MRI experiment

MRI cell schematic

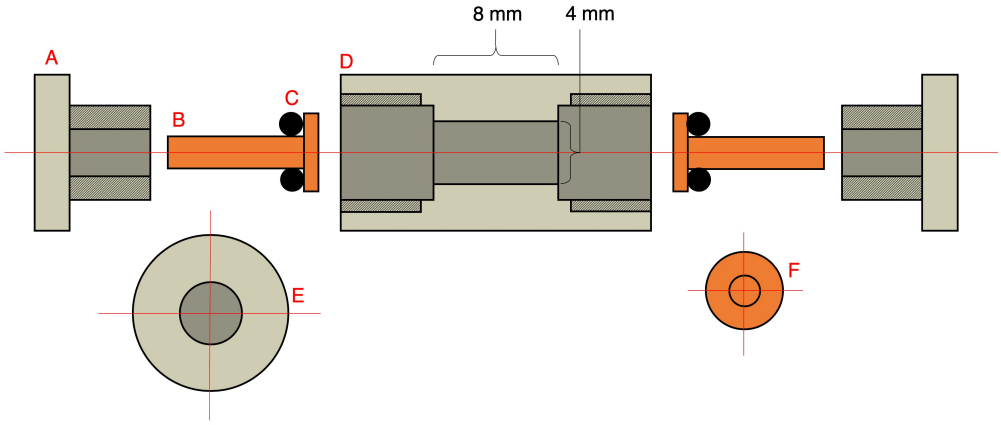


Figure 3.B.5: Schematic of the cylindrical MRI cell, with cross-sectional side views of (A) end caps, (B) copper current collectors, (C) Viton O-rings, and (D) cell electrolyte chamber, and top views of (E) the end caps and (F) the copper current collectors.

Calibration and full MRI profile

Inter-electrode spacing was calibrated with a custom PEEK cell with liquid height of 12 mm. This separate cell, sealed without electrodes, removes noise introduced by metal susceptibility effects at the interface [180]. Figure 3.B.6 compares the overall RF coil signal of a full NMR tube with that of the calibration cell. Additional intensity peaks beyond the bulk electrolyte are residual electrolyte within the threading of the constructed cell, displaced there during cell sealing.

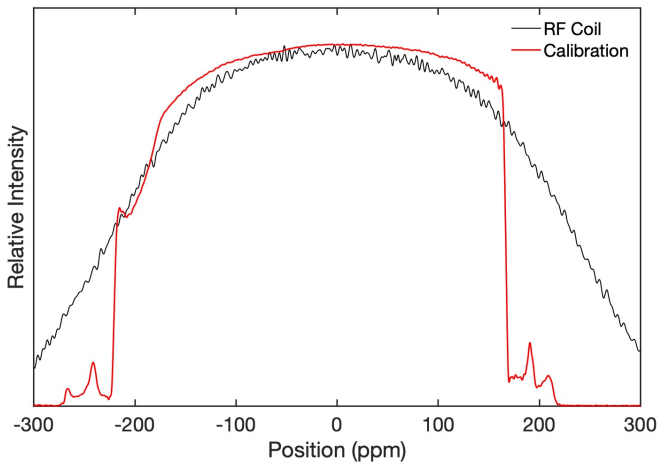


Figure 3.B.6: Intensity profile of calibration cell with 12 mm liquid height (red) and overall RF coil signal (black).

Following the attained calibration, the full intensity profile of the MRI cell during the polarization step is also shown in figure 3.B.7.

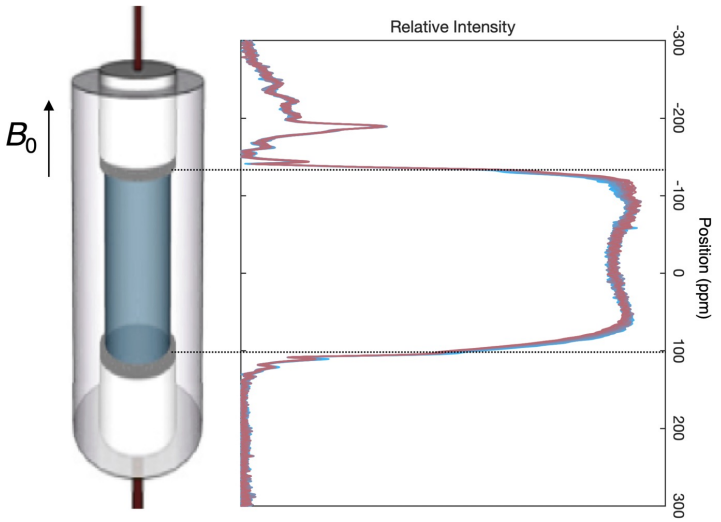


Figure 3.B.7: Initial (blue —) and final (red —) full intensity profiles for 3 M polarization step with identified inter-electrode distance (dashed). Magnetic field B0 orientation is indicated by the arrow with a schematic of the MRI cell.

Estimation of mossy Li growth

For a single polarization experiment, it is expected that any mossy dendritic lithium plated should extend no more than 50 µm into the bulk electrolyte. This estimate is based on the visualization presented in the supporting information by

Wood and coworkers for 1 M $LiPF_6$ in EC:DMC [200]. They observed 50 μm of lithium growth was for 1.25 $mAhcm^{-2}$ of charge passed, at a current density of 5 $mAcm^{-2}$. In this study, a total of 0.95 $mAhcm^{-2}$ of Li is plated, at an order-of-magnitude lower current density of 0.48 $mAcm^{-2}$. Despite this observation, in Fig. 3.3E, a loss of signal intensity extends roughly 500 μm into the bulk electrolyte from the plated electrode and most likely owes to the combined effects of RF attenuation and magnetic susceptibility. Previous work by Ilott et al. showed that quantifying loss of signal intensity of the electrolyte solvent by MRI led to significant overestimation of Li metal growth [203].

Low pass filtering of MRI data

A low pass filter was applied to the raw MRI data to dampen higher-frequency noise. For a sampling time of 258 s for each captured profile, the cutoff (0.2 of the Nyquist frequency) was chosen to process experimental noise with the Butterworth function in MATLAB. Filtering with time was performed at fixed locations, to minimize positional effects of smoothing on the observed concentration profiles. An example of a time-filtered concentration profile on the anodic side of the cell is shown in figure 3.B.8.

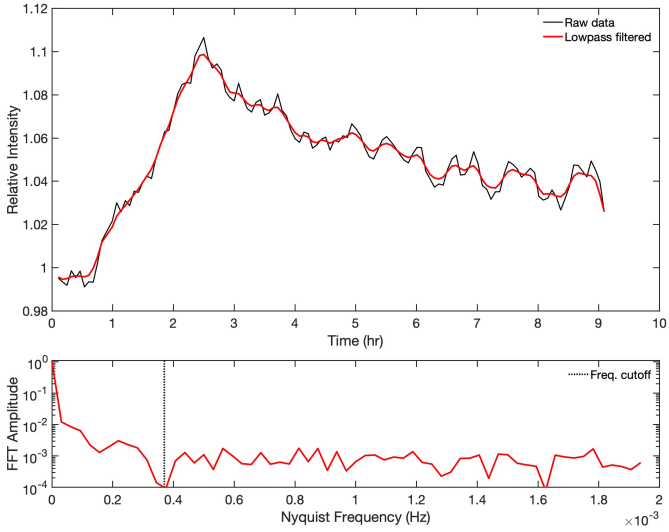


Figure 3.B.8: Example of low-pass-filtered timeseries composition data for MRI raw profiles at a fixed location.

3. Potentiometric MRI of a superconcentrated lithium electrolyte: Testing the irreversible thermodynamics approach

2 molar polarization data

To demonstrate validity of the model and parameters for predicting microscopic states across wider ranges of concentration and current density, a repeat experiment was performed with 2 M $LiPF_6$:EMC, using a 2 hour polarization at a current density of 1.9 mA/cm^2, followed by an open circuit relaxation.

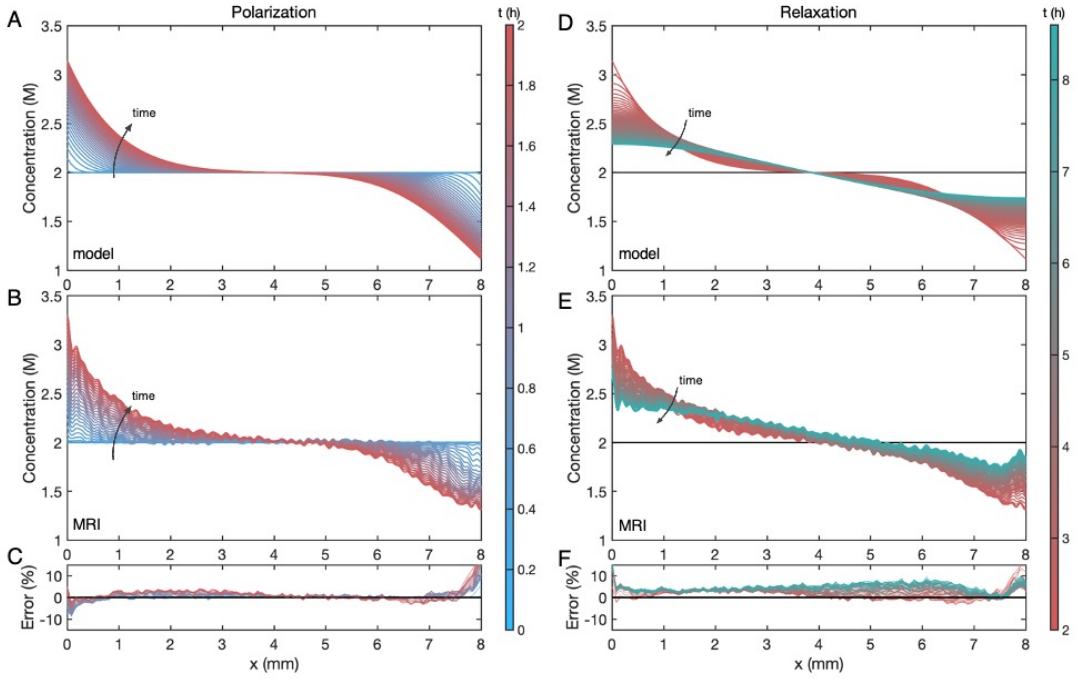


Figure 3.B.9: Comparison between dynamic concentration gradients simulated via the ex situ parametrized model and profiles captured by potentiometric ^{19}F MRI during galvanostatic polarization/relaxation of 2 M $LiPF_6$:EMC between planar Li-metal electrodes at 25 °C. Color corresponds to the timestamp of each profile relative to the overall experiment duration. (A) Model-simulated concentration profiles for a 2 h pulse polarization at 1.9 mA/cm^2. (B) ^{19}F MRI concentration profiles measured for a 2 h pulse polarization at 1.9 mA/cm^2. (C) Percentage error in microscopic concentration between MRI measurements and model predictions during the polarization step. (D) Model-simulated concentration profiles during open-circuit relaxation after the 2 h pulse. (E) ^{19}F MRI concentration profiles measured during open-circuit relaxation after the 2 h pulse. (F) Percentage error between MRI measurements and model predictions during the relaxation step.

3.B.7 Electrochemical response and surface kinetics analysis

Butler–Volmer kinetics fitting

As discussed in the main article, a full characterization of the bulk transport and

thermodynamic properties for super-concentrated $LiPF_6$:EMC allows the combined surface overpotentials (η_s) to be isolated by subtracting the calculated ohmic drop (η_{ohm}) and concentration overpotential (η_c) from the measured symmetric-cell voltage (V):

$$V = \eta_s + \eta_{\text{ohm}} + \eta_c \tag{3.B.22}$$

Here η_{ohm} and η_c may be calculated by integrating across the bulk solution phase in equation 3.B.6:

$$\eta_{\text{ohm}} + \eta_c = \frac{I(t)}{A}\int_L^0 \frac{dx}{\kappa} - \frac{2RT}{F}\int_{c(t,L)}^{c(t,0)} \frac{\chi(1-t_+^0)}{c\left[1+(2\bar{V}_0 - \bar{V}_e)c\right]}dc \tag{3.B.23}$$

The total surface overpotential for a symmetric Li-Li cell can be written as $\eta_s = \eta_+ + \eta_-$, using the surface overpotential for the lithium plating and stripping half reactions [61]. For a single lithium plating reaction at the cathode, the concentration-dependent Butler-Volmer equation with a surface concentration (c_+^{surf}), reference concentration (c_{ref}), symmetry factory (β), and surface overpotential (η_+) is [207]:

$$i = i_{0,\text{ref}}\left(\frac{c_+^{\text{surf}}}{c_{\text{ref}}}\right)^{1-\beta}\left[\exp\left(\frac{(1-\beta)\,F}{RT}\eta_+\right) - \exp\left(\frac{-\beta F}{RT}\eta_+\right)\right], \tag{3.B.24}$$

where i is the applied current density and $i_{0,\text{ref}}$ is the exchange current density, the latter defined with k_a and k_c representing the anodic and cathodic reaction rate constants as

$$i_{0,\text{ref}} = F k_c^{1-\beta} k_a^{\beta} c_{\text{ref}}^{1-\beta}. \tag{3.B.25}$$

Assuming $\beta = 0.5$, the analytical expression may be simplified to

$$i = 2i_{0,\mathrm{ref}}\sqrt{\frac{c_+^{\mathrm{surf}}}{c_{\mathrm{ref}}}}\sinh\left(\frac{F\eta_+}{2RT}\right). \tag{3.B.26}$$

This can then be inverted to isolate the kinetic overpotential, as

$$\eta_+ = \frac{2RT}{F}\sinh^{-1}\left(\frac{i}{2i_{0,\mathrm{ref}}}\sqrt{\frac{c_{\mathrm{ref}}}{c_+^{\mathrm{surf}}}}\right). \tag{3.B.27}$$

Since hyperbolic sine is an odd function, and since two lithium/electrolyte interfaces are present in the cell, the total surface overpotential ($\eta_s = \eta_+ + \eta_-$) during polarization is

$$\eta_s = \frac{2RT}{F}\left(\sinh^{-1}\left(\frac{i}{2i_{0,\mathrm{ref}}}\sqrt{\frac{c_{\mathrm{ref}}}{c_+^{\mathrm{surf}}}}\right) + \sinh^{-1}\left(\frac{i}{2i_{0,\mathrm{ref}}}\sqrt{\frac{c_{\mathrm{ref}}}{c_-^{\mathrm{surf}}}}\right)\right). \tag{3.B.28}$$

From figures 3.3 and 3.4, η_s and surface cation concentrations are known and plotted below in figure 3.B.10. Equation 3.B.28 can then be used to fit data in figure 3.B.10 (with $c_{\mathrm{ref}} = 3$ M) to yield the effective exchange current density $i_{0,\mathrm{ref}}$ during the polarization, as plotted in figure 3.B.11.

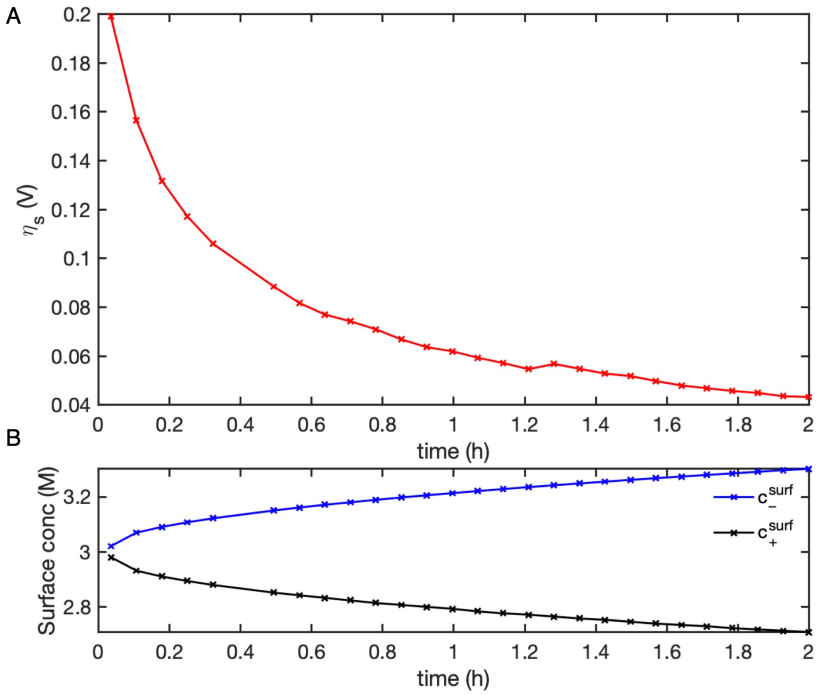


Figure 3.B.10: (A) Surface overpotential η_s during the polarization step. (B) Lithium-ion concentration in solution at the anodic surface (blue) and cathodic surface (black).

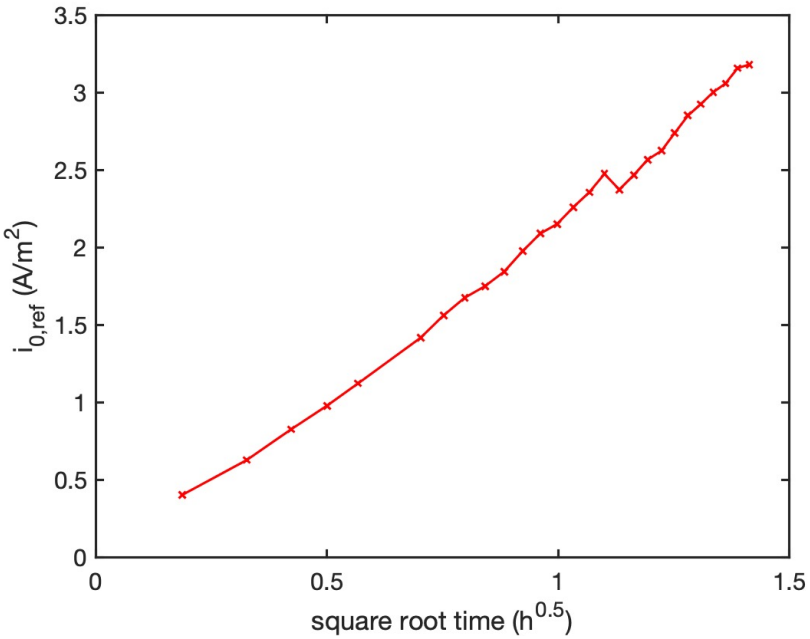


Figure 3.B.11: The effective exchange current density $i_{0,\mathrm{ref}}$ plotted with square root of polarization time, derived from fitting with equation 3.B.28.

As can be seen in figure 3.B.11, the exchange current density during the experiment

increases relatively linearly with the square root of time, suggesting surface roughening during electrodeposition [208]. The Butler–Volmer analysis here includes contributions from electrode kinetics and SEI growth. The evolution of interfacial conditions can have a large impact on electrolyte characterization experiments [128]. In the present case, the monotonic decrease in surface overpotential indicates that any growth in interfacial resistance is outcompeted by the increase in surface area from both lithium deposition and SEI formation during the plating process.

3.B.8 Dynamic viscosities

Viscosities were measured for $LiPF_6$:EMC at temperatures of 20.0, 25.0, and 30.0 °C with a rolling-ball viscometer (Lovis 2000, Anton Paar) with 1.59 and 1.8 mm capillary diameters.

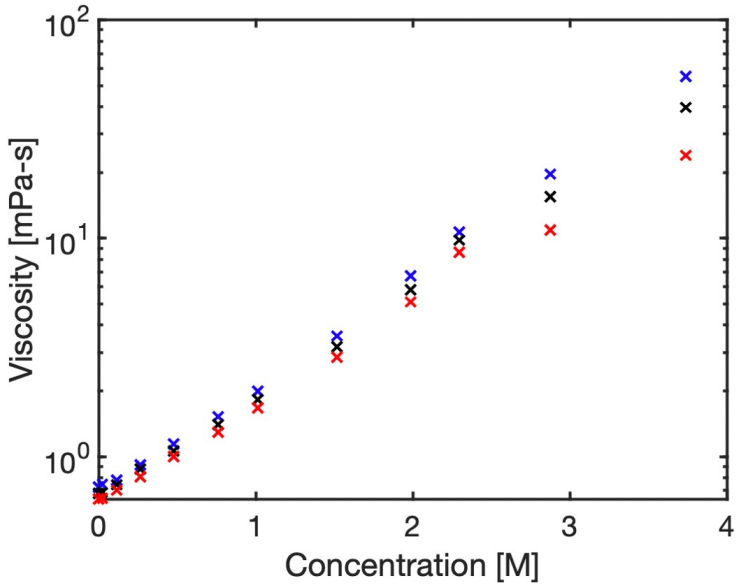


Figure 3.B.12: Semilog plot of dynamic viscosity measured across the molarity range for $LiPF_6$:EMC at 20.0 °C (blue x), 25.0 °C (black x), and 30.0 °C (red x).

3.B.9 Other raw data

Transport and thermodynamic property measurements for $LiPF_6$:EMC were extended from the range studied previously by Wang et al. [118] up to saturation, following the experimental techniques discussed in detail by Hou and Monroe, as

well as Wang et al [102, 118]. Below we summarize the additional raw data that underpin this study's reported property parameterization.

Table 3.B.3: Density composition calibration measurements for $LiPF_6$:EMC solutions. Recorded under an argon atmosphere in a glovebox. Temperature is controlled within 0.02 °C.

ω	$\rho_{25°C}$ [g/L]	$c_{25°C}$ [M]
0.33084	1291.6	2.81
0.34517	1298.7	2.95
0.37359	1326.3	3.26
0.39210	1339.7	3.46
0.41879	1353.9	3.73
0.44633	1352.4	—
0.46776	1355.7	—
0.49981	1351.4	—
0.56003	1350.8	—
0.65174	1353.1	—

Table 3.B.4: Ionic conductivity measurements for $LiPF_6$:EMC solutions.

$\rho_{20\,°C}$ [g/L]	$\kappa_{25\,°C}$ [mS/cm]
1259.4	4.551
1293.5	3.449
1329.0	2.256
1360.6	1.741

Table 3.B.5: Liquid-junction potentials in concentration cells for $LiPF_6$:EMC at 25 °C.

$\rho^A_{25\,°C}$ [g/L]	$\rho^B_{25\,°C}$ [g/L]	U [mV]	Std. Dev. [mV]
1268.1	1285.4	20.75	±0.16
1268.1	1299.8	37.79	±0.13
1285.4	1299.8	16.87	±0.63
1285.4	1317.0	38.41	±0.26
1299.8	1317.0	23.67	±0.07
1299.8	1333.6	43.61	±0.20
1317.0	1333.6	28.76	±0.68
1317.0	1361.4	61.83	±0.43
1333.6	1361.4	59.73	±0.16

Table 3.B.6: Hittorf-cell measurements for $LiPF_6$:EMC solutions.

$\rho_{20°C}^{initial}$ [g/L]	$I_{pulse}T_{pulse}$ [C]	$\rho_{20°C}^{anodic}$ [g/L]	$\rho_{20°C}^{cathodic}$ [g/L]
1298.1	7.1931	1297.1	1299.2
1298.1	7.1931	1297	1299.2
1298.2	7.17936	1297.1	1299.3
1340.3	7.1141	1339.1	1341.4

Table 3.B.7: Restricted diffusion measurements for $LiPF_6$:EMC solutions.

$\rho_{20\,°C}$ [g/L]	slope fit [s^{-1}]	D_{eff} [cm^2/s]	κ_{eff} [mS/cm]	b
1296.9	1.15E-04	4.68E-07	2.27	2.19
1296.9	1.27E-04	5.15E-07	2.65	1.25
1296.9	1.02E-04	4.15E-07	2.51	1.57
1296.9	1.50E-04	6.06E-07	2.84	0.82
1296.9	9.25E-05	3.75E-07	1.75	3.80
1296.9	9.45E-05	3.83E-07	2.09	2.72
1328.8	1.23E-04	5.00E-07	2.03	0.89
1328.8	9.07E-05	3.68E-07	2.34	0.12
1328.8	1.26E-04	5.10E-07	2.34	0.12
1328.8	1.21E-04	4.89E-07	2.16	0.51
1328.8	1.13E-04	4.58E-07	2.34	0.12
1328.8	1.03E-04	4.16E-07	2.21	0.36
1328.8	6.42E-05	2.60E-07	1.61	2.30
1328.8	1.25E-04	5.05E-07	2.31	0.10
1328.8	8.29E-05	3.36E-07	1.99	0.99
1358.0	9.25E-05	3.75E-07	1.32	1.77
1358.0	8.85E-05	3.59E-07	1.76	0.12
1358.0	8.91E-05	3.61E-07	1.61	0.56
1358.0	6.91E-05	2.80E-07	1.54	0.82
1358.0	7.21E-05	2.92E-07	1.54	0.82

3. Potentiometric MRI of a superconcentrated lithium electrolyte: Testing the irreversible thermodynamics approach

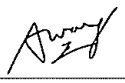
Statement of Authorship for joint/multi-authored papers for PGR thesis

To appear at the end of each thesis chapter submitted as an article/paper

The statement shall describe the candidate's and co-authors' independent research contributions in the thesis publications. For each publication there should exist a complete statement that is to be filled out and signed by the candidate and supervisor **(only required where there isn't already a statement of contribution within the paper itself).**

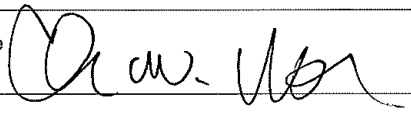
Title of Paper	Potentiometric MRI of a Superconcentrated Lithium Electrolyte: Testing the Irreversible Thermodynamics Approach
Publication Status	Published
Publication Details	Wang, A. A.; Gunnarsdóttir, A. B.; Fawdon, J.; Pasta, M.; Grey, C. P.; Monroe, C. W. Potentiometric MRI of a Superconcentrated Lithium Electrolyte: Testing the Irreversible Thermodynamics Approach. *ACS Energy Lett.* **2021**, 3086–3095. https://doi.org/10.1021/acsenergylett.1c01213.

Student Confirmation

Student Name:	Andrew A. Wang		
Contribution to the Paper	Conceptualization, Methodology, Investigation, Formal Analysis, Writing		
Signature		Date	04/07/2022

Supervisor Confirmation

By signing the Statement of Authorship, you are certifying that the candidate made a substantial contribution to the publication, and that the description described above is accurate.

Supervisor name and title: Charles W. Monroe (Associate Professor)			
Supervisor comments Andrew is first author.			
Signature		Date	5 July 2022

This completed form should be included in the thesis, at the end of the relevant chapter.

4

Current-driven solvent segregation in lithium-ion electrolytes*

Abstract

Liquid lithium-battery electrolytes universally incorporate at least two solvents: one raises conductivity by solvating ions and the other lowers solution viscosity. Almost all continuum models treat cosolvent systems such as ethylene carbonate:ethyl-methyl carbonate (EC:EMC) as single entities, whose constituents travel with identical velocities. Here we test this 'single-solvent approximation' by subjecting $LiPF_6$:EC:EMC blends to constant-current polarization in Hittorf experiments. A Gaussian process regression model trained on density, viscosity, and conductivity is developed to quantify changes in ternary composition across the Hittorf cell. EC and EMC are found to migrate at noticeably different rates under applied current, showing conclusively that the single-solvent approximation is violated, and that concentration polarization of salt concentration is anticorrelated with that of EC. A four-species transport simulation demonstrates extreme solvent segregation near electrode/liquid interfaces: a 5% change in EC:EMC ratio after a Hittorf experiment implies a change of more than 50% adjacent to the interface during the current pulse. Understanding how lithium-ion flux induces local cosolvent or additive imbalances suggests new approaches to electrolyte design and degradation modeling.

*This chapter was reported in *Cell Reports Physical Science* **2022**, DOI: 10.1016/j.xcrp.2022.101047 [212]

4.1 Introduction

Contemporary lithium-ion electrolytes are formulated as mixed-solvent systems, a paradigm that balances competing requirements including interfacial and chemical stability, high ionic conductivity, and low solution viscosity. Pioneering previous work showed that high-viscosity, high-permittivity ethylene carbonate (EC) could be combined with low-viscosity, low-permittivity linear carbonates to meet these criteria. [8, 213]. New cosolvent blends have been designed for advanced applications such as fast charging or compatibility with Li-metal electrodes using analogous design targets. Recent research has focused on innovative concepts such as ultra-concentrated 'solvent-in-salt' electrolytes [20] or 'localized high concentration' electrolytes, wherein high-molarity solvate structures are dispersed within a diluent cosolvent [23]. Developing quantitative understanding of how ions and cosolvents distribute and interact between electrodes is fundamentally important for the future design and optimisation of electrochemical energy storage systems.

Preferential solvation [214] between cosolvents and lithium salts on microscopic length scales has been investigated with both spectroscopic experiments [57, 58, 122] and quantum chemical simulations [194, 215]. Recently, Von Wald Cresce and colleagues reported that lithium hexafluorophosphate ($LiPF_6$) in a bulk 3:7 mol-ratio mix of EC and ethyl-methyl carbonate (EMC) had a 7:3 EC:EMC coordinated-solvent population ratio within the Li^+ solvation shell. [57]. This competitive-solvation phenomenon is understood to correlate with solid-electrolyte interphase (SEI) formation and degradation side reactions in lithium-ion batteries [216]. Beyond microscopic studies, recent work by Miele et al. used Raman optical fibres to reveal local swings in solvation dynamics and EC:EMC ratio within full Li-ion cells during operation [217]. Additional spatial resolution is needed to determine how these changes vary across the domain between electrodes.

At the continuum level, mass transport and thermodynamics in binary electrolytes has been resolved with remarkable fidelity. For a binary system comprising a single solvent and a lithium salt, a consistently parameterized transport model based on Newman's concentrated-solution theory [61, 102] can very accurately

predict spatiotemporal ion distributions under dynamic polarization conditions [96, 218]. The solvent is also increasingly being recognized as a mobile component in and of itself [89, 219]. Various groups have measured bulk velocities of both polymer and liquid electrolytes directly, demonstrating that solvents can migrate under applied currents, despite being charge-neutral chemical species [105, 106, 218].

Given the confirmed presence of solvent drift on the macroscale and preferential ion solvation on the microscale, a question arises: do the different cosolvent species in lithium electrolytes move together? This query was aptly raised in a recent communication by Mistry and Srinivasan [220]. Previous transport characterizations of mixed-solvent lithium-ion battery electrolytes have universally applied a pseudo-single-solvent approximation, whereby cosolvents are treated as a single entity [78, 83, 128], which presumes that each species making up the solvent blend moves at the same rate. Note that this approximation is born out of prohibitive experimental complexity, rather than decisive experimental justification — even a simple cosolvent electrolyte such as $LiPF_6$:EC:EMC, made up of two solvents and a simple salt, requires the parametrization of six independent transport coefficients and six thermodynamic parameters to describe isothermal, isobaric, locally electroneutral transport [61]. If cosolvent motion is not perfectly correlated at the continuum scale, then the differences in transport among solvents could be exploited, both to fine-grain electrolyte simulations and to develop new routes for electrolyte design and discovery.

A rigorous test of the single-solvent approximation must probe whether applied current or salt-concentration polarization induces segregation of cosolvent species. To that end, we performed Hittorf experiments (Figure 1A) to induce salt-composition differences across solutions of $LiPF_6$ salt in a 1:1 mass ratio of EC:EMC cosolvent and investigated whether and how polarization of the salt concentration correlates with polarization of the solvent ratio. This application of a Hittorf cell requires accurate estimation of ternary electrolyte composition, which cannot be achieved with the purely gravimetric or conductometric strategies used in the past [102, 221]. Chemical compositions of the $LiPF_6$:EC:EMC solutions extracted from Hittorf cells were therefore determined using a machine learning approach, based on a Gaussian

process regression model trained with a database of precise physicochemical property data. Alternative approaches to composition measurement based on spectroscopy are a poor fit for this problem, both because of the expected low magnitude of solvent polarization and the chemical similarity of the EC and EMC molecules. Below we report a significant degree of current-driven solvent segregation during Hittorf experiments, showing that $LiPF_6$:EC:EMC indeed violates the single-solvent approximation.

To understand the impact of solvent segregation more clearly, we implement a four-species multicomponent transport model based on Onsager–Stefan–Maxwell theory to estimate what the Hittorf-experiment results — which average current-induced concentration polarization over large volumes — imply about the local cosolvent composition. The transport model suggests that cosolvent ratios change dramatically near electrode surfaces, a local effect that could be tracked to refine degradation or SEI-formation models based on reactions involving EC. Cosolvation environments in liquid electrolytes can also impact the energetics and dynamics of fundamental electrochemical processes relevant to lithium-ion batteries, such as intercalation, electrodeposition, and side reactions.

4.2 Results and discussion

4.2.1 Data-driven composition analysis

Hittorf experiments were performed using the methodology shown schematically in Figure 4.1A. (More details are provided in the Experimental Procedures section below.) Note that the gravimetric Hittorf approach implemented by Hou and Monroe relies on the direct dependence of density on solute concentration in an isothermal binary solution [102, 118], and is inadequate for applications to cosolvent electrolytes. For example, raising the molarity of either $LiPF_6$ or EC in a $LiPF_6$:EC:EMC ternary will increase the solution's density. Hittorf experiments also require sensitivity to very small concentration changes, because species molarity changes induced by the applied current pulse are diluted across the entire volume of each Hittorf-cell chamber before its composition assay [217]. Hence quantitative

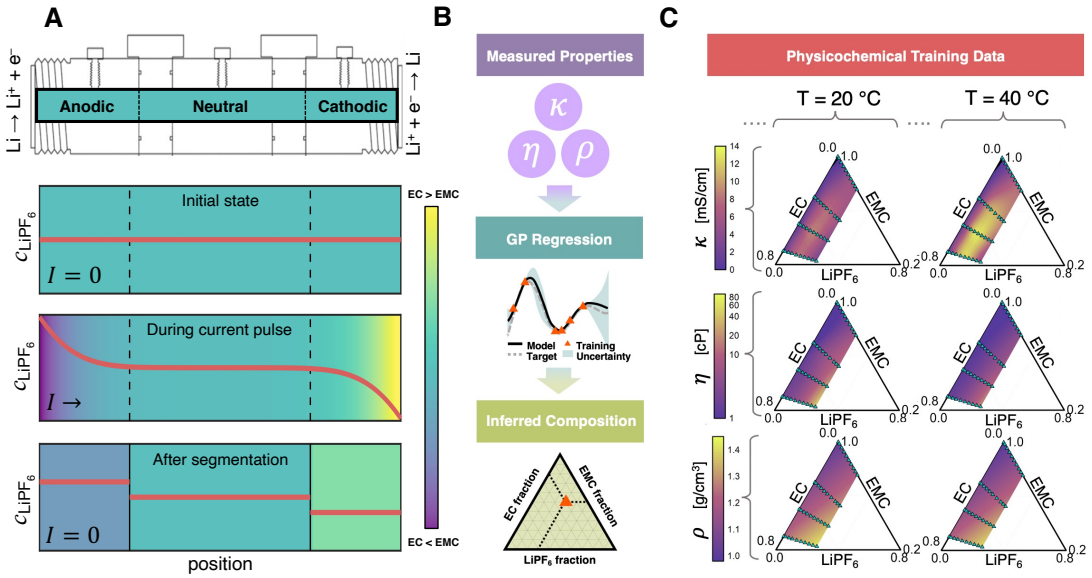


Figure 4.1: Hittorf experiment and Gaussian process regression analysis of cosolvent segregation.
(A) Hittorf cell schematic, showing the valved anodic, neutral, and cathodic chambers in the symmetric cylindrical Li|electrolyte|Li cell. Initially (top) the electrolyte has uniform distributions of salt concentration (red curve) and solvent ratio (background color). As current is passed through the cell (middle), it induces both salt and cosolvent gradients. The valves are then sealed, and each chamber equilibrated (bottom), yielding solutions that are extracted to determine the volume-averaged changes of salt and solvent content in the anodic and cathodic chambers.
(B) Conductivity, viscosity, and density measurements are made at 10, 20, 25, 30, and 40 °C for the electrolytes extracted from the Hittorf cell's anodic and cathodic chambers. A Gaussian process regression model, trained on the dataset of known solvent compositions illustrated in panel (C), is then used to infer the $LiPF_6$, EC, and EMC mass fractions of the electrolytes extracted from the Hittorf cell.
(C) Physicochemical training datasets for the Gaussian process regression model. Ternary diagrams show the solution conductivity, viscosity, and density for $LiPF_6$:EC:EMC electrolytes from 0 to 2 M with EC:EMC mass ratios of 0:1, 3:7, 1:1, and 7:3 (the measured mass fractions are shown as points on the ternary diagrams) at 20 and 40 C. The rest of the training data, at the additional temperatures of 10, 25, and 30 °C, is plotted in Figure 4.B.1.

analytical methods such as confocal Raman spectroscopy, which require careful deconvolution of peak signals, were deemed to have resolution too low for this study. Instead, the Gaussian process (GP) model illustrated in Figure 4.1B and trained on the data sets from Figure 4.1C was used to infer the extent of solvent polarization induced by a current pulse in a Hittorf cell.

The GP model learned from electrolyte properties is found to predict ternary

solution compositions with very high precision. This owes in part to the widely differing trends in how density, viscosity, and ionic conductivity of $LiPF_6$:EC:EMC solutions vary with respect to composition and temperature. Density follows a relatively linear functionality with respect to species molarity, whereas viscosity can vary exponentially; conductivity passes through local maxima with respect to both the salt and EC contents [159, 222]. Importantly, all three physicochemical properties can be measured to several digits of precision under temperature-controlled conditions using standard commercial equipment. Figures 4.1C and 4.B.1 show solution density, viscosity, and ionic conductivity from 0 M to 2 M $LiPF_6$ concentration in solutions with EC:EMC mass ratios of 0:1, 3:7, 1:1, and 7:3, at temperatures of 10, 20, 25, 30, and 40 °C. These measurements provide a comprehensive set of input data for a regression model whose output is ternary composition of the electrolyte. Property measurements at varying cosolvent and salt fractions, plotted in Figure 4.1C, were used to train the GP regression model for composition assay. The average root-mean-square error for mass fractions calculated from leave-one-out cross-validation was found to be 0.003 ± 0.002 when predicting the salt and EMC composition, corresponding to uncertainties of approximately 2.4% and 0.7% for the $LiPF_6$ and EMC mass fractions, respectively (Section 4.B.2-4.B.3).

It is notable that the present application of machine-learning methods aims to predict an electrolyte's composition given its properties, whereas almost all computational-materials work to date has aimed to address the inverse problem, i.e., prediction or optimization of properties given composition [223, 224]. Gaussian process regression is a flexible non-parametric method that makes few assumptions about data-fitting functionality. It is also a Bayesian approach that inherently estimates the uncertainty of predictions [225]. All the physicochemical property data, as well as an implementation of the GP model in the GPy Python framework,[226] are provided in the Supplemental Information and Data Repository that accompany this article [227].

4.2.2 Hittorf results indicate cosolvent segregation

A series of 1:1 mass-ratio EC:EMC electrolytes with salt mass fractions of 0.065, 0.125, and 0.185 (approx. 0.6 M, 1.0 M, and 1.6 M, respectively) were polarized within Hittorf cells under an applied current of 0.5 mA (0.64 $mAcm^{-2}$) for 20 hours. Buoyancy effects were suppressed by orienting the long axis of the Hittorf cells vertically and choosing the sign of current to ensure that plating occurred on the top electrode. Immediately following the passage of charge, the valves separating the anodic, neutral, and cathodic chambers were sealed, and the solutions in the individual chambers were mixed with stir bars to homogenize their compositions before density, conductivity, and viscosity were measured at the five temperatures mentioned previously. The GP model was then used to map the resultant set of property measurements into $LiPF_6$, EC, and EMC mass fractions based on both the magnitudes of the three properties and their relative trends across the five temperatures.

Solvent segregation is clearly observed, indicating that EC and EMC do not move as a single entity. Figure 4.2 presents a ternary diagram showing the results of Hittorf polarization tests for electrolytes with three different concentrations of $LiPF_6$. All three initial compositions (green markers) begin with the same 1:1 cosolvent mass ratio, and as such, they lie along the dashed red curve on the figure. For each of the polarized solutions, the salt concentration is elevated in the anodic chamber (yellow markers) and depleted in the cathodic chamber (purple markers). If EC and EMC were to migrate with identical velocities, then the anodic and cathodic compositions would be polarized along the line of invariant solvent ratio (red dashed line). This is not the case, however, demonstrating that the single-solvent approximation does not hold. Despite the Hittorf experiment operating above the limiting current density in a semi-infinite regime, we discuss later and show in Figure 4.4B that considerable solvent segregation is still expected across geometries relevant to practical Li-ion cells cycling below the limiting current.

The extent of current-driven solvent segregation also increases as salt content rises, indicating that the solvent mobilities are sensitive to ion molarity. For the 1.0 M

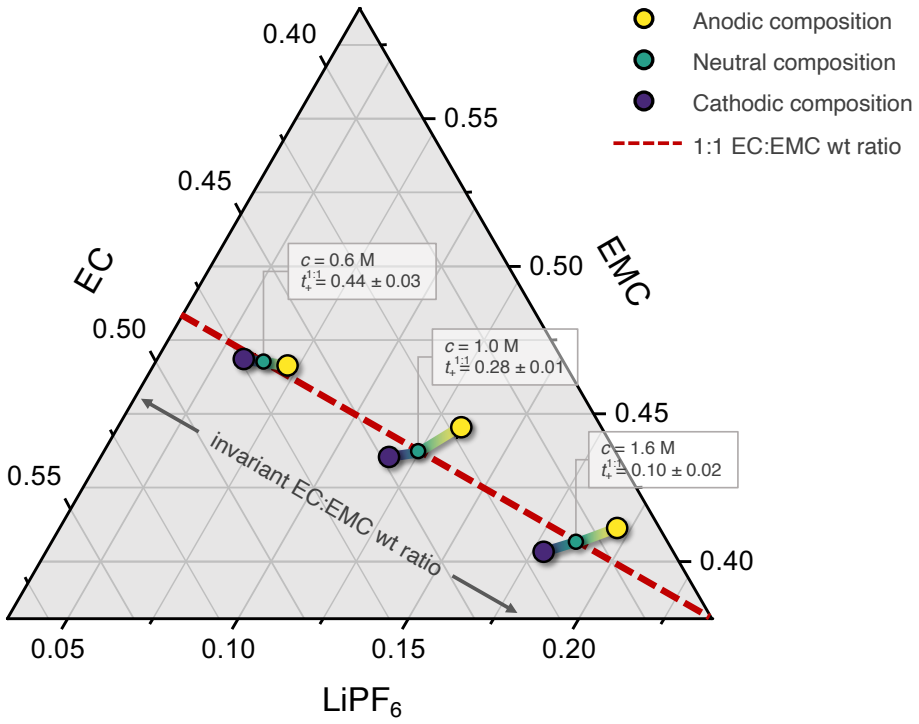


Figure 4.2: Comparison of Hittorf polarizations with predictions of the single-solvent approximation.
Ternary diagram showing anodic-chamber (yellow), neutral-chamber (green), and cathodic-chamber (blue) mass fractions of EC, EMC, and $LiPF_6$ after Hittorf experiments for three salt molarities (0.6, 1.0, 1.6 M) in a 1:1 (by mass) EC:EMC solvent. The marker size encompasses error, accounting both for experimental repeats and variance in the GP prediction, as discussed in section 4.B.2. The red-dashed line indicates an invariant EC:EMC ratio. Since the dumbbell markers for each Hittorf result are not parallel to this line, the single-solvent approximation is not upheld.

salt concentration, the final EC:EMC ratios were 0.96:1 and 1.03:1 in the anodic and cathodic Hittorf chambers, respectively, resulting in an EC mass-fraction difference of 5.1% across the cell. (It should be emphasized that this is the concentration difference that remains after the concentration profiles in surface boundary layers are averaged across the entire chambers of the Hittorf cell.) Full experimental data are provided in the Data Repository associated with this article [227].

Notably, the EMC composition ratio was observed to increase in the anodic chamber, indicating a propensity for EMC, rather than EC, to move with $LiPF_6$. This contrasts the results of equilibrium solvation studies, which generally conclude that EC is more tightly bound to the $LiPF_6$ salt [57]. The counterintuitive result

that EC moves against the salt gradient suggests that a dynamical drag interaction — independent of the classically expected solvation interaction based on the dielectric constant of the solvent species — may be inducing solvent segregation under applied current. This observation can also be considered in light of the coordination numbers reported for cyclic and linear carbonates [122, 194, 215]. By assuming a solvated mobile cation with the structure $[Li(EC)_3(EMC)]^+$, and with the uncoordinated EC and EMC treated with a single-solvent approximation, one would expect that Hittorf polarization of 1 M $LiPF_6$ in a 1:1 mass ratio of EC:EMC (6.2 M of EC and 5.3 M of EMC) would result in final EC:EMC ratios of 1.04:1 and 0.98:1 in the anodic and cathodic Hittorf chambers, respectively — almost exactly opposed to the result reported here.

We expect the solvent-segregation effect quantified here to impact transport-property characterization for practical lithium electrolytes. Effective cation transference numbers $t_+^{1:1}$ were determined using the Li^+ composition changes estimated by GP regression, under an assumption that the cosolvent retains the partial molar volume of neat 1:1 EC:EMC as it is polarized. (Details are provided in section 4.B.5.) The $t_+^{1:1}$ value was found to decrease from 0.44 to 0.10 as the salt concentration rose from 0.6 M to 1.6 M, following a trend consistent with results from similar studies of $LiPF_6$ electrolytes in solvent mixtures made up of cyclic and linear carbonates [78, 83]. If galvanostatic and potentiostatic methods induce salt polarization along with a cosolvent-ratio gradient, the degree of cosolvent segregation will vary with experimental conditions and may be a factor contributing to the wide spread of reported transport-property measurements in the literature, such as those discussed by Bergstrom and coworkers [128]. Extending potentiometric MRI studies to capture dynamic solvent profiles would provide a path to parameterize these electrolyte systems more rigorously within the concentrated-solution theory framework [96].

4.2.3 Amplification of polarization at boundaries

Hittorf-cell results only reveal a volume-averaged change in electrolyte composition after polarization. It is expected that current-induced polarization of both salt

concentration and solvent ratio should be focused within boundary layers near the electrolytes' interfaces, as shown schematically in Figure 4.1A. The transient degree of local solvent segregation may be estimated quantitatively using a four-species multicomponent transport model for the $LiPF_6$:EC:EMC system. Adopting the system of Onsager–Stefan–Maxwell equations presented earlier by Monroe [119], originally derived for metal/oxygen batteries with a binary electrolyte and an additional dissolved neutral species, the cation flux $\vec{N}_+$ and EC flux $\vec{N}_\mathrm{o}$ can be expressed as

$$\vec{N}_+ = -D_\mathrm{e}\vec{\nabla}c - D_\times \left\langle \frac{c}{c_\mathrm{T}} \right\rangle \vec{\nabla}c_\mathrm{o} + \frac{t_+^0}{F}\vec{i}, \tag{4.1}$$

$$\vec{N}_\mathrm{o} = -D_\times \left\langle \frac{c_\mathrm{o}}{c_\mathrm{T}} \right\rangle \vec{\nabla}c - D_\mathrm{o}\vec{\nabla}c_\mathrm{o} - \Xi\frac{\vec{i}}{F}. \tag{4.2}$$

if convection is neglected. Here F is Faraday's constant; c, c_o, and c_T are the $LiPF_6$, EC, and total solution concentrations, respectively; D_e and D_o are respectively the Fickian diffusion coefficients of salt and EC in EMC; and $D_\times$ is the cross diffusivity, which describes how one solute gradient induces flux of the other solute. The cation transference number t_+^0 and EC electro-osmotic coefficient Ξ describe how Li^+ and EC respectively migrate through EMC in response to an applied current density $\vec{i}$. Material balances and boundary conditions that close these flux laws are detailed in section 4.B.2 of the Supplemental Information. Although equations 4.1 and 4.2 neglect convection, it could be included following the method of Liu and Monroe [89].

Solvent segregation effects can be extreme near interfaces. In a Hittorf measurement of $LiPF_6$:EC:EMC that yields a ±5% swing in the volume-averaged EC:EMC ratio, such as the data points measured in the ternary plot Figure 4.2, the electrode surfaces experience more than ±50% excess EC interfacial content during a current pulse. This result is found by solving a transport problem governed by equations 4.1 and 4.2, which allows one to simulate the degree of solvent polarization near the electrode interfaces that is commensurate with the solution concentrations extracted from the Hittorf-cell chambers. As a first approximation, transport parameters were

assumed to be composition independent. We took $D_e = 3 \times 10^{-10}$ m^{2}s^{-1}, a value measured for the LiPF$_6$:EMC binary [96], and $D_o = 5 \times 10^{-10}$ m^{2}s^{-1}, as observed by pulsed gradient spin echo NMR [122]. The cation transference was set at $t_+^0 = 0.24$, as measured here using the standard Hittorf equation. Like the transference number, the electro-osmotic coefficient Ξ can also be extracted from the Hittorf experiment using the change in EC compositions estimated by the GP model. From the GP inferences of net moles of EC moved to the anodic Hittorf chamber, one finds that $\Xi \approx -1.4 \pm 0.1$. Since a precise value of cross-diffusivity is not known, we assumed that $D_\times = 0$, a value that should provide a lower bound on the change in the interfacial solvent ratio. Figures 4.3A and 4.3B compare the maximum degree of polarization during the 1.0 M Hittorf experiment to the equilibrated results using the above parameters. With higher values of cross diffusivity $D_\times$, the solvent swing at the interfaces would be even more severe.

To inform general expectations about current-induced cosolvent segregation in practical lithium-ion-battery electrode geometries, it is useful to observe composition gradients under an applied limiting current density for the 1.0 M LiPF$_6$ EC:EMC 1:1 mass ratio electrolyte. The limiting current density is the largest steady-state current that can be imposed before the charge-carrying salt is completely depleted at the cathode. At the limiting current, gradients of both salt and solvent concentration are sustained across the entire interelectrode gap, as can be seen from the plot of normalized steady-state molarity with respect to dimensionless position across the gap in Figure 4B. Figure 4.4A presents a contour plot expressing the sensitivity of the EC:EMC mass ratio to the cross diffusivity $D_\times$ and EC electro-osmotic coefficient Ξ. The range studied for $D_\times$ represents the bounds based on thermodynamic stability that $0 \leq D_\times < \frac{D_e \langle c_T \rangle}{2\langle c \rangle}$ [119]. Each coloured band represents the possible change — both increase and decrease — in the EC:EMC mass ratio on either boundary of the electrolyte. For example, the 0.45 contour represents the set of parameters that could segregate an initial 1:1 EC:EMC bulk solution to a 1.45:1 and 1:1.45 ratio at the cathode and anode, respectively.

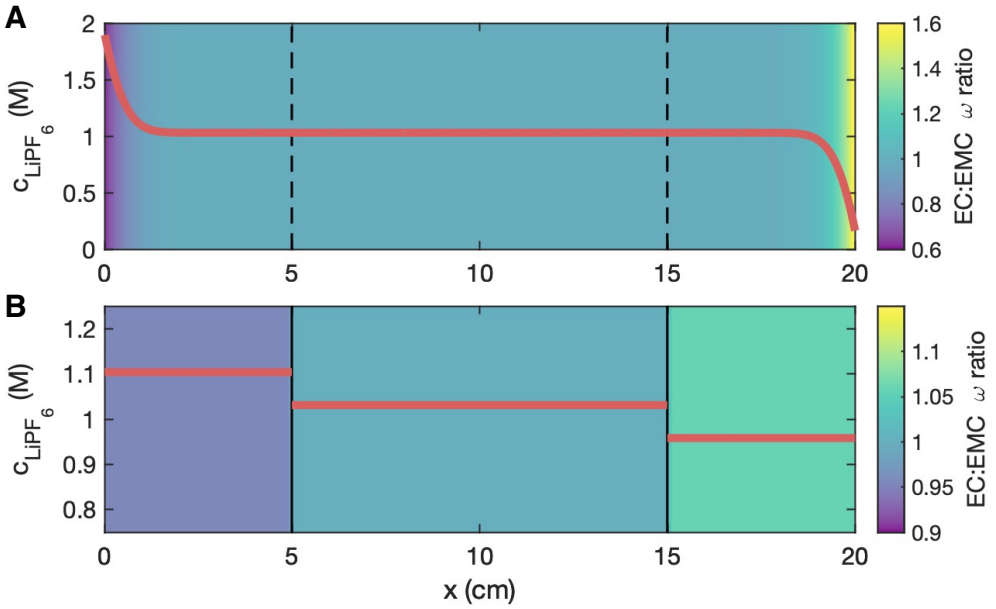


Figure 4.3: Dynamic Hittorf salt and solvent compositions predicted by four-component transport model.
(A) Simulated maximum degree of polarization of the 1 M $LiPF_6$ in 1:1 mass-ratio EC:EMC electrolyte before current cutoff during a Hittorf experiment. Salt concentration is shown with red curves, while solvent ratio is represented by the background colormap. Based on parameter estimates, model simulations show that the majority of solvent segregation occurs in boundary layers very close to the electrode surfaces.
(B) Electrolyte compositions after both Hittorf valves (locations shown by solid vertical lines) are sealed off and the salt and solvent gradients in (A) are allowed to come to equilibrium in each chamber. It is these final compositions that are inferred from property measurements using the GP regression model.

Cosolvent composition variation also alters the electrochemical properties of the electrolyte with respect to its position between the electrodes. For example, (de)solvation energies and kinetics of electrochemical reactions are impacted by the solvation environment of Li^+. Similarly, the electrolyte composition immediately adjacent to the electrode surface will directly alter the nature of SEI formation reactions and SEI composition itself. Continuum-level modelling has shown that electrolyte transport and thermodynamic properties that vary as functions of both salt molarity and temperature are necessary to predict battery behaviour during operational extremes [78]. The results reported here suggest that such higher-fidelity

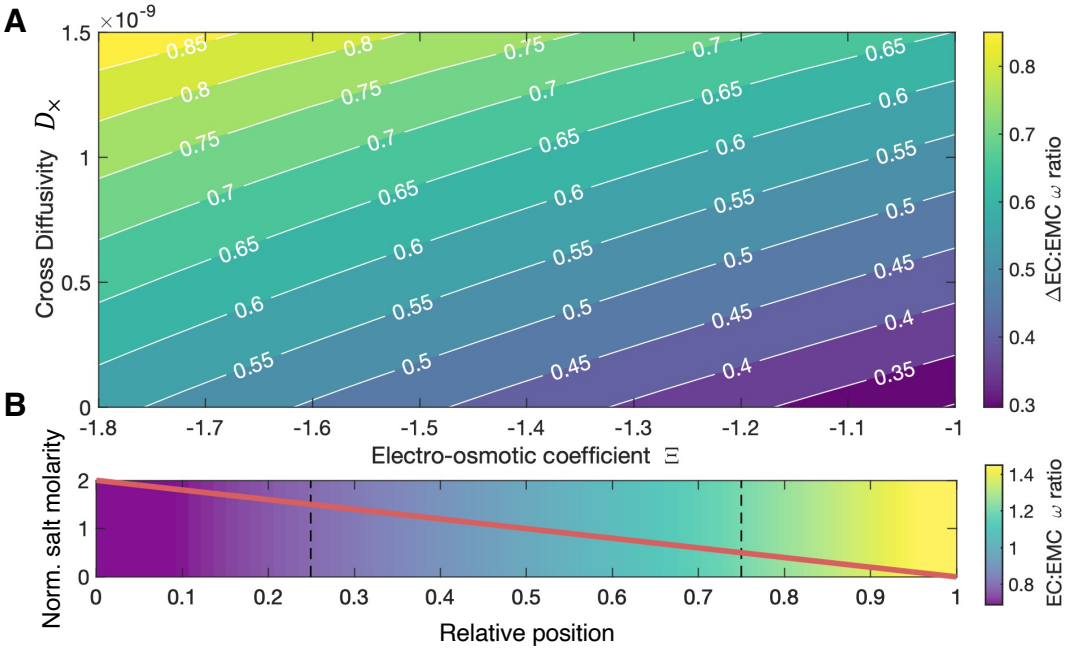


Figure 4.4: Generalized degree of solvent-segregation under steady limiting-current conditions.
(A) Sensitivity sweep of the absolute change in interfacial EC:EMC mass ratio as a function of the cross diffusivity and electro-osmotic coefficient (two transport properties unique to the four-component electrolyte model) for an electrolyte polarized under limiting-current conditions. For example, the 0.45 ΔEC:EMC contour refers to an average polarized electrode boundary EC:EMC solvent ratio of 1.45:1 and 1:1.45 from the initial neutral composition of 1:1 mass-ratio EC:EMC with 1 M $LiPF_6$.
(B) Limiting current salt and solvent-ratio profile for the same initial solvent ratio, with a normalized salt composition and inter-electrode distance.

simulations may need to be broadened to include changes in solvent ratios as well. Significantly, in the case of the anodic interface in Figure 4.4B, the predicted viscosity varies by 22%, based on whether cosolvent segregation is accounted for or not.

4.3 Conclusion

It has been demonstrated that, contrary to the conventional assumption, cosolvents in lithium-ion electrolytes do not move together in fixed proportion when facilitating charge transport. The reported test of the single-solvent approximation relied on a combination of Hittorf experiments and a Gaussian process regression model, trained with a database of physicochemical electrolyte properties, which was used

to infer composition from property measurements. A four-species multicomponent transport simulation was then used to estimate the degree of cosolvent polarization at interfaces. This solvent-segregation phenomenon could be studied with finer spatial resolution using in-situ techniques such as potentiometric MRI or chemical shift imaging. Spatiotemporal measurements of specific solvents under dynamic cycling will enable further understanding of counterintuitive observations such as why EMC, rather than EC, migrates preferentially alongside Li^+. The results emphasize that solvent compositions in batteries not only vary gradually over cycle life, due to decomposition-reaction consumption, but can also experience local intra-cycle variation, induced by current flow. The balance between the two should be studied in practical cell geometries. Cosolvent segregation is expected to occur any situation where Faradaic electrode reactions (intercalation or conversion/plating) induces salt gradients. Our findings suggest that future experiments to track solvent concentrations would enable the parametrization of advanced physics-based models that include local interfacial EC content, which could elucidate more accurate kinetic models of interfacial reactions such as Li intercalation, plating, and SEI formation. Key physical insights in this work show that macroscopic states should also be considered alongside microscopic solvation environments when determining electrolyte behaviour. The same framework for the commonly used $LiPF_6$:EC:EMC electrolyte can also be applied to novel formulations and solution additives to aid the simulation, design, and discovery of higher-performing next-generation batteries.

4.A Experimental procedures

4.A.1 Electrolyte formulation & physicochemical property measurements

Density, viscosity, and conductivity measurements were performed, both on a set of standard solutions used to calibrate the property-composition GP regression model and on electrolytes extracted from Hittorf polarization cells after they were polarized. Stock solutions were prepared within an argon glovebox (Inert Technologies) with vacuum dried $LiPF_6$ (99.99% battery grade, Sigma Aldrich), and EC (99% Sigma-Aldrich) and EMC (99.9% Sigma-Aldrich) solvents that were stored under 3 Å molecular sieves. Pure EC was first melted by heating in a bottle as received within a jacketed glovebox antechamber at 50 °C overnight. Solutions were formulated based on mass fractions using an analytical balance (OHAUS) with a repeatability standard deviation of ±0.0001 g. Densities and dynamic viscosities were measured inside the glovebox with a high-precision oscillating densitometer with an in-line rolling-ball viscometer attachment (DMA4100, Anton Paar). Ionic conductivities were measured with an AC conductivity probe (Orion A212, Thermo Scientific) in a sealed cell with a temperature-controlled water bath (Arctic A25, ThermoFisher). Measurements were taken at increasing temperatures of 10.00±0.01, 20.00±0.01, 25.00±0.01, 30.00±0.01, and 40.00±0.01 °C.

4.A.2 Hittorf cell experimental procedure

The Hittorf cell (Fig. 4.1A) is a 20 cm long cylindrical symmetric Li-Li polarization cell with an electrolyte cavity diameter of 1 cm. More details about the cell itself are provided by Hou and Monroe [102]. The central cavity has two configurations, 'open' and 'closed'. Two stopcocks can be sealed to separate the cylinder into anodic, neutral, and cathodic chambers (the fluid contained within the closed stopcocks is not characterized). Lithium electrodes on either end of the Hittorf cell were prepared by polishing 0.75 mm thick Li foil (99.9% Alfa Aesar) with a PTFE brush before punching into discs. The lithium discs were placed into the threaded endcaps of the Hittorf cell, which were subsequently screwed shut, leaving a 0.785 cm^2

circular lithium surface exposed to the central cavity. A set screw on the side of the cell sealing an access port was then removed and the empty apparatus was put in the 'open' configuration to allow the electrolyte to be loaded. After electrolyte was added through the access port with a volumetric pipette, the set screw was returned to seal the cell. A ringstand was used to orient the cell vertically. To run Hittorf experiments, a constant current of 0.5 mA (passing within the cell from the bottom electrode to the top) was applied for 20 hours with a potentiostat (PGSTAT302N, Metrohm). The current density was chosen to induce a measurable quantity of cosolvent segregation. Based on the cycled lithium (36 C), the Hittorf-cell has an electrolyte loading of approx. 1900 g/(Ah) which allows for the isolation intracycle polarization effects with minimal overall electrolyte composition change due to any possible degradation reactions. Immediately after the current was interrupted, the cell was set in the 'closed' configuration. After each individual chamber was allowed to equilibrate, the electrolytes were extracted and their physicochemical properties measured. More detailed information including theoretical analysis can be found in the papers of Hou et al [102] and Wang et al [118].

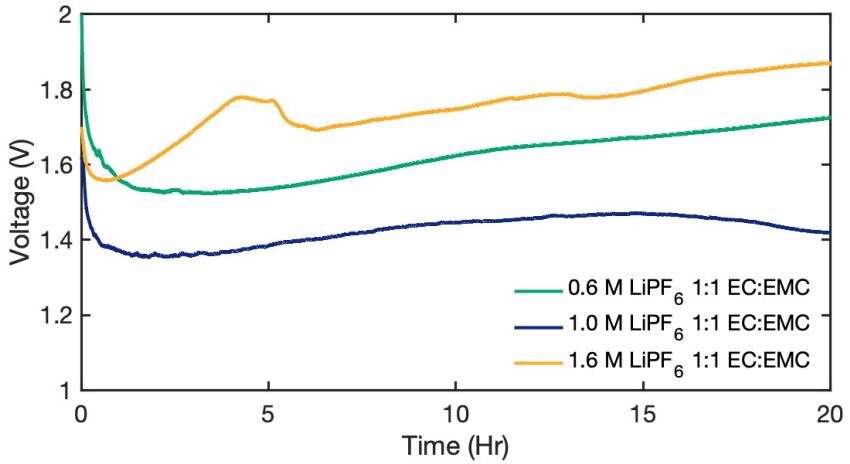


Figure 4.A.1: Representative electrochemical polarization curves recorded during Hittorf cell experiment showing smooth voltage signal during electrodeposition and no Sand's time limit behaviour.

4.A.3 Gaussian process regression

The GP model was implemented in the GPy Python framework [226], with a squared-exponential radial basis function (RBF) kernel and an automatic relevance determination (ARD) structure. The model was trained on input data consisting of solution density, viscosity, and conductivity with a range of compositions, at the temperatures listed in section 4.AA. Each set of 15 input data points (for each of the three properties at the five temperatures) is linked through the GPR model to a single pair of composition outputs, namely the mass fractions of $LiPF_6$ and EMC, with the mass of EC being finally inferred by the fact that the three mass fractions must sum to unity. Cross-validation using the leave-one-out method was performed on the GPR model. The average root-mean-square error for mass fractions was found to be 0.003 ± 0.002, corresponding to an uncertainty of approximately 2.4% and 0.7% for $LiPF_6$ and EMC mass fractions, respectively (Figure 4.B.3). GP model code and training data are accessible in the online Data Repository [227].

4.B Supporting Discussion

4.B.1 Physicochemical training dataset

Full datasets of composition–property training measurements are reported in the Data Repository [227]. Figure 4.B.1 shows graphically how individual properties (temperature, density, viscosity, and conductivity) vary with ternary composition of $LiPF_6$, EC, and EMC.

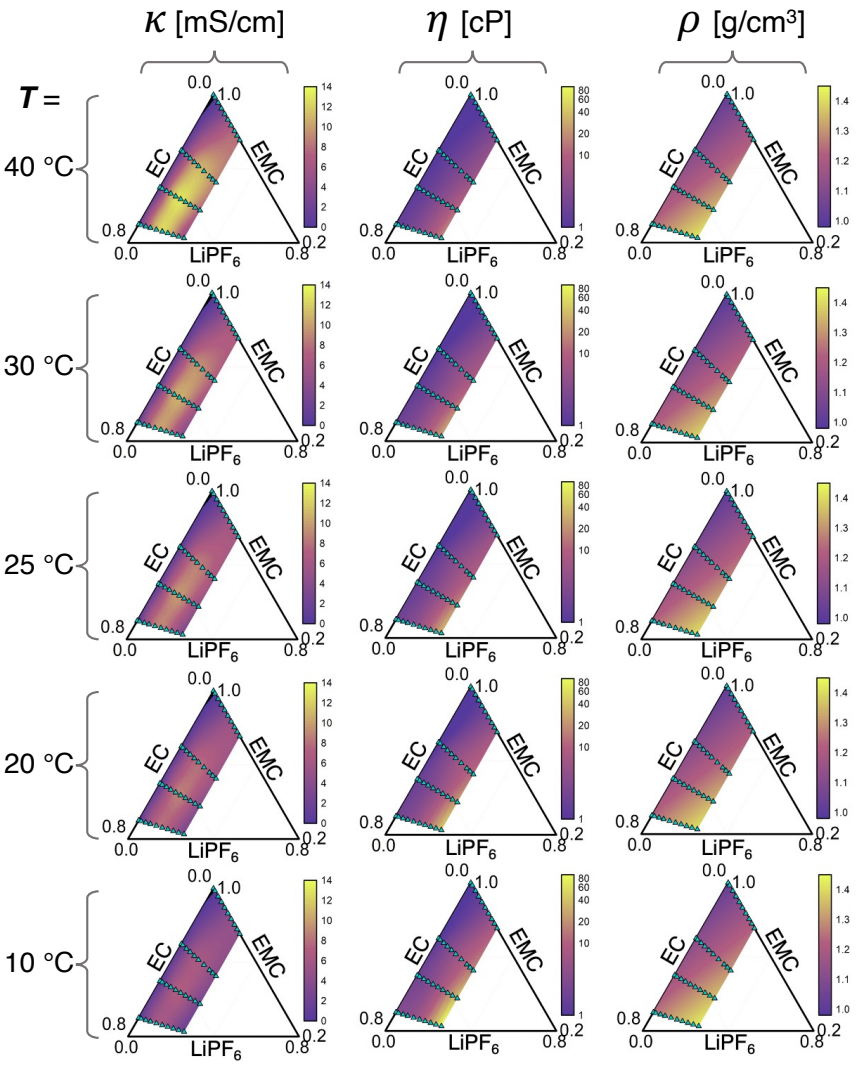


Figure 4.B.1: Physicochemical property variation with respect to the mass fractions of $LiPF_6$, EC, and EMC, as well as the temperature range probed for the training data set. Full data is accessible in the Data Repository that accompanies this article [227].

4.B.2 Cross-validation of the GP regression model

Composition predictions from the leave-one-out cross-validation of the GP regression model are plotted against true composition in Figure 4.B.2. The model uncertainty is indicated by green bands, showing a narrow variance in the region sampled by Hittorf experiments.

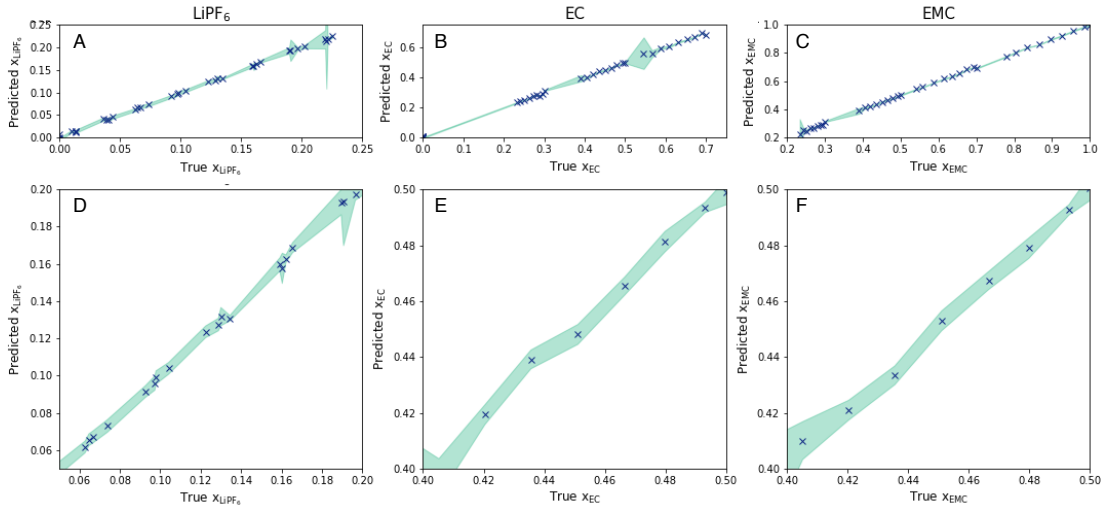


Figure 4.B.2: Comparison between the predicted compositions and true compositions (blue x) output by the GPR model for the leave-one-out cross-validation test. GPR uncertainty is given by the green band about the points. Plots A,B,C show the entire composition range, and plots D,E,F zoomed regions probed for the Hittorf polarization experiments.

The root mean square error (RMSE) from cross validation for the $LiPF_6$ and EMC fractions is reported in Figure 4.B.3.

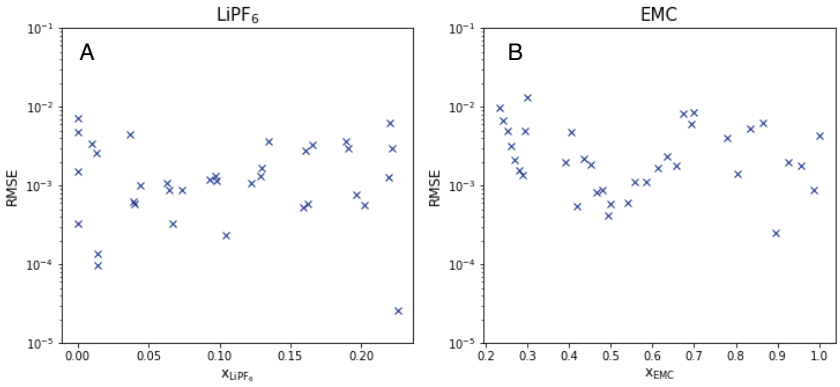


Figure 4.B.3: Root mean square error for (A) $LiPF_6$ and (B) EMC compositions from leave-one-out cross validation of the GP regression model.

4.B.3 Visualizing the GP regression-model fit

The uncertainty between inputs and outputs in the GPR model can also be determined for composition slices across the training mass-fraction range. For example, the variance in properties can be better understood for EC:EMC ratios closer to the degree of cosolvent segregation observed in this study. Figure 4.B.4 presents a composition slice with a fixed EC:EMC ratio of 5:6; Figure 4.B.5 reports the uncertainties associated with solution density, viscosity, and conductivity along this slice across temperatures of 10, 20, 25, 30, and 40 °C.

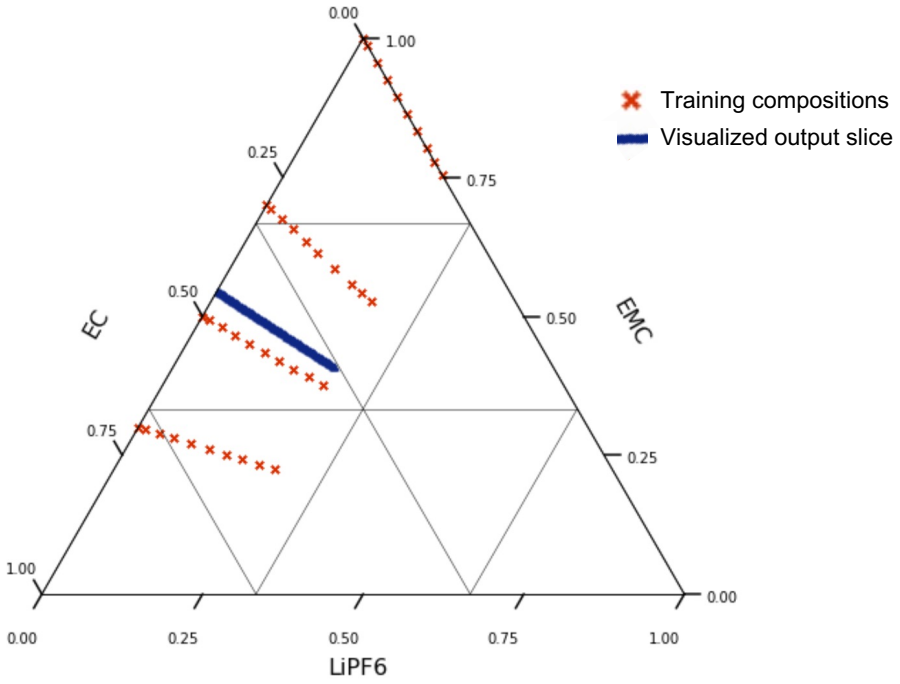


Figure 4.B.4: Ternary diagram depicting the composition slice (blue —) used to visualise GPR input-output uncertainties, relative to the training compositions (red x).

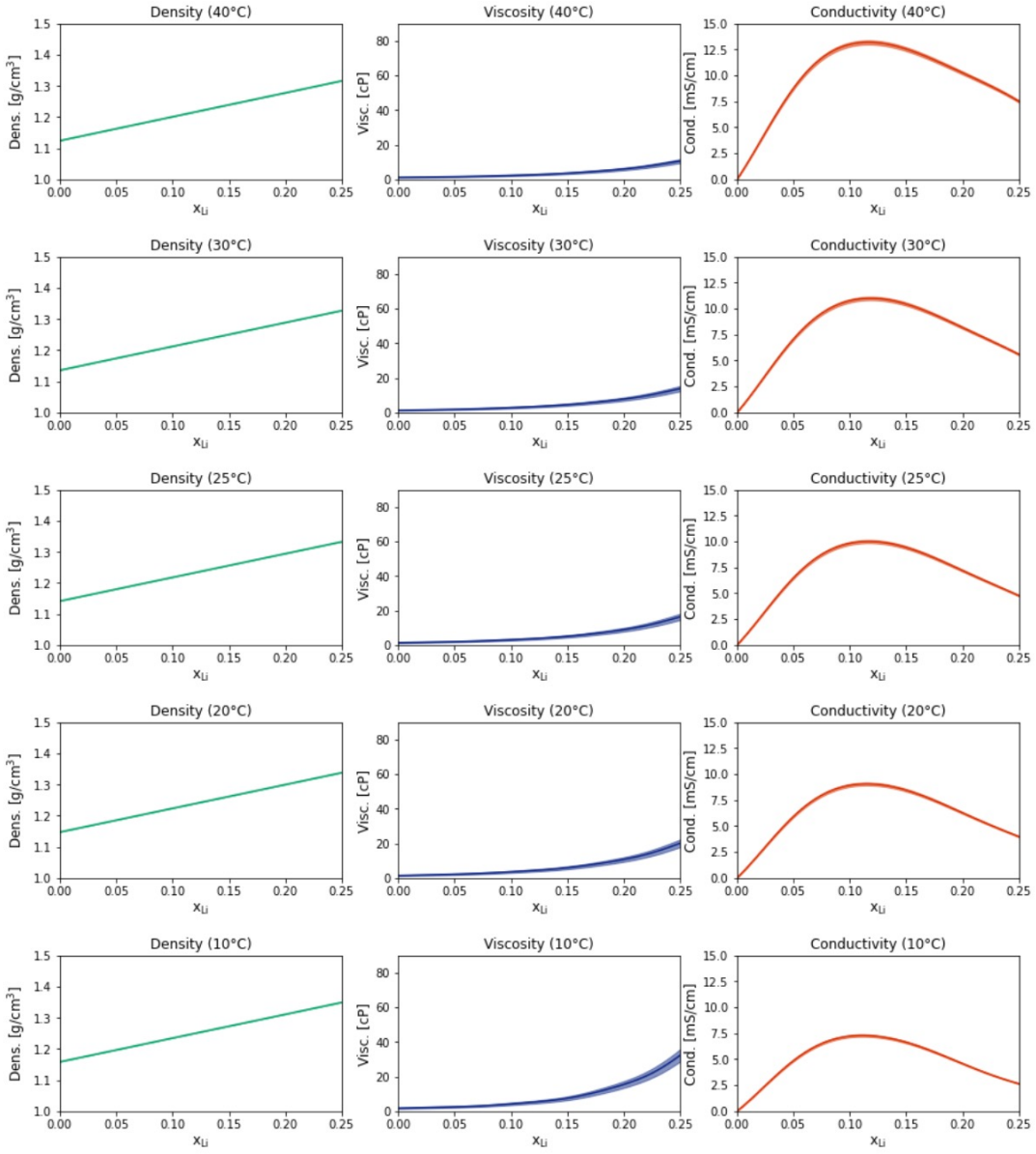


Figure 4.B.5: Predicted values (—) and uncertainties (shaded) in the physicochemical properties with respect to the temperature range probed for the training data set for mass fractions of $LiPF_6$ in the GPR slice plotted in Figure 4.B.4.

4.B.4 Multicomponent transport model

The ternary $LiPF_6$:EC:EMC electrolyte studied here comprises four constituent species: anions, cations, and the two solvents EC and EMC. Under a local electroneutrality approximation, the general description of isothermal mass transport in this system requires two independent expressions for the fluxes of the lithium-

cation and EC species. A suitable set of governing equations is provided by the framework first derived by Monroe for metal/oxygen batteries with a binary electrolyte and an additional dissolved species,[119] summarized below:

Constitutive laws and balances:

$$\vec{N}_+ = -D_\mathrm{e}\vec{\nabla}c - D_\times \left\langle \frac{c}{c_\mathrm{T}} \right\rangle \vec{\nabla}c_\mathrm{o} + \frac{t_+^0}{F}\vec{i} \tag{4.B.1}$$

$$\vec{N}_\mathrm{o} = -D_\times \left\langle \frac{c_\mathrm{o}}{c_\mathrm{T}} \right\rangle \vec{\nabla}c - D_\mathrm{o}\vec{\nabla}c_\mathrm{o} - \Xi\frac{\vec{i}}{F} \tag{4.B.2}$$

$$\frac{\partial c_+}{\partial t} = -\vec{\nabla}\cdot\vec{N}_+ = D_\mathrm{e}\frac{\partial^2 c}{\partial x^2} + D_\times \left\langle \frac{c}{c_\mathrm{T}} \right\rangle \frac{\partial^2 c_\mathrm{o}}{\partial x^2} \tag{4.B.3}$$

$$\frac{\partial c_\mathrm{o}}{\partial t} = -\vec{\nabla}\cdot\vec{N}_\mathrm{o} = D_\times \left\langle \frac{c_\mathrm{o}}{c_\mathrm{T}} \right\rangle \frac{\partial^2 c}{\partial x^2} + D_\mathrm{o}\frac{\partial^2 c_\mathrm{o}}{\partial x^2} \tag{4.B.4}$$

Boundary conditions:

$$\vec{N}_+(t,0) = \frac{\vec{i}}{F} \tag{4.B.5}$$

$$\vec{N}_\mathrm{o}(t,0) = 0 \tag{4.B.6}$$

Initial conditions:

$$c_+(0,x) = \langle c_+ \rangle \tag{4.B.7}$$

$$c_\mathrm{o}(0,x) = \langle c_\mathrm{o} \rangle \tag{4.B.8}$$

Here c, c_o, and c_T represent the $LiPF_6$, EC, and total species concentrations, D_e and D_o are the Fickian diffusion coefficients for salt and EC (e.g., diffusivities

relative to EMC under concentration-gradient driving forces), and $D_\times$ is the Fickian cross diffusivity, which describes how one solute-concentration gradient induces flux of the other solute. The cation transference number t_+^0 and EC electro-osmotic coefficient Ξ describe how Li^+ and EC respectively migrate under an applied current density $\vec{i}$. The brackets $\langle\rangle$ represent the equilibrium value associated with the bracketed quantity. Finally, F is Faraday's constant.

This system of equations was solved with the PDEPE function in MATLAB. The parameters were taken to be composition independent, with values outlined in the table below:

Table 4.B.1: Four species transport model parameters.

Parameter	Value	Reference
D_e	$3 \times 10^{-10}\ \mathrm{m^2 s^{-1}}$	[96]
D_o	$5 \times 10^{-10}\ \mathrm{m^2 s^{-1}}$	[122]
t_+^0	0.28	this work
Ξ	-1.4 ± 0.1	this work
$D_\times$	$0 — 1.5 \times 10^{-9}\ \mathrm{m^2 s^{-1}}$	[119]

4.B.5 Hittorf transference number calculation

The cation transference number is calculated from the change in moles Δn of lithium moved relative to the initial bulk concentration $\langle c\rangle$, given by the density ρ and mass fraction change, and charge passed ($Q = 36$ C) during the experiment. Assuming that the mass-average velocity of the mixed solvent can be taken as the reference velocity, one has that

$$t_+^{1:1} = \frac{\Delta n F}{Q\left(1 - \langle c\rangle \overline{V}_\mathrm{e}\right)} \tag{4.B.9}$$

In the calculation here, we take the partial molar volume $\overline{V}_\mathrm{e}$ from a linear fit of density vs. molarity (i.e. salt mass fraction times solution density divided by

salt molar mass) for the initial 1:1 EC:EMC mass fraction electrolyte, a process that yields $\overline{V}_{\mathrm{e}}$=0.059 L/mol.

Statement of Authorship for joint/multi-authored papers for PGR thesis

To appear at the end of each thesis chapter submitted as an article/paper

The statement shall describe the candidate's and co-authors' independent research contributions in the thesis publications. For each publication there should exist a complete statement that is to be filled out and signed by the candidate and supervisor **(only required where there isn't already a statement of contribution within the paper itself).**

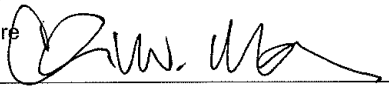
Title of Paper	Current-driven solvent segregation in lithium-ion electrolytes
Publication Status	Submitted for publication
Publication Details	Wang, A. A.; Greenbank, Samuel; Li, Guanchen; Howey, D. A.; Monroe, C. W. Current-driven solvent segregation in lithium-ion electrolytes, **2022.**

Student Confirmation

Student Name:	Andrew A. Wang		
Contribution to the Paper	Conceptualization, Methodology, Investigation, Formal Analysis, Writing		
Signature		Date	04/07/2022

Supervisor Confirmation

By signing the Statement of Authorship, you are certifying that the candidate made a substantial contribution to the publication, and that the description described above is accurate.

Supervisor name and title: Charles W. Monroe (Associate Professor)		
Supervisor comments Andrew is first author.		
Signature 	Date	5 Jul, 2022

This completed form should be included in the thesis, at the end of the relevant chapter.

[H]

5
Conclusion

This thesis aimed to further the practical understanding of mass-transport processes in multicomponent lithium-ion electrolytes. A combined theoretical and experimental approach was taken, with the goal of developing quantitatively accurate descriptions of electrolyte responses immediately applicable to the optimisation of electrochemical cell configurations and operating conditions. Continuum-level electrolytic insights serve here as the pivotal connection between microscopic interactions and device-level behaviour required to push the frontiers of battery technology.

First, an assessment of how an electrolyte's transport and thermodynamic characteristics affect battery performance was performed to motivate the work. We reflected on the interplay between the values of transport properties and the model formulations used to measure them. In Chapter 2 we extended the efficacy of the concentration-cell measurement technique to encompass wider composition ranges. This procedure, which partially underpinned a set of experiments used to measure a full set of transport and thermodynamic properties for two canonical binary electrolytes ($LiPF_6$:PC and $LiPF_6$:EMC), showed that $LiPF_6$:EMC exhibits significant species association at high dilution, whereas $LiPF_6$:PC matches the behaviour expected of a typical strong electrolyte. Further on in Chapter 3, the electrochemical parameterisation toolkit developed in Chapter 2, along with

spectroscopic techniques and magnetic resonance imaging, was used to probe super-concentrated binary electrolytes. An important question answered by this work was that an ostensibly 'complete' transport model based on concentrated solution theory indeed has microscopic predictive capabilities; composition-dependent parameters quantified by the methods described in Chapter 2 accurately reflect the microscopic spatiotemporal distributions of species, as well as cell potentials. Chapter 4 then elucidated a previously unaccounted transport phenomenon in cosolvent Li-ion electrolytes (the currently dominant practical formulation for Li-ion batteries): segregation of the two solvent species under applied current. This observation extends the design space for battery electrolytes.

From an engineer's standpoint, the outcomes of this dissertation research argue for macroscopically observable electrolyte transport effects to be viewed as having merit equal to circumstantial interpretations of microscopic mechanisms. The literature has overwhelmingly focused on revisiting the mystery of interphases. Yet fundamental questions such as: *"what is the salt and solvent molarity at the electrode surface during cycling?"* or *"what is the voltage drop across the solution phase?"* can, to date, only be answered by studying macroscopic bulk properties. Remarkably, we showed in Chapter 3 that a complete understanding of bulk-solution behaviour enabled the deconvolution of electrode-surface effects too. Our community of researchers concerned with transport characterisation will also gain from directly interrogating composition distributions and associated overpotentials, rather than properties such as diffusivities and transference numbers that act as proxies to said phenomena. Fluidity in model frameworks has made it increasingly difficult to benchmark electrolytes based on reported properties. With the rate of advancement in this field, the only path forward is to embrace the sharing of model-independent raw experimental results. This allows one to revisit and reprocess with alternate transport theories. Several initiatives such as the Battery Archive, the Battery Data Genome, and this author's own LiionDB are pioneering in this aspect [1, 228, 229].

Accentuating the electrolyte response has been a guiding principle in attentive experimental design. In-situ spectroscopic techniques have progressed such that they can now provide detailed insight into the internal states in electrolytes during dynamic polarisation [96, 105, 181–183, 186, 218]. The work presented here demonstrated that relaxations can also be studied to isolate individual properties too. It is always important for spectroscopic imaging to be paired with electrochemical data, so that concentration gradients can be connected to thermodynamic overpotentials. Oftentimes we rely only on purely electrochemical measurements to infer the composition and potential distribution across a bulk electrolyte. Practitioners should be aware that current and voltage signals can easily be convoluted by interfacial effects [128]. Several avenues exist to mitigate this. Experiments, when possible, should run galvanostatically, because a constant current fixes the Li^+ flux at system boundaries [102, 230]. Cell geometries can also employ a larger inter-electrode separation to extend diffusion signals [92, 143]. This also reduces path-length uncertainty from mossy electrodeposition on malleable metallic electrodes such as lithium. Finally, low current densities should be used to minimise interference from buoyancy effects [98, 183].

Limitations also arise from the macroscopic approach taken in this work. The methods here let one determine *when* an electrolyte exhibits superior capacity for charge transport, but not necessarily *how* one would tune molecular designs to improve individual transport properties. This is an open question for electrolyte development. For example, rational atomistic strategies intended to raise transference via anion immobilisation in fact lead to much lower values than predicted [112]. Even when transference numbers are elevated, decreases in conductivity may nullify transport-related performance gains [142]. Remembering the OSM transport theory, all of an electrolyte's constituent species exert friction on each other, and affect macroscopic properties concomitantly. Nevertheless, this work has identified relevant metrics for benchmarking novel electrolytes. While a wide salt-molarity regime was explored, only a narrow catalog of solvents and salts was explored, and these at fixed temperatures. To this end, there is an immediate

opportunity to broaden transport analyses to more chemistries at a wider range of temperatures. Experimental intricacy remains a crucial obstacle to overcome for thorough transport characterisations.

Looking forward, several nascent directions show tremendous potential to accelerate battery-electrolyte innovation. Automated and scalable high-throughput experimentation can rapidly assess transport properties and other characteristics. Applying data-driven optimisation methods can also help pinpoint performance maxima across an expansive chemical space [224, 231–234]. By regressing over large volumes of data, these methods have been able to illuminate fundamental physical mechanisms underpinning ionic transport too [235]. Present studies should incorporate standardised procedures for transport properties beyond conductivity. Computational simulations are an attractive way to translate molecular-structural information into continuum-scale transport repercussions [123, 236]. Quantum-chemical models for OSM binary diffusion coefficients could then be used to screen candidate electrolyte blends in silico [237]. Given that any chemistry must satisfy many requirements simultaneously, directly testing electrolytes in full cells may compress development cycles. Combining this pragmatic approach with machine-learning tools can stretch empirical observations into generalisable insights [238, 239]. Undoubtedly, advancements in the field of battery electrolytes will be guided by both faster capabilities and more accurate descriptions of mass transport.

References

[1] Andrew Wang, Simon O'Kane, Ferran Brosa Planella, James Le Houx, Kieran O'Regan, Maxim Zyskin, Jacqueline Sophie Edge, Charles Monroe, Samuel Cooper, David A Howey, Emma Kendrick, and Jamie Michael Foster. "Review of parameterisation and a novel database (LiionDB) for continuum Li-ion battery models". In: *Progress in Energy* (Apr. 2022). DOI: 10.1088/2516-1083/ac692c. URL: https://doi.org/10.1088/2516-1083/ac692c.

[2] Shuang Gu, Bingjun Xu, and Yushan Yan. "Electrochemical Energy Engineering: A New Frontier of Chemical Engineering Innovation". In: *Annual Review of Chemical and Biomolecular Engineering* 5.1 (June 2014), pp. 429–454. DOI: 10.1146/annurev-chembioeng-060713-040114. URL: https://doi.org/10.1146/annurev-chembioeng-060713-040114.

[3] Zachary J. Schiffer, Aditya M. Limaye, and Karthish Manthiram. "Thermodynamic Discrimination between Energy Sources for Chemical Reactions". In: *Joule* 5.1 (Jan. 2021), pp. 135–148. DOI: 10.1016/j.joule.2020.12.014. URL: https://doi.org/10.1016/j.joule.2020.12.014.

[4] John B. Goodenough and Youngsik Kim. "Challenges for Rechargeable Li Batteries". In: *Chemistry of Materials* 22.3 (Aug. 2009), pp. 587–603. DOI: 10.1021/cm901452z. URL: https://doi.org/10.1021/cm901452z.

[5] M. Stanley Whittingham. "Special Editorial Perspective: Beyond Li-Ion Battery Chemistry". In: *Chemical Reviews* 120.14 (July 2020), pp. 6328–6330. DOI: 10.1021/acs.chemrev.0c00438. URL: https://doi.org/10.1021/acs.chemrev.0c00438.

[6] Thomas F Fuller and John N Harb. *Electrochemical Engineering*. en. Nashville, TN: John Wiley & Sons, June 2018.

[7] Derek Pletcher and Frank C. Walsh. *Industrial Electrochemistry*. Springer Netherlands, 1993. DOI: 10.1007/978-94-011-2154-5. URL: https://doi.org/10.1007/978-94-011-2154-5.

[8] Kang Xu. "Nonaqueous Liquid Electrolytes for Lithium-Based Rechargeable Batteries". In: *Chemical Reviews* 104.10 (Sept. 2004), pp. 4303–4418. DOI: 10.1021/cr030203g. URL: https://doi.org/10.1021/cr030203g.

[9] Kang Xu. "Electrolytes and Interphases in Li-Ion Batteries and Beyond". In: *Chemical Reviews* 114.23 (Oct. 2014), pp. 11503–11618. DOI: 10.1021/cr500003w. URL: https://doi.org/10.1021/cr500003w.

[10] Jessie E. Harlow, Xiaowei Ma, Jing Li, Eric Logan, Yulong Liu, Ning Zhang, Lin Ma, Stephen L. Glazier, Marc M. E. Cormier, Matthew Genovese, Samuel Buteau, Andrew Cameron, Jamie E. Stark, and J. R. Dahn. "A Wide Range of Testing Results on an Excellent Lithium-Ion Cell Chemistry to be used as Benchmarks for New Battery Technologies". In: *Journal of The Electrochemical Society* 166.13 (2019), A3031–A3044. DOI: 10.1149/2.0981913jes. URL: https://doi.org/10.1149/2.0981913jes.

[11] Y. Shirley Meng. "Introduction: Beyond Li-Ion Battery Chemistry". In: *Chemical Reviews* 120.14 (July 2020), pp. 6327–6327. DOI: 10.1021/acs.chemrev.0c00412. URL: https://doi.org/10.1021/acs.chemrev.0c00412.

[12] Cyrus Wadia, Paul Albertus, and Venkat Srinivasan. "Resource constraints on the battery energy storage potential for grid and transportation applications". In: *Journal of Power Sources* 196.3 (Feb. 2011), pp. 1593–1598. DOI: 10.1016/j.jpowsour.2010.08.056. URL: https://doi.org/10.1016/j.jpowsour.2010.08.056.

[13] E.R. Logan and J.R. Dahn. "Electrolyte Design for Fast-Charging Li-Ion Batteries". In: *Trends in Chemistry* 2.4 (Apr. 2020), pp. 354–366. DOI: 10.1016/j.trechm.2020.01.011. URL: https://doi.org/10.1016%2Fj.trechm.2020.01.011.

[14] Shashank Sripad and Venkatasubramanian Viswanathan. "The promise of energy-efficient battery-powered urban aircraft". In: *Proceedings of the National Academy of Sciences* 118.45 (Nov. 2021). DOI: 10.1073/pnas.2111164118. URL: https://doi.org/10.1073/pnas.2111164118.

[15] Amruth Bhargav, Jiarui He, Abhay Gupta, and Arumugam Manthiram. "Lithium-Sulfur Batteries: Attaining the Critical Metrics". In: *Joule* 4.2 (Feb. 2020), pp. 285–291. DOI: 10.1016/j.joule.2020.01.001. URL: https://doi.org/10.1016/j.joule.2020.01.001.

[16] Jake Christensen, Paul Albertus, Roel S. Sanchez-Carrera, Timm Lohmann, Boris Kozinsky, Ralf Liedtke, Jasim Ahmed, and Aleksandar Kojic. "A Critical Review of Li/Air Batteries". In: *Journal of The Electrochemical Society* 159.2 (2011), R1–R30. DOI: 10.1149/2.086202jes. URL: https://doi.org/10.1149/2.086202jes.

[17] Hansen Wang, Zhiao Yu, Xian Kong, Sang Cheol Kim, David T. Boyle, Jian Qin, Zhenan Bao, and Yi Cui. "Liquid electrolyte: The nexus of practical lithium metal batteries". In: *Joule* 6.3 (Mar. 2022), pp. 588–616. DOI: 10.1016/j.joule.2021.12.018. URL: https://doi.org/10.1016/j.joule.2021.12.018.

[18] Paul Albertus et al. "Challenges for and Pathways toward Li-Metal-Based All-Solid-State Batteries". In: *ACS Energy Letters* (Mar. 2021), pp. 1399–1404. DOI: 10.1021/acsenergylett.1c00445. URL: https://doi.org/10.1021/acsenergylett.1c00445.

[19] Heather Au, Maria Crespo-Ribadeneyra, and Maria-Magdalena Titirici. "Beyond Li-ion batteries: performance, materials diversification, and sustainability". In: *One Earth* 5.3 (Mar. 2022), pp. 207–211. DOI: 10.1016/j.oneear.2022.02.014. URL: https://doi.org/10.1016/j.oneear.2022.02.014.

[20] Oleg Borodin, Julian Self, Kristin A. Persson, Chunsheng Wang, and Kang Xu. "Uncharted Waters: Super-Concentrated Electrolytes". In: *Joule* 4.1 (Jan. 2020), pp. 69–100. DOI: 10.1016/j.joule.2019.12.007. URL: https://doi.org/10.1016%2Fj.joule.2019.12.007.

[21] Yuki Yamada, Jianhui Wang, Seongjae Ko, Eriko Watanabe, and Atsuo Yamada. "Advances and issues in developing salt-concentrated battery electrolytes". In: *Nature Energy* 4.4 (Mar. 2019), pp. 269–280. DOI: 10.1038/s41560-019-0336-z. URL: https://doi.org/10.1038/s41560-019-0336-z.

[22] Liumin Suo, Oleg Borodin, Tao Gao, Marco Olguin, Janet Ho, Xiulin Fan, Chao Luo, Chunsheng Wang, and Kang Xu. ""Water-in-salt" electrolyte enables high-voltage aqueous lithium-ion chemistries". In: *Science* 350.6263 (Nov. 2015), pp. 938–943. DOI: 10.1126/science.aab1595. URL: https://doi.org/10.1126/science.aab1595.

[23] Xia Cao, Hao Jia, Wu Xu, and Ji-Guang Zhang. "Review—Localized High-Concentration Electrolytes for Lithium Batteries". In: *Journal of The Electrochemical Society* 168.1 (Jan. 2021), p. 010522. DOI: 10.1149/1945-7111/abd60e. URL: https://doi.org/10.1149/1945-7111/abd60e.

[24] Douglas R. MacFarlane, Naoki Tachikawa, Maria Forsyth, Jennifer M. Pringle, Patrick C. Howlett, Gloria D. Elliott, James H. Davis, Masayoshi Watanabe, Patrice Simon, and C. Austen Angell. "Energy applications of ionic liquids". In: *Energy Environ. Sci.* 7.1 (2014), pp. 232–250. DOI: 10.1039/c3ee42099j. URL: https://doi.org/10.1039/c3ee42099j.

[25] Yong-Sheng Hu and Yaxiang Lu. "The Mystery of Electrolyte Concentration: From Superhigh to Ultralow". In: *ACS Energy Letters* 5.11 (Nov. 2020), pp. 3633–3636. DOI: 10.1021/acsenergylett.0c02234. URL: https://doi.org/10.1021/acsenergylett.0c02234.

[26] Yangyuchen Yang, Yijie Yin, Daniel M. Davies, Minghao Zhang, Matthew Mayer, Yihui Zhang, Ekaterina S. Sablina, Shen Wang, Jungwoo Z. Lee, Oleg Borodin, Cyrus S. Rustomji, and Y. Shirley Meng. "Liquefied gas electrolytes for wide-temperature lithium metal batteries". In: *Energy &amp Environmental Science* 13.7 (2020), pp. 2209–2219. DOI: 10.1039/d0ee01446j. URL: https://doi.org/10.1039/d0ee01446j.

[27] Rochelle Weber, Matthew Genovese, A. J. Louli, Samuel Hames, Cameron Martin, Ian G. Hill, and J. R. Dahn. "Long cycle life and dendrite-free lithium morphology in anode-free lithium pouch cells enabled by a dual-salt liquid electrolyte". In: *Nature Energy* 4.8 (July 2019), pp. 683–689. DOI: 10.1038/s41560-019-0428-9. URL: https://doi.org/10.1038/s41560-019-0428-9.

[28] Richard May, Yumin Zhang, Steven R Denny, Venkatasubramanian Viswanathan, and Lauren E Marbella. "Leveraging cation identity to engineer solid electrolyte interphases for rechargeable lithium metal anodes". en. In: *Cell Reports Physical Science* 1.11 (Nov. 2020), p. 100239.

[29] Zhenrong Lu, Li Yang, and Yaju Guo. "Thermal behavior and decomposition kinetics of six electrolyte salts by thermal analysis". In: *Journal of Power Sources* 156.2 (June 2006), pp. 555–559. DOI: 10.1016/j.jpowsour.2005.05.085. URL: https://doi.org/10.1016/j.jpowsour.2005.05.085.

[30] Xiaolu Tian, Yikun Yi, Binren Fang, Pu Yang, Te Wang, Pei Liu, Long Qu, Mingtao Li, and Shanqing Zhang. "Design Strategies of Safe Electrolytes for Preventing Thermal Runaway in Lithium Ion Batteries". In: *Chemistry of Materials* 32.23 (Nov. 2020), pp. 9821–9848. DOI: 10.1021/acs.chemmater.0c02428. URL: https://doi.org/10.1021/acs.chemmater.0c02428.

[31] Xuning Feng, Dongsheng Ren, Xiangming He, and Minggao Ouyang. "Mitigating Thermal Runaway of Lithium-Ion Batteries". In: *Joule* 4.4 (Apr. 2020), pp. 743–770. DOI: 10.1016/j.joule.2020.02.010. URL: https://doi.org/10.1016/j.joule.2020.02.010.

[32] Ziqi Zeng, Vijayakumar Murugesan, Kee Sung Han, Xiaoyu Jiang, Yuliang Cao, Lifen Xiao, Xinping Ai, Hanxi Yang, Ji-Guang Zhang, Maria L. Sushko, and Jun Liu. "Non-flammable electrolytes with high salt-to-solvent ratios for Li-ion and Li-metal batteries". In: *Nature Energy* 3.8 (July 2018), pp. 674–681. DOI: 10.1038/s41560-018-0196-y. URL: https://doi.org/10.1038/s41560-018-0196-y.

[33] Makoto Ue, Hiroyuki Tokuda, Tomohiro Kawai, Miwa Yanagidate, and Yumiko Otake. "Thermal Behavior of Ionic Liquid Electrolytes in Lithium-ion Cells". In: *ECS Transactions* 16.35 (May 2009), pp. 173–181. DOI: 10.1149/1.3123138. URL: https://doi.org/10.1149/1.3123138.

[34] Long Chen, Longsheng Cao, Xiao Ji, Singyuk Hou, Qin Li, Ji Chen, Chongyin Yang, Nico Eidson, and Chunsheng Wang. "Enabling safe aqueous lithium ion open batteries by suppressing oxygen reduction reaction". In: *Nature Communications* 11.1 (May 2020). DOI: 10.1038/s41467-020-16460-w. URL: https://doi.org/10.1038/s41467-020-16460-w.

[35] Marita Pigłowska, Beata Kurc, Maciej Galiński, Paweł Fuć, Michalina Kamińska, Natalia Szymlet, and Paweł Daszkiewicz. "Challenges for Safe Electrolytes Applied in Lithium-Ion Cells—A Review". In: *Materials* 14.22 (Nov. 2021), p. 6783. DOI: 10.3390/ma14226783. URL: https://doi.org/10.3390/ma14226783.

[36] Robert M. Darling, Kevin G. Gallagher, Jeffrey A. Kowalski, Seungbum Ha, and Fikile R. Brushett. "Pathways to low-cost electrochemical energy storage: a comparison of aqueous and nonaqueous flow batteries". In: *Energy Environ. Sci.* 7.11 (Sept. 2014), pp. 3459–3477. DOI: 10.1039/c4ee02158d. URL: https://doi.org/10.1039/c4ee02158d.

[37] Anna B. Gunnarsdóttir, Sundeep Vema, Svetlana Menkin, Lauren E. Marbella, and Clare P. Grey. "Investigating the effect of a fluoroethylene carbonate additive on lithium deposition and the solid electrolyte interphase in lithium metal batteries using iin situ/i NMR spectroscopy". In: *Journal of Materials Chemistry A* 8.30 (2020), pp. 14975–14992. DOI: 10.1039/d0ta05652a. URL: https://doi.org/10.1039/d0ta05652a.

[38] Rotem Marom, Ortal Haik, Doron Aurbach, and Ion C. Halalay. "Revisiting LiClO[sub 4] as an Electrolyte for Rechargeable Lithium-Ion Batteries". In: *Journal of The Electrochemical Society* 157.8 (2010), A972. DOI: 10.1149/1.3447750. URL: https://doi.org/10.1149/1.3447750.

[39] Johan Scheers, Du-Hyun Lim, Jae-Kwang Kim, Elie Paillard, Wesley A. Henderson, Patrik Johansson, Jou-Hyeon Ahn, and Per Jacobsson. "All fluorine-free lithium battery electrolytes". In: *Journal of Power Sources* 251 (Apr. 2014), pp. 451–458. DOI: 10.1016/j.jpowsour.2013.11.042. URL: https://doi.org/10.1016/j.jpowsour.2013.11.042.

[40] Christina Sauter, Raphael Zahn, and Vanessa Wood. "Understanding Electrolyte Infilling of Lithium Ion Batteries". In: *Journal of The Electrochemical Society* 167.10 (Jan. 2020), p. 100546. DOI: 10.1149/1945-7111/ab9bfd. URL: https://doi.org/10.1149/1945-7111/ab9bfd.

[41] Zhe Deng, Zhenyu Huang, Yue Shen, Yunhui Huang, Han Ding, Aidan Luscombe, Michel Johnson, Jessie E. Harlow, Roby Gauthier, and Jeff R. Dahn. "Ultrasonic Scanning to Observe Wetting and "Unwetting" in Li-Ion Pouch Cells". In: *Joule* 4.9 (Sept. 2020), pp. 2017–2029. DOI: 10.1016/j.joule.2020.07.014. URL: https://doi.org/10.1016/j.joule.2020.07.014.

[42] Yuki Yamada and Atsuo Yamada. "Review—Superconcentrated Electrolytes for Lithium Batteries". In: *Journal of The Electrochemical Society* 162.14 (2015), A2406–A2423. DOI: 10.1149/2.0041514jes. URL: https://doi.org/10.1149/2.0041514jes.

[43] D Aurbach, K Gamolsky, B Markovsky, Y Gofer, M Schmidt, and U Heider. "On the use of vinylene carbonate (VC) as an additive to electrolyte solutions for Li-ion batteries". In: *Electrochimica Acta* 47.9 (Feb. 2002), pp. 1423–1439. DOI: 10.1016/s0013-4686(01)00858-1. URL: https://doi.org/10.1016/s0013-4686(01)00858-1.

[44] Hideki Nakai, Tadahiko Kubota, Akinori Kita, and Atsumichi Kawashima. "Investigation of the Solid Electrolyte Interphase Formed by Fluoroethylene Carbonate on Si Electrodes". In: *Journal of The Electrochemical Society* 158.7 (May 2011), A798–A801. DOI: 10.1149/1.3589300. URL: https://doi.org/10.1149/1.3589300.

[45] Tao Li, Xue-Qiang Zhang, Nan Yao, Yu-Xing Yao, Li-Peng Hou, Xiang Chen, Ming-Yue Zhou, Jia-Qi Huang, and Qiang Zhang. "Stable Anion-Derived Solid Electrolyte Interphase in Lithium Metal Batteries". In: *Angewandte Chemie* 133.42 (Sept. 2021), pp. 22865–22869. DOI: 10.1002/ange.202107732. URL: https://doi.org/10.1002/ange.202107732.

[46] Matthew Li, Chunsheng Wang, Zhongwei Chen, Kang Xu, and Jun Lu. "New Concepts in Electrolytes". In: *Chemical Reviews* 120.14 (Feb. 2020), pp. 6783–6819. DOI: 10.1021/acs.chemrev.9b00531. URL: https://doi.org/10.1021/acs.chemrev.9b00531.

[47] Robert Anthony Robinson and Robert Harold Stokes. *Electrolyte solutions*. Courier Corporation, 2002.

[48] Daniel M. Seo, Oleg Borodin, Sang-Don Han, Quang Ly, Paul D. Boyle, and Wesley A. Henderson. "Electrolyte Solvation and Ionic Association". In: *Journal of The Electrochemical Society* 159.5 (2012), A553–A565. DOI: 10.1149/2.jes112264. URL: https://doi.org/10.1149/2.jes112264.

[49] Jianhui Wang, Yuki Yamada, Keitaro Sodeyama, Ching Hua Chiang, Yoshitaka Tateyama, and Atsuo Yamada. "Superconcentrated electrolytes for a high-voltage lithium-ion battery". In: *Nature Communications* 7.1 (June 2016). DOI: 10.1038/ncomms12032. URL: https://doi.org/10.1038/ncomms12032.

[50] Shuru Chen, Jianming Zheng, Donghai Mei, Kee Sung Han, Mark H. Engelhard, Wengao Zhao, Wu Xu, Jun Liu, and Ji-Guang Zhang. "High-Voltage Lithium-Metal Batteries Enabled by Localized High-Concentration Electrolytes". In: *Advanced Materials* 30.21 (Mar. 2018), p. 1706102. DOI: 10.1002/adma.201706102. URL: https://doi.org/10.1002/adma.201706102.

[51] Kang Xu and Chunsheng Wang. "Batteries: Widening voltage windows". In: *Nature Energy* 1.10 (Oct. 2016). DOI: 10.1038/nenergy.2016.161. URL: https://doi.org/10.1038/nenergy.2016.161.

[52] Sang Cheol Kim, Xian Kong, Rafael A. Vilá, William Huang, Yuelang Chen, David T. Boyle, Zhiao Yu, Hansen Wang, Zhenan Bao, Jian Qin, and Yi Cui. "Potentiometric Measurement to Probe Solvation Energy and Its Correlation to Lithium Battery Cyclability". In: *Journal of the American Chemical Society* 143.27 (June 2021), pp. 10301–10308. DOI: 10.1021/jacs.1c03868. URL: https://doi.org/10.1021/jacs.1c03868.

[53] Zhiao Yu, Paul E. Rudnicki, Zewen Zhang, Zhuojun Huang, Hasan Celik, Solomon T. Oyakhire, Yuelang Chen, Xian Kong, Sang Cheol Kim, Xin Xiao, Hansen Wang, Yu Zheng, Gaurav A. Kamat, Mun Sek Kim, Stacey F. Bent, Jian Qin, Yi Cui, and Zhenan Bao. "Rational solvent molecule tuning for high-performance lithium metal battery electrolytes". In: *Nature Energy* 7.1 (Jan. 2022), pp. 94–106. DOI: 10.1038/s41560-021-00962-y. URL: https://doi.org/10.1038/s41560-021-00962-y.

[54] Gustavo M. Hobold, Jeffrey Lopez, Rui Guo, Nicolò Minafra, Abhik Banerjee, Y. Shirley Meng, Yang Shao-Horn, and Betar M. Gallant. "Moving beyond 99.9% Coulombic efficiency for lithium anodes in liquid electrolytes". In: *Nature Energy* 6.10 (Oct. 2021), pp. 951–960. DOI: 10.1038/s41560-021-00910-w. URL: https://doi.org/10.1038/s41560-021-00910-w.

[55] Eibar Flores, Gustav Åvall, Steffen Jeschke, and Patrik Johansson. "Solvation structure in dilute to highly concentrated electrolytes for lithium-ion and sodium-ion batteries". In: *Electrochimica Acta* 233 (Apr. 2017), pp. 134–141. DOI: 10.1016/j.electacta.2017.03.031. URL: https://doi.org/10.1016/j.electacta.2017.03.031.

[56] Julian Self, Kara D. Fong, E. R. Logan, and Kristin A. Persson. "Ion Association Constants for Lithium Ion Battery Electrolytes from First-Principles Quantum Chemistry". In: *Journal of The Electrochemical Society* 166.15 (2019), A3554–A3558. DOI: 10.1149/2.1061914jes. URL: https://doi.org/10.1149/2.1061914jes.

[57] Arthur von Wald Cresce, Oleg Borodin, and Kang Xu. "Correlating Lisup/sup Solvation Sheath Structure with Interphasial Chemistry on Graphite". In: *The Journal of Physical Chemistry C* 116.50 (Dec. 2012), pp. 26111–26117. DOI: 10.1021/jp303610t. URL: https://doi.org/10.1021/jp303610t.

[58] Xavier Bogle, Rafael Vazquez, Steven Greenbaum, Arthur von Wald Cresce, and Kang Xu. "Understanding Li+ - Solvent Interaction in Nonaqueous Carbonate Electrolytes with 17O NMR". In: *The Journal of Physical Chemistry Letters* 4.10 (May 2013), pp. 1664–1668. DOI: 10.1021/jz400661k. URL: https://doi.org/10.1021/jz400661k.

[59] Arthur V. Cresce, Selena M. Russell, Oleg Borodin, Joshua A. Allen, Marshall A. Schroeder, Michael Dai, Jing Peng, Mallory P. Gobet, Steven G. Greenbaum, Reginald E. Rogers, and Kang Xu. "Solvation behavior of carbonate-based electrolytes in sodium ion batteries". In: *Physical Chemistry Chemical Physics* 19.1 (2017), pp. 574–586. DOI: 10.1039/c6cp07215a. URL: https://doi.org/10.1039/c6cp07215a.

[60] Mengyun Nie, Daniel P. Abraham, Daniel M. Seo, Yanjing Chen, Arijit Bose, and Brett L. Lucht. "Role of Solution Structure in Solid Electrolyte Interphase Formation on Graphite with LiPFsub6/sub in Propylene Carbonate". In: *The Journal of Physical Chemistry C* 117.48 (Nov. 2013), pp. 25381–25389. DOI: 10.1021/jp409765w. URL: https://doi.org/10.1021/jp409765w.

[61] John Newman and Karen E Thomas-Alyea. *Electrochemical systems*. John Wiley & Sons, 2012.

[62] Deep B. Shah, Hong Keun Kim, Hien Q. Nguyen, Venkat Srinivasan, and Nitash P. Balsara. "Comparing Measurements of Limiting Current of Electrolytes with Theoretical Predictions up to the Solubility Limit". In: *The Journal of Physical Chemistry C* 123.39 (Sept. 2019), pp. 23872–23881. DOI: 10.1021/acs.jpcc.9b07121. URL: https://doi.org/10.1021/acs.jpcc.9b07121.

[63] Aashutosh Mistry, Francois L. E. Usseglio-Viretta, Andrew Colclasure, Kandler Smith, and Partha P. Mukherjee. "Fingerprinting Redox Heterogeneity in Electrodes during Extreme Fast Charging". In: *Journal of The Electrochemical Society* 167.9 (Jan. 2020), p. 090542. DOI: 10.1149/1945-7111/ab8fd7. URL: https://doi.org/10.1149/1945-7111/ab8fd7.

[64] Pankaj Arora, Marc Doyle, and Ralph E. White. "Mathematical Modeling of the Lithium Deposition Overcharge Reaction in Lithium-Ion Batteries Using Carbon-Based Negative Electrodes". In: *Journal of The Electrochemical Society* 146.10 (Oct. 1999), pp. 3543–3553. DOI: 10.1149/1.1392512. URL: https://doi.org/10.1149/1.1392512.

[65] Hee Jung Chang, Andrew J. Ilott, Nicole M. Trease, Mohaddese Mohammadi, Alexej Jerschow, and Clare P. Grey. "Correlating Microstructural Lithium Metal Growth with Electrolyte Salt Depletion in Lithium Batteries Using sup7/supLi MRI". In: *Journal of the American Chemical Society* 137.48 (Nov. 2015), pp. 15209–15216. DOI: 10.1021/jacs.5b09385. URL: https://doi.org/10.1021/jacs.5b09385.

[66] Peng Bai, Ju Li, Fikile R. Brushett, and Martin Z. Bazant. "Transition of lithium growth mechanisms in liquid electrolytes". In: *Energy &amp Environmental Science* 9.10 (2016), pp. 3221–3229. DOI: 10.1039/c6ee01674j. URL: https://doi.org/10.1039/c6ee01674j.

[67] C. Delacourt. "Modeling Li-Ion Batteries with Electrolyte Additives or Contaminants". In: *Journal of The Electrochemical Society* 160.11 (2013), A1997–A2004. DOI: 10.1149/2.033311jes. URL: https://doi.org/10.1149/2.033311jes.

[68] Kyle M. Diederichsen, Eric J. McShane, and Bryan D. McCloskey. "Promising Routes to a High Lisup/sup Transference Number Electrolyte for Lithium Ion Batteries". In: *ACS Energy Letters* 2.11 (Oct. 2017), pp. 2563–2575. DOI: 10.1021/acsenergylett.7b00792. URL: https://doi.org/10.1021/acsenergylett.7b00792.

[69] Martin Ebner, Ding-Wen Chung, R. Edwin Garcıa, and Vanessa Wood. "Tortuosity Anisotropy in Lithium-Ion Battery Electrodes". In: *Advanced Energy Materials* 4.5 (Oct. 2013), p. 1301278. DOI: 10.1002/aenm.201301278. URL: https://doi.org/10.1002/aenm.201301278.

[70] Indrajeet V. Thorat, David E. Stephenson, Nathan A. Zacharias, Karim Zaghib, John N. Harb, and Dean R. Wheeler. "Quantifying tortuosity in porous Li-ion battery materials". In: *Journal of Power Sources* 188.2 (Mar. 2009), pp. 592–600. DOI: 10.1016/j.jpowsour.2008.12.032. URL: https://doi.org/10.1016/j.jpowsour.2008.12.032.

[71] Rebecca E. Ciez and Daniel Steingart. "Asymptotic Cost Analysis of Intercalation Lithium-Ion Systems for Multi-hour Duration Energy Storage". In: *Joule* 4.3 (Mar. 2020), pp. 597–614. DOI: 10.1016/j.joule.2020.01.007. URL: https://doi.org/10.1016/j.joule.2020.01.007.

[72] Mihai Duduta, Bryan Ho, Vanessa C. Wood, Pimpa Limthongkul, Victor E. Brunini, W. Craig Carter, and Yet-Ming Chiang. "Semi-Solid Lithium Rechargeable Flow Battery". In: *Advanced Energy Materials* 1.4 (May 2011), pp. 511–516. DOI: 10.1002/aenm.201100152. URL: https://doi.org/10.1002/aenm.201100152.

[73] Honghe Zheng, Jing Li, Xiangyun Song, Gao Liu, and Vincent S. Battaglia. "A comprehensive understanding of electrode thickness effects on the electrochemical performances of Li-ion battery cathodes". In: *Electrochimica Acta* 71 (June 2012), pp. 258–265. DOI: 10.1016/j.electacta.2012.03.161. URL: https://doi.org/10.1016/j.electacta.2012.03.161.

[74] Christian Heubner, Michael Schneider, and Alexander Michaelis. "Diffusion-Limited C-Rate: A Fundamental Principle Quantifying the Intrinsic Limits of Li-Ion Batteries". In: *Advanced Energy Materials* 10.2 (Nov. 2019), p. 1902523. DOI: 10.1002/aenm.201902523. URL: https://doi.org/10.1002/aenm.201902523.

[75] Venkat Srinivasan and John Newman. "Design and Optimization of a Natural Graphite/Iron Phosphate Lithium-Ion Cell". In: *Journal of The Electrochemical Society* 151.10 (2004), A1530. DOI: 10.1149/1.1785013. URL: https://doi.org/10.1149/1.1785013.

[76] Scott G. Marquis, Valentin Sulzer, Robert Timms, Colin P. Please, and S. Jon Chapman. "An Asymptotic Derivation of a Single Particle Model with Electrolyte". In: *Journal of The Electrochemical Society* 166.15 (2019), A3693–A3706. DOI: 10.1149/2.0341915jes. URL: https://doi.org/10.1149/2.0341915jes.

[77] Valentin Sulzer, Scott G. Marquis, Robert Timms, Martin Robinson, and S. Jon Chapman. "Python Battery Mathematical Modelling (PyBaMM)". In: *Journal of Open Research Software* 9.1 (June 2021), p. 14. DOI: 10.5334/jors.309. URL: https://doi.org/10.5334/jors.309.

[78] Johannes Landesfeind and Hubert A. Gasteiger. "Temperature and Concentration Dependence of the Ionic Transport Properties of Lithium-Ion Battery Electrolytes". In: *Journal of The Electrochemical Society* 166.14 (2019), A3079–A3097. DOI: 10.1149/2.0571912jes. URL: https://doi.org/10.1149/2.0571912jes.

[79] Allen J. Bard and Larry R. Faulkner. *Electrochemical Methods: Fundamentals and Applications*. 2nd. Wiley, 2001.

[80] L S Darken. "Diffusion, mobility and their interrelation through free energy in binary metallic systems". In: *Trans. Aime* 175 (1948), pp. 184–201.

[81] Adrien M. Bizeray, David A. Howey, and Charles W. Monroe. "Resolving a Discrepancy in Diffusion Potentials, with a Case Study for Li-Ion Batteries". In: *Journal of The Electrochemical Society* 163.8 (2016), E223–E229. DOI: 10.1149/2.0451608jes. URL: https://doi.org/10.1149/2.0451608jes.

[82] Per Chr Hemmer, Helge Holden, and Signe Kjelstrup Ratkje. *The Collected Works of Lars Onsager*. WORLD SCIENTIFIC, Aug. 1996. DOI: 10.1142/3027. URL: https://doi.org/10.1142/3027.

[83] Lars Ole Valøen and Jan N Reimers. "Transport properties of LiPF6-based Li-ion battery electrolytes". In: *Journal of The Electrochemical Society* 152.5 (2005), A882.

[84] Athinthra Krishnaswamy Sethurajan, Sergey A. Krachkovskiy, Ion C. Halalay, Gillian R. Goward, and Bartosz Protas. "Accurate Characterization of Ion Transport Properties in Binary Symmetric Electrolytes Using In Situ NMR Imaging and Inverse Modeling". In: *The Journal of Physical Chemistry B* 119.37 (Sept. 2015), pp. 12238–12248. DOI: 10.1021/acs.jpcb.5b04300. URL: https://doi.org/10.1021/acs.jpcb.5b04300.

[85] R.B. Bird, W.E. Stewart, and E.N. Lightfoot. *Transport Phenomena*. J. Wiley, 2002. URL: https://books.google.co.uk/books?id=wYnRQwAACAAJ.

[86] Kara D. Fong, Helen K. Bergstrom, Bryan D. McCloskey, and Kranthi K. Mandadapu. "Transport phenomena in electrolyte solutions: Nonequilibrium thermodynamics and statistical mechanics". In: *AIChE Journal* 66.12 (Nov. 2020). DOI: 10.1002/aic.17091. URL: https://doi.org/10.1002/aic.17091.

[87] Kevin W. Gao, Chao Fang, David M. Halat, Aashutosh Mistry, John Newman, and Nitash P. Balsara. "The Transference Number". In: *ENERGY &amp ENVIRONMENTAL MATERIALS* 5.2 (Apr. 2022), pp. 366–369. DOI: 10.1002/eem2.12359. URL: https://doi.org/10.1002/eem2.12359.

[88] Priyamvada Goyal and Charles W. Monroe. "Thermodynamic factors for locally non-neutral, concentrated electrolytic fluids". In: *Electrochimica Acta* 371 (Mar. 2021), p. 137638. DOI: 10.1016/j.electacta.2020.137638. URL: https://doi.org/10.1016/j.electacta.2020.137638.

[89] Jing Liu and Charles W. Monroe. "Solute-volume effects in electrolyte transport". In: *Electrochimica Acta* 135 (July 2014), pp. 447–460. DOI: 10.1016/j.electacta.2014.05.009. URL: https://doi.org/10.1016/j.electacta.2014.05.009.

[90] Marc Doyle, Thomas F. Fuller, and John Newman. "Modeling of Galvanostatic Charge and Discharge of the Lithium/Polymer/Insertion Cell". In: *Journal of The Electrochemical Society* 140.6 (June 1993), pp. 1526–1533. DOI: 10.1149/1.2221597. URL: https://doi.org/10.1149/1.2221597.

[91] Giles W Richardson, Jamie M Foster, Rahifa Ranom, Colin P Please, and Angel M Ramos. "Charge transport modelling of lithium ion batteries". In: (2020). DOI: 10.48550/ARXIV.2002.00806. URL: https://arxiv.org/abs/2002.00806.

[92] John Newman and Thomas W. Chapman. "Restricted diffusion in binary solutions". In: *AIChE Journal* 19.2 (Mar. 1973), pp. 343–348. DOI: 10.1002/aic.690190220. URL: https://doi.org/10.1002/aic.690190220.

[93] Mohammad Farkhondeh, Mark Pritzker, Michael Fowler, and Charles Delacourt. "Transport property measurement of binary electrolytes using a four-electrode electrochemical cell". In: *Electrochemistry Communications* 67 (June 2016), pp. 11–15. DOI: 10.1016/j.elecom.2016.02.025. URL: https://doi.org/10.1016/j.elecom.2016.02.025.

[94] Henrik Lundgren, Mårten Behm, and Göran Lindbergh. "Electrochemical characterization and temperature dependency of mass-transport properties of LiPF6 in EC: DEC". In: *Journal of The Electrochemical Society* 162.3 (2014), A413.

[95] Sandra Zugmann, Matthias Fleischmann, Marius Amereller, Ruth M. Gschwind, Martin Winter, and Heiner J. Gores. "Salt Diffusion Coefficients, Concentration Dependence of Cell Potentials, and Transference Numbers of Lithium Difluoromono(oxalato)borate-Based Solutions". In: *Journal of Chemical &amp Engineering Data* 56.12 (Oct. 2011), pp. 4786–4789. DOI: 10.1021/je2007814. URL: https://doi.org/10.1021/je2007814.

[96] Andrew A. Wang, Anna B. Gunnarsdóttir, Jack Fawdon, Mauro Pasta, Clare P. Grey, and Charles W. Monroe. "Potentiometric MRI of a Superconcentrated Lithium Electrolyte: Testing the Irreversible Thermodynamics Approach". In: *ACS Energy Letters* 6.9 (Aug. 2021), pp. 3086–3095. DOI: 10.1021/acsenergylett.1c01213. URL: https://doi.org/10.1021/acsenergylett.1c01213.

[97] Jing Liu and Charles W. Monroe. "On the characterization of battery electrolytes with polarization cells". In: *Electrochimica Acta* 167 (June 2015), pp. 357–363. DOI: 10.1016/j.electacta.2015.03.104. URL: https://doi.org/10.1016/j.electacta.2015.03.104.

[98] Javor K. Novev and Richard G. Compton. "Natural convection effects in electrochemical systems". In: *Current Opinion in Electrochemistry* 7 (Jan. 2018), pp. 118–129. DOI: 10.1016/j.coelec.2017.09.010. URL: https://doi.org/10.1016/j.coelec.2017.09.010.

[99] Yizhak Marcus and Glenn Hefter. "Standard Partial Molar Volumes of Electrolytes and Ions in Nonaqueous Solvents". In: *Chemical Reviews* 104.7 (June 2004), pp. 3405–3452. DOI: 10.1021/cr030047d. URL: https://doi.org/10.1021/cr030047d.

[100] Max Schammer, Birger Horstmann, and Arnulf Latz. "Theory of Transport in Highly Concentrated Electrolytes". In: *Journal of The Electrochemical Society* 168.2 (Feb. 2021), p. 026511. DOI: 10.1149/1945-7111/abdddf. URL: https://doi.org/10.1149/1945-7111/abdddf.

[101] Andreas Nyman, Mårten Behm, and Göran Lindbergh. "Electrochemical characterisation and modelling of the mass transport phenomena in LiPF6–EC–EMC electrolyte". In: *Electrochimica Acta* 53.22 (2008), pp. 6356–6365.

[102] Tianhong Hou and Charles W. Monroe. "Composition-dependent thermodynamic and mass-transport characterization of lithium hexafluorophosphate in propylene carbonate". In: *Electrochimica Acta* 332 (Feb. 2020), p. 135085. DOI: 10.1016/j.electacta.2019.135085. URL: https://doi.org/10.1016/j.electacta.2019.135085.

[103] Henrik Lundgren, Johan Scheers, Mårten Behm, and Göran Lindbergh. "Characterization of the mass-transport phenomena in a superconcentrated litfsi: Acetonitrile electrolyte". In: *Journal of The Electrochemical Society* 162.7 (2015), A1334.

[104] Aashutosh Mistry, Lorena S. Grundy, David M. Halat, John Newman, Nitash P. Balsara, and Venkat Srinivasan. "Effect of Solvent Motion on Ion Transport in Electrolytes". In: *Journal of The Electrochemical Society* 169.4 (Apr. 2022), p. 040524. DOI: 10.1149/1945-7111/ac6329. URL: https://doi.org/10.1149/1945-7111/ac6329.

[105] David M. Halat, Chao Fang, Darby Hickson, Aashutosh Mistry, Jeffrey A. Reimer, Nitash P. Balsara, and Rui Wang. "Electric-Field-Induced Spatially Dynamic Heterogeneity of Solvent Motion and Cation Transference in Electrolytes". In: *Physical Review Letters* 128.19 (May 2022). DOI: 10.1103/physrevlett.128.198002. URL: https://doi.org/10.1103/physrevlett.128.198002.

[106] Florian Schmidt and Monika Schönhoff. "Solvate Cation Migration and Ion Correlations in Solvate Ionic Liquids". In: *The Journal of Physical Chemistry B* 124.7 (2020), pp. 1245–1252. DOI: 10.1021/acs.jpcb.9b11330. URL: https://doi.org/10.1021/acs.jpcb.9b11330.

[107] Florian Schmidt, Andrea Pugliese, Catherine C. Santini, Franca Castiglione, and Monika Schönhoff. "Spectral deconvolution in electrophoretic NMR to investigate the migration of neutral molecules in electrolytes". In: *Magnetic Resonance in Chemistry* 58.3 (Jan. 2020), pp. 271–279. DOI: 10.1002/mrc.4978. URL: https://doi.org/10.1002/mrc.4978.

[108] Mark P. Rosenwinkel and Monika Schönhoff. "Polymer-Induced Inversion of the Li sup/sup Drift Direction in Ionic Liquid-Based Ternary Polymer Electrolytes". In: *Macromolecular Chemistry and Physics* 223.8 (Nov. 2021), p. 2100320. DOI: 10.1002/macp.202100320. URL: https://doi.org/10.1002/macp.202100320.

[109] Hong-Keun Kim, Nitash P. Balsara, and Venkat Srinivasan. "Continuum Description of the Role of Negative Transference Numbers on Ion Motion in Polymer Electrolytes". In: *Journal of The Electrochemical Society* 167.11 (July 2020), p. 110559. DOI: 10.1149/1945-7111/aba790. URL: https://doi.org/10.1149/1945-7111/aba790.

[110] Danielle M. Pesko, Ksenia Timachova, Rajashree Bhattacharya, Mackensie C. Smith, Irune Villaluenga, John Newman, and Nitash P. Balsara. "Negative Transference Numbers in Poly(ethylene oxide)-Based Electrolytes". In: *Journal of The Electrochemical Society* 164.11 (2017), E3569–E3575. DOI: 10.1149/2.0581711jes. URL: https://doi.org/10.1149/2.0581711jes.

[111] Irune Villaluenga, Danielle M. Pesko, Ksenia Timachova, Zhange Feng, John Newman, Venkat Srinivasan, and Nitash P. Balsara. "Negative Stefan-Maxwell Diffusion Coefficients and Complete Electrochemical Transport Characterization of Homopolymer and Block Copolymer Electrolytes". In: *Journal of The Electrochemical Society* 165.11 (2018), A2766–A2773. DOI: 10.1149/2.0641811jes. URL: https://doi.org/10.1149/2.0641811jes.

[112] Kara D. Fong, Julian Self, Kyle M. Diederichsen, Brandon M. Wood, Bryan D. McCloskey, and Kristin A. Persson. "Ion Transport and the True Transference Number in Nonaqueous Polyelectrolyte Solutions for Lithium Ion Batteries". In: *ACS Central Science* 5.7 (June 2019), pp. 1250–1260. DOI: 10.1021/acscentsci.9b00406. URL: https://doi.org/10.1021/acscentsci.9b00406.

[113] Julian Self, Kara D. Fong, and Kristin A. Persson. "Transport in Superconcentrated LiPFsub6/sub and LiBFsub4/sub/Propylene Carbonate Electrolytes". In: *ACS Energy Letters* 4.12 (Nov. 2019), pp. 2843–2849. DOI: 10.1021/acsenergylett.9b02118. URL: https://doi.org/10.1021/acsenergylett.9b02118.

[114] Rasmus Andersson, Fabian Årén, Alejandro A. Franco, and Patrik Johansson. "Ion Transport Mechanisms via Time-Dependent Local Structure and Dynamics in Highly Concentrated Electrolytes". In: *Journal of The Electrochemical Society* 167.14 (Nov. 2020), p. 140537. DOI: 10.1149/1945-7111/abc657. URL: https://doi.org/10.1149/1945-7111/abc657.

[115] Zhou Yu, Nitash P. Balsara, Oleg Borodin, Andrew A. Gewirth, Nathan T. Hahn, Edward J. Maginn, Kristin A. Persson, Venkat Srinivasan, Michael F. Toney, Kang Xu, Kevin R. Zavadil, Larry A. Curtiss, and Lei Cheng. "Beyond Local Solvation Structure: Nanometric Aggregates in Battery Electrolytes and Their Effect on Electrolyte Properties". In: *ACS Energy Letters* 7.1 (Dec. 2021), pp. 461–470. DOI: 10.1021/acsenergylett.1c02391. URL: https://doi.org/10.1021/acsenergylett.1c02391.

[116] Michael McEldrew, Zachary A. H. Goodwin, Sheng Bi, Martin Z. Bazant, and Alexei A. Kornyshev. "Theory of ion aggregation and gelation in super-concentrated electrolytes". In: *The Journal of Chemical Physics* 152.23 (June 2020), p. 234506. DOI: 10.1063/5.0006197. URL: https://doi.org/10.1063/5.0006197.

[117] Kaoru Dokko, Daiki Watanabe, Yosuke Ugata, Morgan L. Thomas, Seiji Tsuzuki, Wataru Shinoda, Kei Hashimoto, Kazuhide Ueno, Yasuhiro Umebayashi, and Masayoshi Watanabe. "Direct Evidence for Li Ion Hopping Conduction in Highly Concentrated Sulfolane-Based Liquid Electrolytes". In: *The Journal of Physical Chemistry B* 122.47 (Nov. 2018), pp. 10736–10745. DOI: 10.1021/acs.jpcb.8b09439. URL: https://doi.org/10.1021/acs.jpcb.8b09439.

[118] Andrew A. Wang, Tianhong Hou, Minnie Karanjavala, and Charles W. Monroe. "Shifting-reference concentration cells to refine composition-dependent transport characterization of binary lithium-ion electrolytes". In: *Electrochimica Acta* 358 (Oct. 2020), p. 136688. DOI: 10.1016/j.electacta.2020.136688. URL: https://doi.org/10.1016/j.electacta.2020.136688.

[119] Charles W. Monroe. "Does Oxygen Transport Affect the Cell Voltages of Metal/Air Batteries?" In: *Journal of The Electrochemical Society* 164.11 (2017), E3547–E3551. DOI: 10.1149/2.0521711jes. URL: https://doi.org/10.1149/2.0521711jes.

[120] Sun Ung Kim and Venkat Srinivasan. "A Method for Estimating Transport Properties of Concentrated Electrolytes from Self-Diffusion Data". In: *Journal of The Electrochemical Society* 163.14 (2016), A2977–A2980. DOI: 10.1149/2.0541614jes. URL: https://doi.org/10.1149/2.0541614jes.

[121] Zhange Feng, Kenneth Higa, Kee Sung Han, and Venkat Srinivasan. "Evaluating Transport Properties and Ionic Dissociation of LiPFsub6/subin Concentrated Electrolyte". In: *Journal of The Electrochemical Society* 164.12 (2017), A2434–A2440. DOI: 10.1149/2.0941712jes. URL: https://doi.org/10.1149/2.0941712jes.

[122] Satoshi Uchida and Tetsu Kiyobayashi. "How does the solvent composition influence the transport properties of electrolyte solutions? LiPF6 and LiFSA in EC and DMC binary solvent". In: *Physical Chemistry Chemical Physics* 23.18 (2021), pp. 10875–10887. DOI: 10.1039/d1cp00967b. URL: https://doi.org/10.1039/d1cp00967b.

[123] Aashutosh Mistry, Zhou Yu, Brandon L. Peters, Chao Fang, Rui Wang, Larry A. Curtiss, Nitash P. Balsara, Lei Cheng, and Venkat Srinivasan. "Toward Bottom-Up Understanding of Transport in Concentrated Battery Electrolytes". In: *ACS Central Science* (June 2022). DOI: 10.1021/acscentsci.2c00348. URL: https://doi.org/10.1021/acscentsci.2c00348.

[124] E. R. Logan, Erin M. Tonita, K. L. Gering, and J. R. Dahn. "A Critical Evaluation of the Advanced Electrolyte Model". In: *Journal of The Electrochemical Society* 165.14 (2018), A3350–A3359. DOI: 10.1149/2.0471814jes. URL: https://doi.org/10.1149/2.0471814jes.

[125] Yunqi Shao, Harish Gudla, Daniel Brandell, and Chao Zhang. "Transference Number in Polymer Electrolytes: Mind the Reference-Frame Gap". In: *Journal of the American Chemical Society* 144.17 (Apr. 2022), pp. 7583–7587. DOI: 10.1021/jacs.2c02389. URL: https://doi.org/10.1021/jacs.2c02389.

[126] S. Zugmann, M. Fleischmann, M. Amereller, R.M. Gschwind, H.D. Wiemhöfer, and H.J. Gores. "Measurement of transference numbers for lithium ion electrolytes via four different methods, a comparative study". In: *Electrochimica Acta* 56.11 (Apr. 2011), pp. 3926–3933. DOI: 10.1016/j.electacta.2011.02.025. URL: https://doi.org/10.1016/j.electacta.2011.02.025.

[127] Kang Xu. "Navigating the minefield of battery literature". In: *Communications Materials* 3.1 (May 2022). DOI: 10.1038/s43246-022-00251-5. URL: https://doi.org/10.1038/s43246-022-00251-5.

[128] Helen K. Bergstrom, Kara D. Fong, and Bryan D. McCloskey. "Interfacial Effects on Transport Coefficient Measurements in Li-ion Battery Electrolytes". In: *Journal of The Electrochemical Society* 168.6 (June 2021), p. 060543. DOI: 10.1149/1945-7111/ac0994. URL: https://doi.org/10.1149/1945-7111/ac0994.

[129] Andreas Ehrl, Johannes Landesfeind, Wolfgang A. Wall, and Hubert A. Gasteiger. "Determination of Transport Parameters in Liquid Binary Lithium Ion Battery Electrolytes". In: *Journal of The Electrochemical Society* 164.4 (2017), A826–A836. DOI: 10.1149/2.1131704jes. URL: https://doi.org/10.1149/2.1131704jes.

[130] Mark P. Rosenwinkel and Monika Schönhoff. "Lithium Transference Numbers in PEO/LiTFSA Electrolytes Determined by Electrophoretic NMR". In: *Journal of The Electrochemical Society* 166.10 (2019), A1977–A1983. DOI: 10.1149/2.0831910jes. URL: https://doi.org/10.1149/2.0831910jes.

[131] Nitash P. Balsara and John Newman. "Relationship between Steady-State Current in Symmetric Cells and Transference Number of Electrolytes Comprising Univalent and Multivalent Ions". In: *Journal of The Electrochemical Society* 162.14 (2015), A2720–A2722. DOI: 10.1149/2.0651514jes. URL: https://doi.org/10.1149/2.0651514jes.

[132] P BRUCE. "Conductivity and transference number measurements on polymer electrolytes". In: *Solid State Ionics* 28-30 (Sept. 1988), pp. 918–922. DOI: 10.1016/0167-2738(88)90304-9. URL: https://doi.org/10.1016/0167-2738(88)90304-9.

[133] Peter G. Bruce and Colin A. Vincent. "Steady state current flow in solid binary electrolyte cells". In: *Journal of Electroanalytical Chemistry and Interfacial Electrochemistry* 225.1-2 (June 1987), pp. 1–17. DOI: 10.1016/0022-0728(87)80001-3. URL: https://doi.org/10.1016/0022-0728(87)80001-3.

[134] Aashutosh Mistry et al. "A Minimal Information Set To Enable Verifiable Theoretical Battery Research". In: *ACS Energy Letters* 6.11 (Oct. 2021), pp. 3831–3835. DOI: 10.1021/acsenergylett.1c01710. URL: https://doi.org/10.1021/acsenergylett.1c01710.

[135] Kenneth S Pitzer and CRC Press. *Activity coefficients in electrolyte solutions*. Vol. 2. CRC press Boca Raton, FL, 1991.

[136] Sarah Stewart and John Newman. "Measuring the salt activity coefficient in lithium-battery electrolytes". In: *Journal of The Electrochemical Society* 155.6 (2008), A458.

[137] Nathan Craig, Scott A. Mullin, Russell Pratt, and Gabriel B. Crane. "Determination of Transference Number and Thermodynamic Factor by use of Anion-Exchange Concentration Cells and Concentration Cells". In: *Journal of The Electrochemical Society* 166.13 (2019), A2769–A2775. DOI: 10.1149/2.0351913jes. URL: https://doi.org/10.1149/2.0351913jes.

[138] Deep B Shah, Hien Q Nguyen, Lorena S Grundy, Kevin R Olson, Sue J Mecham, Joseph M DeSimone, and Nitash P Balsara. "Difference between approximate and rigorously measured transference numbers in fluorinated electrolytes". In: *Physical Chemistry Chemical Physics* 21.15 (2019), pp. 7857–7866.

[139] Michael D. Galluzzo, Whitney S. Loo, Andrew A. Wang, Amber Walton, Jacqueline A. Maslyn, and Nitash P. Balsara. "Measurement of Three Transport Coefficients and the Thermodynamic Factor in Block Copolymer Electrolytes with Different Morphologies". In: *The Journal of Physical Chemistry B* 124.5 (Jan. 2020), pp. 921–935. DOI: 10.1021/acs.jpcb.9b11066. URL: https://doi.org/10.1021/acs.jpcb.9b11066.

[140] Yanping Ma, Marc Doyle, Thomas F Fuller, Marca M Doeff, Lutgard C De Jonghe, and John Newman. "The measurement of a complete set of transport properties for a concentrated solid polymer electrolyte solution". In: *Journal of the Electrochemical Society* 142.6 (1995), p. 1859.

[141] Edward Armand Guggenheim. "Thermodynamics. An advanced treatment for chemists and physicists". In: *Zeitschrift für Naturforschung A* 5.4 (1950), pp. 236–236.

[142] Liumin Suo, Yong-Sheng Hu, Hong Li, Michel Armand, and Liquan Chen. "A new class of Solvent-in-Salt electrolyte for high-energy rechargeable metallic lithium batteries". In: *Nature Communications* 4.1 (Feb. 2013). DOI: 10.1038/ncomms2513. URL: https://doi.org/10.1038/ncomms2513.

[143] Susan D. Thompson and John Newman. "Differential Diffusion Coefficients of Sodium Polysulfide Melts". In: *Journal of The Electrochemical Society* 136.11 (Nov. 1989), pp. 3362–3369. DOI: 10.1149/1.2096451. URL: https://doi.org/10.1149/1.2096451.

[144] Astrid Fagertun Gunnarshaug, Signe Kjelstrup, Dick Bedeaux, Frank Richter, and Odne Stokke Burheim. "The reversible heat effects at lithium iron phosphate- and graphite electrodes". In: *Electrochimica Acta* 337 (Mar. 2020), p. 135567. DOI: 10.1016/j.electacta.2019.135567. URL: https://doi.org/10.1016/j.electacta.2019.135567.

[145] Yizhak Marcus and Glenn Hefter. "Ion Pairing". In: *Chemical Reviews* 106.11 (Oct. 2006), pp. 4585–4621. DOI: 10.1021/cr040087x. URL: https://doi.org/10.1021/cr040087x.

[146] Jonas Mindemark, Matthew J. Lacey, Tim Bowden, and Daniel Brandell. "Beyond PEO—Alternative host materials for Li+-conducting solid polymer electrolytes". In: *Progress in Polymer Science* 81 (June 2018), pp. 114–143. DOI: 10.1016/j.progpolymsci.2017.12.004. URL: https://doi.org/10.1016/j.progpolymsci.2017.12.004.

[147] James Evans, Colin A. Vincent, and Peter G. Bruce. "Electrochemical measurement of transference numbers in polymer electrolytes". In: *Polymer* 28.13 (Dec. 1987), pp. 2324–2328. DOI: 10.1016/0032-3861(87)90394-6. URL: https://doi.org/10.1016/0032-3861(87)90394-6.

[148] Thomas F. Fuller, Marc Doyle, and John Newman. "Simulation and Optimization of the Dual Lithium Ion Insertion Cell". In: *Journal of The Electrochemical Society* 141.1 (Jan. 1994), pp. 1–10. DOI: 10.1149/1.2054684. URL: https://doi.org/10.1149/1.2054684.

[149] Peter Josef William Debye et al. "collected papers of Peter JW Debye". In: (1954).

[150] Andrew R. Crothers, Clayton J. Radke, and John M. Prausnitz. "110th Anniversary: Theory of Activity Coefficients for Lithium Salts in Aqueous and Nonaqueous Solvents and in Solvent Mixtures". In: *Industrial & Engineering Chemistry Research* 58.39 (July 2019), pp. 18367–18377. DOI: 10.1021/acs.iecr.9b02657. URL: https://doi.org/10.1021/acs.iecr.9b02657.

[151] George Gabriel Stokes. *Mathematical and physical papers*. Vol. 3. 1901.

[152] Christian Schreiner, Sandra Zugmann, Robert Hartl, and Heiner J. Gores. "Fractional Walden Rule for Ionic Liquids: Examples from Recent Measurements and a Critique of the So-Called Ideal KCl Line for the Walden Plot". In: *Journal of Chemical & Engineering Data* 55.5 (Dec. 2009), pp. 1784–1788. DOI: 10.1021/je900878j. URL: https://doi.org/10.1021/je900878j.

[153] Bernhard Tjaden, Samuel J Cooper, Daniel JL Brett, Denis Kramer, and Paul R Shearing. "On the origin and application of the Bruggeman correlation for analysing transport phenomena in electrochemical systems". In: *Current Opinion in Chemical Engineering* 12 (May 2016), pp. 44–51. DOI: 10.1016/j.coche.2016.02.006. URL: https://doi.org/10.1016/j.coche.2016.02.006.

[154] Giles Richardson, Jamie M. Foster, Athinthra K. Sethurajan, Sergey A. Krachkovskiy, Ion C. Halalay, Gillian R. Goward, and Bartosz Protas. "The Effect of Ionic Aggregates on the Transport of Charged Species in Lithium Electrolyte Solutions". In: *Journal of The Electrochemical Society* 165.9 (2018), H561–H567. DOI: 10.1149/2.0981809jes. URL: https://doi.org/10.1149/2.0981809jes.

[155] Koshi Matsubara, Rie Kaneuchi, and Noriko Maekita. "13C NMR estimation of preferential solvation of lithium ions in non-aqueous mixed solvents". In: *Journal of the Chemical Society, Faraday Transactions* 94.24 (1998), pp. 3601–3605. DOI: 10.1039/a807010e. URL: https://doi.org/10.1039/a807010e.

[156] Y. Marcus. "The effectivity of solvents as electron pair donors". In: *Journal of Solution Chemistry* 13.9 (Sept. 1984), pp. 599–624. DOI: 10.1007/bf00650369. URL: https://doi.org/10.1007/bf00650369.

[157] Niels Janniksen Bjerrum. *Untersuchungen über Ionenassoziation*. AF Høst, 1926.

[158] D. J. Xiong, M. Bauer, L. D. Ellis, T. Hynes, S. Hyatt, D. S. Hall, and J. R. Dahn. "Some Physical Properties of Ethylene Carbonate-Free Electrolytes". In: *Journal of The Electrochemical Society* 165.2 (2018), A126–A131. DOI: 10.1149/2.0511802jes. URL: https://doi.org/10.1149/2.0511802jes.

[159] E. R. Logan, Erin M. Tonita, K. L. Gering, Jing Li, Xiaowei Ma, L. Y. Beaulieu, and J. R. Dahn. "A Study of the Physical Properties of Li-Ion Battery Electrolytes Containing Esters". In: *Journal of The Electrochemical Society* 165.2 (2018), A21–A30. DOI: 10.1149/2.0271802jes. URL: https://doi.org/10.1149%2F2.0271802jes.

[160] Makoto Ue and Shoichiro Mori. "Mobility and Ionic Association of Lithium Salts in a Propylene Carbonate-Ethyl Methyl Carbonate Mixed Solvent". In: *Journal of The Electrochemical Society* 142.8 (Aug. 1995), pp. 2577–2581. DOI: 10.1149/1.2050056. URL: https://doi.org/10.1149%2F1.2050056.

[161] Chibueze V. Amanchukwu. "The Electrolyte Frontier: A Manifesto". In: *Joule* 4.2 (Feb. 2020), pp. 281–285. DOI: 10.1016/j.joule.2019.12.009. URL: https://doi.org/10.1016%2Fj.joule.2019.12.009.

[162] Michael.J. Lain and Emma Kendrick. "Understanding the limitations of lithium ion batteries at high rates". In: *Journal of Power Sources* 493 (May 2021), p. 229690. DOI: 10.1016/j.jpowsour.2021.229690. URL: https://doi.org/10.1016%2Fj.jpowsour.2021.229690.

[163] Johannes Kasnatscheew, Uta Rodehorst, Benjamin Streipert, Simon Wiemers-Meyer, Rene Jakelski, Ralf Wagner, Isidora Cekic Laskovic, and Martin Winter. "Learning from Overpotentials in Lithium Ion Batteries: A Case Study on the LiNisub1/3/subCosub1/3/subMnsub1/3/subOsub2/sub(NCM) Cathode". In: *Journal of The Electrochemical Society* 163.14 (2016), A2943–A2950. DOI: 10.1149/2.0461614jes. URL: https://doi.org/10.1149%2F2.0461614jes.

[164] Roger D. Perkins, Alfred V. Randall, Xiangchun Zhang, and Gregory L. Plett. "Controls oriented reduced order modeling of lithium deposition on overcharge". In: *Journal of Power Sources* 209 (July 2012), pp. 318–325. DOI: 10.1016/j.jpowsour.2012.03.003. URL: https://doi.org/10.1016/j.jpowsour.2012.03.003.

[165] Anna B. Gunnarsdóttir, Chibueze V. Amanchukwu, Svetlana Menkin, and Clare P. Grey. "Noninvasive iIn Situ/i NMR Study of "Dead Lithium" Formation and Lithium Corrosion in Full-Cell Lithium Metal Batteries". In: *Journal of the American Chemical Society* 142.49 (Nov. 2020), pp. 20814–20827. DOI: 10.1021/jacs.0c10258. URL: https://doi.org/10.1021/jacs.0c10258.

[166] David T. Boyle, William Huang, Hansen Wang, Yuzhang Li, Hao Chen, Zhiao Yu, Wenbo Zhang, Zhenan Bao, and Yi Cui. "Corrosion of lithium metal anodes during calendar ageing and its microscopic origins". In: *Nature Energy* 6.5 (Mar. 2021), pp. 487–494. DOI: 10.1038/s41560-021-00787-9. URL: https://doi.org/10.1038/s41560-021-00787-9.

[167] A. J. Louli, A. Eldesoky, Rochelle Weber, M. Genovese, Matt Coon, Jack deGooyer, Zhe Deng, R. T. White, Jaehan Lee, Thomas Rodgers, R. Petibon, S. Hy, Shawn J. H. Cheng, and J. R. Dahn. "Diagnosing and correcting anode-free cell failure via electrolyte and morphological analysis". In: *Nature Energy* 5.9 (Aug. 2020), pp. 693–702. DOI: 10.1038/s41560-020-0668-8. URL: https://doi.org/10.1038/s41560-020-0668-8.

[168] David S. Hall, Jing Li, Katherine Lin, Nikolai Stakheiko, Jazmin Baltazar, and J. R. Dahn. "A Tale of Two Additives: Effects of Glutaric and Citraconic Anhydrides on Lithium-Ion Cell Performance". In: *Journal of The Electrochemical Society* 166.4 (2019), A793–A801. DOI: 10.1149/2.1251904jes. URL: https://doi.org/10.1149/2.1251904jes.

[169] Q. Q. Liu, R. Petibon, C. Y. Du, and J. R. Dahn. "Effects of Electrolyte Additives and Solvents on Unwanted Lithium Plating in Lithium-Ion Cells". In: *Journal of The Electrochemical Society* 164.6 (2017), A1173–A1183. DOI: 10.1149/2.1081706jes. URL: https://doi.org/10.1149/2.1081706jes.

[170] Edmund J.F. Dickinson and Andrew J. Wain. "The Butler-Volmer equation in electrochemical theory: Origins, value, and practical application". In: *Journal of Electroanalytical Chemistry* 872 (Sept. 2020), p. 114145. DOI: 10.1016/j.jelechem.2020.114145. URL: https://doi.org/10.1016/j.jelechem.2020.114145.

[171] Ziyang Cao, Michihiro Hashinokuchi, Takayuki Doi, and Minoru Inaba. "Improved Cycle Performance of LiNisub0.8/subCosub0.1/subMnsub0.1/subOsub2/sub Positive Electrode Material in Highly Concentrated LiBFsub4/sub/DMC". In: *Journal of The Electrochemical Society* 166.2 (2019), A82–A88. DOI: 10.1149/2.0291902jes. URL: https://doi.org/10.1149/2.0291902jes.

[172] Zhe Peng, Xia Cao, Peiyuan Gao, Haiping Jia, Xiaodi Ren, Swadipta Roy, Zhendong Li, Yun Zhu, Weiping Xie, Dianying Liu, Qiuyan Li, Deyu Wang, Wu Xu, and Ji-Guang Zhang. "High-Power Lithium Metal Batteries Enabled by High-Concentration Acetonitrile-Based Electrolytes with Vinylene Carbonate Additive". In: *Advanced Functional Materials* 30.24 (Apr. 2020), p. 2001285. DOI: 10.1002/adfm.202001285. URL: https://doi.org/10.1002/adfm.202001285.

[173] Michael McEldrew, Zachary A. H. Goodwin, Sheng Bi, Martin Z. Bazant, and Alexei A. Kornyshev. "Theory of ion aggregation and gelation in super-concentrated electrolytes". In: *The Journal of Chemical Physics* 152.23 (June 2020), p. 234506. DOI: 10.1063/5.0006197. URL: https://doi.org/10.1063/5.0006197.

[174] Liumin Suo, Fang Zheng, Yong-Sheng Hu, and Liquan Chen. "FT-Raman spectroscopy study of solvent-in-salt electrolytes". In: *Chinese Physics B* 25.1 (Jan. 2016), p. 016101. DOI: 10.1088/1674-1056/25/1/016101. URL: https://doi.org/10.1088/1674-1056/25/1/016101.

[175] Dengpan Dong, Fabian Sälzer, Bernhard Roling, and Dmitry Bedrov. "How efficient is Lisup/sup ion transport in solvate ionic liquids under anion-blocking conditions in a battery?" In: *Physical Chemistry Chemical Physics* 20.46 (2018), pp. 29174–29183. DOI: 10.1039/c8cp06214e. URL: https://doi.org/10.1039/c8cp06214e.

[176] Viktor Nilsson, Diana Bernin, Daniel Brandell, Kristina Edström, and Patrik Johansson. "Interactions and Transport in Highly Concentrated LiTFSI-based Electrolytes". In: *ChemPhysChem* 21.11 (2020), pp. 1166–1176. DOI: 10.1002/cphc.202000153. URL: https://doi.org/10.1002/cphc.202000153.

[177] Charles W. Monroe and Charles Delacourt. "Continuum transport laws for locally non-neutral concentrated electrolytes". In: *Electrochimica Acta* 114 (Dec. 2013), pp. 649–657. DOI: 10.1016/j.electacta.2013.10.006. URL: https://doi.org/10.1016/j.electacta.2013.10.006.

[178] Henrik Lundgren, Mårten Behm, and Göran Lindbergh. "Electrochemical Characterization and Temperature Dependency of Mass-Transport Properties of LiPF6in EC:DEC". In: *Journal of The Electrochemical Society* 162.3 (Dec. 2014), A413–A420. DOI: 10.1149/2.0641503jes. URL: https://doi.org/10.1149/2.0641503jes.

[179] Jan Robert Selman and John Newman. "Free-Convection Mass Transfer with a Supporting Electrolyte". In: *Journal of The Electrochemical Society* 118.7 (1971), p. 1070. DOI: 10.1149/1.2408249. URL: https://doi.org/10.1149/1.2408249.

[180] Matilda Klett, Marianne Giesecke, Andreas Nyman, Fredrik Hallberg, Rakel Wreland Lindström, Göran Lindbergh, and István Furó. "Quantifying Mass Transport during Polarization in a Li Ion Battery Electrolyte by in Situ 7Li NMR Imaging". In: *Journal of the American Chemical Society* 134.36 (Aug. 2012), pp. 14654–14657. DOI: 10.1021/ja305461j. URL: https://doi.org/10.1021/ja305461j.

[181] Jack Fawdon, Johannes Ihli, Fabio La Mantia, and Mauro Pasta. "Characterising lithium-ion electrolytes via operando Raman microspectroscopy". In: *Nature Communications* 12.1 (June 2021). DOI: 10.1038/s41467-021-24297-0. URL: https://doi.org/10.1038/s41467-021-24297-0.

[182] Daiko Takamatsu, Akio Yoneyama, Yusuke Asari, and Tatsumi Hirano. "Quantitative Visualization of Salt Concentration Distributions in Lithium-Ion Battery Electrolytes during Battery Operation Using X-ray Phase Imaging". In: *Journal of the American Chemical Society* 140.5 (Jan. 2018), pp. 1608–1611. DOI: 10.1021/jacs.7b13357. URL: https://doi.org/10.1021/jacs.7b13357.

[183] J. David Bazak, J. P. Allen, S. A. Krachkovskiy, and G. R. Goward. "Mapping of Lithium-Ion Battery Electrolyte Transport Properties and Limiting Currents with In Situ MRI". In: *Journal of The Electrochemical Society* 167.14 (Oct. 2020), p. 140518. DOI: 10.1149/1945-7111/abc0c9. URL: https://doi.org/10.1149/1945-7111/abc0c9.

[184] Athinthra Sethurajan, Sergey Krachkovskiy, Gillian Goward, and Bartosz Protas. "Bayesian uncertainty quantification in inverse modeling of electrochemical systems". In: *Journal of Computational Chemistry* 40.5 (Dec. 2018), pp. 740–752. DOI: 10.1002/jcc.25759. URL: https://doi.org/10.1002/jcc.25759.

[185] Sergey A. Krachkovskiy, J. David Bazak, Peter Werhun, Bruce J. Balcom, Ion C. Halalay, and Gillian R. Goward. "Visualization of Steady-State Ionic Concentration Profiles Formed in Electrolytes during Li-Ion Battery Operation and Determination of Mass-Transport Properties by in Situ Magnetic Resonance Imaging". In: *Journal of the American Chemical Society* 138.25 (June 2016), pp. 7992–7999. DOI: 10.1021/jacs.6b04226. URL: https://doi.org/10.1021/jacs.6b04226.

[186] J. David Bazak, Sergey A. Krachkovskiy, and Gillian R. Goward. "Multi-Temperature in Situ Magnetic Resonance Imaging of Polarization and Salt Precipitation in Lithium-Ion Battery Electrolytes". In: *The Journal of Physical Chemistry C* 121.38 (Sept. 2017), pp. 20704–20713. DOI: 10.1021/acs.jpcc.7b07218. URL: https://doi.org/10.1021/acs.jpcc.7b07218.

[187] Athinthra K. Sethurajan, Jamie M. Foster, Giles Richardson, Sergey A. Krachkovskiy, J. David Bazak, Gillian R. Goward, and Bartosz Protas. "Incorporating Dendrite Growth into Continuum Models of Electrolytes: Insights from NMR Measurements and Inverse Modeling". In: *Journal of The Electrochemical Society* 166.8 (2019), A1591–A1602. DOI: 10.1149/2.0921908jes. URL: https://doi.org/10.1149/2.0921908jes.

[188] Kazutaka Kondo, Mitsuru Sano, Akio Hiwara, Takehiko Omi, Miho Fujita, Akio Kuwae, Masayasu Iida, Koichi Mogi, and Haruhiko Yokoyama. "Conductivity and Solvation of Li+ Ions of LiPF6 in Propylene Carbonate Solutions". In: *The Journal of Physical Chemistry B* 104.20 (Apr. 2000), pp. 5040–5044. DOI: 10.1021/jp000142f. URL: https://doi.org/10.1021/jp000142f.

[189] Sunwook Hwang, Dong-Hui Kim, Jeong Hee Shin, Jae Eun Jang, Kyoung Ho Ahn, Chulhaeng Lee, and Hochun Lee. "Ionic Conduction and Solution Structure in LiPF6 and LiBF4 Propylene Carbonate Electrolytes". In: *The Journal of Physical Chemistry C* 122.34 (Aug. 2018), pp. 19438–19446. DOI: 10.1021/acs.jpcc.8b06035. URL: https://doi.org/10.1021/acs.jpcc.8b06035.

[190] Sang-Don Han, Sung-Hyun Yun, Oleg Borodin, Daniel M. Seo, Roger D. Sommer, Victor G. Young, and Wesley A. Henderson. "Solvate Structures and Computational/Spectroscopic Characterization of LiPF6 Electrolytes". In: *The Journal of Physical Chemistry C* 119.16 (Apr. 2015), pp. 8492–8500. DOI: 10.1021/acs.jpcc.5b00826. URL: https://doi.org/10.1021/acs.jpcc.5b00826.

[191] Andreas Heckmann, Johannes Thienenkamp, Kolja Beltrop, Martin Winter, Gunther Brunklaus, and Tobias Placke. "Towards high-performance dual-graphite batteries using highly concentrated organic electrolytes". In: *Electrochimica Acta* 260 (Jan. 2018), pp. 514–525. DOI: 10.1016/j.electacta.2017.12.099. URL: https://doi.org/10.1016/j.electacta.2017.12.099.

[192] J. E. Katon and M. D. Cohen. "The Vibrational Spectra and Structure of Dimethyl Carbonate and its Conformational Behavior". In: *Canadian Journal of Chemistry* 53.9 (May 1975), pp. 1378–1386. DOI: 10.1139/v75-191. URL: https://doi.org/10.1139/v75-191.

[193] Lukas Haneke, Joop Enno Frerichs, Andreas Heckmann, Michael M. Lerner, Taner Akbay, Tatsumi Ishihara, Michael Ryan Hansen, Martin Winter, and Tobias Placke. "Editors' Choice—Mechanistic Elucidation of Anion Intercalation into Graphite from Binary-Mixed Highly Concentrated Electrolytes via Complementary 19F MAS NMR and XRD Studies". In: *Journal of The Electrochemical Society* 167.14 (Nov. 2020), p. 140526. DOI: 10.1149/1945-7111/abc437. URL: https://doi.org/10.1149/1945-7111/abc437.

[194] Daniel M. Seo, Stefanie Reininger, Mary Kutcher, Kaitlin Redmond, William B. Euler, and Brett L. Lucht. "Role of Mixed Solvation and Ion Pairing in the Solution Structure of Lithium Ion Battery Electrolytes". In: *The Journal of Physical Chemistry C* 119.25 (June 2015), pp. 14038–14046. DOI: 10.1021/acs.jpcc.5b03694. URL: https://doi.org/10.1021/acs.jpcc.5b03694.

[195] H. Yoon, P. C. Howlett, A. S. Best, M. Forsyth, and D. R. MacFarlane. "Fast Charge/Discharge of Li Metal Batteries Using an Ionic Liquid Electrolyte". In: *Journal of The Electrochemical Society* 160.10 (2013), A1629–A1637. DOI: 10.1149/2.022310jes. URL: https://doi.org/10.1149/2.022310jes.

[196] S. Klamor, K. Zick, T. Oerther, F. M. Schappacher, M. Winter, and G. Brunklaus. "7Li in situ 1D NMR imaging of a lithium ion battery". In: *Physical Chemistry Chemical Physics* 17.6 (2015), pp. 4458–4465. DOI: 10.1039/c4cp05021e. URL: https://doi.org/10.1039/c4cp05021e.

[197] Andrew A. Wang. *EMC-MRI-model: First release of GalPol model*. 2021. DOI: 10.5281/ZENODO.4767883. URL: https://zenodo.org/record/4767883.

[198] Jorn M. Reniers, Grietus Mulder, and David A. Howey. "Review and Performance Comparison of Mechanical-Chemical Degradation Models for Lithium-Ion Batteries". In: *Journal of The Electrochemical Society* 166.14 (2019), A3189–A3200. DOI: 10.1149/2.0281914jes. URL: https://doi.org/10.1149/2.0281914jes.

[199] Sarah G. Stewart and John Newman. "The Use of UV/vis Absorption to Measure Diffusion Coefficients in LiPF[sub 6] Electrolytic Solutions". In: *Journal of The Electrochemical Society* 155.1 (2008), F13. DOI: 10.1149/1.2801378. URL: https://doi.org/10.1149/1.2801378.

[200] Kevin N. Wood, Eric Kazyak, Alexander F. Chadwick, Kuan-Hung Chen, Ji-Guang Zhang, Katsuyo Thornton, and Neil P. Dasgupta. "Dendrites and Pits: Untangling the Complex Behavior of Lithium Metal Anodes through Operando Video Microscopy". In: *ACS Central Science* 2.11 (Oct. 2016), pp. 790–801. DOI: 10.1021/acscentsci.6b00260. URL: https://doi.org/10.1021/acscentsci.6b00260.

[201] Kuan-Hung Chen, Kevin N. Wood, Eric Kazyak, William S. LePage, Andrew L. Davis, Adrian J. Sanchez, and Neil P. Dasgupta. "Dead lithium: mass transport effects on voltage, capacity, and failure of lithium metal anodes". In: *Journal of Materials Chemistry A* 5.23 (2017), pp. 11671–11681. DOI: 10.1039/c7ta00371d. URL: https://doi.org/10.1039/c7ta00371d.

[202] Aashutosh Mistry, Conner Fear, Rachel Carter, Corey T. Love, and Partha P. Mukherjee. "Electrolyte Confinement Alters Lithium Electrodeposition". In: *ACS Energy Letters* 4.1 (Dec. 2018), pp. 156–162. DOI: 10.1021/acsenergylett.8b02003. URL: https://doi.org/10.1021/acsenergylett.8b02003.

[203] Andrew J. Ilott, Mohaddese Mohammadi, Hee Jung Chang, Clare P. Grey, and Alexej Jerschow. "Real-time 3D imaging of microstructure growth in battery cells using indirect MRI". In: *Proceedings of the National Academy of Sciences* 113.39 (Sept. 2016), pp. 10779–10784. DOI: 10.1073/pnas.1607903113. URL: https://doi.org/10.1073/pnas.1607903113.

[204] Andrew J. Ilott, S. Chandrashekar, Andreas Klöckner, Hee Jung Chang, Nicole M. Trease, Clare P. Grey, Leslie Greengard, and Alexej Jerschow. "Visualizing skin effects in conductors with MRI: Li MRI experiments and calculations". In: *Journal of Magnetic Resonance* 245 (Aug. 2014), pp. 143–149. DOI: 10.1016/j.jmr.2014.06.013. URL: https://doi.org/10.1016/j.jmr.2014.06.013.

[205] Shoujun Xu, Elad Harel, David J. Michalak, Charles W. Crawford, Dmitry Budker, and Alexander Pines. "Flow in porous metallic materials: A magnetic resonance imaging study". In: *Journal of Magnetic Resonance Imaging* 28.5 (Nov. 2008), pp. 1299–1302. DOI: 10.1002/jmri.21532. URL: https://doi.org/10.1002/jmri.21532.

[206] G. Richardson, I. Korotkin, R. Ranom, M. Castle, and J.M. Foster. "Generalised single particle models for high-rate operation of graded lithium-ion electrodes: Systematic derivation and validation". In: *Electrochimica Acta* 339 (Apr. 2020), p. 135862. DOI: 10.1016/j.electacta.2020.135862. URL: https://doi.org/10.1016/j.electacta.2020.135862.

[207] Charles Monroe and John Newman. "Dendrite Growth in Lithium/Polymer Systems". In: *Journal of The Electrochemical Society* 150.10 (2003), A1377. DOI: 10.1149/1.1606686. URL: https://doi.org/10.1149/1.1606686.

[208] Akihiro Kushima, Kang Pyo So, Cong Su, Peng Bai, Nariaki Kuriyama, Takanori Maebashi, Yoshiya Fujiwara, Martin Z. Bazant, and Ju Li. "Liquid cell transmission electron microscopy observation of lithium metal growth and dissolution: Root growth, dead lithium and lithium flotsams". In: *Nano Energy* 32 (Feb. 2017), pp. 271–279. DOI: 10.1016/j.nanoen.2016.12.001. URL: https://doi.org/10.1016/j.nanoen.2016.12.001.

[209] Yangyang Liu, Xieyu Xu, Matthew Sadd, Olesya O. Kapitanova, Victor A. Krivchenko, Jun Ban, Jialin Wang, Xingxing Jiao, Zhongxiao Song, Jiangxuan Song, Shizhao Xiong, and Aleksandar Matic. "Insight into the Critical Role of Exchange Current Density on Electrodeposition Behavior of Lithium Metal". In: *Advanced Science* 8.5 (Jan. 2021), p. 2003301. DOI: 10.1002/advs.202003301. URL: https://doi.org/10.1002/advs.202003301.

[210] Kara D. Fong, Julian Self, Bryan D. McCloskey, and Kristin A. Persson. "Ion Correlations and Their Impact on Transport in Polymer-Based Electrolytes". In: *Macromolecules* 54.6 (Feb. 2021), pp. 2575–2591. DOI: 10.1021/acs.macromol.0c02545. URL: https://doi.org/10.1021/acs.macromol.0c02545.

[211] Laura Cabo-Fernandez, Alex R. Neale, Filipe Braga, Igor V. Sazanovich, Robert Kostecki, and Laurence J. Hardwick. "Kerr gated Raman spectroscopy of LiPF6 salt and LiPF6-based organic carbonate electrolyte for Li-ion batteries". In: *Physical Chemistry Chemical Physics* 21.43 (2019), pp. 23833–23842. DOI: 10.1039/c9cp02430a. URL: https://doi.org/10.1039/c9cp02430a.

[212] Andrew A. Wang, Samuel Greenbank, Guanchen Li, David A. Howey, and Charles W. Monroe. "Current-driven solvent segregation in lithium-ion electrolytes". In: *Cell Reports Physical Science* (Sept. 2022), p. 101047. DOI: 10.1016/j.xcrp.2022.101047. URL: https://doi.org/10.1016/j.xcrp.2022.101047.

[213] David S. Hall, Julian Self, and J. R. Dahn. "Dielectric Constants for Quantum Chemistry and Li-Ion Batteries: Solvent Blends of Ethylene Carbonate and Ethyl Methyl Carbonate". In: *The Journal of Physical Chemistry C* 119.39 (Sept. 2015), pp. 22322–22330. DOI: 10.1021/acs.jpcc.5b06022. URL: https://doi.org/10.1021/acs.jpcc.5b06022.

[214] D. Feakins, R. O'Neill, and E. Waghorne. "Preferential solvation of ions and solvent transport". In: *Pure and Applied Chemistry* 54.12 (Jan. 1982), pp. 2317–2326. DOI: 10.1351/pac198254122317. URL: https://doi.org/10.1351/pac198254122317.

[215] Oleg Borodin, Marco Olguin, P. Ganesh, Paul R. C. Kent, Joshua L. Allen, and Wesley A. Henderson. "Competitive lithium solvation of linear and cyclic carbonates from quantum chemistry". In: *Physical Chemistry Chemical Physics* 18.1 (2016), pp. 164–175. DOI: 10.1039/c5cp05121e. URL: https://doi.org/10.1039/c5cp05121e.

[216] Kang Xu, Yiufai Lam, Sheng S. Zhang, T. Richard Jow, and Timothy B. Curtis. "Solvation Sheath of Li+ in Nonaqueous Electrolytes and Its Implication of Graphite-Electrolyte Interface Chemistry". In: *The Journal of Physical Chemistry C* 111.20 (May 2007), pp. 7411–7421. DOI: 10.1021/jp068691u. URL: https://doi.org/10.1021/jp068691u.

[217] Ermanno Miele, Wesley M. Dose, Ilya Manyakin, Michael H. Frosz, Zachary Ruff, Michael F. L. De Volder, Clare P. Grey, Jeremy J. Baumberg, and Tijmen G. Euser. "Hollow-core optical fibre sensors for operando Raman spectroscopy investigation of Li-ion battery liquid electrolytes". In: *Nature Communications* 13.1 (Mar. 2022). DOI: 10.1038/s41467-022-29330-4. URL: https://doi.org/10.1038/s41467-022-29330-4.

[218] Hans-Georg Steinrück, Christopher J. Takacs, Hong-Keun Kim, David G. Mackanic, Benjamin Holladay, Chuntian Cao, Suresh Narayanan, Eric M. Dufresne, Yuriy Chushkin, Beatrice Ruta, Federico Zontone, Johannes Will, Oleg Borodin, Sunil K. Sinha, Venkat Srinivasan, and Michael F. Toney. "Concentration and velocity profiles in a polymeric lithium-ion battery electrolyte". In: *Energy & Environmental Science* 13.11 (2020), pp. 4312–4321. DOI: 10.1039/d0ee02193h. URL: https://doi.org/10.1039/d0ee02193h.

[219] M. Farkhondeh, M. Pritzker, C. Delacourt, S. S.-W. Liu, and M. Fowler. "Method of the Four-Electrode Electrochemical Cell for the Characterization of Concentrated Binary Electrolytes: Theory and Application". In: *The Journal of Physical Chemistry C* 121.8 (Feb. 2017), pp. 4112–4129. DOI: 10.1021/acs.jpcc.6b11501. URL: https://doi.org/10.1021/acs.jpcc.6b11501.

[220] Aashutosh Mistry and Venkat Srinivasan. "Do we need an accurate understanding of transport in electrolytes?" In: *Joule* 5.11 (Nov. 2021), pp. 2773–2776. DOI: 10.1016/j.joule.2021.10.007. URL: https://doi.org/10.1016/j.joule.2021.10.007.

[221] B. J. Steel and R. H. Stokes. "A Hittorf Transference Number Apparatus Employing Conductimetric Analysis of the Solutions". In: *The Journal of Physical Chemistry* 62.4 (Apr. 1958), pp. 450–452. DOI: 10.1021/j150562a019. URL: https://doi.org/10.1021/j150562a019.

[222] M. S. Ding, K. Xu, S. S. Zhang, K. Amine, G. L. Henriksen, and T. R. Jow. "Change of Conductivity with Salt Content, Solvent Composition, and Temperature for Electrolytes of LiPF[sub 6] in Ethylene Carbonate-Ethyl Methyl Carbonate". In: *Journal of The Electrochemical Society* 148.10 (2001), A1196. DOI: 10.1149/1.1403730. URL: https://doi.org/10.1149/1.1403730.

[223] Volker L. Deringer, Albert P. Bartók, Noam Bernstein, David M. Wilkins, Michele Ceriotti, and Gábor Csányi. "Gaussian Process Regression for Materials and Molecules". In: *Chemical Reviews* 121.16 (Aug. 2021), pp. 10073–10141. DOI: 10.1021/acs.chemrev.1c00022. URL: https://doi.org/10.1021/acs.chemrev.1c00022.

[224] Adarsh Dave, Jared Mitchell, Kirthevasan Kandasamy, Han Wang, Sven Burke, Biswajit Paria, Barnabás Póczos, Jay Whitacre, and Venkatasubramanian Viswanathan. "Autonomous Discovery of Battery Electrolytes with Robotic Experimentation and Machine Learning". In: *Cell Reports Physical Science* 1.12 (Dec. 2020), p. 100264. DOI: 10.1016/j.xcrp.2020.100264. URL: https://doi.org/10.1016/j.xcrp.2020.100264.

[225] Christopher K Williams and Carl Edward Rasmussen. *Gaussian processes for machine learning*. Vol. 2. 3. MIT press Cambridge, MA, 2006.

[226] GPy. *GPy: A Gaussian process framework in python*. http://github.com/SheffieldML/GPy. since 2012.

[227] Ndrewwang. *ndrewwang/SolventSeg: v1.0.0*. 2022. DOI: 10.5281/ZENODO.6299956. URL: https://zenodo.org/record/6299956.

[228] Valerio De Angelis, Yuliya Preger, and Babu R. Chalamala. "Battery Lifecycle Framework: A Flexible Repository and Visualization Tool for Battery Data from Materials Development to Field Implementation". In: (Mar. 2021). DOI: 10.1149/osf.io/h7c24. URL: https://doi.org/10.1149/osf.io/h7c24.

[229] Logan Ward et al. *Principles of the Battery Data Genome*. 2021. DOI: 10.48550/ARXIV.2109.07278. URL: https://arxiv.org/abs/2109.07278.

[230] Hooman Hafezi and John Newman. "Verification and Analysis of Transference Number Measurements by the Galvanostatic Polarization Method". In: *Journal of The Electrochemical Society* 147.8 (2000), p. 3036. DOI: 10.1149/1.1393644. URL: https://doi.org/10.1149/1.1393644.

[231] Shoichi Matsuda, Guillaume Lambard, and Keitaro Sodeyama. "Data-driven automated robotic experiments accelerate discovery of multi-component electrolyte for rechargeable Li–O2 batteries". In: *Cell Reports Physical Science* 3.4 (Apr. 2022), p. 100832. DOI: 10.1016/j.xcrp.2022.100832. URL: https://doi.org/10.1016/j.xcrp.2022.100832.

[232] Anand Narayanan Krishnamoorthy, Christian Wölke, Diddo Diddens, Moumita Maiti, Youssef Mabrouk, Peng Yan, Mariano Grünebaum, Martin Winter, Andreas Heuer, and Isidora Cekic-Laskovic. "Data-Driven Analysis of High-Throughput Experiments on Liquid Battery Electrolyte Formulations: Unraveling the Impact of Composition on Conductivity∗∗". In: *Chemistry–Methods* (June 2022). DOI: 10.1002/cmtd.202200008. URL: https://doi.org/10.1002/cmtd.202200008.

[233] Felix Hildenbrand, Felix Aupperle, Gereon Stahl, Egbert Figgmeier, and Dirk Uwe Sauer. "Selection of Electrolyte Additive Quantities for Lithium-Ion Batteries Using Bayesian Optimization". In: *Batteries &amp Supercaps* (Mar. 2022). DOI: 10.1002/batt.202200038. URL: https://doi.org/10.1002/batt.202200038.

[234] Hiroshi Ohno and Akitoshi Suzumura. "Electrolyte recommender system for batteries using ensemble Bayesian optimization". In: *IFAC Journal of Systems and Control* 16 (June 2021), p. 100158. DOI: 10.1016/j.ifacsc.2021.100158. URL: https://doi.org/10.1016/j.ifacsc.2021.100158.

[235] Eibar Flores, Christian Wölke, Peng Yan, Martin Winter, Tejs Vegge, Isidora Cekic-Laskovic, and Arghya Bhowmik. "Learning the laws of lithium-ion transport in electrolytes using symbolic regression". In: *Digital Discovery* (2022). DOI: 10.1039/d2dd00027j. URL: https://doi.org/10.1039/d2dd00027j.

[236] Kevin L. Gering. "Prediction of Electrolyte Conductivity: Results from a Generalized Molecular Model Based on Ion Solvation and a Chemical Physics Framework". In: *Electrochimica Acta* 225 (Jan. 2017), pp. 175–189. DOI: 10.1016/j.electacta.2016.12.083. URL: https://doi.org/10.1016/j.electacta.2016.12.083.

[237] Lei Cheng, Rajeev S. Assary, Xiaohui Qu, Anubhav Jain, Shyue Ping Ong, Nav Nidhi Rajput, Kristin Persson, and Larry A. Curtiss. "Accelerating Electrolyte Discovery for Energy Storage with High-Throughput Screening". In: *The Journal of Physical Chemistry Letters* 6.2 (Jan. 2015), pp. 283–291. DOI: 10.1021/jz502319n. URL: https://doi.org/10.1021/jz502319n.

[238] Aashutosh Mistry, Alejandro A. Franco, Samuel J. Cooper, Scott A. Roberts, and Venkatasubramanian Viswanathan. "How Machine Learning Will Revolutionize Electrochemical Sciences". In: *ACS Energy Letters* (Mar. 2021), pp. 1422–1431. DOI: 10.1021/acsenergylett.1c00194. URL: https://doi.org/10.1021/acsenergylett.1c00194.

[239] Austin D. Sendek, Brandi Ransom, Ekin D. Cubuk, Lenson A. Pellouchoud, Jagjit Nanda, and Evan J. Reed. "Machine Learning Modeling for Accelerated Battery Materials Design in the Small Data Regime". In: *Advanced Energy Materials* n/a (), p. 2200553.